

**Scanning Tunneling Microscopy Studies on Enhanced
Electron Field Emission Properties of Modified
Nanostructured Diamond Films**

by

KALPATARU PANDA
(Enrolment No: PHYS02200704023)

Indira Gandhi Centre for Atomic Research, Kalpakkam, India

*A thesis submitted to the
Board of Studies in Physical Sciences
In partial fulfilment of requirements
For the Degree of*

DOCTOR OF PHILOSOPHY

Of

HOMI BHABHA NATIONAL INSTITUTE, MUMBAI



May, 2013

Homi Bhabha National Institute

Recommendations of the Viva Voce Board

As members of the Viva Voce Board, we certify that we have read the dissertation prepared by Kalpataru Panda entitled "Scanning Tunneling Microscopy Studies on Enhanced Electron Field Emission Properties of Modified Nanostructured Diamond Films" and recommend that it may be accepted as fulfilling the dissertation requirement for the Degree of Doctor of Philosophy.

C. S. Sundar Date: 27/8/2013
Chairman – C. S. Sundar

B. K. Panigrahi Date: 27-08-2013
Convener/Guide – B. K Panigrahi

K. G. M Nair Date: 27-08-2013
Member – K. G. M Nair

G. Amarendra Date: Aug 27, 2013
Member – G. Amarendra

External Examiner – D.K. AVASTHI Date: 27/08/2013

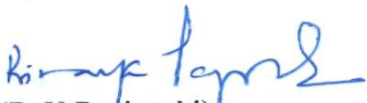
Final approval and acceptance of this dissertation is contingent upon the candidate's submission of the final copies of dissertation to HBNI.

Date: 27-08-2013
Place: Kalpakkam

CERTIFICATE

I hereby certify that I have read this dissertation prepared under my direction and recommend that it may be accepted as fulfilling the dissertation requirement.

Date: 30/05/2013
Place: Kalpakkam


(B. K Panigrahi)

STATEMENT BY AUTHOR

This dissertation has been submitted in partial fulfilment of requirements for an advanced degree at Homi Bhabha National Institute (HBNI) and is deposited in the library to be made available to borrowers under rules of the HBNI.

Brief quotations from this dissertation are allowable without special permission, provided that accurate acknowledgement of source is made. Requests for permission for extended quotation from or reproduction of this manuscript in whole or in part may be granted by the Competent Authority of HBNI when in his or her judgment the proposed use of the material is in the interests of scholarship. In all other instances, however, permission must be obtained from the author

Kalpataru Panda
(Kalpataru Panda)
Ph. D Candidate

DECLARATION

Dedicated to

I, hereby declare that the investigation presented in the thesis has been carried out by me. The work is original and has not been submitted earlier as a whole or in part for a degree / diploma at this or any other Institution / University.

Signature of

Kalpataru Panda
(Kalpataru Panda)
Ph. D Candidate

Dedicated to
All
Visionaries & Well wishers of Mankind

A space for

My Parents

ACKNOWLEDGEMENT

First of all, I express sincere gratitude to my research supervisor Dr. Binaya Kumar Panigrahi, Head, Ion Beam & Computer Simulation Section, IGCAR, for his wholehearted support, encouragement, caring and guidance during my PhD period. His willingness towards learning, enthusiasm, experience and friendliness has made my research life more smooth and enjoyable. He has provided me freedom in research and extended his helping hand whenever it is necessary.

I thank my doctoral committee member, Dr. C. S Sundar, Director, Material Science Group for his consistent help, support and encouragement. I specially thank him for allowing me to work on diamond films. I thank Dr. K.G.M Nair, Head, AMSS, IGCAR for his support and correcting chapters of my thesis. I thank Dr. G. Amarendra, Head, MPD, IGCAR for his support and encouragement during my research period.

I thank Dr. Baldev Raj, former Director, IGCAR for his encouragement, friendliness and creating a research spirit in JRF enclave. I am thankful to Dr. P. R Vasudeva Rao, Director, IGCAR, for his support and encouragement. I thank Shri M. C Valsakumar, former Head, MPD for motivation and support. I also convey my hearty thanks to Dr. M. Sai Baba, Associate Director, RMG, IGCAR for his help, support and for providing best facilities at JRF enclave.

I am deeply thankful to Dr. Balakrishnan Sundaravel, for his consistent help, encouragement and support throughout my research period. He is the person who introduced me to the field of diamond films and sketches a plan for my research. I especially thank my collaborator Prof. I-Nan Lin, Tamkang University, Taiwan for his consistent help, support and encouragement. Without his timely help and support, it would be difficult for me to finish my research work. I sincerely thank Dr. S. Amrithapandian for his consistent encouragement, moral support throughout my research period and thoroughly going through my thesis chapters. I gratefully thank Dr. Niranjana Kumar for his consistent help, encouragement and moral support during all the up and down situations. I learned a lot from him during my PhD period. I am thankful

to Mr. P. Maudapathy for his help in ion implantation experiments. I am especially influenced by his simple and helping nature. I would like to thank Mr. C. David, Dr. P. Gangopadhya, Mr. Sachin Kumar Srivastava, Mr. P. Jagdesan, Mr. S. Balaji, Ms. Sumita santra, Mr. J. Navas, Mr. Vaskaran, Mr. Dasarathan, Mr. Dandapani for their kind help and support during my PhD period. I sincerely thank my seniors Dr. Sathana raman, Dr. Saravan kumar, Dr. Arun kumar for their help, support and encouragement. Dr. Santhana raman helped me a lot in experiments during my initial PhD period. I am very much thankful to each MSG member for creating a frank and lively environment in the group which helped me a lot. I am thankful to Mr. Nanda Gopal Krishnan, for his help in XPS experiments. I thank Shyamala Rao for his help in FESEM experiments. I sincerely thank Dr. Sandip Dhara for allowing me to carryout Raman measurements in his lab. I would like to thank Mr. K. J Sankaran, National Tsing-Hua University, Taiwan for providing diamond films for my research. I thank Dr. Hung-Chin Chen, Tamkang University, Taiwan for his help in TEM experiments.

It is my pleasure to keep a special thank to Bishnu (bhakate). I am fortunate to have friends around me like Prasana, Asit, Saravanakumar, Kamalakanta whose presence makes my staying more exciting and enjoyable in Kalpakkam. My special gratitude to my close intimates Manas, Sudhansu, Pradeep, Saswat, Alok, Karunakar, Haribabu, Joysankar, Herojit, Rahul, Girish, Varghese, Rajini, Subhra, Madhusmita, Nithila, pravati, Sorb, Baban, Kamalakanan, Sunasira, Bonu, Subhrat, Susil, Ashok and all research scholar friends for making my life more Friendly and charming during my stay at JRF Enclave, Kalpakkam.

In the last and above all, I would like to express my heartiest gratitude and honor to my parents, Sri Avimanyu Panda and Smt. Minati Panda, my elder brothers and all family members for always extending their love, affection and emotional support.

(Kalpataru Panda)

Synopsis

Introduction

Diamond and related materials have enormous potential applications due to their interesting physical and chemical properties. It exhibits a synergetic combination of better electrical, thermal, tribological and biocompatible properties, which enable the material to generate multifunctional devices from macro to nanoscale. These multifunctional devices include i) field emission (FE) cathodes and high-frequency X-ray sources ii) coatings for mechanical pump seals iii) MEMS/NEMS devices iv) biomedical devices v) biosensors vi) platform for developmental biology.

Diamond a wide-band-gap semiconductor ($E_g=5.5$ eV) with high resistivity, do not appear to be a suitable material for electron field emission (EFE) applications. In case of an undoped diamond, the concentration of electrons in the conduction band is almost too negligible to be emitted. In spite of the above-mentioned disadvantages, diamond has a series of excellent physical and chemical properties, which make it one of the strongly contending cold cathode materials for field emission (FE) applications. It has low work function and negative electron affinity (NEA) properties. Diamond has strongly bonded crystal structure, such that FE devices from diamond could operate with maximum stability and reliability. Furthermore, diamond can operate at high temperature or high power because of its high electrical breakdown field and thermal conductivity that are beneficial for field emission processes. With these attractive features of the diamond surface, adding the new ability to deposit diamond thin film on a variety of substrates using various low-pressure chemical vapour deposition (CVD)

techniques has created strong interest in the applications of diamond as an electron field emitter.

Ultrananocrystalline diamond (UNCD) film is a special form of diamond that has recently caught great attention from researchers because of its better EFE properties. Along with the ultra-small (3 to 5 nm) diamond grain size, UNCD film has very smooth surface characteristics. The grains are of diamond, having a sp^3 character whereas the grain boundaries have a mixture of sp^2 , sp^3 , hydrocarbon and amorphous carbon, where sp^2 character is predominant. Large field emission current density from UNCD film, as compared to other forms of diamond films (nanocrystalline or microcrystalline), makes it a suitable candidate for application in the field of cold cathode emitters and other vacuum microelectronic devices. However, the EFE properties of UNCD films are still not sufficiently good as compared to those of nano-carbon materials. There are many different approaches to modify the surface of diamond films so as to enhance the EFE properties.

Incorporating nitrogen (N) into conventional microcrystalline diamond (MCD) with micron-sized grains to improve the conductivity was not effective, because N forms a deep donor level and does not enhance the conductivity. In contrast, the conductivity of UNCD films has been improved by incorporating N into the grain boundaries of UNCD films and hence facilitates for enhanced EFE properties of these films. However, N incorporation via adding N_2 gas in the growth plasma is not efficient due to the small size of the UNCD grains. On the other hand, ion implantation has been a traditional technique to modify the properties of materials through controlled doping of variety of dopants. Ion implantation can introduce defects and break the C-C and

hydrocarbon bonds to form sp^2 carbon. It can also be used to tailor the sp^3/sp^2 ratio for diamond and related materials by properly selecting the dose and energy of the implantation. However, the EFE properties of N implanted materials are still not satisfactory implying the fact that most of the sample surfaces do not have the negative electron affinity characteristics because they are not re-constructed (100) surfaces. There are other methods to modify the surface of diamond films to increase the NEA characteristics. Among the approaches, a thin layer of metallic coating on diamond films, followed by post-annealing in H_2 atmosphere significantly improves the EFE properties.

This thesis work presents the significant enhancement in EFE properties of diamond films by different surface modification techniques such as by (i) N^+ ion implantation to UNCD films (ii) N^+ ion implantation to hybrid structured diamond films, where a UNCD interlayer is used for the growth of microcrystalline diamond (MCD) films and (iii) by depositing a thin layer of iron (Fe) on MCD and UNCD films followed by post-annealing. An attempt has been made to understand the underlying mechanisms that drive the EFE properties for these surface modified diamond films by various experimental techniques.

Outline of the Research work

Chapter 1 Introduction

This chapter gives a brief overview on EFE properties of different grain sized diamond thin films, emphasizing the benefit of it for EFE applications over other metal and semiconductor films. Further, a brief review of different surface modification techniques described in literature for obtaining better EFE properties are discussed. The

reasons behind enhanced EFE behaviour of surface modified diamond films are described in detail. Further, the motivation for using N ion implantation and metallic Fe coating/post-annealing process to improve the EFE properties of diamond films is discussed along with a brief outline of the organization of thesis.

Chapter 2 Experimental Techniques

Chapter 2 discusses the synthesis procedures and experimental techniques used in the thesis. The nanostructured diamond films were synthesized using microwave plasma enhanced chemical vapour deposition (MPECVD) technique. A brief summary of MPECVD technique and ion implantation methods are described. A description of a setup to measure the EFE properties of diamond films is described.

The samples were investigated by several analytical tools such as ultra high vacuum scanning tunneling microscope (UHV STM), Transmission electron microscope (TEM), field emission scanning electron microscope (FESEM), X-ray photo electron spectrometer (XPS), Raman spectrometer, glancing incident X-ray diffraction (GIXRD). A short description of each characterization technique is also presented.

Chapter 3 Mechanism of enhanced electron field emission in nitrogen ion implanted ultrananocrystalline diamond (UNCD) films

UNCD film is a special form of diamond having 3 to 5 nm diamond grains with fine grain boundaries, has better EFE properties than micro or nanocrystalline diamond films. The EFE properties are further improved by N⁺ ion implantation/post-annealing process. However, the reasons for improved EFE properties of N⁺ implanted UNCD

films are still not clear. Several mechanisms have been proposed to explain the observed field emission behaviour, while no single mechanism alone could give a complete picture.

This chapter deals with the possible reasons for the enhancement in EFE properties of nitrogen implanted UNCD films. Scanning tunnelling spectroscopy (STS) has been used to determine the local electronic density of states (DOS) at the grain, grain boundary and the possible electron emission sites. XPS measurements show sp^2 fraction and C–N bonding phase increase upon N^+ ion implantation and post-annealing processes. Significant change in current-voltage (I-V) curves at the grain and grain boundary is observed from STS measurements. From the variation of normalized conductance $\frac{dI/dV}{IV}$ versus V, band gap is measured to be 4.8 eV at the diamond grain and 3.8 eV at the grain boundary for as prepared UNCD films. Upon N^+ ion implantation and annealing, the band gap decreases for both grain and grain boundary and density of states are introduced in the band gap. Current imaging tunnelling spectroscopy (CITS) images show grain boundaries have higher conductivity than grains and are the prominent electron emission sites. The enhancement in EFE properties upon N^+ implantation is accounted for by the decrease in band gap, increase in density of states in the band gap, formation of new bonds at the diamond grains and increase in conductivity at the grain boundaries.

Chapter 4 Direct Observation of Enhanced Electron field emission Sites in Nitrogen ion implanted Hybrid structured nanocrystalline diamond films

The non-diamond phase (sp^2 , amorphous carbon, nanographite etc) content and the size of diamond grains play a crucial role for the EFE properties of diamond films.

In an effort to increase the non-diamond phase content in diamond film and thus to improve the EFE properties, a modified nucleation and growth process, which utilized a layer of UNCD film as the nucleation layer for the growth of a hybrid structured diamond (MCD/UNCD) film, is discussed in this chapter. Such a unique hybrid structured film exhibits better EFE properties than the conventional micro, nano or ultrananocrystalline diamond films.

This chapter describes a detailed study on the effect of N^+ ion implantation in modifying the microstructure and EFE properties of MCD/UNCD hybrid structured diamond films. XPS measurements show increased sp^2 content and C-N bonding fraction in N^+ ion implanted and post-annealed films. Scanning tunnelling spectroscopy (STS) in current imaging tunnelling spectroscopy mode clearly shows increased number density of emission sites in N^+ implanted/post-annealed MCD/UNCD hybrid structured films than as-prepared one. TEM analysis reveals, N implantation/post-annealing processes induced formation of defects in the diamond grains that increased the density of states within the band gap of diamond. Moreover, the formation of nanographitic phase surrounding the small diamond grains enhances the conductivity at the diamond grain boundaries. Both the phenomena enhanced the EFE properties. The role of the nanographitic phase in improving the field emission sites in N^+ ion implanted and post-annealed films is explained by high resolution CITS images.

Chapter 5 Direct Observation and Mechanism of Enhanced Electron Field emission in Iron coated microcrystalline and ultrananocrystalline diamond films

Metallic Fe-coating and post-annealing processes at high temperatures is observed to markedly modify the surface characteristics and enhance the EFE properties of MCD

and UNCD films. This chapter is divided into two parts: the first part describes the enhanced EFE properties of Fe coated/post-annealed MCD films and the second part deals with the effect of Fe coating/post-annealing processes on the EFE properties of UNCD films.

The evolution of surface morphology and structure of MCD and UNCD films with post-annealing temperature is investigated in more detailed. The Fe coated and post-annealed (at 900 °C) MCD films [(Fe/MCD)₉₀₀], exhibit better EFE properties, with a turn on field (E_0) of 3.42 V/ μm and attain EFE current density (J_e) of 170 $\mu\text{A}/\text{cm}^2$ at 7.5 V/ μm . XPS measurements show sp^2 phase fraction and concentration of Fe (or Fe₃C) phases are more in ((Fe/MCD)₉₀₀) films, which have better EFE properties compared to films annealed at higher temperatures. STS in CITS mode clearly shows increased number densities of emission sites in (Fe/MCD)₉₀₀ films than the as-deposited ones. I-V curves show ohmic behaviour, whereas $\frac{dI/dV}{I/V}$ versus V curves show nearly metallic band gap, at the grain boundaries of Fe (or Fe₃C) nanoparticles, as observed from STS measurements. Microstructural analysis indicates the mechanism of enhanced EFE properties is due to the formation of nanographitic phase at the boundaries of the Fe (or Fe₃C) nanoparticles, which are formed due to the reaction of Fe clusters with diamond films during the annealing process. The nanographitic phase is formed by the re-precipitation of carbon species, which is dissolved in the Fe clusters, a process similar to the growth of carbon nanotubes via Fe clusters as catalyst.

Moreover, the Fe-coating/post-annealing processes enhanced the EFE properties of UNCD films more than that on MCD films. A detailed study has been made to understand the enhancement in EFE properties of Fe-coated/post-annealed UNCD films

than that of MCD films. The higher enhancement in EFE properties of Fe-coated/post-annealed UNCD films is attributed to the unique granular structure of these films. The nano-sized and uniformly distributed grains of UNCD films resulted in markedly smaller and densely populated Fe-clusters, which, in turn, induced more finer and higher populated nano-graphite clusters. The best EFE properties, with a turn on field (E_0) of 1.98 V/ μm and current density (J_e) of 705 $\mu\text{A}/\text{cm}^2$ at 7.5 V/ μm , are obtained for UNCD films, which are Fe-coated/post-annealed at 900 °C in H_2 atmosphere. The mechanism behind the enhanced EFE properties of the Fe coated/post-annealed UNCD films are explained by the TEM analysis which shows formation of nanographitic phase surrounding the Fe (or Fe_3C) nanoparticles. The role of the nanographitic phase in improving the emission sites of Fe coated/post-annealed UNCD films is revealed by the high resolution CITS images. The CITS images clearly show significant emission sites in Fe-coated/post-annealed UNCD films compared to as-deposited one. Enhanced emission sites are mostly seen around the boundaries of the Fe (or Fe_3C) nanoparticles which are formed due to the Fe-coating/post-annealing processes. The normalized conductance curves in STS indicate metallic type band gap at the boundaries of the Fe (or Fe_3C) nanoparticles.

Chapter 6

This chapter summarizes the major research finding, implications and scope for future work.

Appendix Tribological Properties of Nitrogen Ion Implanted Ultrananocrystalline Diamond Films

The tribological properties of nitrogen ion implanted UNCD films are discussed. UNCD films exhibit better tribological properties due to their nanocrystalline grain size. However, the tribological properties of UNCD films improve after N^+ ion implantation and post-annealing processes. This study aims to explore the possible reasons for the improvement in tribological properties of nitrogen ion implanted/post-annealed UNCD films. Detailed structural characteristics have been analyzed by various analytical techniques which explain the nanomechanical and tribological behavior of N^+ ion implanted/post-annealed UNCD films.

Friction coefficient is found to be 0.15 in as-prepared films comparing to 0.09 and 0.05 in N^+ ion implanted and post-annealed films, respectively. Such a modification of friction coefficient is a characteristic of the transformation of sp^3 to graphitized/amorphized sp^2 bonded carbon network. Graphitization/amorphization in wear track observed by micro Raman spectroscopy is found to be the prominent mechanism for the reduction in friction coefficient.

Contents

	Page No.
Synopsis	ix
List of figures	xxii
List of Tables	xxix
List of abbreviations	xxx
Chapter 1	
Introduction	1
1.1 Nanostructured Carbon Materials	3
1.2 Electron field emission behavior and their application	9
1.3 Electron emission mechanism in diamond cathodes	12
1.4 Microstructure and EFE properties of MCD/NCD/UNCD films	17
1.4.1 Electronic Behaviour of Diamond Films	20
1.4.2 Improvement in EFE Properties of Diamond Films by Doping	21
1.4.3 Doping by ion implantation	24
1.5 Motivation and Overview of Thesis	26
1.6 References	29
Chapter 2	
Experimental Techniques	36
2.1 Introduction	36
2.2 Growth of Diamond films	36
2.2.1 Microwave Plasma Enhanced Chemical Vapour Deposition (MPECVD)	37
2.3 Surface modification of diamond films	41
2.3.1 Ion implantation	41
2.4 Structural and morphological characterization	43
2.4.1 Scanning tunneling microscope (STM)	43
2.4.1.1 Instrumentation	44
2.4.1.2 Principle of Operation	46
2.4.1.3 Scanning tunneling spectroscopy (STS)	48
2.4.1.4 Acquisition of STS data	52
2.4.1.5 Data interpretation	53
2.4.2 Transmission Electron Microscopy (TEM)	54

	2.4.2.1 Principle	54
	2.4.2.2 Components of TEM	56
	2.4.3 Scanning Electron Microscope (SEM)	59
2.5	Electron field emission	60
2.6	X-ray Photoelectron Spectroscopy (XPS)	61
2.7	Raman spectroscopy	63
2.8	X-ray diffraction (XRD)	63
2.9	Tribometer	65
	2.9.1 CSM Tribometer	65
2.10	Nanoindentation technique	66
2.11	Scratch testing	67
2.12	Conclusion	68
2.13	References	69
CHAPTER 3	Mechanism of Enhanced Electron Field Emission in Nitrogen Ion Implanted Ultrananocrystalline Diamond Films	72
3.1	Introduction	72
3.2	Experimental Details	74
3.3	Results and Discussions	75
	3.3.1 Material Characteristics	75
	3.3.2 Transmission Electron Microscopy Results	81
	3.3.3 Scanning Tunneling Spectroscopy (STS)	86
3.4	Discussion	94
3.5	Conclusion	97
3.6	References	98
CHAPTER 4	Direct Observation of Enhanced Electron Emission Sites in Nitrogen Ion Implanted Hybrid Structured nanocrystalline Diamond Films	101
4.1	Introduction	101
4.2	Experimental Details	103
4.3	Results and Discussions	104
	4.3.1 Material Characteristics	104

	4.3.2 XPS Results	110
	4.3.3 Scanning Tunneling Spectroscopy (STS)	112
	4.3.4 Transmission Electron Microscopy Results	118
4.4	Discussion	124
4.5	Conclusion	126
4.6	References	127
CHAPTER 5	Direct Observation and Mechanism of Enhanced Electron Field Emission in Iron Coated Microcrystalline and Ultrananocrystalline Diamond Films	130
5.1	Introduction	130
5.2	Experimental Details	132
5.3	PART-1 Electron Field Emission Properties of Fe-coated/post-annealed microcrystalline diamond films	135
	5.3.1 Results	135
	5.3.1.1 General Characteristics	135
	5.3.1.2 XPS Results	140
	5.3.1.3 Transmission Electron Microscopy Results	144
	5.3.1.4 Scanning tunneling spectroscopy	147
5.4	PART-2 Electron Field Emission Properties of Fe-coated/post-annealed ultrananocrystalline diamond (UNCD) films	153
	5.4.1 Results	153
	5.4.1.1 General characteristics	153
	5.4.1.2 XPS Results	157
	5.4.1.3 Transmission Electron Microscopy Results	161
	5.4.1.4 Scanning Tunneling Spectroscopy	166
	5.4.2 Why EFE properties of Fe-coated/post-annealed UNCD films are better than that of Fe-coated/post-annealed MCD films?	175
5.5	Conclusion	177
5.6	References	178

CHAPTER 6	Brief Summary of the Thesis Work and Future Prospectives	181
6.1	Summary with future Prospectives	181
6.2	Reference	185
Appendix	Tribological Properties of Nitrogen Ion Implanted Ultrananocrystalline Diamond Films	186
A.1	Introduction	186
A.2	Experimental methods	188
A.3	Results and discussion	190
	A.3.1 Surface morphology of UNCD film examined by FESEM	190
	A.3.2 XPS analysis of UNCD films	191
	A.3.3 Raman spectroscopy of UNCD films	193
A.4	Mechanical properties of UNCD films	196
	A.4.1 Nanoindentation	196
	A.4.2 Micro scratch test of UNCD films	197
	A.4.3 Tribological properties of UNCD films	199
A.5	Wear track analysis	203
	A.5.1 EDAX analysis of wear track	203
	A.5.2 Raman spectral analysis of wear track	204
A.6	Conclusion	206
A.7	References	207
	Journal Publication and Conference Proceedings	211

LIST OF FIGURES

Figure	Figure Caption	Page No.
Fig.1.1	Diamond crystal structure	3
Fig. 1.2	Illustration of the potential application of diamond films in vacuum microelectronic technology for high power, high-frequency applications	5
Fig. 1.3	Geometric electric-field enhancement at the top of a sharpened conductive cone. (a) An electric field applied to the sharpened conductive cone produces electron emission at the top of the cone. The emission occurs at average electric field values that are lower than those needed for emission from a smooth metal surface. (b) The plot of potential energy as a function of distance from the cone tip to vacuum, where E_F is the Fermi energy in the metal, illustrates the magnitude of the potential-energy barrier Φ at the metal-vacuum interface. To be emitted from the conductive cone, electrons must tunnel a distance x through the potential barrier	12
Fig. 1.4	Cross section of metal-semiconductor and NEA-semiconductor surface-vacuum interfaces for Schottky-diode electric field enhancement with a semiconductor doped with an electron donor impurity. (a) When an electric field is applied across the semiconductor, the dopants become positively ionized and form a depletion region at the metal-semiconductor interface. Electrons tunnel from the metal into the semiconductor, and are emitted at the NEA-semiconductor surface-vacuum interface. (b) the plot of potential energy as a function of distance, where E_F is the Fermi energy in the metal, illustrating the potential-energy barrier Ψ at the metal-semiconductor interface. To be emitted from the metal substrate, electrons must tunnel a distance y through the potential barrier	14
Fig. 1.5	Triple junction (metal-semiconductor-vacuum) electric-field enhancement (a) The combination of an impurity-donor-doped semiconductor and the high mobility of electrons at the NEA-semiconductor surface-vacuum interface causes electrons to tunnel from the metal substrate onto the surface of semiconductor. Depending upon the angle θ between the semiconductor-vacuum interface and the metal substrate, as shown in figure 1.5 (a), the electric-field enhancement can be larger than that obtained with the two mechanisms discussed in figure 1.3 (a) and figure 1.4 (a). (b) The plot of potential energy along the semiconductor-vacuum interface, where E_F is the Fermi energy in the metal, illustrates the potential-energy barrier. To be emitted at the semiconductor-vacuum interface, electrons must tunnel a distance z from the metal substrate into the triple-junction region. The potential	16

barrier, while difficult to determine, is known to be less than the potential barrier for the geometric electric-field enhancement mechanism

Fig. 1.6	Schematic model diagram of (a) MCD, (b) NCD, and (c) UNCD films The white and black regions represent diamond and nondiamond contents (amorphous and/or graphitic carbon), respectively. Band diagrams of single-crystal (d) diamond and (e) graphite. The nondiamond carbon contents in the film are extremely essential for the easy electron conduction inside the matrix and also from back to front surface of the film before being emitted from the edges of the diamond grain experiencing a lower work function of 3.5 eV	18
Fig. 1.7	Comparison of the local electronic density of states in the diamond grain boundary averaged over the atoms in the grain boundary region (solid curve) with that in the perfect bulk crystal (dashed curve). The shaded region indicates states localized at sp^2 dimers; the striped region indicates states localized at sp^3 sites. The Fermi level at 3.5 eV is indicated by an arrow	21
Fig. 1.8	Band alignment and position of N donor states in diamond	23
Fig. 1.9	Band bending and reduced tunneling distance at the back contact due to a depletion layer of ionized nitrogen donors	23
Fig. 2.1	IPLAS MPECVD system used for the growth of diamond film in the present work	38
Fig. 2.2	Cross-Section Geometry of a IPLAS microwave Plasma Source	38
Fig. 2.3	Schematic diagram of the physical and chemical processes occurring during the CVD diamond growth	39
Fig. 2.4	Schematic diagram of the 150 kV ion accelerator	42
Fig. 2.5	Photograph of the 150 kV ion accelerator and the parts of the accelerator are given	42
Fig. 2.6	Schematic diagram of STM	45
Fig. 2.7	Schematic diagram of a STM head	46
Fig. 2.8	Schematic diagram of tunneling spectroscopy using idealized band structure in which the tip is modeled, as a metal as continuous occupation to the Fermi level, and the sample is imaged as semiconductor with surface states. Shaded areas refer to energy regions in which states are occupied	47
Fig. 2.9	The bright field and dark field modes for imaging	56
Fig. 2.10	Schematic diagram of TEM showing the two basic modes of operation (a) diffraction mode and (b) image mode	57
Fig. 2.11	Schematic diagram of the field emission set up used for measuring the field emission properties of diamond films	61
Fig. 2.12	CSM Tribometer used for tribological studies	66

Fig. 2.13	Optical micrograph of CSM Revetest	68
Fig. 3.1	(a) Fowler-Nordheim plot of the EFE property of UNCD film for (1) as deposited, (2) nitrogen ion implanted, (3) nitrogen ion implanted and post-annealed UNCD films. The inset shows the corresponding J-E curves	76
Fig. 3.2	Raman spectra taken with 514.5 nm line of Ar ⁺ ion laser from (a) as prepared, (b) N ⁺ ion implanted and (c) post-implantation annealed UNCD films.	77
Fig. 3.3	C-1s XPS spectra from (a) as prepared, (b) N ⁺ ion implanted and (c) post-implantation annealed UNCD samples	79
Fig. 3.4	The low magnification bright field micrographs with the inset showing the SAED pattern for (a) as-deposited, (b) N ⁺ ion implanted and (c) post-implantation annealed UNCD films	82
Fig. 3.5	TEM structure image of the (a) small grain region and (b) large grain region of N ⁺ ion implanted UNCD films. The inset shows the corresponding fourier transform images.	83
Fig. 3.6	The (a) bright field image of the post-implantation annealed UNCD films, which were N ion implanted with a fluence of 5×10 ¹⁵ ions/cm ² and annealed at 600°C for 30 min; (b, c) the structure images of the large grain region (b) and small grain regions (c). The insets FT ₁ and FT ₂ are the FT-images of the upper and lower part of large grains region in (b), whereas inset FT ₃ is the FT-image of the smaller grain region in (c)	85
Fig. 3.7	(a) UHV STM picture of as-prepared UNCD sputter cleaned with Ar ions, (b) STS taken in CITS mode showing the current map and (c) normalized differential conductance, $\frac{dI/dV}{I/V}$, at the grain and grain boundary	87
Fig. 3.8	(a) UHV STM image of UNCD after N ⁺ ion implantation with a fluence of 5×10 ¹⁵ ions/cm ² showing globular clusters; (b) high resolution UHV STM image of the same film showing UNCD grains of 2-5 nm size and grain boundaries; (c, d) STS taken in CITS mode showing (c) the current map and (d) $\frac{\partial I}{\partial V}$ map at a negative bias of 3.255 V in N ⁺ ion implanted UNCD	89
Fig. 3.9	(a) UHV STM picture of post-implantation annealed UNCD and (b) STS taken in CITS mode showing the current map (c) high resolution UHV STM image from region “5” in Figure 3.9(a) and its corresponding CITS image (d) showing the current map	90
Fig. 3.10	I-V curves at the grain (i) and grain boundary (ii) of N ⁺ ion implanted UNCD films [marked as “3” & “4” in the high resolution UHV STM image, Fig. 3.8(b)] and at the grain (iii) and grain boundary (iv) of UNCD films after post-implantation annealing [marked as “5” & “6” in	92

	the high resolution UHV STM image, Fig. 3.9(b)]. In each region 10 numbers of I-V curves have been shown	
Fig. 3.11	(a) Normalized differential conductance ($\frac{dI/dV}{I/V}$) at the (i) grain and (ii) grain boundaries of N ⁺ ion implanted UNCD, (b) at (iii) grain and (iv) grain boundaries after post-implantation annealing. Each spectrum is averaged over 10 scanned spectra shown in the figure 3.10	93
Fig. 4.1	Schematic diagram of N ⁺ ion implanted MCD/UNCD films	103
Fig. 4.2	Electron field emission properties of (I) as-prepared UNCD, (II) as prepared MCD/UNCD (III) N ⁺ ion implanted MCD/UNCD and (IV) post-annealed MCD/UNCD films. The inset shows the F-N plot of the corresponding J-E graph	105
Fig. 4.3	SEM micrograph of the (a) as-prepared UNCD, (b) as-prepared MCD/UNCD (c) N ⁺ ion implanted and (d) post-annealed MCD/UNCD films	107
Fig. 4.4	Raman spectra from (a) as-prepared, (b) N ⁺ ion implanted and (c) post-annealed MCD/UNCD films recorded with 514.5 nm laser line	108
Fig. 4.5	C-1s XPS spectra from (a) as-prepared, (b) N ⁺ ion implanted and (c) post- annealed MCD/UNCD films	110
Fig. 4.6	The STM image of (a) as-prepared MCD/UNCD films with (b) the corresponding CITS image; the STM image of (c) N ⁺ ion implanted MCD/UNCD films with (d) the corresponding CITS; the STM image of (e) post-annealed MCD/UNCD films with (f) the corresponding CITS	113
Fig. 4.7	The high resolution STM (HRSTM) image of (a) N ⁺ ion implanted MCD/UNCD films with (b) the corresponding CITS image; (c) that of the post-annealed MCD/UNCD films with (d) the corresponding CITS	115
Fig. 4.8	The local I-V curves obtained in STS measurements at (1) the grain and (2) the grain boundary of N ⁺ ion implanted MCD/UNCD films [marked as “i” and “ii” in high resolution STM image in figure 4.7(a)]; those at (3) the grain and (4) the grain boundary of post-implantation annealed MCD/UNCD films [marked as “iii” and “iv” in high resolution STM image in figure 4.7(c)]. The thick line drawn corresponds to the average of 10, I-V curves at the designated points	117
Fig. 4.9	The bright field TEM micrographs for (a) as-prepared, (b) N ⁺ ion implanted and (c) post-implantation annealed MCD/UNCD films	119
Fig. 4.10	The HRTEM image corresponding to the large diamond aggregates for (a) as-prepared, (b) N ⁺ ion implanted and (c) post-annealed MCD/UNCD films. The insets FT _{0a} , FT _{0b} and FT _{0c} show the FT images corresponding to the whole structure images “a”, “b” and “c”, respectively, and the FT ₁ to FT ₆ show the FT images corresponding to the areas “1” to “6”, respectively. In ‘1.d’ d represents diamond at the marked positions 1	120
Fig. 4.11	(a) The bright field TEM micrograph and (b) the HRTEM image of a	123

typical ultra-small grain region for as-prepared MCD/UNCD films; (b, c) the HRTEM image corresponding to a typical ultra-small grain region of (c) the N^+ ion implanted and (d) the post-annealed MCD/UNCD films. The insets FT_{0a}, FT_{0b}, FT_{0c} and FT_{0d} show the FT images corresponding to the whole structure images “a”, “b” and “c”, respectively, and the FT₁ to FT₆ show the FT images corresponding to the areas “1” to “6”, respectively. In ‘1.d’ d represents diamond at the marked positions 1

Fig. 4.12	Normalized differential conductance ($dI/dV)/(I/V)$ at (1) the grain and (2) the grain boundary of N^+ ion implanted MCD/UNCD films [marked as “i” and “ii” in high resolution STM image in figure 4.7(a)]; those at (3) the grain and (4) the grain boundary of post-implantation annealed MCD/UNCD films [marked as “iii” and “iv” in high resolution STM image in figure 4.7(c)]. Each spectrum is averaged over 10 scanned spectra shown in figure 4.8	124
Fig. 5.1	The EFE properties of as-deposited MCD (i), Fe-coated and post-annealed MCD films at (ii) 950 °C (iii) 925 °C (iv) 900 °C. Inset shows the F-N plot for the corresponding J-E curves	136
Fig. 5.2	SEM image of Fe-coated/post-annealed (900 °C) MCD film with the inset showing the SEM picture of as-prepared MCD film	137
Fig. 5.3	GIXRD pattern of Fe coated MCD film post-annealed at 900 °C	138
Fig. 5.4	Raman spectra of as-deposited (i), Fe-coated/post-annealed MCD films at (ii) 950 °C (iii) 925 °C and (iv) 900 °C	139
Fig. 5.5	XPS C-1s spectra of (a) as-deposited MCD films. (b), (c), and (d) are for Fe-coated/post-annealed MCD films, annealed at temperatures of 900 °C, 925 °C and 950 °C respectively	141
Fig. 5.6	XPS spectra for Fe-2p spectra of Fe coated/post annealed MCD films at different temperatures of (a) 900 °C (b) 925 °C (c) 950 °C respectively	143
Fig. 5.7	The (a) bright field (BF) and (b) dark field (DF) images of a typical region in (Fe/MCD) ₉₀₀ film. Inset shows the SAED pattern for the whole area	144
Fig. 5.8	The HRTEM micrographs corresponding to the (a) region “i” and (b) region “ii” in Fig. 5.7(a), showing the presence of Fe ₃ C particles and the associated graphitic layer. The insets show the Fourier-transformed diffractogram of the designated areas	145
Fig. 5.9	(a) UHV STM image of as-deposited MCD films with the corresponding CITS image in (b). (c) Fe coated/post-annealed (900 °C) MCD film with corresponding CITS image in (d). The CITS images are taken in STS mode at a sample bias of -3.5 V. The increased emission sites after the Fe coating and annealing process is clearly seen in the CITS image (d) than (b)	148
Fig. 5.10	(a) HRSTM image of Fe-coated/post-annealed (900 °C) MCD film (b) corresponding CITS image taken in STS mode at a sample bias of -3.5 V	149

Fig. 5.11	(a) Tunneling current vs. voltage (I-V) curves and (b) normalized differential conductance (dI/dV)/(I/V) curves at various locations: (i) at boundaries of nano-particles, marked as '6' and '8' in Fig. (5.10a), (ii) on the smaller-sized (~5 nm) Fe ₃ C nanoparticles, marked as '7' in Fig. 5.10(a), and (iii) on the bigger-sized (20-25 nm) oxidized Fe nanoparticle, marked as '5' in Fig. 5.10(a)	151
Fig. 5.12	FESEM image of (a) as-deposited (b) 900 °C (c) 925 °C (d) 950 °C Fe-coated/post-annealed UNCD films. Presence of Fe nanoparticles is clearly seen as white contrast on the surface of UNCD films	153
Fig. 5.13	GIXRD pattern of Fe-coated/post-annealed (900 °C) UNCD film showing the presence of Fe ₃ C phase on the surface	154
Fig. 5.14	EFE properties of (i) as- deposited UNCD films and (ii) 950 °C (iii) 925 °C (iv) 900 °C Fe-coated/post-annealed UNCD films. Inset shows the F-N plots derived from the corresponding J-E curves	155
Fig. 5.15	Raman spectra of as-deposited (i) and Fe-coated/post-annealed UNCD films at (ii) 950 °C (iii) 925 °C and (iv) 900 °C respectively	157
Fig. 5.16	The XPS C-1s spectra of (a) as-deposited UNCD films and (b) 900 °C (c) 925 °C and (d) 950 °C Fe-coated/post-annealed UNCD films. The enhanced <i>sp</i> ² phase is clearly seen in Fe-coated UNCD film annealed at 900 °C	158
Fig. 5.17	Fe 2p XPS spectra of Fe-coated/post-annealed UNCD films, at (a) 900 °C (b) 925 °C (c) 950 °C	160
Fig. 5.18	The (a) STEM bright field, BF, and (b) high angle annular dark field, HAADF, images corresponding to BF image for the UNCD films, which were Fe-coated/post-annealed at 900 °C	162
Fig. 5.19	The EDS (STEM) spectra for the UNCD films, which were Fe-coated/post-annealed at 900 °C. The spectra 1 to 6 correspond to the locations 1 to 6 designated in Fig. 5.7(b)	163
Fig. 5.20	The HRTEM images corresponding to (a) the yellow region and (b) the cyan region in the HAADF image (Fig. 5.18(b)) for the UNCD films, which are Fe-coated/post-annealed at 900 °C. Fourier transformed diffractogram [FT _{0a}] is marked as 0 _a , FT _{0b} as 0 _b and 1.d, 2.d represents diamond at marked location 1 and 2 respectively.	165
Fig. 5.21	The TEM 3D-tomography of the UNCD films, which were Fe-coated/post-annealed at 900 °C showing the presence of Fe (red color), Fe ₃ C (white) and nanodiamond or nanographite (yellow) phases on the surface : (a) the stereographic projection and (b) the X-Y projection	166
Fig. 5.22	(a) UHV STM image of as-deposited UNCD films with the corresponding CITS image in (b). (c) Fe coated/post-annealed UNCD film at 900 °C with corresponding CITS image in (d). Enhanced emission sites of the Fe-coated/post-annealed film are clearly seen in the CITS image (d) than as-deposited one in (b)	168
Fig. 5.23	HRSTM image of (a) as-deposited UNCD film with the corresponding CITS image in (b) Fe-coated/post-annealed UNCD film at 900 °C (c)	170

	with the corresponding CITS image in (d)	
Fig. 5.24	The (a) I-V characteristic curves (thick curve represents the average over the 10 I-V curves at each mentioned point) and (b) normalized differential conductance $(dI/dV)/(I/V)$ curves at various locations: (i) boundaries of nano-particles, marked as '6' and '8' in Fig. 5.23 with the green colored arrow positions, (ii) on the yellow arrow marked nanoparticles, marked in Fig. 5.23(c), and (iii) on the oxidized Fe nanoparticle, marked as '7' in Fig. 5.23(c)	173
Fig. A.1	FESEM surface morphology of (a) UNCD(I) (b) UNCD(II) and (c) UNCD(III) films	190
Fig. A.2	XPS C-1s spectra of (a) UNCD(I) (b) UNCD(II) and (c) UNCD(III) films	191
Fig. A.3	Raman spectra of (a) UNCD(I) (b) UNCD(II) and (c) UNCD(III) films	194
Fig. A.4	Nanoindentation load-displacement curves of (a) UNCD(I) (b) UNCD(II) and (c) UNCD(III) films	197
Fig. A.5	Scratch resistance test of (a) UNCD(I) (b) UNCD(II) and (c) UNCD(III) films, optical images are shown with the corresponding film	198
Fig. A.6	Coefficient of friction recorded on (a) UNCD(I) (b) UNCD(II) and (c) UNCD(III). In inset of this figure, the evolution of the coefficient of friction during the initial passes is shown. Optical images of ball sliding face are shown. In inset friction coefficient of initial passes are drawn	200
Fig. A.7	Penetration depth and wear rate of (a) UNCD(I) (b) UNCD(II) and (c) UNCD(III)	200
Fig. A.8	EDAX analysis of the wear track formed in (a) UNCD(I) (b) UNCD(II) and (c) UNCD(III) films	203
Fig. A.9	Raman spectroscopy of wear track on films (a) UNCD(I) (b) UNCD(II) and (c) UNCD(III)	205

LIST OF TABLES

Table	Table Heading	Page No.
Table 1.1	properties of diamond	4
Table 1.2	Electrical properties of diamond	4
Table 1.3	EFE properties of films prepared in different deposition mediums. The EFE properties are better for UNCD films prepared without H ₂ plasma medium	19
Table 3.1	Relative intensities of various components of C-1s XPS spectra from as-prepared, N ⁺ ion implanted and post-annealed UNCD samples	80
Table 4.1	The EFE performances of as-prepared, N ⁺ ion implanted and post-annealed MCD/UNCD films. EFE properties of as-prepared UNCD are given for comparison. E ₀ : the turn-on field estimated from the Fowler-Nordheim plots as the interception of the line segment extrapolated from high field and low field regime. J _e : EFE current density at an applied field of 17 V/μm	106
Table 4.2	Relative intensities of various components of C-1s XPS spectra from as-prepared, N ⁺ ion implanted and post-annealed MCD/UNCD films	111
Table 5.1	The EFE properties of as-prepared and Fe-coated/post-annealed MCD films at different temperatures	137
Table 5.2	Relative intensities of various components of (a) C-1s XPS spectra and (b) Fe 2p _{3/2} spectra from as-prepared, (Fe/MCD) ₉₀₀ , (Fe/MCD) ₉₂₅ and (Fe/MCD) ₉₅₀ films	142
Table 5.3	The EFE properties of the as-deposited and Fe-coated/post-annealed UNCD films	156
Table 5.4	The C-1s and Fe 2p XPS peaks of the as-deposited and Fe-coated/post annealed UNCD films	159
Table A.1	XPS results of UNCD(I), UNCD(II) and UNCD(III) films.	192
Table A.2	Raman spectroscopic results of (a) UNCD(I) (b) UNCD(II), (c) UNCD(III).	194
Table A.3	Raman spectroscopic results obtained from the wear tracks of UNCD (a) films UNCD(I) (b) UNCD(II), (c) UNCD(III).	206

LIST OF ABBREVIATION

Å	Angstrom
1D	One Dimensional
3D	Three Dimensional
AFM	Atomic Force Microscopy
CNT	Carbon Nanotube
CVD	Chemical Vapor Deposition
CITS	Current Imaging Tunnelling Spectroscopy
DP	Diffraction Pattern
DOS	Density of State
EFE	Electron Field Emission
EDX	Energy Dispersive X-Ray Spectroscopy
FE	Field Emission
FESEM	Field Emission Scanning Electron Microscope
FFT	Fast Fourier Transform
F-N	Fowler–Nordheim
GIXRD	Glancing Incident X-ray Diffraction
GB	Grain boundary
HRTEM	High Resolution Transmission Electron Microscopy
HAADF	High Angle Annular Dark Field
MCD	Microcrystalline Diamond Film
NCD	Nanocrystalline Diamond Film
NEA	Negative Electron Affinity
N ⁺	Nitrogen ion
nm	Nanometer
n-G	Nanographitic
MPECVD	Microwave Plasma Enhanced Chemical Vapor Deposition
LED	Light Emitting Diode
RT	Room Temperature
SAD	Selected Area Diffraction
STM	Scanning Tunneling Microscope
STS	Scanning Tunneling Spectroscopy
HRSTM	High Resolution Scanning Tunneling Microscope
TEM	Transmission Electron Microscopy
UHV	Ultra High Vacuum
UNCD	Ultrananocrystalline Diamond
XPS	X-ray Photoelectron Spectroscopy

Introduction

Nanoscale materials have attracted great attention from the research community due to their fascinating and often unrivalled properties. They show interesting properties that are significantly different from their three dimensional (3D) counterparts. Exceptionally, large surface area-to-volume ratios of nanomaterials relative to their bulk, produces variation in surface state populations that have numerous consequences on materials properties [1, 2]. When the nanostructures dimensions approach the characteristic length scale, such materials exhibit several unexpected properties, such as energy quantization, ballistic transport, single electron tunneling, metastable phase formation, plasmonic coupling, magnetic/electric behavior, and superhydrophobicity [3, 4]. Appropriate control of the properties of nanometer-scale structures can lead to new science as well as new devices, technologies, and products.

The science of carbon materials is at an important juncture. Historically independent scientific communities had shown interest in studying graphite-based materials, fullerenes, carbon nanotubes and diamond, as they exhibit interesting properties at the nanoscale. While the current popularity of carbon nanostructures to a large extent is due to fullerenes, carbon nanotubes and graphenes, other members of the nanocarbon family such as nanostructured diamond films are also attracting steady attention [5-7]. Nanostructured diamond films possess exceptional mechanical, electrical and optical properties [5-7]. Diamond, a wide-band-gap semiconductor ($E_g = 5.5$ eV) with high resistivity, do not appear to be a suitable material for electron field emission (EFE) applications. In the case of an undoped diamond, the

concentration of electrons in the conduction band is almost too negligible to be emitted. In spite of the above-mentioned disadvantages, diamond has a series of excellent physical and chemical properties, which make it one of the strongly contending cold cathode materials for field emission applications. It has low work function and negative electron affinity (NEA) properties, that are suitable for electron field emission process [1]. Furthermore, diamond can operate at high temperature or high power because of its high electrical breakdown field and thermal conductivity that are beneficial for field emission (FE) processes. With these attractive features of the diamond surface and with the recent ability to deposit diamond thin films on a variety of substrates using various low-pressure chemical vapor deposition (CVD) techniques, has created strong interest in the applications of it as an electron field emitter. However, the EFE properties of as-deposited diamond films are not satisfactory due to the presence of lower sp^2 , nanographitic and amorphous carbon phases [5-7] and hence diamond films have been extensively investigated to improve their EFE properties for electron field emitter application by modification of their surface.

In this thesis work, a systematic study has been made to improve and understand the mechanism of electron field emission properties of diamond films. This chapter gives an introduction to (i) Nanostructured carbon materials including their properties and applications (ii) Electron Field emission behavior and (iii) Improvement in EFE properties of diamond films by doping, ion implantation and other techniques.

1.1 Nanostructured Carbon Materials

Structures, properties, and numerous applications of nanostructured carbon materials, which belongs to a broad group of so-called new carbon materials, have been recently summarized in a book and a review by Inagaki [8, 9]. Diamond is a fascinating material in the solid crystalline form of carbon in which all carbon atoms are sp^3 bonded. It has a well-known cubic structure as shown in figure 1.1. It consists of two face-centered-cubic (fcc) lattices, one of which is displaced by $(\frac{1}{4}a, \frac{1}{4}a, \frac{1}{4}a)$, where a is the lattice constant of diamond, $a = 3.567 \text{ \AA}$ ($1 \text{ \AA} = 0.1 \text{ nm}$). There are eight carbon (C) atoms in a crystallographic unit cell. Each carbon atom has four sp^3 bonds with the neighbouring four atoms with bond length of 1.54 \AA each. The atomic density of diamond is $1.77 \times 10^{23} \text{ atoms/cm}^3$. Diamond is the hardest material in nature and has high elastic modulus. It is a good electric insulator but excellent thermal conductor and has a low thermal expansion coefficient. Diamond is also chemically very inert [10]. A summary of the properties of bulk diamond and its electrical properties are given in Table 1.1 and Table 1.2 respectively. The superior properties of diamond make it attractive for industrial machining such as grinding, sawing, and drilling. In recent years it has been this unique combination of properties that have made it attractive to the electronics community (*e.g.* high resistivity with high thermal conductivity).

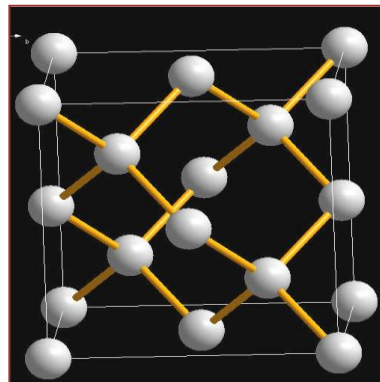


Fig.1.1 Diamond crystal structure

Table 1.1 properties of diamond

PROPERTY	VALUE	UNITS
Mechanical hardness	1.0×10^4	Kg/mm ²
Tensile Strength	>1.2	GPa
Compressive Strength	>110	GPa
Coefficient of Friction	0.03	Dimensionless
Sound Velocity	1800	m/s
Density	3.52	g/cm ³
Thermal Conductivity	20	W/cm-K
Thermal Coefficient of Expansion	1.1×10^{-6}	K ⁻¹
Debye Temperature	2200	K
Optical Index of Refraction at 591 nm	2.41	Dimensionless
Optical Transmissivity in the far IR	225	Dimensionless

Table 1.2 Electrical properties of diamond

Dielectric Constant	5.7	Dimensionless
Dielectric Strength	1.0×10^7	V/cm
Electron Mobility	2200	cm ² /Vs
Hole Mobility	1600	cm ² /Vs
Electron Saturation velocity	2.7×10^7	cm/s
Hole Saturation velocity	1.0×10^7	cm/s
Work Function	3.5	eV
Band gap	5.45	eV
Resistivity	$10^{13} - 10^{16}$	ohm-cm

A schematic representation of potential application of diamond film for electronic power devices in comparison with other films is shown in figure. 1.2.

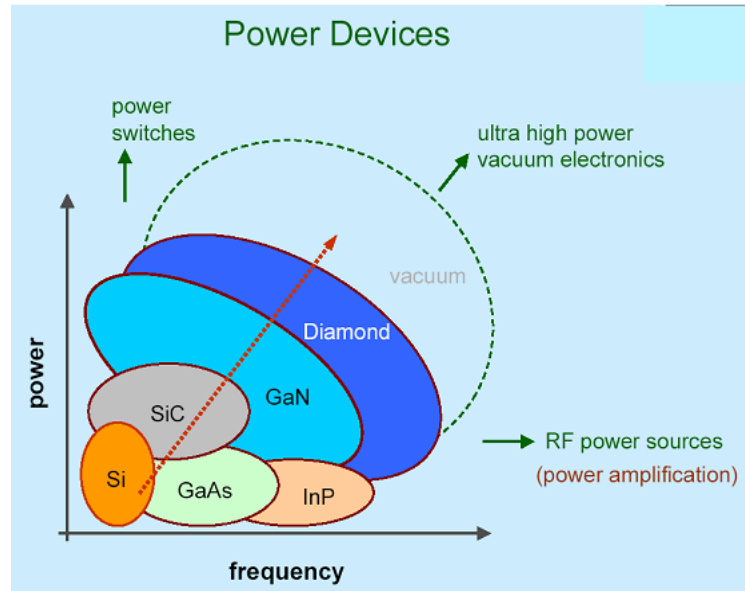


Fig. 1.2 Illustration of the potential application of diamond films in vacuum microelectronic technology for high power, high-frequency applications [11].

Different approaches can be used to classify carbon nanostructures. The appropriate classification scheme depends on the field of application of the nanostructures. For example, a classification can be based on an analysis of the dimensionalities of the nanostructures. The entire range of dimensionalities is represented in the nanocarbon world, beginning with zero-dimensional structures (fullerenes, diamond clusters), one-dimensional structures (nanotubes, diamond nanorods), two-dimensional structures (graphite sheets, diamond nanoplatelets), and three-dimensional structures (nanocrystalline diamond films, agglomerates, fullerite, nanotubes). In terms of a more fundamental basis for the classification of carbon nanostructures, it would be logical to use a classification scheme based on the nature of bonding in macroscopic carbon materials. Elemental carbon exists in three bonding

states corresponding to sp^3 , sp^2 , and sp^1 hybridization of the atomic orbitals, and the corresponding three carbon allotropes are diamond, graphite, and carbene [12] respectively.

While the history of synthetic graphite begins in the 19th century [13], artificial diamonds were not synthesized until the middle of the 20th century. Within the graphite-based group, new materials (new carbon) [8] such as carbon fibers, glass-like carbons, pyrolytic carbons, etc. were developed in the early 1960s, and found broad industrial applications [8, 9]. The most significant, relatively recent application of this class of carbon material is probably lithium rechargeable batteries that uses nanostructured graphite anodes, which have made possible portable electronic devices [8]. A new era in carbon materials began in the mid 1980's when the buckyballs was discovered, [14] followed by the discovery of fullerene nanotubes (buckytubes) [15]. The discovery of these nanostructures set in motion a new world-wide boom that seems to be growing. The fullerene nanotubes and graphite-based materials are inherently connected, and researchers who produced carbon filaments had been unknowingly growing nanotubes decades before Iijima's publication [15].

Nanostructured diamond films possess exceptional mechanical, electrical and optical properties [16]. Diamond film growth has become a profitable business over the past few years. Advances in film quality, growth methods, and polishing make it possible for diamond to compete with other existing nanomaterials. This progression has been aided by the discovery of nanocrystalline and ultrananocrystalline diamond (NCD and UNCD) films. These films are smoother than traditional polycrystalline diamond (PCD) films, therefore they can be used in applications where PCD films are not suitable. These nanostructured diamond films find its enormous potential

applications due to their interesting physical and chemical properties [17-19]. It exhibits a synergetic combination of better electrical, thermal, tribological and biocompatible properties, which enable it to generate multifunctional devices from macro to nanoscale. These multifunctional devices include i) field-emission cathodes and high-frequency X-ray sources [20, 21]; ii) coatings for mechanical pump seals [22, 23]; iii) MEMS/NEMS devices; [24, 25]; iv) biomedical devices [26]; v) biosensors [27] and vi) platform for developmental biology [28]. Now-a-days diamond films are commercially available as a coating on drill bits, reamer and countersinks. Diamond tipped saw is also used to cut nonferrous materials. Additionally, diamond surgical blades are now used in medical applications e.g. Ophthalmology and neural surgery that can make precision cuts and have the capability of integrating optics [29]. Diamond's unique combination of extreme hardness, wear resistance, low coefficient of friction and thermal properties makes it ideal for these applications [30].

With a thermal conductivity of $25 \text{ W cm}^{-1} \text{ K}^{-1}$, which exceeds copper by a factor of five, diamond is considered perfect for thermal management purposes. Therefore, diamond is being used as a heat sink for high power devices such as microprocessors, small microwave IC's, laser diodes, detector arrays and microwave tubes [10, 31, 32]. Diamond's high thermal conductivity allows it to uniformly remove heat from devices eliminating hot spots [33]. There are several benefits associated with the use of diamond heat spreaders including increased performance and reliability.

Diamond has better chemical stability than other microelectronic compatible substrates such as gold, glass, silicon and metal oxides and hence it is attractive for biosensing applications [10]. Furthermore, scientists have successfully functionalized diamond films with DNA and proteins using ultraviolet (UV) photo attachment and

thermal decomposition of benzoyl peroxide [34]. Once diamond films have been functionalized they can be used in conjunction with other microelectronic processes to produce biosensor devices. Chemical vapour deposited diamond films are being incorporated into mobile communication devices, television tuners, and optical communication devices in the form of surface acoustic wave (SAW) filters or resonators [35]. Diamond's combination of high elastic constant and high surface acoustic wave velocity makes it more desirable than existing materials.

As mentioned previously, diamond films are being used in optical applications. Optical grade diamond lenses, domes and windows are being made for X- Ray, ultraviolet and infrared frequencies [10]. Diamond's combination of thermal, chemical and optical properties (*e.g.* its transparency to UV, visible and far infrared bands) makes it ideal for these applications. Improvements in growth techniques and diamond processing (*e.g.* polishing, laser cutting etc.) have lead to additional application of diamond films. Significant research on CVD diamond films is still needed to continually increase its viability as a commercial product.

The first significant growth of low pressure diamond was achieved by A. Lettington and K. E. Spears, of the Union Carbide Corporation in 1952 [36,37]. Even with the early success of CVD diamond films; it has taken many years for the significant advancement in the deposition techniques for diamond film's growth. The first major breakthroughs came in 1971 when Ishihara [38] and his co-workers reported the use of atomic hydrogen to remove graphitic phase during the diamond film's growth process. With this knowledge, Vickery of Diamond Squared Industries developed a diamond growth process using a 95% H₂/ 5% hydrocarbon mixture [39]. Further development followed in 1976 when Russian scientist Deryagin et al. [40]

reported faceted diamond growth on non-diamond substrates [40]. This was a major step because all previous growth had been done on pre-existing diamond substrates. In 1982 the first high quality diamond films were grown at the National Institute for Research in Inorganic Material (NIRM) by Matsumoto and Setaka [41]. These major advancements spearheaded renewed interest in diamond as an engineering material. Since then many CVD systems and gas mixtures have been used to grow synthetic diamond films.

Apart from the applications for cutting tools, thermal management, optics, diamond is gradually beginning to appear in electronic applications. Particularly, one potential application which is of great interest is the electron field emission properties of diamond nanostructures for field emission sources. Diamond has the most strongly bonded crystal structure, such that field emission devices from diamond could operate with maximum stability and reliability.

The finding of *n*-type electrical conductivity [42] in nanostructured diamond films allow one to explore a variety of research areas where the electronic properties of the films play an important role. Theoretical calculations and photoemission measurements by Himpsel et al. [43] have demonstrated a negative electron affinity for (111) planes of unreconstructed single crystal diamond which is responsible for good EFE properties for these films. A brief introduction to electron field emission behavior behaviour and their application is given in next section.

1.2 Electron field emission behavior and their application

Electron field emission is a unique quantum-mechanical effect of electrons tunnelling from a solid surface to vacuum. Electrons can be removed from the solid

surface either by providing electrons sufficient kinetic energy to overcome the potential barrier at the surface, or by reducing or thinning the height of the barrier, so that electrons can penetrate the barrier and escape by virtue of their wave characteristics *i.e* tunnelling. Sufficient kinetic energy can be given to electrons by application of heat, resulting in thermionic emission, or by absorption of light quanta of sufficient energy to cause photoelectric emission. Reduction and thinning of the barrier could be brought about by application of high electric fields, leading to electron emission. However, in case of EFE process, a strong external electric field must be applied to a thin potential barrier (width ~ 1.5 nm) at the solid/vacuum interface, thereby allowing electrons to quantum-mechanically tunnel into vacuum. Such, an observation was early made in the middle of eighteenth century when Jean-Antoine Nollet and William Morgan showed the passage of electrical discharge in a partially evacuated tube produced a glow between the electrodes. In 1922, Lilienfeld demonstrated that an X-ray tube with a pointed cold cathode passed a current of a few milliamperes when subjected to a strong electric field [44]. A first attempt to explain the emission of electrons from cold metal at high field strengths was made by Schottky [45] who attempted to correlate the various electron emissions, including the thermionic and field emission. In 1928, Fowler and Nordheim summarised the field emission processes in the Fowler-Nordheim relation equation which became a classical theory in the field emission study [46].

Several commonly used electronic devices are based on electron sources. Presently, the most widely employed electron source is the ‘bulky’ thermionic cathodes which are used in television sets, X-ray generators and microwave amplifiers. Many of the electron sources in these devices have relied upon thermionic

electron emission. The operating principle in these thermionic emitters are based on the heating of filaments ($> 1000\text{ }^{\circ}\text{C}$) by currents where electrons gain enough thermal energy to be ejected from the solid (*i.e.* the filament) to vacuum. However thermionic emitters have a number of drawbacks. Most importantly, the large heat dissipation due to heating causes large energy consumption. Furthermore, the cathodes limit the lifetime of the tube due to mechanical wear. In addition, the thermionic electrons have random spatial distributions. As a result, fine focusing of the electron beam is very difficult [47].

Advances in electron emission source technology have a profound impact on a whole range of applications. In the quest for miniaturization, power savings, recent requirements for electron sources used in flat panel displays, parallel electron beam microscopy, nanolithography, compact microwave amplifiers and portable X-ray tubes have motivated worldwide research on alternative electron sources, which are smaller and more efficient. Compared to the commonly used thermionic emission based on hot filament, the field emission sources are more power efficient. In addition, field emission sources also offer several attractive characteristics such as instantaneous response to field variation and resistance to temperature fluctuation and radiation [48].

Recently, significant effort has been made towards the field emission applications of nanostructured materials. Most of the nanostructured materials such as Carbon nanotubes (CNTs) [49], graphene [50], zinc oxide nanowires [51], gallium nitride nanowires [52], diamond like carbon (53) have great promise for field emission applications. However, EFE properties from carbon based materials such as diamond thin films and nanostructured diamond have caught great interest as the EFE properties can be changed by tuning the sp^2/sp^3 ratio [54], grain size [55], surface

modification and doping methods [56, 57]. Moreover, field emission devices from diamond films have more longevity, ability to work in harsh environment and have more emission current density. A good field emission device requires low operating voltage, high and stable emission current for potential applications [58].

1.3 Electron emission mechanism in diamond cathodes

There are three common field emission mechanisms (i) Geometric electric-field enhancement mechanism (ii) Schottky-diode electric-field enhancement mechanism and (iii) Triple-junction electric-field enhancement or surface emission mechanism [59]. The most commonly used mechanism, illustrated in Figure 1.3, is the geometric electric-field enhancement at the top of a sharpened conductive cone. This technique applies an electric field to a sharpened conductive cone with a high aspect ratio of height to base diameter.

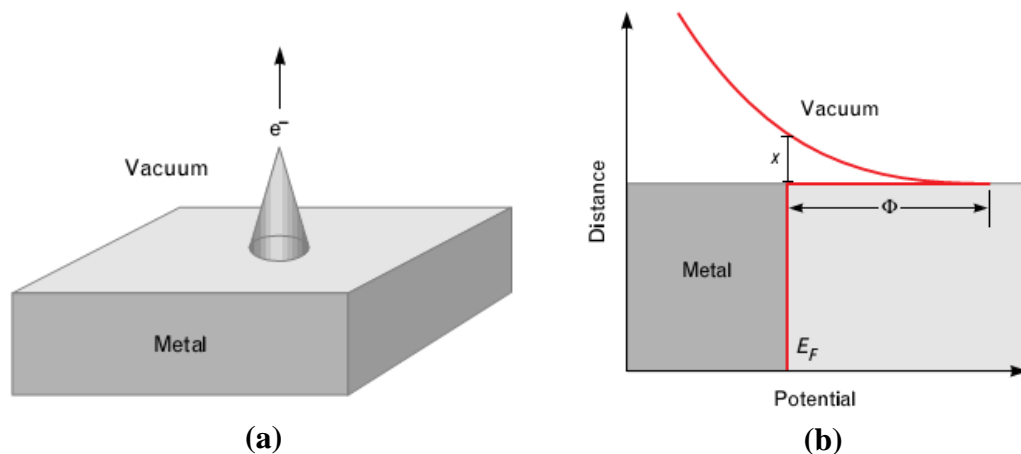


Fig. 1.3 Geometric electric-field enhancement at the top of a sharpened conductive cone. (a) An electric field applied to the sharpened conductive cone produces electron emission at the top of the cone. The emission occurs at average electric field values that are lower than those needed for emission from a smooth metal surface. (b) The plot of potential energy as a function of distance from the cone tip to vacuum, where E_F is the Fermi energy in the metal, illustrates the magnitude of the potential-energy barrier Φ at the metal-vacuum interface. To be emitted from the conductive cone, electrons must tunnel a distance x through the potential barrier [59].

According to theory, no measurable emission occurs from a perfectly smooth metal surface at fields less than 10^9 V m^{-1} . But emission occurs with the sharpened conductive cone at average applied fields of 10^7 to 10^8 V m^{-1} .

The emission-current density J (in A m^{-2}) is related to the local electric field E (in V m^{-1}) at the emitting surface by the Fowler-Nordheim equation,

$$J = \frac{eE^2}{8\pi h\phi} \exp \left[-\frac{4}{3} \sqrt{\frac{8\pi 2m}{h^2}} \phi^{\frac{3}{2}} \frac{V(E, \phi)}{(e^{3/2}E)} \right] \quad (1.1)$$

where Φ is the work function of the cone material in eV, e is the charge of an electron ($1.602 \times 10^{-19} \text{ C}$), h is Planck's constant ($4.136 \times 10^{-15} \text{ eV-sec}$), m is the mass of an electron ($9.109 \times 10^{-31} \text{ kg}$), and $V(E, \Phi)$ is Nordheim's elliptic function [60]. For practical applications, arrays of cathodes consisting of metal cones and a metal grid structure spaced 100 nm to 10 μm apart [61] require 20 to 200 V between the cones and the grid to obtain average current densities greater than 10 A m^{-2} .

Figure 1.4 illustrates the second electron-emission mechanism, known as Schottky-diode electric-field enhancement. Figure 1.4 (a) shows the cross section of metal-semiconductor and NEA-semiconductor surface-vacuum interfaces for Schottky-diode electric-field enhancement with a semiconductor doped with an electron donor impurity. This mechanism requires a semiconductor that is doped with an electron donor impurity and has an NEA-semiconductor surface-vacuum interface. The semiconductor forms a Schottky diode with the metal substrate. The magnitude of the emitted current is limited by electrons tunnelling through the metal-semiconductor Schottky diode and not by electron emission from the semiconductor into vacuum. When an electric field is applied across the semiconductor, the dopants become

positively ionized and form a depletion region at the metal-semiconductor junction [62]. If diamond is used as the semiconductor, the electric field at this junction is often greater than 10^9 V m^{-1} , causing the electrons to tunnel from the metal into the semiconductor. Electrons in the semiconductor can be easily injected into the vacuum.

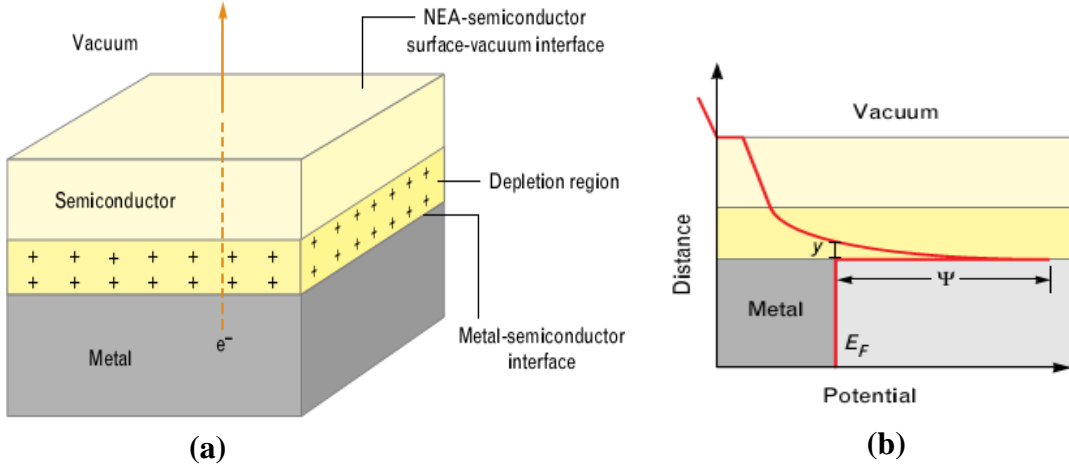


Fig. 1.4 Cross section of metal-semiconductor and NEA-semiconductor surface-vacuum interfaces for Schottky-diode electric field enhancement with a semiconductor doped with an electron donor impurity. (a) When an electric field is applied across the semiconductor, the dopants become positively ionized and form a depletion region at the metal-semiconductor interface. Electrons tunnel from the metal into the semiconductor, and are emitted at the NEA-semiconductor surface-vacuum interface. (b) the plot of potential energy as a function of distance, where E_F is the Fermi energy in the metal, illustrating the potential-energy barrier Ψ at the metal-semiconductor interface. To be emitted from the metal substrate, electrons must tunnel a distance y through the potential barrier. [59].

The current density J is related to the semiconductor doping density n (in m^{-3}), the potential-energy barrier height Ψ (in eV) at the metal-semiconductor interface, and the potential drop V across the semiconductor by

$$\begin{aligned}
 J &= \frac{en}{\pi h \epsilon \epsilon_0} \frac{1}{p^2} \exp \left[- \left(\frac{\pi V}{h} \right) \sqrt{\frac{\epsilon \epsilon_0 m_e}{en}} T \right] \\
 &\approx a_1 V^2 \exp \left[\frac{-b_1}{\sqrt{V}} \right] \text{ for } V \gg \Psi,
 \end{aligned} \tag{1.2}$$

where

$$T = D + \frac{(1-D^2)}{2} \ln \left[\frac{(1-D)}{(1+D)} \right] \approx \frac{2D^3}{3} + \frac{2D^5}{15},$$

$$P = -D \ln \left[\frac{(1-D)}{(1+D)} \right] \approx 2D^2 + \frac{2D^4}{3},$$

$$D^2 = \frac{\Psi}{V},$$

where ϵ_0 is the permittivity of vacuum (8.85×10^{-12} F m⁻¹), ϵ is the dielectric constant of the semi-conductor (5.7 for diamond), m_e is the effective mass of the electron in the semiconductor, and a_1 and b_1 are functions of ϵ , Ψ , m_e , and n . This equation was derived by using the WKB approximation [62].

The electron emission increases as the doping density n increases and the dielectric constant ϵ , the effective mass of the electron m_e , and the barrier height Ψ decrease. Although the functional form of Equation 1.2 is substantially different from Equation 1.1, both functions will usually describe the data when the measured emitted current density from a cathode is plotted against the voltage required for emission. Thus we cannot easily distinguish between the two mechanisms on the basis of the emission parameters of the cathode. As with Equation 1.1, accurate emission current calculations using Equation 1.2 are almost impossible because not enough of the parameters are known to sufficient accuracy [62].

Figure 1.5 (a) illustrates the third electron-emission mechanism, known as triple-junction electric-field enhancement, or surface emission. Surface emission combines two physical phenomena – electric field enhancement at a triple junction

[63] and high electron mobility at an NEA-semiconductor surface-vacuum interface [64].

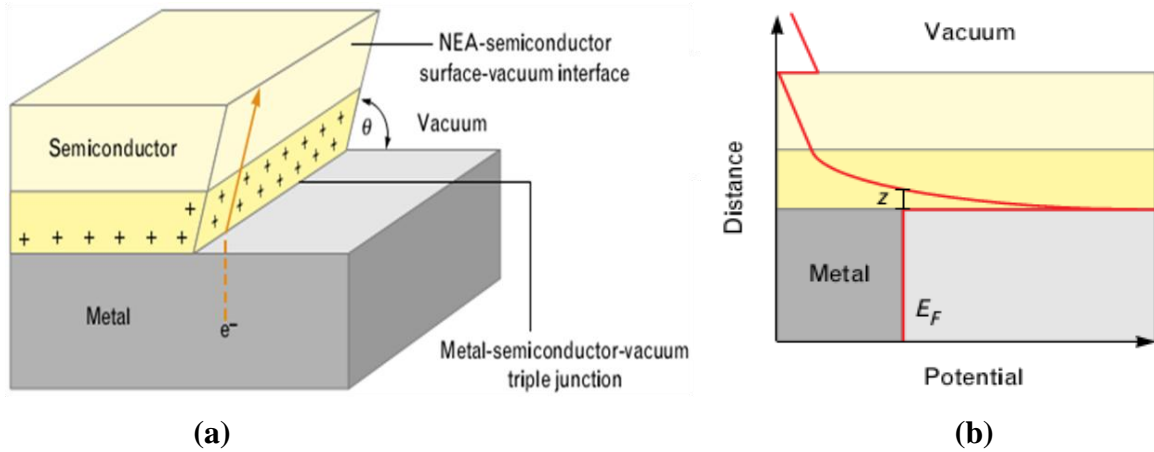


Fig. 1.5 Triple junction (metal-semiconductor-vacuum) electric-field enhancement (a) The combination of an impurity-donor-doped semiconductor and the high mobility of electrons at the NEA-semiconductor surface-vacuum interface causes electrons to tunnel from the metal substrate onto the surface of semiconductor. Depending upon the angle θ between the semiconductor-vacuum interface and the metal substrate, as shown in figure 1.5 (a), the electric-field enhancement can be larger than that obtained with the two mechanisms discussed in figure 1.3 (a) and figure 1.4 (a). (b) The plot of potential energy along the semiconductor-vacuum interface, where E_F is the Fermi energy in the metal, illustrates the potential-energy barrier. To be emitted at the semiconductor-vacuum interface, electrons must tunnel a distance z from the metal substrate into the triple-junction region. The potential barrier, while difficult to determine, is known to be less than the potential barrier for the geometric electric-field enhancement mechanism [59].

In this mechanism, an impurity-donor-doped NEA semiconductor is used in the triple-junction geometry. When a negative bias on the metal substrate produces an electric field along the semiconductor surface, a substantial positive charge can form on the surface and in the bulk of the semiconductor near the triple junction. Part of this charge comes from the Schottky diode, and is formed by the semiconductor and the metal substrate. If the field is large enough, electrons tunnel from the metal substrate

onto the semiconducting surface with sufficient energy to cause secondary electron emission, which further increases positive charge at the surface. Depending upon the angle θ between the semiconductor-vacuum interface and the metal substrate, as shown in Figure 1.5(a), the electric-field enhancement can be larger than that obtained with the two mechanisms discussed previously. Figure 1.5 (b) shows the plot of potential energy along the semiconductor-vacuum interface. The surface-emission mechanism explains many observed diamond-cathode emission properties, and has brought about changes in diamond-cathode design and fabrication, resulting in considerable improvement in performance [65].

1.4 Microstructure and EFE properties of MCD/NCD/UNCD films

Depending on the percentage of precursor gas *i.e* CH₄/Ar/H₂ ratio, during the diamond film growth, different grain sized diamond films such as microcrystalline (MCD, grain size > 100 nm size), nanocrystalline (NCD, grain size < 100 nm size) and ultrananocrystalline (UNCD, grain size < 10 nm size) can be synthesized. Interestingly, the EFE properties of these films vary depending on the grain size. To explain the emission behaviour from different grain sized diamond films *i.e* MCD, NCD and UNCD, a schematic model diagram is presented in figure 1.6. The gray and white regions in figure 1.6 (a), figure 1.6 (b) and figure 1.6 (c) are represented as nondiamond contents and diamond grains, respectively. The turn-on field from the MCD film (30 V/ μ m) is the highest among the diamond films which vary slightly depending upon the deposition conditions [55].

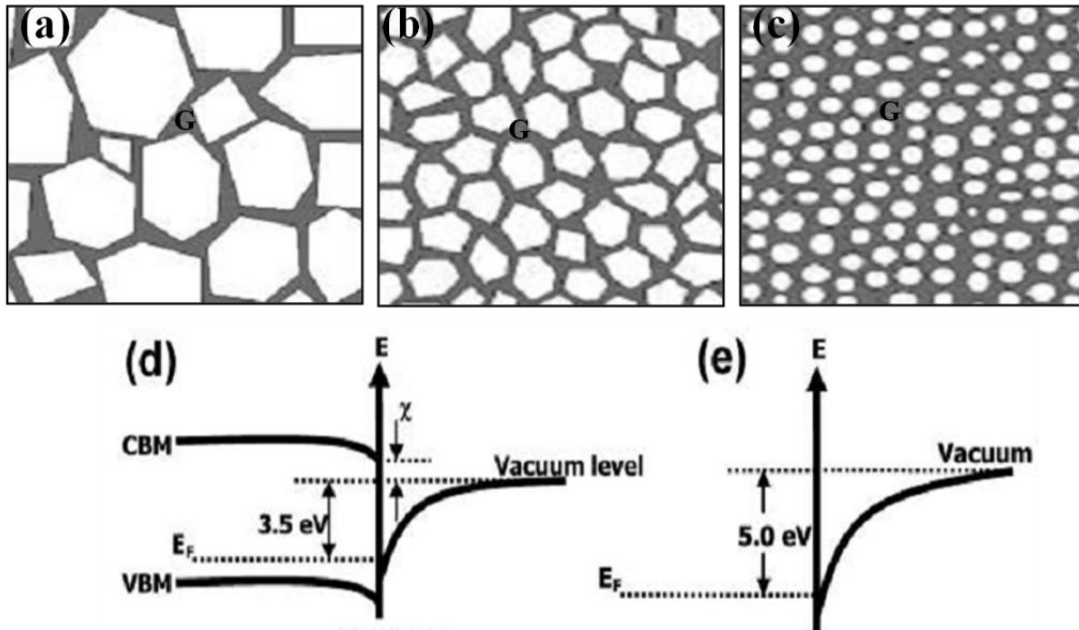


Fig. 1.6 Schematic model diagram of (a) MCD, (b) NCD, and (c) UNCD films. The white and black regions represent diamond and nondiamond contents (amorphous and/or graphitic carbon), respectively. Band diagrams of single-crystal (d) diamond and (e) graphite. The nondiamond carbon contents in the film are extremely essential for the easy electron conduction inside the matrix and also from back to front surface of the film before being emitted from the edges of the diamond grain experiencing a lower work function of 3.5 eV [55].

Table 1.3 shows the EFE properties of diamond films prepared in different deposition medium. The MCD film was generally deposited in a complete H_2 medium, making the surface partially hydrogenated, which could reduce the electron affinity and promote emission at a lower applied field. The smaller work function of diamond (3.5 eV) as compared to graphite (5.0 eV), as shown in the band diagram (Fig. 1.6 (d,e)), is another reason for easy electron emission from the MCD film. Despite all of these favorable properties, a higher turn-on field from the MCD film in comparison to UNCD films (deposited in a H_2 -free atmosphere) is not suited to obtain higher FE properties. The larger size diamond grain reduces the electron conduction in the MCD film and therefore requires a higher electric field for emission to occur. When

deposition is performed at a lower H_2 medium, which produces NCD film, it shows field emission properties at a relatively lower turn-on field ($13 \text{ V}/\mu\text{m}$) and current density is more than that of MCD films [55]. This is obviously due to the higher concentration of CH_4 used in the deposition of the NCD film, which not only reduces the diamond grain size but also increases the nondiamond contents inside the film. This indicates that the grain sizes and nondiamond contents in the diamond films are prime requirements for FE to occur at a lower turn-on field. Interestingly, a further decrease in the grain size to $< 10 \text{ nm}$ in case of the UNCD film shows a lower turn-on field of $8.69 \text{ V}/\mu\text{m}$.

Table 1.3 EFE properties of films prepared in different deposition mediums. The EFE properties are better for UNCD films prepared without H_2 plasma medium [55].

Sample	Deposition medium (%)	Turn-on field ($\text{V}/\mu\text{m}$)	Current density (mA/cm^2)
MCD	CH_4/H_2	30	0.85×10^{-5}
NCD	CH_4/H_2	13	2.35
UNCD	CH_4/H_2	8.69	0.35

Moreover, the discovery of UNCD diamond films deposited from hydrogen poor plasma has led significant research in the properties and applications of this material. The fine grain size of this material results in a high grain boundary volume fraction containing sp^3 , graphitic and amorphous-carbon phases that determine the electrical properties for these films [55-57]. UNCD is one of the emerging materials, offering a wide range of applicability over the conventional CVD microcrystalline diamond [16]. Apart from the robust chemical, mechanical, and thermal properties of CVD UNCD films, it possesses certain distinct properties including smaller grain size (3 to 5 nm), higher density of grain boundary volume fraction, smoother and more uniform surface

morphology, n -type electrical conductivity at room temperature by nitrogen incorporation, increased degree of sp^2 -bonded carbon content, increased hardness and lowered internal stress [16, 55, 57]. Interestingly, this material can be deposited with other active electronic devices, *viz.*, semiconductors, metals, and insulators. These properties of UNCD films can be effectively controlled and reproduced. The grain size, sp^2 -carbon and n -type dopant are strong field enhancement factors, elevating the utility of these diamond films for vacuum micro/nanoelectronic device applications.

1.4.1 Electronic Behaviour of Diamond Films

To explore the electronic behaviour of diamond films at the diamond grain and grain boundary (GB), quantum mechanics based tight-binding-molecular-dynamics (IBMD) simulations were performed by P. Keblinski et al. [66]. Figure 1.7 compares the local electronic density of states (DOS) averaged over the atoms in the GB region (solid curve) with that in the grain region of a bulk crystal (dashed curve). The perfect crystal exhibits a well-defined bandgap (similar to the experimental value of 5.45 eV) separating the σ (bonding) states in the upper region of the valence band and the σ^* (anti-bonding) states in the lower region of the conduction band. The presence of sp^2 bonded dimers and chain segments and sp^3 hybridized dangling bonds in the grain boundary introduces states in the perfect-crystal bandgap [66]. However, because of the lack of spatial connectivity among these sp^2 bonded defects, the associated gap states do not form continuous graphite like π band but are localized. The electrical conductivity cannot therefore be expected to be metallic as in graphite [67]. However, because of the possibility of transitions among these states, the effective electronic gap in the grain boundary region is much smaller than that in the perfect crystal.

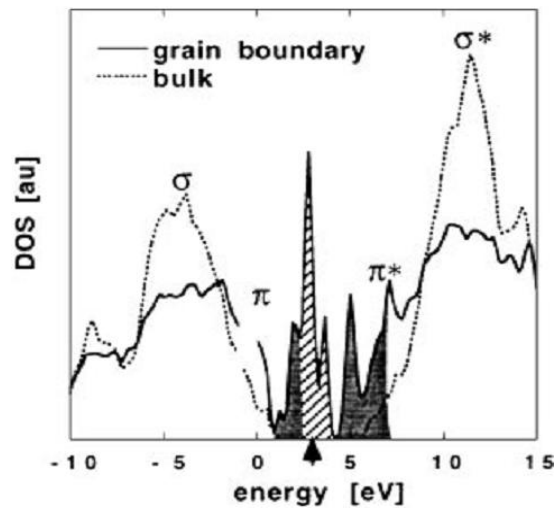


Fig. 1.7 Comparison of the local electronic density of states in the diamond grain boundary averaged over the atoms in the grain boundary region (solid curve) with that in the perfect bulk crystal (dashed curve). The shaded region indicates states localized at sp^2 dimers; the striped region indicates states localized at sp^3 sites. The Fermi level at 3.5 eV is indicated by an arrow [66].

1.4.2 Improvement in EFE Properties of Diamond Films by Doping

The high resistivity of diamond films hinders its application for electronic devices. At room temperature, diamond is a good electrical insulator with a resistivity of approximately 10^{16} ohm-cm. The conductivity of diamond can be modified by hydrogen termination or by doping with impurities [68, 55, 57]. P. Zopal et al. [69] showed that insertion of silicon and hydrogen into the twist GBs in diamond do not lead to improve the electrical properties [69]. However, more studies are needed to investigate how different hydrogen concentrations and formation of complexes with other impurities and dopants affect the electronic properties of this material. Further, the electron field emission properties of carbon doped diamond films are not satisfactory [70]. Moreover, J. P Goss et al. [71] used density-functional calculations to predict the stability and electrical activity of Li and Na doping in diamond films. They found although interstitial Li may be a good candidate donor, it is insoluble,

mobile, and is likely to form complexes with other impurities rendering it electrically inactive. Specifically, co-doping to form Li-B-Li and Li-O-Li complexes does not result in n-type activity. Additionally, interstitial Na is a deep donor, with Na-Na and Na-X-Na complexes generally following the properties of the Li counterparts. It was concluded that alkali metal doping via interstitial Li or Na is unlikely to produce the elusive *n*-type material and better electron transport in diamond [71].

Moreover, much of the current work focuses on the search for a suitable *n*-type dopant in diamond, as it is well known that boron acts as a *p*-type dopant for diamond with a state 0.38 eV above the valance band edge [72, 73]. *n*-type doping of diamond is difficult, as doping of bulk diamond with nitrogen produces a deep donor level of 1.7 eV below the conduction band [74]. Other *n*-type dopants have been attempted, such as sulfur and phosphorus, but with only limited success as they are found to be quite insoluble in diamond matrix [75, 76]. N doping of UNCD, in particular, is of considerable interest for a variety of reasons. It has been reported that the conductivity of UNCD increases by as much as five orders of magnitude (to $140 \text{ } \Omega^{-1} \text{ cm}^{-1}$) when nitrogen is added to the plasma during growth [77, 78]. P. Zapol et al. [69] by tight binding molecular simulation showed in N doped UNCD films nitrogen predominantly goes to the GB sites which makes it more conducting.

The band alignment and position of N donor states in diamond are schematically illustrated in figure 1.8. One therefore only obtains conduction electrons in diamond by injection from the back contact over the large barrier [79]. Hence, emission currents will tend to be controlled by Fowler-Nordheim tunnelling through the back barrier. Now, although the N donor levels are deep, they still lie well above E_F of the

back contact material, so the back contact forms a strong depletion layer by the ionisation of these donor states. The resulting band-bending is shown in figure 1.9, under an applied field. This band-bending in the depletion layer reduces the tunnelling distance at the back contact at higher N contents [80]. The depletion width can be calculated, and it is found that the tunnelling distance is reduced for N concentrations above about 3×10^{24} atoms m^{-3} .

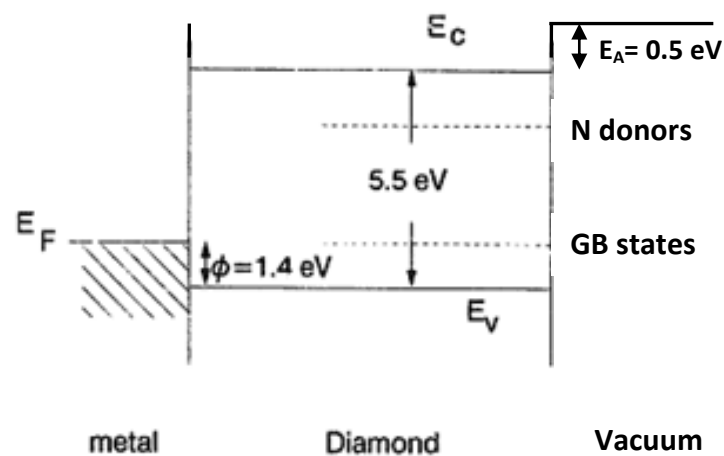


Fig. 1.8 Band alignment and position of N donor states in diamond.

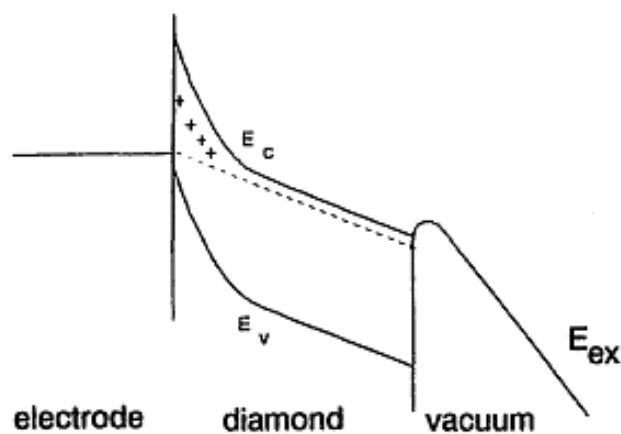


Fig. 1.9 Band bending and reduced tunneling distance at the back contact due to a depletion layer of ionized nitrogen donors [79].

The depletion layer due to this higher N content gives a considerable reduction in the tunnelling distance and accounts for the very low observed threshold fields. Thus, the main role of N in diamond is to reduce the tunnelling distance at the back-contact by providing a depletion layer of ionised donors [81].

1.4.3 Doping by ion implantation

Nitrogen (N) incorporation via adding the N₂ gas during the growth plasma is not efficient due to the small size of the UNCD grains. On the other hand, ion implantation has been a traditional technique to modify the properties of materials through controlled doping of a variety of dopants [82, 83, 84]. Doping of foreign impurities to diamond by means of ion implantation is a well known method [85]. Ion implantation is a harsh, non-equilibrium method to insert atoms into a material. It introduces high levels of radiation damage. Ion implantation followed by suitable annealing to remove or minimize the damage, has become a preferred method to introduce dopant atoms into standard semiconductors such as silicon. It allows tight control over the density and distribution of the dopant atoms than alternative treatments such as in diffusion. In the case of diamond, ion implantation offers the added advantage that it supplies a means to force any possible dopant atom, independent of size or solubility, into this tightly bound thermodynamically metastable, crystal lattice. Ion implantation can also introduce defects and break the C-C and hydrocarbon bonds to form sp^2 carbon and can be used to tailor their sp^3/sp^2 ratio for the diamonds or related carbon materials by properly selecting the dose and energy of implantations [83, 84]. Generally, low-dose ion implantation induced the point defects, which introduced the presence of inter-band energy level, facilitating the jump of electrons from valence band to conduction band and thus reducing the turn-on

for field emission [86]. Annealing removed the defects and correspondingly diminish the enhanced EFE properties. High-dose ion implantation mainly results in the formation of defect complexes, amorphous and nanographite phase, and possibly the incorporation of the implanted species into the grain boundaries. These defects or secondary phases do not induce the presence of inter-band energy level, even after the annealing process. Therefore, the high-dose ion implantation & annealing insignificantly changes the E_0 value. However, B also induces the same amount of defects as N does. But why the B-ion implantation, which induces the same kind of defects for the UNCD films as the N-ion implantation does, but affects the EFE properties of UNCD in so much different manner from the N ion implantation process, is not clear. Apparently, forming the defects is not the major factor altering the EFE properties of UNCD films. The B & N doping in UNCD films behave totally differently, *i.e.*, the N ion implantation enhances the EFE of UNCD films, but the B does not. Moreover, previous reports indicated that the incorporation of N species by CVD process leads to *n*-type conductivity for UNCD films, [87] possibly via the transfer-doping model, *viz.* the conversion of UNCD grains into semiconducting via surface transfer doping process [88]. Although both the implanted B and N ions are residing at grain boundary region, only the N ions contain one extra electron, which can be transferred to UNCD grains, converting the UNCD grains into semiconducting. The B ions react with carbons forming $B\equiv C$ bond and are not able to transfer the charges to UNCD grains [89]. In contrast, it may eliminate the mid gap states and degrade the EFE properties.

1.5 Motivation and Overview of Thesis

As discussed earlier in section 1.4.3, the EFE properties of UNCD films are enhanced by N^+ ion implantation/post-annealing process [84, 89]. However, the mechanisms of EFE properties in N implanted UNCD films are still not clear. Several mechanisms have been proposed to explain the observed field enhancement behavior of N implanted UNCD films, while no single mechanism alone could give a complete picture [90, 91]. Ion implantation in UNCD can cause desorption of hydrogen from the hydrocarbons at the grain boundaries resulting in depassivation of dangling bonds and a rise in the intergap states that results in increased conductivity and a reduction in band gap [92] which contributes for the enhanced field emission behavior. However, there is no direct evidence of enhanced emission sites of N implanted diamond films in literature. In this thesis, a ultra high vacuum scanning tunnelling microscope (UHV STM), which can detect emission sites at nanoscale, is used to directly observe the emission sites after the N implantation and post-annealing processes. Scanning tunnelling spectroscopy (STS) has been used to determine the local electronic density of states (DOS) at the grain and grain boundary and the possible electron emission sites. STS in current imaging tunnelling spectroscopy (CITS) mode is used to directly examine the modification in electronic properties as well as the emission sites in these diamond films.

Besides doping by ion implantation method, there are many other efforts on modifying the surface of diamond films to improve the EFE properties. Among the various approaches, a thin layer of metallic coating (Au, Cr, CsI, Ni) followed by post-annealing improves the EFE properties of diamond films significantly [93, 94]. It is believed that the negative electron affinity properties of diamond films improves after

the metallic coating and hence improves the EFE properties [94]. However, the mechanism of EFE from the metal coated diamond films is not clear [93, 94].

In this thesis systematic studies has been made to improve and understand the mechanism of electron field emission by (i) N ion implantation to UNCD films (ii) N ion implantation to hybrid structured diamond (MCD/UNCD) films, where a UNCD interlayer is used for the growth of MCD films and by (iii) Fe-coating followed by post-annealing of MCD and UNCD films. An attempt has been made to understand the underlying mechanisms that drive the EFE properties of these surface modified diamond films by UHV STM, transmission electron microscopy (TEM), X-ray photo electron spectroscopy (XPS) and Raman spectroscopy.

Chapter 2 briefly covers the experimental and characterization techniques used in this thesis work. Diamond thin films are synthesized by microwave plasma enhanced chemical vapour deposition (MPECVD) method. A brief summary of MPECVD technique, ion implantation methods used for surface modification of diamond films are described. A description of a setup to measure the EFE properties of diamond films is described in this chapter. The samples are investigated by a variety of analytical tools such as UHV STM, High resolution transmission electron microscope (HRTEM), field emission scanning electron microscopy (FESEM), XPS, Raman spectroscopy, glancing incident X-ray diffraction (GIXRD). A short description of each characterization technique is presented in this chapter. Scanning tunneling spectroscopy in current imaging tunneling spectroscopy (CITS) mode is used to investigate the local electronic properties of diamond thin films.

Chapter 3 deals with the enhancement in EFE properties of nitrogen ion implanted UNCD films. Nitrogen implanted and subsequently post-annealed UNCD films show better EFE properties than as-deposited UNCD films. However, the mechanisms of EFE properties in N-implanted UNCD films are still not clear. STM, XPS and TEM techniques were used to investigate the reasons of enhanced EFE behavior of UNCD films upon N ion implantation. The enhancement in EFE properties upon nitrogen implantation is accounted for the decrease in band gap, increase in density of states in the band gap and formation of new bonds at the diamond grains and increase in conductivity at the grain boundaries.

In chapter 4, results of EFE properties of a hybrid structured diamond film is presented. The hybrid structured diamond films are prepared by a modified nucleation and growth process, which utilized a layer of UNCD film as the nucleation layer for the growth of a MCD film on it. Further, the effect of N ion implantation and subsequent annealing process on the EFE properties of the hybrid structured diamond films are studied. CITS in STS mode is used to directly detect the increased emission site densities in N implanted/post-annealed films compared to the as-prepared ones in a nanometre scale. TEM is used to investigate the microstructural evolution of the film surface before and after the N implantation/post-annealing processes. Further, the possible reasons for enhancement in EFE properties of these hybrid films are discussed on the basis of XPS, CITS and TEM observations.

Chapter 5 deals with the enhancement in EFE properties of Fe-coated and post-annealed MCD and UNCD films. The underlying reason for the enhancement in EFE properties of Fe-coated/post-annealed MCD and UNCD films are investigated by variety of analytical tools. Moreover, the Fe-coating/annealing processes enhance the

EFE properties of UNCD films more than that on MCD films. The mechanism behind the enhanced EFE properties of the Fe coated/post-annealed UNCD films are explained by the microstructural analysis which shows formation of nanographitic phase surrounding the Fe (or Fe₃C) nanoparticles. The role of the nanographitic phase in improving the emission sites of Fe coated/post-annealed UNCD films is clearly revealed by the CITS images. The CITS images clearly show significant increase in emission sites in Fe-coated/post-annealed UNCD films than as-deposited ones.

Chapter 6 summarizes the major research finding and scope for future work.

Moreover, N implanted UNCD films show better tribological properties than as deposited films. These results are reported in appendix.

1.6 References

- [1] H. Pan, Y. P Feng, ACS Nano **2**, 2410 (2008).
- [2] R. Calarco, Nano letters **5**, 981 (2005).
- [3] D. K. Ferry, S. M. Goodnick, Transport in Nanostructures, ISBN: 0521877482 (2009).
- [4] C. Dupas, P. Houdy, M. Lahmani, Nanoscience Nanotechnologies and Nanophysics, Springer, ISBN-10 3-540-28616-0 (2007).
- [5] D. M. Gruen, Annu. Rev. Mater. Sci. **29**, 211 (1999).
- [6] V. Y. Dolmatov, Russ. Chem. Rev. **70**, 607 (2001).
- [7] O. Shenderova, V. Zhirnov, D. Brenner, Solid State Mater. Sci. **27**, 227 (2002).
- [8] M. Inagaki, New carbons, Amsterdam, Elsevier, (2000).

- [9] M. Inagaki, K. Kaneko, T. Nishizawa, *Carbon* **42**, 1401 (2004).
- [10] V. N. Mochalin, O. Shenderova, D. Ho, Y. Gogotsi, *Nature Nanotechnology* **7**, 11 (2012).
- [11] A. Denisenko, Department of Electron Devices and Circuits, University of Ulm, 89069 Ulm, Germany.
- [12] R. B. Heimann, S. E. Evsyukov, Y. Koga, *Carbon* **35**, 1654 (1997).
- [13] G. Collin, *CFI – Ceram. Forum Int.* **77**, 28 (2000).
- [14] H. W. Kroto, J. R. Heath, S. C. O'Brien, R. F. Curl, R. E. Smalley, *Nature*, **318**, 162 (1985).
- [15] S. Iijima, *Nature* **354**, 56 (1991).
- [16] O. Auciello, A. V. Sumant, *Diamond Relat. Mater.* **19**, 699 (2010).
- [17] J. E. Field, *The Properties of Diamonds*, Academic, London (1979).
- [18] H. Liu and D. S. Dandy, *Diamond Relat. Mater.* **4**, 1173 (1995).
- [19] J. C. Angus, H. A. Will, W. S. Stanko, *J. Appl. Phys.* **39**, 2915 (1968).
- [20] A. R. Krauss, M. Q. Ding, O. Auciello, D. M. Gruen, Y. Huang, V. V. Zhirnov, E. I. Givargizov, A. Breskin, R. Chechen, E. Shefer, V. Konov, S. Pimenov, A. Karabutov, A. Rakhimov, N. Suetin, *J. Appl. Phys.* **89**, 2958 (2001).
- [21] J. M. Garguilo, F. A. M. Koeck, R. J. Nemanich, X. C. Xiao, J. A. Carlisle, O. Auciello, *Phys. Rev. B* **72**, 165404 (2005).
- [22] A.V. Sumant, A. R. Krauss, D. M. Gruen, O. Auciello, A. Erdemir, M. Williams, A. F. Artiles, W. Adams, *Tribol. Trans.* **48**, 24 (2005).
- [23] www.thindiamond.com.
- [24] O. Auciello, S. Pacheco, A. V. Sumant, C. Gudeman, S. Sampath, A. Datta, R. W. Carpick, O. Auciello, S. Pacheco, A. V. Sumant, C. Gudeman, S. Sampath, A. Datta, R. W. Carpick, V.P. Adiga, P. Zurcher, Z. Ma, H. C. Yuan, J. A. Carlisle,

- B. Kabius, J. Hiller, IEEE Microw. Mag. **8**, 61 (2008).
- [25] A.V. Sumant, O. Auciello, R.W. Carpick, S. Srinivasan, J.E. Butler, MRS Bulletin **35**, 281 (2010).
- [26] X. Xiao, J. Wang, J. A. Carlisle, B. Mech, R. Greenberg, R. Freda, M. S.Humayun, J. Weiland, O. Auciello, J. Biomed. Mater. **77B**, 273 (2006).
- [27] W. Yang, O. Auciello, J.E. Butler, W. Cai, J. A. Carlisle, J. E. Gerbi, D. M. Gruen, T. Knickerbocker, T. Lasseter, J.N. Russell, L.M. Smith, R.J. Hamers, Nat. Mater. **1**, 253 (2002).
- [28] B. Shi, Q. Jin, L. Chen, O. Auciello, Diamond Relat. Mater. **18**, 596 (2009).
- [29] Kohn, M. Adamschik, P. Schmid S. Ertl, A Floter, Proc. ADC/FCT 1999, 420, August 31- September 4, 1999, Tsukuba, Japan.
- [30] A. Grill, Wear **168**, 143 (1993).
- [31] M. Labudobic, M. Burka, components and packing technologies **26**, 575 (2003).
- [32] <http://trove.nla.gov.au/version/8844809>
- [33] J. E. Graebner, S. Jin, G. W. Kammlott, J. A. Herb, C. F. Gardinier, Nature **359**, 401 (1992).
- [34] S. Ida, T. Tsubota, S. Tanii, M. Nagata, and Y. Matsumot., Langmuir **19**, 9693 (2003).
- [35] Shin-ichi Shikata, CVD Diamond for Surface Acoustic Wave Filters
http://link.springer.com/content/pdf/10.1007%2F978-3-642-71992-9_14.pdf
- [36] A. Lettington, J. W. Steeds, Thin Film Diamond, Chapman & Hall, New York (1994).
- [37] K. E. Spears, J.P. Dismukes, Synthetic diamond: Emerging CVD Science and technology, John Wiley & Son, INC NY (1993).
- [38] M. Ishihara, T. Nakmura, Y. Koga, F. Kokai, Proc. ADC/FCT 1999, Tsukuba,

Japan (1999).

- [39] E. C. Vickery , U. S. Patent 3, 714, 334 (1973).
- [40] B. V. Deryagin, D. V. Fodoseev D. V , B. V. Spitsyn , L. L. Builov , A. A. Klochkov , A. E. Gurodetski, A. V. Smolyaninove, Synthesis of diamond on non-diamond substrates Dokl. Akad. Nauk SSSR 231 333- 335 (1976).
- [41] S. Matsumoto, Y. Sato, M. Tsutsumi, N. Setaka, J. Mater. Sci **17**, 3106 (1982).
- [42] P. T. Joseph, N. H. Tai, I. N. Lin, Appl. Phys. Lett. **97**, 042107 (2010).
- [43] F. J Himpsel, J. A Knapp, J. A Van Vechten, D. E Eastman, Phys. Rev. B **20**, 2 (1979).
- [44] J. E.Lilienfeld, Phys. Z. **23**, 506 (1922).
- [45] W.Z. Schottky, Phys. **14**, 80 (1923).
- [46] R.H. Fowler, L.W. Nordheim, Proc. Roy.Soc. A **119**, 173 (1928).
- [47] N. Sinha, D.R. Mahapatra, J. T. W. Yeow, ‘Modeling the Field Emission Current Fluctuation in Carbon Nanotube Thin Films’ (2007).
- [48] F. S. Baker, A. R. Osborn, J. Williams, Nature **239**, 96 (1972).
- [49] S. Park, H. C. Kim, M. H. Yum, J. H. Yang, C. Y. Park, K. Chun, B. Eom, Nanotechnology **19**, 445304 (2008).
- [50] S. Santandrea, F. Giubileo, V. Grossi, S. Santucci, M. Passacantando, T. Schroeder, G. Lupina, A. Di Bartolomeo, Appl. Phys. Lett. **98** 163109 (2011).
- [51] F-H Chu, C-W Huang, C-L Hsin, C-W Wang, S-Y Yu, P-H Yeh, W-W Wu, Nanoscale, **4**, 1471 (2012).
- [52] D. K. T Ng, M. H. Hong, L. S. Tan, Y. W. Zhu, C. H. Sow, Nanotechnology **18**, 375707 (2007).
- [53] O. Gröning, O. M. Küttel, P. Gröning, L. Schlapbach, Applied Surface Science **111**, 135 (1997).

- [54] Y. Umehara, S. Murai, Y. Koide, M. Murakami, *Diamond & Rel. Material* **11**, 142 (2002).
- [55] Debabrata Pradhan, I. Nan Lin, *ACS Applied Materials & Interfaces* **7**, 1444 (2009).
- [56] P.T. Joseph, N.H. Tai, H. Niu, U.A. Palnitkar, W.F. Pong, H.F. Cheng, I.N. Lin, *Diamond & Rel. Material* **17**, 1812 (2008).
- [57] P-C Huang, W-C Shih, H-C Chen, I-Nan Lin, *Japanese Journal of Applied Physics*, **50** 08KE04 (2011)
- [58] V. Baranauskas, M. Fontana, H. J. Ceragioli, A. C. Peterlevitz, *Nanotechnology* **15**, S678 (2004)
- [59] W. G. Michael, N. E. Nikolay Jr., K. E. Krohn, J. C. Twichell, T. M. Lyszczarz, R. Kalish, A. J. Greer, D. T. Martin, *The Lincoln Laboratory Journal* **10**, 1 (1997).
- [60] W. D. Dyke, W. W. Dolan, L. Marton, *Academic, New York* **8**, 89 (1956).
- [61] C. A. Spindt, I. Brodie, L. Humphrey, E. R. Westerberg, *J. Appl. Phys.* **47**, 5248 (1976).
- [62] M. W. Geis, J. C. Twichell, T. M. Lyszczarz, *J. Vac. Technol. B* **14**, 2060 (1996).
- [63] C. H. de Turreil, K.D. Srivastava, *IEEE Trans. Electr. Insul.* **8**, 17 (1973).
- [64] C.C. Grimes, *Surf. Sci.* **73**, 379 (1978).
- [65] M. W. Geis, N. N. Efremow, K. E. Krohn, J. C. Twichell, T. M. Lyszczarz, R. Kalish, J. A. Greer, M. D. Tabaat, *Nature* **393**, 431 (1998).
- [66] P. Keblinski, D. Wolf, F. Cleri, S. R. Phillpot, H. Gleiter, *MRS Bull.* **23**, 36 (1998).
- [67] D. M Gruen, *Annu. Rev. Mater. Sci.* **29**, 211 (1999).
- [68] O. A. Williams, R. B. Jackman, *Semicond. Sci. Technol.* **18**, S34 (2003).

- [69] P. Zopal, M. Sternberg, L. A. Curtiss, T. Frauenheim, D. M Gruen, Phys. Rev. B **65**, 045403 (2001)
- [70] V. D Vankar, N. Dilawar, Vacuum **47**, 11 (1996).
- [71] J. P. Goss, P. R. Briddon, Phys. Rev. B **75**, 075202 (2007).
- [72] L. L. G. Silva, M. K. Franco, F. Yokaichiya, N. G. Ferreira, E. J. Corat, Diamond Relat. Mater. **11**, 153 (2002).
- [73] R. F. Mamin, T. Inushima, Phys. Rev. B **63**, 033201 (2001)
- [74] J. Birrell, J. E. Gerbi, O. Auciello, J. M. Gibson, D. M. Gruen, J. A. Carlisle, J. Appl. Phys. **93**, 9 (2003)
- [75] S. Koizumi, T. Teraji, H. Kanda, Diamond Relat. Mater. **9**, 935 (2000).
- [76] Sakaguchi, M. N-Gamo, Y. Kikuchi, E. Yasu, H. Haneda, Phys. Rev. B **60**, R2139 (1999).
- [77] S. Bhattacharyya, O. Auciello, J. Birrell, J. A. Carlisle, L. A. Curtiss, A. N. Goyette, D. M. Gruen, A. R. Krauss, J. Schlueter, A. Sumant, P. Zapol, Appl. Phys. Lett. **79**, 1441 (2001).
- [78] P.T. Joseph, N.H. Tai, H. Niu, U. A. Palnitkar, W. F. Pong, H. F. Cheng, I.N. Lin, Diamond Relat. Mater. **17**, 1812 (2008).
- [79] M. W. Geis, J. C. Twichell, T. M. Lyszczarz, J. Vac. Sci. Technol. B **14**, 2060 (1996).
- [80] P. Lerner, P. H. Cutler, N. M. Mishovsky, J. Vac. Sci. Technol. B **15**, 337 (1997).
- [81] K. Okano, S. Koizumi, S. R. P. Silva, G. A. J. Amaratunga, Nature **381**, 140 (1996).
- [82] E. Rohrer, C. F. O. Graeff, R. Janssen, C. E. Nebel, H. Guettler, R. Zachai, Phys. Rev. B **54**, 7874 (1996).
- [83] R. Kalish, Carbon **37**, 781 (1999).

- [84] S. Praver, R. Kalish, Phys. Rev. B **51**, 15711 (1995).
- [85] H. A. Hoff, D. J. Vestyck, J. E. Butler, J. F. Prins, Appl. Phys. Lett. **62**, 34 (1993).
- [86] W. Zhu, G. P. Kochanski, S. Jin, L. Seibles, D. C. Jacobson, M. McCormack, A. E. White, Appl. Phys. Lett. **67**, 1157 (1995).
- [87] O. A. Williams, S. Curat, J. E. Gerbi, D. M. Gruen, R. B. Jackman, Appl. Phys. Lett. **85**, 1680 (2004).
- [88] C. E. Nebel, Science **318**, 1391 (2007).
- [89] P. T Joseph, N-H Tai, C-Y Lee, H. Niu, H-F Cheng, W-F Pong, I-Nan Lin, Plasma Process. Polym. **6**, S834 (2009).
- [90] E. Rohrer, C. F. O. Graeff, R. Janssen, C. E. Nebel, H. Guettler, R. Zachai, Phys. Rev. B **54**, 7874 (1996).
- [91] P. Strobel, M. Riedel, J. Ristein, L. Ley, Nature **430**, 439 (2004).
- [92] A. C. Ferrari, J. Robertson, Phys. Rev. B **63**, 121405 (2001).
- [93] A. Lamouri, Y. Wang, G. T. Mearini, I. L. Krainsky, J. A. Jr Dayton, J. W. Mueller, Vac. Sci. Technol. B **14**, 2046 (1996).
- [94] I. N. Lin, Y. H. Chen, H. F. Cheng, Diamond Relat. Mater. **9**, 1574 (2000).

Experimental Techniques

2.1 Introduction

The growth of diamond films with their surface modifications and characterizations were performed using variety of experimental techniques. The diamond films were prepared by microwave plasma enhanced chemical vapour deposition (MPECVD) method. The surface of the diamond films were chemically modified by nitrogen ion implantation and iron (Fe) film deposition followed by post-annealing. The as-prepared as well as the surface modified diamond films were characterized by various experimental techniques such as field emission scanning electron microscope (FESEM), ultra high vacuum scanning tunneling microscope (UHV STM), transmission electron microscope (TEM), X-ray photo electron spectroscopy (XPS), Raman scattering, glancing incident X-ray diffraction (GIXRD) and electron field emission (EFE) measurement. This chapter provides the details of the experimental methods/techniques employed in the present thesis.

2.2 Growth of Diamond films

Two main methods were initially invented for the artificial fabrication of diamond. Those methods are high pressure and high temperature (HPHT) synthesis [1, 2] and chemical vapor deposition (CVD) [3, 4]. In HPHT synthesis, graphite is subjected to high pressure (~ GPa) and heated to over 2000 K in the presence of some metal catalyst which leads to crystallization of diamond. However, this process is intrinsically limited in its

ability to cover surfaces in the form of thin film coatings and to produce large diamond crystal size. To overcome this, CVD processes have been introduced, which are in general, generating atomic hydrogen and the excitation of hydrocarbons. The CVD processes can broadly be classified as thermal CVD and plasma CVD. In thermal CVD process, the decomposition of precursor gases is accomplished by thermal activation, whereas in plasma CVD, it occurs by electron–molecule interaction. First, all CVD systems have some way to activate reactant gases, whether it is by thermal, electrical or by combustion methods. Secondly, a carbon source is needed to extend the diamond lattice. Finally, condition in the system must be such that diamond growth is encouraged while graphite formation is suppressed. Various precursor gases have been used in combination with hydrogen to grow CVD diamond films including methane [3, 4], alcohols [5], carbon monoxide [6] and carbon dioxide and halides [7, 8].

2.2.1 Microwave Plasma Enhanced Chemical Vapour Deposition (MPECVD)

Diamond film growth by MPECVD is now the most widely used technique. In a microwave reactor, microwave power is coupled into the chamber via a dielectric window (usually quartz) in order to create a discharge. The microwave couple energy into the gas phase electrons, which transfer its energy to the gas through collisions. This leads to heating and dissociation of the gas molecules, the formation of active species and finally diamond deposition onto a substrate, which is kept in the plasma. The image of the commercial 2.45 GHz 6” CYRANNUS plasma source from IPLAS GmbH, Troisdorf, Germany which is used for the growth of diamond film is shown in figure 2.1. The cross section geometry of this system is shown in figure 2.2.

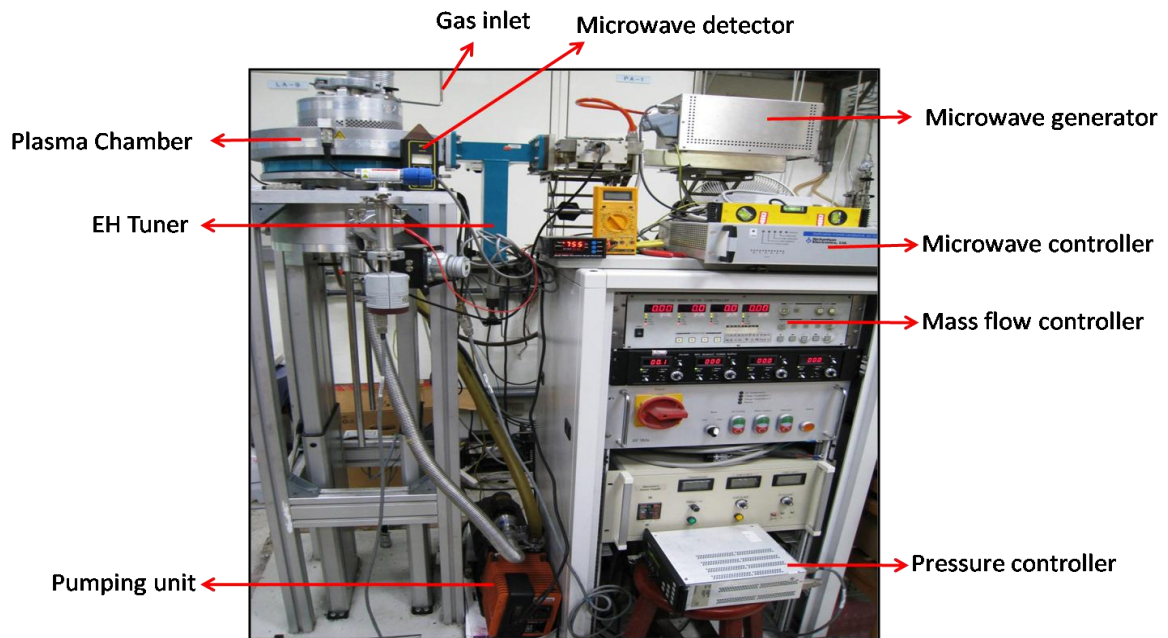


Fig. 2.1 IPLAS MPECVD system used for the growth of diamond film in the present work.

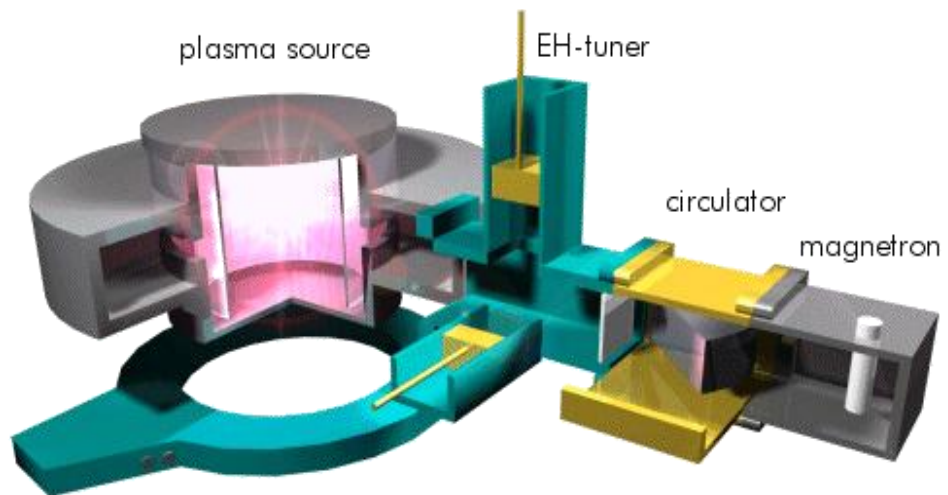


Fig. 2.2 Cross-Section Geometry of a IPLAS microwave Plasma Source [9]

The EH-tuner is a tuning element for tuning the impedance of the plasma source. Depending on the impedance tuning, reflected power is lead back to the circulator, where it is absorbed in a water load. Tuning of microwave power is required because impedance is influenced by various parameters of plasma source and plasma properties. Microwave has shorter wavelength or higher frequency and therefore it can produce high density plasma. In a MPECVD reactor, the growth of high quality diamond films are ensured at relatively high pressure (upto 1000 mbar) and operating temperatures. Being an electrode less deposition, the films produced can be free of contamination. The plasma generated by microwave is stable for a long time. The complex physical and chemical processes occurring during CVD diamond growth process are illustrated in figure 2.3.

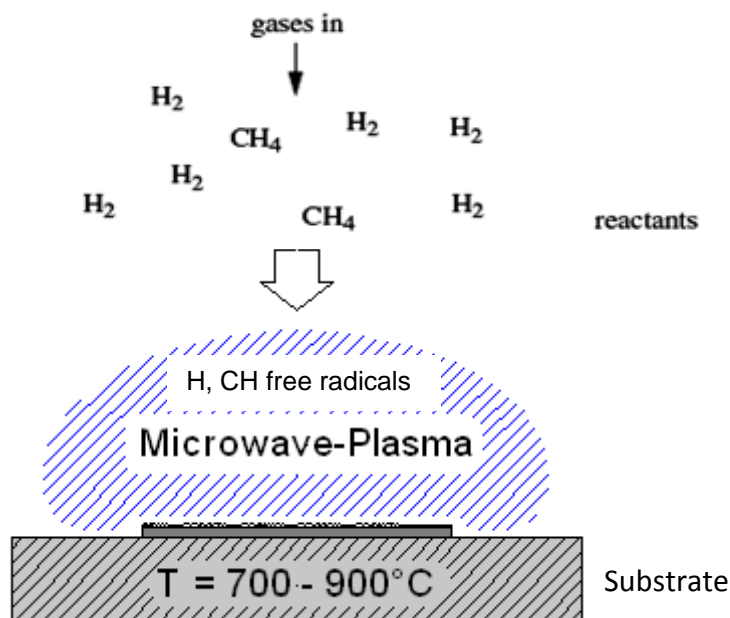


Fig. 2.3 Schematic diagram of the physical and chemical processes occurring during the CVD diamond growth.

The mechanism involves the dissociation of precursor gases by electron impact which makes the suitable plasma. Atoms and reactive species diffuse to the substrate surface, where they absorb and coalesce to form a carbon film. If the deposition conditions are favorable, the formation of diamond film occurs. The conventional CVD diamond growth uses CH_4/H_2 plasma and the control of growth parameters can lead to the growth of various grain sizes of diamond films [10, 11, 12]. The size can be controlled continuously and reproducibly over this range by changing the gas-phase chemistry of the CVD process [11, 12].

For standard growth of diamond on non-diamond substrates, using MPECVD, a surface pretreatment, or “seeding,” (called ultrasonication, embedding diamond particles, micro or nano on the surface) process is required to enhance the nucleation for diamond film growth [12-15]. Ultrasonication of the substrates has been done using nanodiamond powder containing methanol solution (in the form of slurry) for 45 minutes, followed by cleaning it in acetone thoroughly. After seeding, the standard thin film deposition methods, based on MPECVD, deposits microcrystalline diamond (MCD, 1–5 μm diamond grains) on the pre-seeded substrate in hydrogen-rich condition [H_2 (balance)/ CH_4 (0.1 to 4%)] [14, 15], and nanocrystalline diamond (NCD, 10–100 nm diamond grains) in [H_2 (balance)/ 4% CH_4] condition. The growth process was carried out at low temperature (< 465 °C) for 180 min. The grain size can be reduced to 3 to 5 nm, which are the characteristic of UNCD films, by using a novel argon rich chemistry [Ar (99%)/ CH_4 (1%)].

During the UNCD film growth which uses a argon-rich plasma, without any hydrogen, carbon dimers (C_2) are produced which shows in the plasma, from methane decomposition, *i.e* reactions (2.1) and (2.2) below:



While the Ar-rich/ CH_4 plasma produces a complex mixture of carbon (C_2 dimers) and hydrocarbon species, including CH_3 and other hydrocarbons, the C_2 dimers have been proposed to play a critical role in the UNCD nucleation and growth process [16, 17]. Calculations predict that the C_2 dimers have low activation energy (~ 6 kcal/mol) for insertion into the surface of the growing film, thus establishing the growth characteristic of UNCD. Moreover, any new method which have been used or investigated in the present thesis, other than the above used methods are explained in the subsequent sections.

2.3 Surface modification of diamond films

2.3.1 Ion implantation

The grown UNCD films were modified with low energy ion implantation. A schematic diagram of the ion implanter, which is an indigenously upgraded version of an accelerator from Sames, France, is shown in figure 2.4. The photograph of the same accelerator in our laboratory used for ion implantation is shown in figure 2.5. The 150 kV ion implanter consists of a gaseous RF plasma source which generates gaseous ions. Only ions of gaseous elements such as Hydrogen, Helium, Oxygen, Nitrogen, Argon and

Krypton can be accelerated in this accelerator. The desired gases are filled in a gas bottle at 2 bar pressure.

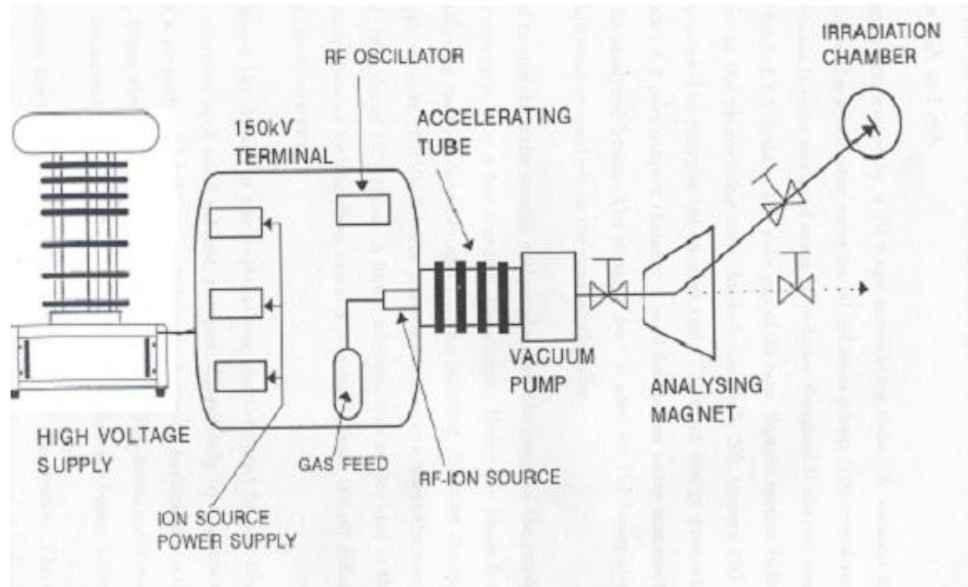


Fig. 2.4 Schematic diagram of the 150 kV ion accelerator.

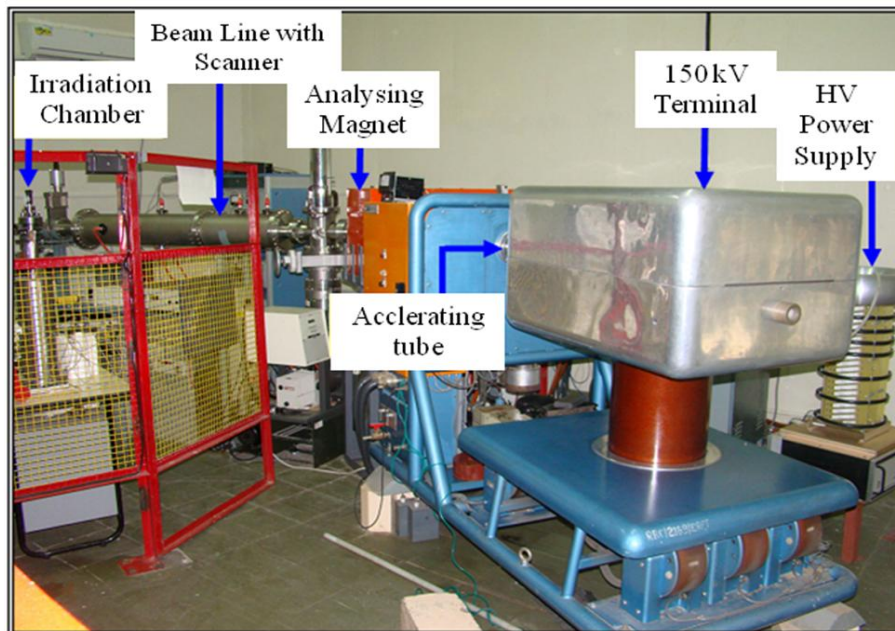


Fig. 2.5 Photograph of the 150 kV ion accelerator and the parts of the accelerator are given.

The gas is fed into the quartz tube through a fine needle valve, where radio-frequency (RF) voltage (100 MHz and 100 W) is applied. The RF generator is capacitatively coupled to the plasma discharge quartz tube. The plasma is generated by coupling of RF power of few hundred watts to a gas at a pressure of 10^{-3} to 10^{-2} mbar. The ions are extracted from the ion source and accelerated to the needed voltage in the range of 30 to 150 kV. The extracted ions are accelerated in an accelerating column. The accelerated energetic ions are mass analyzed by a 45° electromagnet. The analyzed ion beam is collimated and allowed to impinge on the sample kept in an irradiation chamber. A beam scanner is provided to scan the beam uniformly on the sample. The target chamber is maintained at a high vacuum of 10^{-7} to 10^{-8} mbar by a turbo-molecular pump. The sample, mounted on a copper block in the sample manipulator is insulated from the rest of the irradiation chamber, to facilitate beam current measurement. The beam current and dose (ions/cm²) are measured using a current integrator.

In the present study, this ion implanter is used for the implantation of N⁺ ions to diamond films to investigate the effect of N⁺ ions on the electron field emission properties.

To reveal the mechanism of electron field emission (EFE), the structural, electronic and morphological characterization of the diamond films are carried out with a number of analytical tools which are explained in the following section.

2.4 Structural and morphological characterization

2.4.1 Scanning tunneling microscope (STM)

STM is a microscopy technique, with which it is possible to visualize conducting/semi-conducting surfaces in atomic-scale. It has also been proven that it is an

extremely powerful tool for studying the electronic properties of nanostructured materials in atomic scale resolution. The STM was invented by Binnig and Rohrer in 1981 [18]. The power of the technique was quickly recognized, and in 1986, the inventors were awarded the Nobel Prize in physics. Since the initial experiments of Binnig *et al.*, the field of STM has experienced rapid growth. Several related methods have since been developed, such as atomic force microscope (AFM) [19], the scanning near field optical microscope (SNOM) [20], the magnetic force microscope (MFM) [21] and the ballistic-electron-emission microscope (BEEM) [22]. Microscopes are currently available in several commercial models designed for performing experiments on a variety of samples in many different environments. Because of this scanning mechanism, all these techniques are summarized as scanning probe microscope (SPM).

2.4.1.1 Instrumentation

The fundamental physical phenomenon on which STM is based is the quantum mechanical tunneling of electrons through a potential energy barrier. The STM is composed of the scanning assembly with a sample-tip approach mechanism, sometimes referred as the head, a vibration isolation system, electronics that include computer controlled circuits (voltage and current amplifiers, digital to analog and analog to digital converters, etc.), computers and high-resolution monitor for image display. A schematic of the STM is shown in figure 2.6. A probe tip, usually made of tungsten (W) or Pt-Ir alloy, is attached to piezodrives, which consists of three mutually perpendicular piezoelectric transducers *i.e.*, x , y and z piezo.

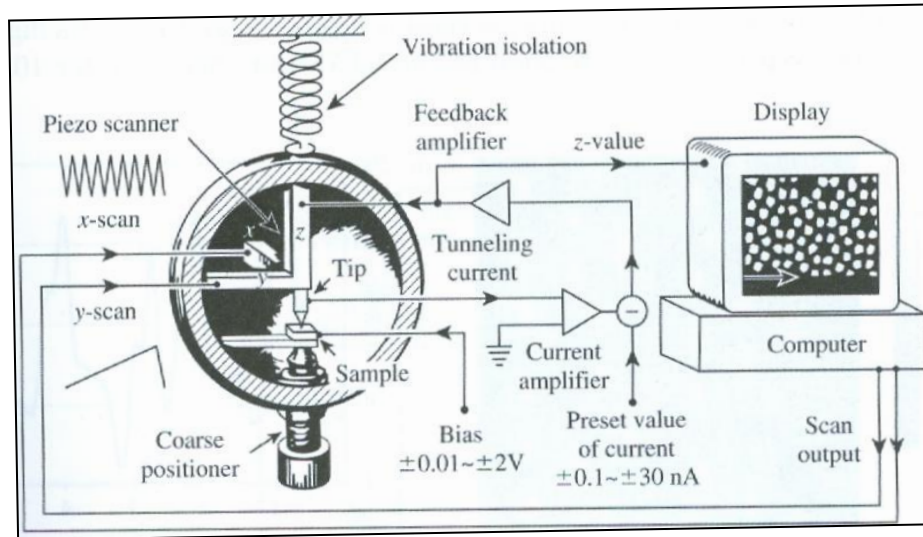


Fig. 2.6 Schematic diagram of STM [19]

The piezoelectric transducers expand or contract upon a small change in applied voltage. By applying a saw tooth voltage on the x piezo and a voltage ramp on the y piezo, the tip scans on the xy plane. The distance between the tip and the sample, usually within a fraction of nanometer, is monitored by the coarse positioner and a z piezo.

A schematic diagram of a STM head is shown in figure 2.7. The sample is placed on a tantalum sample holder which is fixed with the spring clips. The tip is placed on a scanner tube via a macro holder which can be controlled by applied voltage for scanning the surface of the sample in x , y and z direction. The scanner tube is connected to the piezo tube by a fitting rod for the movement of the tip. This arrangement enables the motion of the tip to be controlled with sub-nanometer precision.

The high resolution STM imaging, *i.e.* 0.1 \AA vertically and 1.0 \AA laterally, imposes the requirement that noise from any source should be less than 0.01 \AA in z and 0.1 \AA in x and y . Mechanical vibrations are a large component of the noise and it is particularly

challenging to reduce these to less than a hundredth of an angstrom in the vertical direction. Vibrations that can reach the sample-tip junction originate from the building, to the table/chamber system on which the microscope sits, or possibly components of the microscope itself. The performance of STM relies on the sharpness of the tip. Hence, fine etched W tips, are preferred for STM measurements. Alternatively, an inert, cut platinum or iridium wire can also be used. The choice of the tip material depends on the specific application of the STM. Usually STM experiments are performed in vacuum, to minimize the effect of the atmospheric contaminants on the tunneling current.

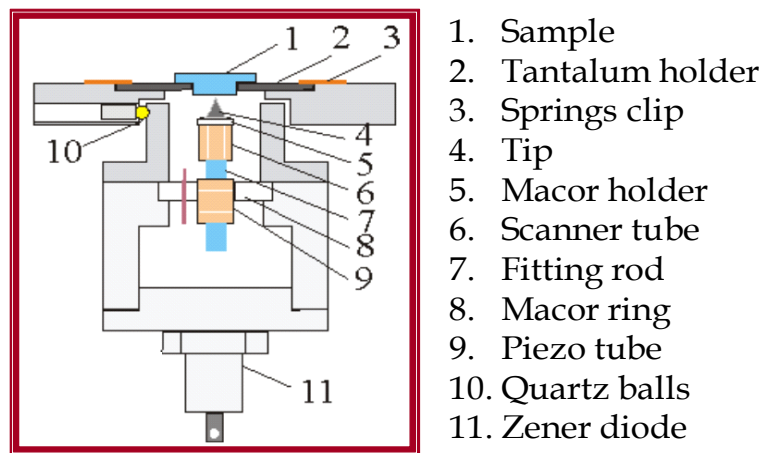


Fig. 2.7 Schematic diagram of a STM head [19].

2.4.1.2 Principle of Operation

When the electron wave function of the tip overlaps the electron wave functions of the sample surface, a finite tunneling conductance is generated. By applying a bias voltage between the tip and the sample, a tunneling current is generated. Depending upon the polarity of the bias voltage V to the sample, the electrons start to flow between the sample

and the tip. The most widely convention is that the tip is virtually grounded. If the sample bias $V < 0$, *i.e* the sample is negatively biased with respect to tip, the electrons are tunneling from the occupied states of the sample into the empty states of the tip. If $V > 0$, the electrons are tunneling from the occupied states of the tip into the empty states of the sample. The ideal band structure in figure 2.8 schematically illustrates the current flow in positive/negative bias to the sample. When, a bias is applied between the sample and tip, the Fermi levels of the two materials are displaced with respect to each other. As the bias is ramped, either positively or negatively, the current varies in response to the changing electron density in the energy window. Ramping in both directions probes both the occupied and unoccupied energy states, with the magnitude of the current at a specific voltage directly related to the density of states of the sample.

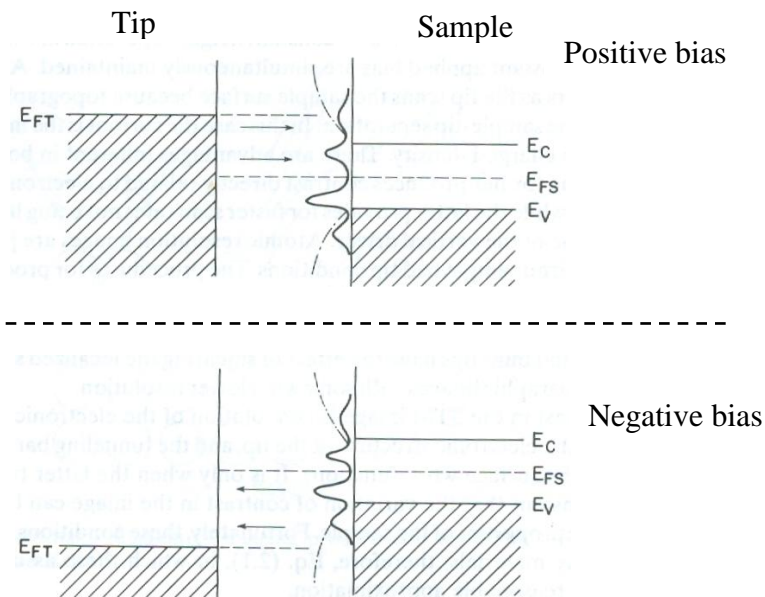


Fig. 2.8 Schematic diagram of tunneling spectroscopy using idealized band structure in which the tip is modeled, as a metal as continuous occupation to the Fermi level, and the sample is imaged as semiconductor with surface states. Shaded areas refer to energy regions in which states are occupied [23].

A pre-amplifier converts the tunneling current to a voltage, which is then compared with a reference value. The difference is amplified to drive the z piezo. The phase of the amplifier is so chosen to provide a negative feedback, *i.e.*, if the absolute value of the tunneling current is larger than the reference value, then the voltage applied to the z piezo tends to withdraw the tip from the sample surface and vice versa. Therefore, an equilibrium z position is established. As the tip scans over the x - y plane, a two-dimensional array of equilibrium z positions, representing a counter plot of the equal tunneling current surface, is obtained. If the tip is moved across the sample in the x - y plane, the changes in surface height and density of states cause changes in tunneling current. The counter plot is displayed and stored in a computer memory. These changes are mapped in images. This change in current with respect to position can be measured itself, or the height, z , of the tip corresponding to a constant current can be measured. These two modes are called constant height mode and constant current mode, respectively. In constant current mode, feedback electronics adjust the height by a voltage to the piezoelectric height (z) control mechanism [24]. This leads to a height variation and thus the image comes from the tip topography across the sample and gives a constant charge density surface; this means contrast on the image is due to variations in charge density [25]. In constant height mode, the voltage and height are both held constant while the current changes to keep the voltage from not changing; this leads to an image made of current changes over the surface, which can be related to charge density [25].

2.4.1.3 Scanning tunneling spectroscopy (STS)

One of the most fascinating potentials of the STM is its capability to obtain spectroscopic data in atomic resolution [24]. In addition to scanning across the sample,

information on the electronic structure at a given location in the sample can be obtained by sweeping voltage and measuring current [24]. This type of measurement is called Scanning tunneling spectroscopy (STS) and typically results in a plot of the local current (I in nA) as a function of input bias voltage (V in volt). STS provides the possibility for probing the local electronic structure of metals, semiconductors, and thin insulators on a scale unobtainable with other spectroscopic methods. Additionally, topographic and spectroscopic data can be recorded simultaneously. STS performed in the STM provides information about the electronic structure of the sample by probing the sample density of states as a function of energy. The concept is similar to traditional sandwich junction spectroscopy or inelastic tunneling spectroscopy (IETS). The primary difference is that a vacuum gap exists between the two electrodes rather than an insulator in case of IETS. There are also two methods of acquiring spectroscopic information with an STM. The first referred to as point spectroscopy, involves moving the tip to a feature of interest, disengaging the feedback mechanism, modulating the tip bias and recording the variation in current as discussed in figure 2.8.

When the distance between the tip and substrate is few Å, there is an overlap between the electron wave functions of the tip and substrate resulting in a tunnelling current. The tunnelling current depends on the work function of the tip and the sample and the distance between them as given in Equation 2.3

$$I_t = C\rho_s\rho_t \exp(-2\kappa z) \quad (2.3)$$

Chapter 2

where ρ_s and ρ_t are the electron densities of the sample surface and probe tip, respectively. C is proportionately constant, $\kappa = [2\pi/\hbar][2m\phi]^{1/2}$, here effective work function, $\phi = (\phi_s - eV_{bias} + \phi_t)/2$ and z is the distance between the tip and sample.

The contrast in the STM image is the convolution of the electronic structure of the sample, the electronic structure of the tip and the tunnelling barrier function (related to the surface work function). It is only when the latter two functions are constant, then the variations of contrast in the image can be attributed to electronic properties of the sample. These conditions can be easily achieved on many materials; therefore, Eq. (2.3), in which these assumptions are implicit, is a reasonable approximation.

The method of obtaining spectroscopic information involves simultaneous collection of images at various biases. This can be accomplished by modulating the bias at a high frequency and recording the current at several discrete values of applied bias or by using the same sample and holding method of point spectroscopy at every image point. The simultaneous collection of image points is referred to as current imaging tunneling spectroscopy (CITS).

Understanding the expressions for the tunneling current is important since STS relies on tunneling phenomena and measurement of the tunneling current or its derivative. Using the modified Bardeen transfer Hamiltonian method, which treats tunneling as a perturbation, the tunneling current (I) is found to be

$$I = \frac{4\pi e}{\hbar} \int_{-\infty}^{\infty} [f(E_F - eV + \epsilon) - f(E_F + \epsilon)] \rho_S(E_F - eV + \epsilon) \rho_T(E_F + \epsilon) |M_{\mu\nu}|^2 d\epsilon \quad (2.4)$$

where $f(E)$ is the Fermi distribution function, ρ_S and ρ_T are the density of states (DOS) of the sample and tip, respectively, and $M_{\mu\nu}$ is the tunneling matrix element between the modified wave functions of the tip and the sample surface.

For low temperatures and a constant tunneling matrix element, the tunneling current becomes

$$I \propto \int_0^{eV} \rho_S(E_F - eV + \epsilon) \rho_T(E_F + \epsilon) d\epsilon, \quad (2.5)$$

which is a convolution of the DOS of the tip and the sample [26]. Generally, STS experiments attempt to probe the sample DOS, but Eq. (2.5) shows that the tip DOS must be known for the measurement to have meaning. Eq. (2.5) implies that

$$\frac{dI}{dV} \propto \rho_S(E_F - eV + \epsilon), \quad (2.6)$$

under the assumption that the DOS of the tip is constant. For these ideal assumptions, the tunneling conductance is directly proportional to the DOS of sample [26].

For higher bias voltages, the predictions of simple planar tunneling models using the Wentzel-Kramers Brillouin (WKB) approximation are useful. In the WKB theory, the tunneling current is predicted to be

$$I = \int_0^{eV} \rho_S(r, E) \rho_T(r, E - eV) T(E, eV, r) dE, \quad (2.7)$$

where $T(E, eV, r)$ is the energy- and bias-dependent electron tunneling transition probability, given by

$$T = \exp\left(-\frac{2Z\sqrt{2m}}{\hbar} \sqrt{\frac{\phi_s + \phi_t}{2} + \frac{eV}{2} - E}\right), \quad (2.8)$$

where ϕ_s and ϕ_t are the respective work functions of the sample and tip [27].

2.4.1.4 Acquisition of STS data

Acquiring standard STM topographs at many different tip-sample biases and comparing to experimental topographic information is the most straight-forward spectroscopic method. The tip-sample bias can also be changed on a line-by-line basis during a single scan. This method creates two interleaved images at different biases. Since only the states between the Fermi levels of the sample and the tip contribute to I , this method is a quick way to determine whether there are any interesting bias-dependent features on the surface.

By using modulation techniques, a constant current topograph and the spatially resolved dI/dV can be acquired simultaneously. A small, high frequency sinusoidal modulation voltage is superimposed on the *D.C* tip-sample bias. The *A.C.* component of the tunneling current is recorded using a lock-in amplifier, and the component in-phase with the tip-sample bias modulation gives dI/dV directly.

In order to obtain I - V curves simultaneously with a topograph, a sample-and-hold circuit is used in the feedback loop for the z piezo signal. A sample-and-hold amplifier freezes the z piezo feedback signal, which holds the tip-sample spacing constant by preventing the feedback system from changing the bias applied to the z piezo [28]. The tip-sample bias is swept between the specified values, and the tunneling current is recorded. After the spectra acquisition, the tip-sample bias is returned to the scanning value, and the

scan resumes. Using this method, the local electronic structure of semiconductors can be probed [29].

2.4.1.5 Data interpretation

The band gap of the sample at the location of the I - V measurement can be determined from the measured I - V data. By plotting the magnitude of I in log scale versus the tip-sample bias, the band gap can clearly be determined. Although determination of the band gap is possible from a linear plot of the I - V curve, the log scale increases the sensitivity [30]. Alternatively, a plot of the conductance, dI/dV , versus the tip-sample bias, V , allows one to locate the band edges that determine the band gap [31].

The plot of dI/dV as a function of the tip-sample bias, is associated with the density of states of the surface, when the tip-sample bias is less than the work functions of the tip and the sample. Usually, the WKB approximation for the tunneling current is used to interpret the measurements at low tip-sample bias relative to the tip and sample work functions. The derivative of Eq. (2.7), I in the WKB approximation, is

$$\frac{dI}{dV} = \rho_s(r, eV) \rho_t(r, 0) T(eV, eV, r) + \int_0^{eV} \rho_s(r, E) \rho_t(r, E - eV) \frac{dT(E, eV, r)}{dV} dE, \quad (2.9)$$

Although the tunneling transmission probability T is generally unknown, at a fixed location, T increases smoothly and monotonically with the tip-sample bias. Hence, structure in the dI/dV is usually assigned to features in the density of states in the first term of Eq. (2.9) [29]. Interpretation of dI/dV as a function of position is more complicated. Spatial variations in T show up in measurements of dI/dV as an inverted topographic

background. When images are obtained in constant current mode, the images of the spatial variation of dI/dV contain a convolution of topographic and electronic structure.

Since both the tunneling current, Eq. (2.7), and the conductance, Eq. (2.9), depend on the tip DOS and the tunneling transition probability, T , quantitative information about the sample DOS is very difficult to obtain. Additionally, the voltage dependence of T , which is usually unknown, can vary with position due to local fluctuations in the electronic structure of the surface [27]. For some cases, normalizing dI/dV by dividing by I/V can minimize the effect of the voltage dependence of T and influence of the tip-sample spacing.

2.4.2 Transmission Electron Microscopy (TEM)

Transmission electron microscopy is a versatile and indispensable tool in the study of materials due to its high spatial resolution. In TEM, the image is formed by electrons passing through the sample. The principle of operation of TEM is almost same as that of an optical microscope. However, TEM uses magnetic lens instead of glass lens in optical microscope and electrons instead of photons. TEM has magnification and resolution capabilities that are over a thousand times beyond that offered by the optical microscope. TEM is able to analyze the morphology, localized crystal structure, composition and defect structure with high spatial resolution leading to an understanding of materials property. It provides useful information about the specimen chemistry and crystallography.

2.4.2.1 Principle

In transmission electron microscopy, much smaller wavelength electrons (0.03 \AA) are used instead of photons ($\lambda > 1000 \text{ \AA}$), providing much higher resolution. The beam of

Chapter 2

electron emitted by the electron gun is focused by a condenser lens into a small spot (~2 to 3 μm) on the sample and after passing through the sample, it is focused by the objective lens to project the magnified image on the screen. The objective lens forms a diffraction pattern in the back focal plane and a magnified image of the sample in the image plane. A number of intermediate lens are used to project either the image or the diffraction pattern onto a fluorescent screen or film in most conventional TEMs.

As the wavelength of the electron beam used in TEM is comparable to atomic dimensions, so electrons are strongly diffracted from the regular array of atoms at the surface of the crystal. The electrons are diffracted by atomic planes inside the materials as in the case of X-rays. It is therefore possible to form a transmission electron diffraction pattern from electrons that have passed through a ultra thin specimen. If the transmitted electrons could be focused, their very short wavelength would allow the specimen to be imaged.

If the sample is thin (< 200 nm) and constituted of light chemical elements, the image presents a very low contrast when it is focused. To obtain amplitude contrasted image, an objective diaphragm is inserted in the back focal plane to select the transmitted beam (and possibly few diffracted beam): the crystalline parts in Bragg orientation appear dark and the amorphous or the non-Bragg oriented parts appear bright. This imaging mode is called the bright field mode (BF) [figure 2.9]. If the diffraction is constituted by many diffracting phases, each of them can be differentiated by selecting one of its diffracted beams with the objective diaphragm. To do that, the incident beam must be tilted so that the diffracted beam is put on the objective lens axis to avoid the off-axis aberrations

[Fig. 2.9]. This mode is called the dark field mode (DF). The BF and DF modes are used for imaging materials to nanometer scale.

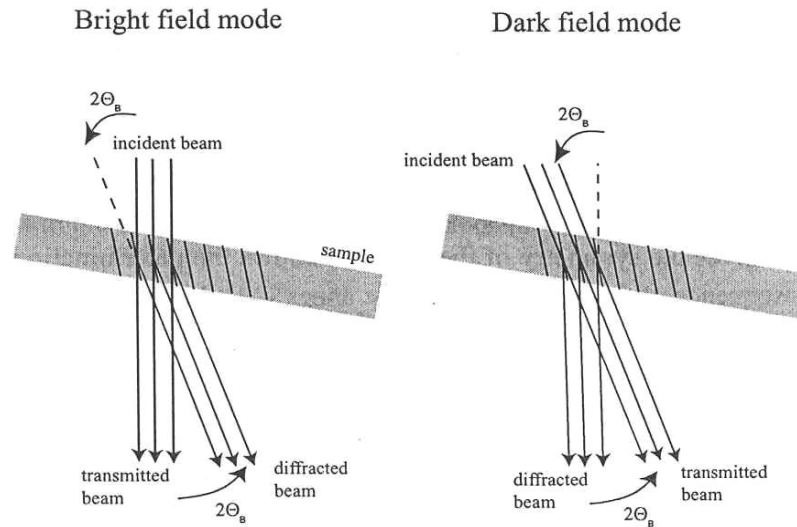


Fig. 2.9 The bright field and dark field modes for imaging.

The selected area diaphragm is used to select only one part of the imaged sample for example a particle or a precipitate. This mode is called selected area diffraction (SAED). The spherical aberrations of the objective lens limit the area of the selected object to a few hundred nanometer. Nevertheless, it is possible to obtain diffraction patterns of a smaller object by focusing the electron beam with the projector lenses to obtain a small spot size on the object surface (2-10 nm).

2.4.2.2 Components of TEM

The TEM system can be divided mainly into three sections, namely 1) the illuminating system, 2) the specimen stage and 3) the imaging stage. The illuminating stage is situated at the top of the microscope column and consists of the electron gun

(composed of the filament, shield and anode) and the condenser lens. It can be operated in two principal modes; parallel beam [for imaging and selected area electron diffraction (SAED)] and convergent beam [for STEM, analysis using X-ray and electron spectrometer, and convergent beam electron diffraction (CBED)]. Two basic modes of operation involves the (a) diffraction mode where the diffraction pattern (DP) is projected onto the viewing screen, and (b) image mode where the images are projected on the viewing screen [Fig. 2.10].

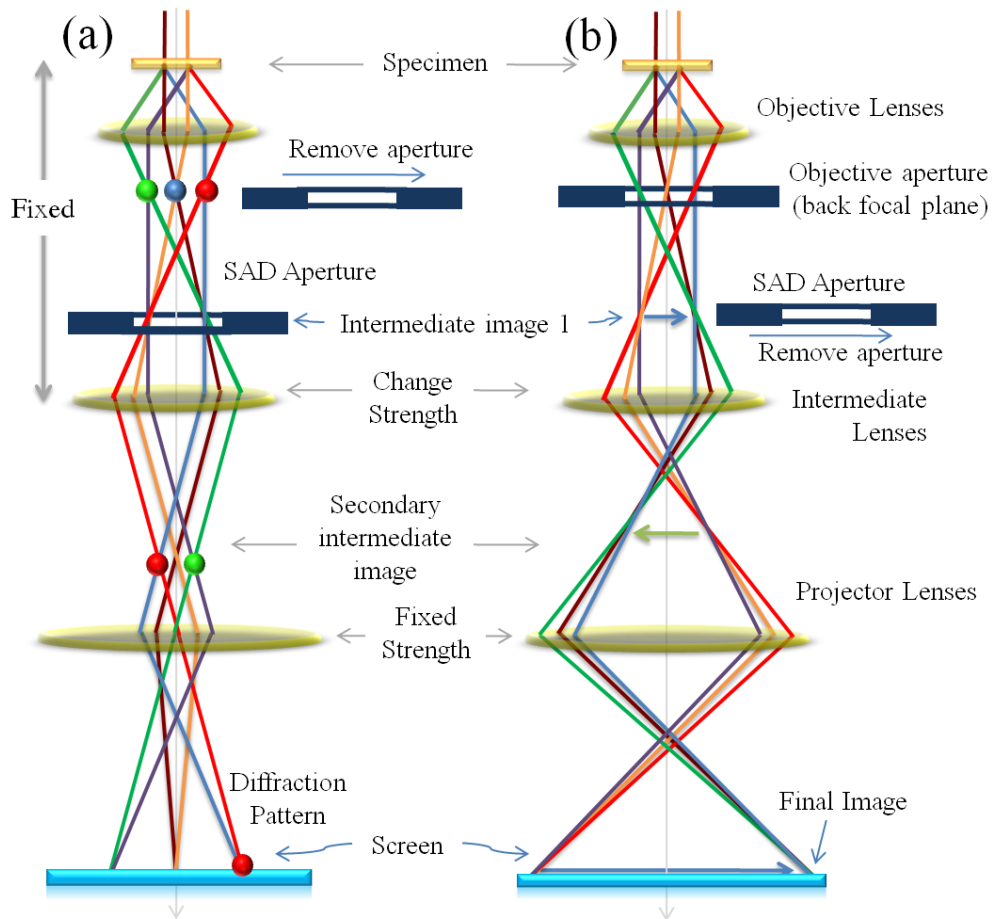


Fig. 2.10 Schematic diagram of TEM showing the two basic modes of operation (a) diffraction mode and (b) image mode [32].

In each case the intermediate lens selects either the (a) back focal point or the (b) image plane of the objective lens as its object [32]. The electron gun is the source of electrons. The standard filament or cathode is composed of a V-shaped tungsten wire approximately 0.1 mm in diameter. The specimen stage is designed to hold the specimen and to view all possible regions of the specimen by moving it horizontally and tilting. The imaging system includes the objective lens, objective aperture, objective stigmator, selected area aperture, intermediate, and projector lens that are involved in forming, focusing, magnifying and projection of the final image on the viewing screen as well as the camera that is used to record the image.

As opposed to conventional microscopy, HRTEM does not use amplitudes, i.e. absorption by the sample, for image formation. Instead, contrast arises from the interference in the image plane of the electron wave's interference with itself. When the electron beam interacts with the sample, the electron exit wave, below the sample $\varphi_e(\mathbf{x}, \mathbf{u})$ as a function of the spatial coordinate \mathbf{x} is a superposition of a plane wave and a multitude of diffracted beams with different in plane spatial frequencies \mathbf{u} (high spatial frequencies correspond to large distances from the optical axis). The phase change of $\varphi_e(\mathbf{x}, \mathbf{u})$ compared to the incident wave peaks at the location of the atom columns. The exit wave now passes through the imaging system of the microscope where it undergoes further phase change and interferes as the image wave in the imaging plane (photo plate or CCD). The relationship between the exit wave and the image wave is a highly nonlinear one and is a function of the aberrations of the microscope.

In the present study, a TEM, JEOL 2100F operated at 200 kV is used to observe the detailed microstructure of the diamond films

2.4.3 Scanning Electron Microscope (SEM)

The Scanning Electron Microscope (SEM) is an indispensable characterization tool in materials science. SEM uses a focused beam of high-energy electrons to generate a variety of signals at the surface of solid specimens. The signals that derive from electron-sample interactions reveal information about the sample including external morphology (texture), chemical composition, and crystalline structure and orientation of materials. The field emission gun (FEG), acts as an electron source. The FEG source has a number of advantages than the conventional thermionic emitter. It has high brightness, low evaporation of cathode material and low thermal drift during operation. These aspects enhance the resolution limits of a field emission SEM (FESEM). The FEG generates electrons and accelerates them to energy in the range 0.1 – 30 keV towards the sample. A series of lenses focus the electron beam on to the sample where it interacts with the sample to a depth of approximately 1 μm .

Accelerated electron beam in a SEM carry significant amounts of kinetic energy, and this energy is dissipated as a variety of signals produced by electron-sample interactions when the incident electrons are decelerated in the solid sample. These signals include secondary electrons (that produce SEM images), backscattered electrons (BSE), diffracted backscattered electrons (EBSD) that are used to determine crystal structures and orientations of minerals), photons (characteristic X-rays that are used for elemental analysis and continuum X-rays), visible light, and heat. Secondary electrons and

backscattered electrons are most commonly used for imaging samples. Secondary electrons are most valuable for showing morphology and topography on samples and backscattered electrons are most valuable for illustrating contrasts in a composition of multiphase samples (*i.e.* for rapid phase discrimination and topography).

In this study, a FESEM (Model Zeiss SUPRA 55) is used to examine the morphology and structure of the diamond films. The energy dispersive X-ray spectrometer (EDS) equipped with FESEM was used for the elemental characterization of the tracks during the tribological studies.

2.5 Electron field emission

The electron field emission properties of the diamond films are measured by a tuneable parallel plate capacitor setup [33]. The samples are mounted on a steel plate of 50 mm in diameter that is kept in a spherical steel chamber. This chamber is maintained at a vacuum of 2×10^{-7} mbar. The samples are of 10 mm \times 10 mm in size. Silver paste is used to mount the samples on the steel plate because that gives a good contact between sample and the steel plate. The diamond thin film on the substrate acts as a cathode mounted on steel plate. Molybdenum (Mo) tip of 3 mm diameter is used as anode. The face of the tip and the sample surface are held parallel to each other. The positive terminal of the high voltage source (1.2 kV) has been connected to the tip (anode) where voltage is supplied for electron emission from diamond film cathode. The schematic of the field emission set up is shown in figure 2.11.

The emission current has been derived indirectly by measuring the voltage across the 100 k Ω resistor applying the voltage to the anode in step of 20 V from 0 -1000 V from a

voltage source of 1.2 kV. The separation of the anode (Mo) tip from the sample was measured using a digital micrometer (with accuracy of 1 μm) and an optical microscope. The EFE behaviour of materials was explained using Fowler–Nordheim (F–N) model.

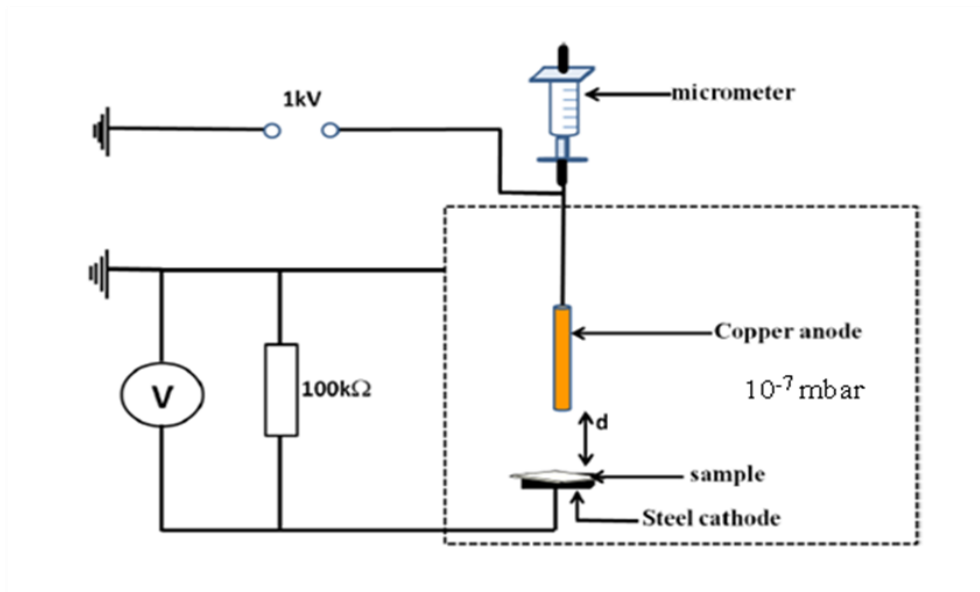


Fig. 2.11 Schematic diagram of the field emission set up used for measuring the field emission properties of diamond films.

2.6 X-ray Photoelectron Spectroscopy (XPS)

X-ray Photoelectron Spectroscopy (XPS) or Electron Spectroscopy for Chemical Analysis (ESCA) is a surface analysis technique which is unique in providing information regarding the bonding state of an element in a material. XPS also finds its wide application for oxidation state determination of elements, surface analysis of semi-conducting and insulating materials, and identification of the chemical state of the metal oxide films etc [34-36]. The phenomenon is based on the photoelectric effect outlined by Einstein in 1905

where the concept of the photon was used to describe the ejection of electrons from a surface when photons impinge upon it.

In X-ray photoelectron spectroscopy, soft X-ray sources are used for X-ray beam. Photons of energy $h\nu$ impinge upon a sample and cause emission of electrons which are collected by an electron lens system and subsequently detected by an energy-selective analyser. When the photon beam falls on the sample surface, results in absorption by an atom in the sample which leads to the photoemission of the electrons from the core-levels as well as from the valence levels. The photon energy, $h\nu$ ($h = 6.63 \times 10^{-34}$ J.s), should be greater than the binding energy (B. E) in order to obtain electron photoemission. As a consequence, photoelectric effect is produced and, thus, the sample emits electrons with a kinetic energy:

$$E_k = h\nu - E_b , \quad (2.10)$$

where E_b is the binding energy of the electron, which is a characteristic of each element and E_k is the initial kinetic energy of the impinging photo electrons. The emitted electrons from the sample pass through an electrostatic hemispherical energy analyzer, where they are discriminated on the basis of their kinetic energy E_k or E_b to produce a spectrum of electron intensity, expressed as counts, counts/s, versus electron energy. The so obtained E_k or E_b gives information about the surface chemical composition and bonding state of the material.

In this study, a SPECS make XPS photoelectron spectrometer is used which uses monochromatic Al K_α radiation at 1486.74 eV as a probe with an energy resolution of 0.1 eV.

2.7 Raman spectroscopy

Raman spectroscopy is one of many light scattering phenomena which originate from the principle that the intensity of a light beam attenuates measurably when it passes through a non-absorbing medium. The Raman effect is named after C. V. Raman who first observed this phenomenon, with K. S. Krishnan in 1928 [37]. It belongs to the class of molecular-scattering phenomena.

Raman spectroscopy is an optical analysis technique that measures the intensity of inelastically scattered light over a range of frequencies. During the Raman scattering process, a small portion of the incident photons (1 in 10^6 - 10^7) are scattered inelastically due to their interaction with the vibrations or rotations of atoms or molecules. The inelastic exchange occurs because the photons either lose or gain energy from the material under examination. In the case of the solid state lattice of silicon, the photons scatter due to their interaction with lattice vibrations (phonons). By collecting the scattered photons of inelastic scattered light across a range of frequencies, which shows the energy shift of the incident beam from where it is possible to know the particular vibrational modes of a sample.

In the present thesis, the Raman spectra are recorded using Renishaw micro-Raman spectrometer (Model-INVIA) with laser excitation wavelengths of 514 nm.

2.8 X-ray diffraction (XRD)

X-rays are electromagnetic radiation with typical photon energies in the range of 100 eV to 100 keV. For diffraction applications, only short wavelength X-rays in the range of a few angstroms to 0.1 \AA (1 keV to 120 keV) are used. These energetic X-rays can

penetrate deep into the materials and provide information about the bulk structure. X-rays are produced generally by either X-ray tubes or rotating anode or synchrotron radiation.

X-rays primarily interact with electrons in atoms, collide and some photons from the incident beam are deflected away from their original wavelength. If the wavelength of these scattered X-rays did not change, the process is called elastic scattering. These diffracted X-rays are measured to extract information about the crystal structure, since they carry information about the electron distribution in the material. Diffracted waves from different atoms can interfere with each other and the resultant intensity distribution is strongly modulated by this interaction. Diffraction maxima are produced when the subtended angle formed between the emergent and incident X-ray beams, 2θ , satisfies the Bragg's condition:

$$2d\sin\theta = n\lambda \quad (2.11)$$

where d is the distance between crystallographic planes; n is a natural number, and λ is the radiation wavelength. Peak distribution accounts for crystallographic planes parallel to the sample surface. The Debye- Scherrer's formula is used for determining the crystallite size (D), and it can be expressed as

$$D = \frac{0.9\lambda}{\beta \cdot \cos\theta} \quad (2.12)$$

where D is the crystallite size, λ is the wavelength of incident X-ray, β is full width half maximum value of the diffraction peak and θ is the diffraction angle.

In the present thesis, X-ray diffractometer (GIXRD – STOE, German made) in 2θ range of 20° – 90° at an angle of incidence 0.2° is used, which indicates the structure of the

thin film and compared to the tabulated references obtained from the Joint Committee for Powder Diffraction Studies (JCPDS).

2.9 Tribometer

Tribotesting is performed to determine the coefficient of friction of diamond films and their wear life. Figure 2.12 shows the Tribometer from CSM Instruments, Switzerland. The principal measured parameter is coefficient of friction in real time.

2.9.1 CSM Tribometer

The CSM tribometer, used in the present studies, has a load range of 1 to 10 N and load can be applied in steps of few mN to 1 N. It can work both in linear reciprocating mode and circular mode. Environment conditions like humidity, working atmosphere and lubrication inside the tribo test chamber can be controlled. The tangential force is measured by the deflection of elastic arm (shown in Fig. 2.12) using a linear variable differential transformer (LVDT) sensor. In tribometry, a sphere, a pin or flat is loaded onto the test sample with a precisely known force. The pin is mounted on a stiff lever, designed as a frictionless force transducer. The friction coefficient is determined during the test by measuring the deflection of the elastic arm.

Wear coefficients for the pin and disk materials are calculated from the volume of material lost during the test,

$$V = K.F.s \quad (2.13)$$

where V is the wear volume, F is the normal load, s is the sliding distance and K is a constant called, wear rate. This simple method facilitates the study of friction and wear behavior of almost every solid state material in combination with or without lubricant.

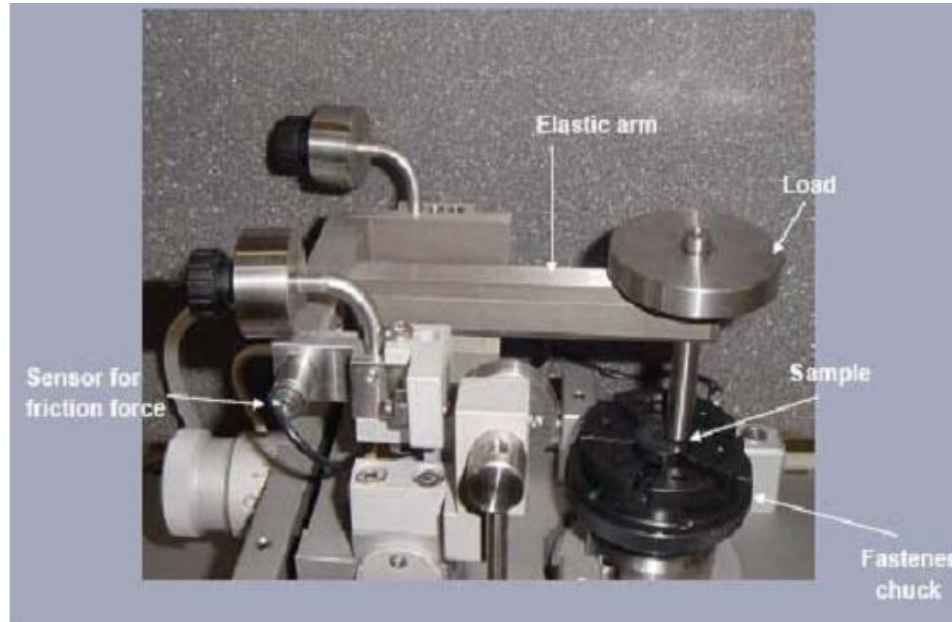


Fig. 2.12 CSM Tribometer used for tribological studies.

2.10 Nanoindentation technique

Nanoindentation is a novel technique to measure the local mechanical properties of bulk materials and thin films [38]. The technique allows depth resolved indentation and facilitates indentation of thin films and coatings. Surface and sub-surface mechanical properties can be evaluated. In this technique, the load-displacement curves are considered as mechanical fingerprints of materials. The two major properties measured using nanoindentation technique, are the hardness (H) and elastic modulus (Young's modulus, E). Oliver and Pharr have developed a methodology to extract mechanical

properties from homogeneous, isotropic materials which exhibit no time dependence in their deformation behavior like visco-elasticity or creep [39]. A typical load-displacement curve generated during a full indentation cycle consists of a loading and an unloading part. The loading part generally involves elastic and plastic deformation of a material. However, the unloading part of the curve is purely elastic. The advantage of nanoindentation testing technique over conventional indentation technique lies in the determination of contact area without measuring the residual impression dimensions. Also, the contact area is measured at maximum load without unloading the indenter.

2.11 Scratch testing

Scratch test is a routinely used technique to evaluate cohesion and adhesion of thin films and coatings deposited on a substrate. It involves a large number of parameters to be controlled [40]. In-situ capturing of acoustic signals makes it a more versatile and effective technique to find the critical loads for coating failure. Revetest (CSM Instruments, Switzerland) is a robust and fully automated scratch tester. LVDT sensors are used to apply the loads and to measure the penetration depth during a scratch test. The load range of the instrument is from 1 to 300 N with a load resolution of 3 mN. It has a force feedback loop control for controlling the imposed load during the scratch test. The maximum penetration depth is 1 mm with a resolution of 1.5 nm. Scratch speed can be varied from 0.4 to 600 mm/min. The maximum frictional force which can be measured during scratch test is 200 N with a frictional force resolution of 3 mN. Optical micrograph of CSM Revetest is shown in figure 2.13.



Fig. 2.13 Optical micrograph of CSM Revetest.

In this process, a diamond indenter is moved across the coating surface with normal force acting on it. During scratch, the applied force can be kept constant or can be progressively increased or decreased. The penetration depth during scratch is also measured. Tangential force acting on the indenter is measured using a force sensor. The measured tangential force is then used to calculate the coefficient of friction. An acoustic emission sensor is used to capture the acoustic signals generated during a failure event.

2.12 Conclusion

In this chapter, diamond film preparation methods by MPECVD, surface modification techniques like ion implantation, and the characterization techniques like FESEM, STM, XPS, TEM, GIXRD, Raman scattering and field emission measurements have been discussed.

2.13 References

- [1] J. E. Field, 'The Properties of Diamond', Academic press, New York, (1979).
- [2] J. E. Field, 'The Properties of Natural and Synthetic Diamond', Academic Press, London, (1992).
- [3] S. Matsumoto, Y. Sato, M. Tsutsumi, N. Setaka, J. Mater. Sci. **17**, 3106 (1982).
- [4] F. G. Celii, J. E. Butler, Ann. Rev. Phys. Chem., **42**, 643 (1991).
- [5] Y. Tzeng, 'Proc of ADC/FCT', Tsukuba, Japan 1999.
- [6] Y. Satito, K. Sato, K. Gomi, H. Miyadera, J. Mater. Sci. **25**, 1246 (1993).
- [7] C. A. Rego, R. S. Tsang, M.N.R. Ashford, K.N. Rosser, J. Appl. Phys. **79**, 9 (1996).
- [8] B. J. Bai, C. J. Chu, D. E. Patterson, R. H. Hague, J. L. Margrave, J. Mater. Res. **8**, 233 (1993).
- [9] Electronic reference: <http://www.cyrannus.com/pages/welcome.html>.
- [10] J. Angus, K Spear, J. P Dismukes, 'Growth of Diamond film in CH₄/H₂ plasma' New York, Wiley (1994).
- [11] M. A Prelas, G. Popovici, L. K Bigelow, 'Handbook of Industrial Diamonds and Diamond Films', New York, Marcel Dekker, (1997).
- [12] D. M. Gruen, S. Liu, A. R. Krauss, J. Luo, X. Pan, Appl. Phys. Lett. **64**, 1502 (1994).
- [13] S. Jiao, A.V. Sumant, M. A. Kirk, D. M. Gruen, A. R. Krauss, O. Auciello, J. Appl. Phys. **90**, 118 (2001).
- [14] J. E. Butler, H. Windischmann, MRS Bull. **23**, 9 (1998).
- [15] J. E. Butler, A.V. Sumant, Chem. Vap. Deposition **14**, 145 (2008).
- [16] M. Sternberg, P. Zapol, L.A. Curtiss, Phys. Rev. B **68**, 205330 (2003).
- [17] D.M. Gruen, MRS Bull. **23**, 32 (1998).

- [18] G. Binnig, H. Rohrer, IBM Journal of Research and Development **30**, 4 (1986).
- [19] G. Binnig, C. F. Quate, Phys. Rev. Lett. **56**, 9 (1986).
- [20] D. W. Pohl, W. Denk, M. Lanz, Appl. Phys. Lett. **44**, 651 (1984).
- [21] M. De Graef, Y. Zhu, Experimental Methods in the Physical Sciences **36**, 3 (2001),
- [22] W. J. Kaiser, L. D. Bell, Phys. Rev. Lett., **60**, 14 (1988).
- [23] D. A. Bonnell, Trans. Am. Cer. Soc. (1988)
- [24] K. Oura, V. G. Lifshits, A. A. Saranin, A. V. Zotov, M. Katayama, 'Surface science: an introduction', Springer-Verlag. ISBN 3-540-00545-5, (2003).
- [25] D. A. Bonnell, B. D. Huey, 'Scanning Tunneling Microscopy and Spectroscopy'
New York: Wiley-VCH. ISBN 0-471-24824-X, (2001).
- [26] C. Julian Chen, 'Introduction to Scanning Tunneling Microscopy' Oxford University Press, New York, (1993).
- [27] R. J. Hamers, D. F. Padowitz, 'Methods of Tunneling Spectroscopy with the STM',
New York: Wiley-VCH, Inc., (2001).
- [28] R. C. Barrett, S. Park, Ed. by W. J. Kaiser, J. A. Stroscio, San Diego, 'Design Considerations for an STM System', Academic Press, Inc., (1993).
- [29] R. Wiesendanger, 'Scanning Probe Microscopy and Spectroscopy: Methods and Applications', Cambridge University Press, (1994).
- [30] R. M. Feenstra, J. A. Stroscio, "Methods of Tunneling Spectroscopy," from Scanning Tunneling Microscopy, Ed. by W. J. Kaiser and J. A. Stroscio, San Diego: Academic Press, Inc., (1993).
- [31] R. M. Feenstra, P. Martensson, Phys. Rev. Lett., **61**, 4 (1988).
- [32] D. B. Williams, C. B. Carter, 'Transmission Electron Microscopy', Springer, (2009).

Chapter 2

- [33] P. Mahanandia, P. N. Viswakarma, P. V. Bhotla, S. V. Subramanyam, K. Nanda, Bull. Mater. Sci., **33**, 3 (2010).
- [34] H. C. Swart, G. L. P. Berning, Mater. Chem. Phys, **41**, 251 (1995).
- [35] J. H. Liu, R. Mendonça, R.W. Bosch, M. J. Konstantinovic, J Nucl Mater, **393**, 242 (2009).
- [36] J. M. Sanz, L. Soriano, P. Prieto, G. Tyuliev, C. Morant, E. Elizalde, Thin Solid Films, **332** 209 (1998).
- [37] B. C Norman, L. H. Daly, S. E. Wiberley, ‘Introduction to Infrared and Raman Spectroscopy’, Academic Press, New York (1990).
- [38] X. Li, B. Bhushan, Materials Characterization, **48**, 1 (2002).
- [39] W. C. Oliver, G. M. Pharr, J. Mater. Res. **7**, 1564 (1992).
- [40] S. J. Bull, E.G. Berasetegui, Tribo. Intl. **39**, 99 (2006).

Mechanism of Enhanced Electron Field Emission in Nitrogen Ion Implanted Ultrananocrystalline Diamond Films

3.1 Introduction

Ultra-nanocrystalline diamond (UNCD) film is a special form of diamond, which has recently caught great attention from researchers because of its better electron field emission (EFE) properties [1]. UNCD film has ultra-small grains (2 to 5 nm) separated by fine grain boundaries (1 to 2 nm) and very smooth surface characteristics [1]. The grains are of diamond, having sp^3 character whereas the grain-boundaries have a mixture of sp^2 , sp^3 , hydrocarbon and amorphous carbon while sp^2 -character is predominant [2]. Because of the large field emission current density from UNCD, as compared to other forms of diamond (nanocrystalline or microcrystalline), this material shows potential applications in cold cathode emitters and other vacuum microelectronic devices [1]. Incorporating nitrogen (N) into conventional microcrystalline diamond (MCD) with micron-sized grains to improve the conductivity is not effective, because N forms a deep donor level and does not enhance the conductivity [3]. In contrast, the conductivity of UNCD films has been improved by incorporating N into the grain boundaries of UNCD films, so as to enhance the EFE properties of these films [1, 3, 4]. However, N incorporation via adding N_2 gas in the growth plasma is not efficient due to the small size of the UNCD grains. On the other hand, ion implantation has been a long practice to modify the properties of materials through controlled doping of variety of dopants [5–7]. Ion implantation can introduce

defects, break the C-C and hydrocarbon bonds to form sp^2 carbon and can be used to tailor the sp^3/sp^2 ratio for diamond or related carbon materials by properly selecting the dose and energy of the implantation [6, 7]. Much work has been carried out for microcrystalline diamond and nanocrystalline diamond films to modify their properties which include the efforts to improve the field emission by ion implantation process [7-8]. There are not much report on nitrogen implanted UNCD. Ion implantation in UNCD can cause desorption of hydrogen from the hydrocarbons at the grain boundaries which results in depassivation of dangling bonds and increase in number of intergap states which results in increased conductivity and a reduction in band gap. All these factors contribute to the enhanced field emission behavior of N implanted UNCD films [9]. Low dose ion implantation in UNCD introduces defects which enhance the field emission but the property reverts back upon annealing [10]. High dose nitrogen implantation gives rise to good field emission even after annealing, but it makes a major part of the film into nanographite [10]. Several mechanisms have been proposed to explain the observed field enhancement behavior of N implanted UNCD films, while no single mechanism alone could give a complete picture [3, 10]. One of the proposed mechanisms is surface transfer doping mechanism, where the grain boundaries can transfer electrons to the grains, make them semiconducting and emit from these sites [11]. Another one is conductive channel mechanism where the grain boundaries make interconnected path through the sample surface and mostly emit from these sites [12].

In this chapter, the possible reasons for the enhancement in electron field emission properties of nitrogen ion implanted UNCD films are examined by scanning tunnelling microscopy (STM), X-ray photoelectron spectroscopy (XPS) and Transmission electron

microscopy (TEM). Scanning tunnelling spectroscopy (STS) has been used to determine the local electronic density of states (DOS) at the grain and grain boundary and the possible electron emission sites.

3.2 Experimental Details

UNCD films were grown on *n*-type silicon (Si) substrates in a microwave plasma enhanced chemical vapour deposition (MPECVD) system (IPLAS-Cyrannus) [10]. Ultrasonication of the substrates has been done using nanodiamond powder containing methanol solution for 45 minutes, followed by thoroughly cleaning in acetone. UNCD films were deposited on cleaned Si substrates using a CH₄ (1%)/Ar plasma for 3 hr with a microwave power of 1200 W. The pressure and the flow rate were maintained at 150 Torr and 100 sccm, respectively. The growth process was carried out at low temperatures (< 475 °C) without any intentional heating of the substrate. A 150 kV-ion implanter has been used to implant 75 keV nitrogen ions (N⁺) on the UNCD film at room temperature and a pressure below 2×10⁻⁷ mbar with a ion fluence of 5×10¹⁵ ions/cm². 75 keV nitrogen ions have a projected range of 90 nm in diamond with a straggling of 18 nm as simulated from SRIM-2003 Monte Carlo program [13]. This fluence is chosen, as a critical fluence of over 1×10¹⁵ ions/cm² is required to improve the EFE properties of UNCD films [10]. After implantation, the films were annealed at 600°C in N₂ atmosphere for 30 minutes. Field emission measurements are carried out in a home built tuneable parallel plate capacitor setup described in section 2.5. The EFE behaviour of materials is explained using Fowler–Nordheim (F–N) model [14]. The Raman spectra were recorded in back scattering geometry using 514.5 nm line of an Ar-ion laser using Renishaw micro-Raman

spectrometer (Model-INVIA). The chemical bonding structures were investigated by XPS using SPECS make photoelectron spectrometer. The detailed microstructure of the UNCD films is examined using high resolution TEM (JEOL-2100F). STM measurements are done using a commercial UHV-STM (150 Aarhus, SPECS GmbH). The imaging is performed with a set current of 0.59 nA and with a relatively high bias voltage between 2.5 and 3.5 volts. The STS spectra are obtained during scanning and the data presented here are the average of many reproducible spectra acquired during subsequent scans.

3.3 Results and Discussions

3.3.1 Material Characteristics

Figure 3.1 shows the field emission behaviour of as-deposited (1), N ion implanted (2) and post-implantation annealed (3) UNCD films (inset) and the F-N plot showing the variation of $\ln(J/E^2)$ versus $1/E$, of the corresponding field emission data. The turn-on field (E_0) decreases from 14.7 V/ μm in case of as deposited UNCD film to 13.7 V/ μm for films implanted with N^+ ions to a fluence of 5×10^{15} ions/ cm^2 . The turn-on field for inducing the EFE process is decreased further to 13.0 V/ μm upon post-implantation annealing. The turn-on field (E_0) designated here is the lowest value of the F-N plot, corresponding to the intersection of the low and high electric field segments. The current density (J_c) of UNCD at an applied field of 50.0 V/ μm is increased from 0.03 to 43 mA/ cm^2 after implantation. The slope of the F-N curve increases from 127 to 245 upon nitrogen ion implantation and decreases slightly to 222 upon post-implantation annealing. Overall the implanted nitrogen enhances the field emission properties of UNCD even after post-implantation annealing, in agreement with the earlier results reported by Joseph

et al [10]. Several mechanisms have been proposed to explain the observed field enhancement behavior while no single mechanism alone could give a complete picture [10, 15-21]. To understand the enhancement of field emission in nitrogen implanted UNCD samples, Raman, XPS, TEM, STM and STS measurements have been carried out in more detail. STS in CITS mode is used to confirm the emission sites in the nitrogen implanted UNCD samples.

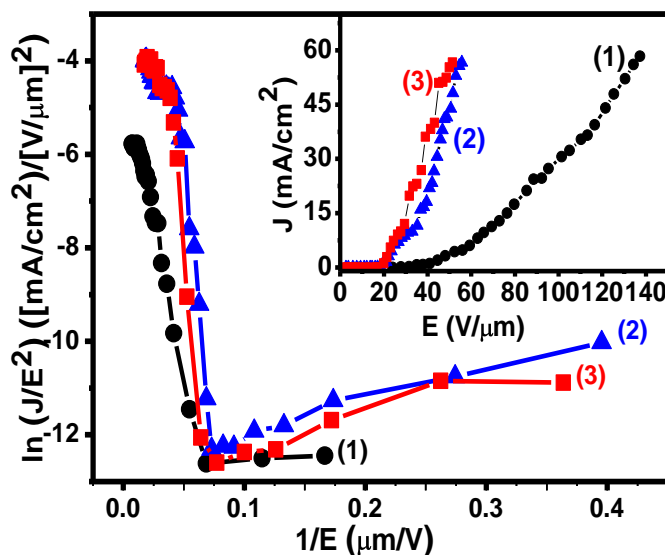


Fig. 3.1 (a) Fowler-Nordheim plot of the EFE property of UNCD film for (1) as deposited, (2) nitrogen ion implanted, (3) nitrogen ion implanted and post-annealed UNCD films. The inset shows the corresponding J-E curves.

Figure 3.2 shows the Raman spectra of (a) as-deposited, (b) N^+ ions implanted and (c) post-annealed UNCD films. The Raman spectra were de-convoluted by using multippeak Lorentzian fitting method. Peaks at around 1170 cm^{-1} and 1450 cm^{-1} are attributed to the ν_1 (stretching) and ν_3 (breathing) modes of transpolyacetylene (trans-PA) phases present at the grain boundaries of UNCD films [22]. A broadened peak around

1350 cm^{-1} (designated as D-band), which corresponds to the disordered sp^2 bonded carbon, is observed for UNCD films [1]. The sharp Raman peak at 1332 cm^{-1} corresponding to F_{2g} zone center optical phonon of diamond is not observed in UNCD as visible Raman spectroscopy is 50 to 230 times more sensitive to sp^2 sites because the π electrons are preferentially excited with visible photons [23]. So, the absence of 1332 cm^{-1} peak doesn't imply the absence of diamond in the film. The G-band of the UNCD film is observed at around 1560 cm^{-1} which corresponds to the graphite.

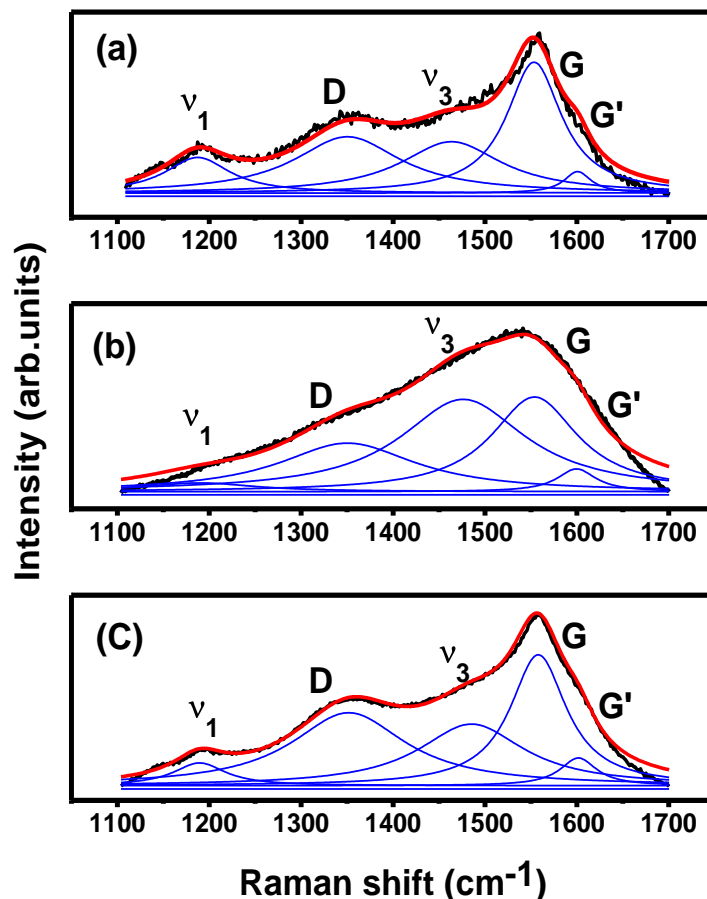


Fig. 3.2 Raman spectra taken with 514.5 nm line of Ar^+ ion laser from (a) as prepared, (b) N^+ ion implanted and (c) post-implantation annealed UNCD films.

A shoulder peak around 1600 cm^{-1} (designated as G'-band) is seen, which is possibly arising from the nanocrystalline graphitic content in the films [23].

Figure 3.2(b) shows the effect of N^+ ion implantation at the fluence of 5×10^{15} ions/ cm^2 on altering the bonding characteristics of the UNCD films. It shows higher intensities of D and G peaks indicating amorphization and graphitization type of transitions [5]. The position of the ν_1 and ν_3 bands shifted to higher wave numbers. The shifting is probably a sign of the breaking of trans-PA chains due to high doses of N^+ ion implantation [22]. Moreover, N^+ ion implantation shifted the G-band to a peak around 1580 cm^{-1} . Post-implantation annealing at $600\text{ }^\circ\text{C}$ has reduced the bonding disorder in these films (figure. 3.2(c)). The Raman spectra show I_D/I_G values (ratio of intensities of D-peak to G-peak) 0.79, 0.78 and 1.05 for as-prepared, N-implanted and post-implantation annealed samples, respectively. The G-peaks are found to be at 1553.4, 1554.0 and 1560.8 cm^{-1} for as-prepared, N-implanted and post-implantation annealed samples, respectively. The increase of the I_D/I_G value from 0.78 to 1.05 and G-band shift to higher wave number implies the formation of nanographite and decrease in sp^3 content from amorphous carbon according to a three-stage model of increasing disorder in carbon materials *i.e.* there is conversion of sp^3 to sp^2 content [23, 24]. It is to be noted that visible Raman spectroscopy can only give information on sp^2 -bonded carbon and cannot give information on the relative sp^3 content. The presence of defects and increase in sp^2 content upon N-implantation can enhance the field emission properties as observed in figure 3.1.

In order to understand how N^+ ion implantation/post-annealing processes changes the chemical bonding of UNCD films more precisely, XPS measurements have been

carried out. The C-1s photoemission spectrum of the as-prepared, N⁺ ion implanted and post-annealed UNCD film is shown in figure 3.3. The data are fitted with Lorentzian peaks with binding energies at 284.4, 285.1, 286.0, 286.9 and 287 eV corresponding to *sp*² C=C, *sp*³ C-C, C=N, C-N and CO/C-O-C bonds and their relative intensities are tabulated in Table 3.1. The background was subtracted using Shirley's method [25].

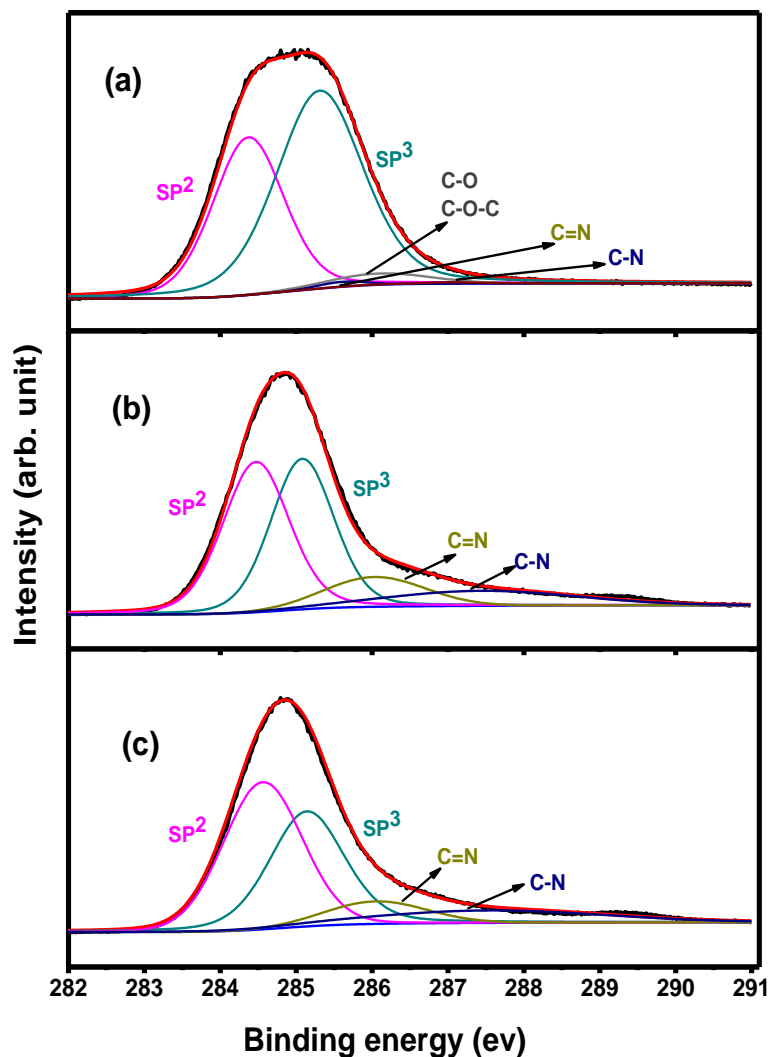


Fig. 3.3 C-1s XPS spectra from (a) as prepared, (b) N⁺ ion implanted and (c) post-implantation annealed UNCD samples.

Table 3.1 Relative intensities of various components of C-1s XPS spectra from as-prepared, N⁺ ion implanted and post-annealed UNCD samples.

(eV)	Chemical bonding	Peak intensity (%)		
		As prepared	N implanted	Post annealed
284.4	sp^2 C=C	36.9	40.4	44.6
285.1	sp^3 C-C	58.5	38	36.2
286.0	C=N	0.7	11	8.45
286.9	C-N	0.3	10.5	10.7
287.0	CO/ C-O-C	3.4	-	-

The measurement was conducted without ion sputtering etching to avoid reconfiguration of the bonds. In as-prepared UNCD, sp^3 C–C bonding is predominant with a peak intensity of 58.5% while sp^2 C=C intensity is 36.9%. The CO/C–O–C peak is seen with an intensity of 3.4% at binding energy of 287 eV and it disappeared if surface is ion sputtering etched. There is a little amount of nitrogen present in the as prepared UNCD film with less than 1% intensity of C-N and C=N peaks. After N⁺ ion implantation, sp^3 C–C peak intensity decreases to 38% and sp^2 C=C peak intensity increases to 40.4 %. The N⁺ ion implanted film clearly shows the presence of C–N and C=N bonds. The appearance of these two peaks indicates the chemical bonding between C and N atoms is formed after the implantation of nitrogen.

Upon post-implantation annealing, sp^2 peak C=C peak intensity increases further to 44.6% (sp^3 C–C peak intensity decreases to 36.2%) and C=N peak intensity is found to decrease. The increase in sp^2 content upon N-implantation is consistent with the Raman data (Fig. 3.2) and the reported results [7]. Decrease in intensity of C=N peak upon annealing implies that C=N bonds possess lower thermal stability [26]. There could be some loss of nitrogen and rearrangement of carbon atoms to form sp^2 C=C bonds [26].

3.3.2 Transmission Electron Microscopy Results

Figure 3.4 shows the TEM microstructure of (a) as-deposited, (b) N^+ ion implanted and (c) post-implantation annealed UNCD films, along with the selected area electron diffraction (SAED) patterns (insets). The as-deposited UNCD films contain nano-sized clusters (~5 nm), which are very uniform in size distribution (not shown here). SAED (inset *i* in figure 3.4(a)) contains sharp diffraction rings corresponding to (111), (220) and (311) diamond lattices (shown as arrow marks), which confirm that the nano-sized clusters are diamond. There appears diffused ring in the center of SAED, indicating the existence of amorphous carbon, which is presumably contributed from the trans-PA located in the grain boundaries. The image of grain boundaries is very diffuse (inset *ii*, figure 3.4(a)) that is resulted from the finite thickness of the grain boundary phase with amorphous nature. These results are in accord with the Raman and XPS observations that the UNCD films contain large proportion of sp^2 -bonded materials. Occasionally, there appear large aggregates around hundreds of nano-meters is size. However, these aggregates are actually soft-agglomerates of nano-sized grains rather than large diamond grains, as electron irradiation during TEM examination was observed to induce the separation of the nano-sized grain (not shown).

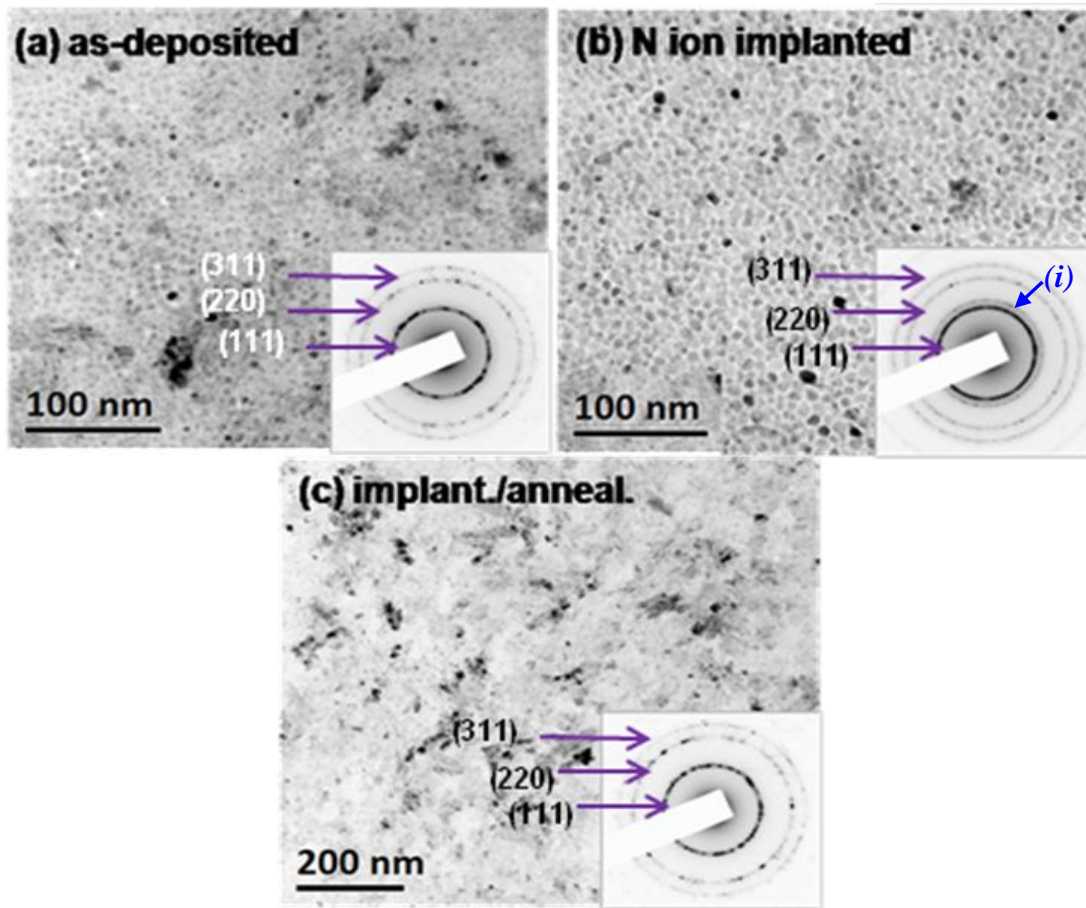


Fig. 3.4 The low magnification bright field micrographs with the inset showing the SAED pattern for (a) as-deposited, (b) N^+ ion implanted and (c) post-implantation annealed UNCD films.

Interestingly, N^+ ion implantation renders the granular structure of UNCD films more sharply defined (Fig. 3.4(b)). Contrary to the large variation in contrast for the as-deposited UNCD films, there is no variation in contrast for the bright field image of N^+ ion implanted films. It seems that N^+ ion implantation clears up all the irregularity, the soft agglomerates and the sp^2 -bonded species. Detailed examination on the SAED (inset, Fig. 3.4(b)) shows an extra diffraction ring outside the (111) diamond ring (indicated by arrow), that corresponds to a meta-stable phase of carbon, the *i-carbon* with cubic structure with a lattice constant of 4.25 Å [27].

The high resolution TEM (HRTEM) image shown in figure 3.5(a) for N ion implanted films reveals that, while the size of diamond grains is insignificantly altered, the grain boundaries were widened up considerably due to N^+ ion implantation. The strong diffused ring in the center of Fourier-transformed diffractogram (FT image, inset in figure 3.5(a)) indicates that the grain boundaries contain mostly the amorphous carbons. Occasionally, there appears a large aggregate for N ion implanted films (figure 3.5(b)). FT image (inset, figure 3.5(b)) shows the presence of rel-rod (streaks in horizontal direction) associated with all the major diffraction spots, indicating that the parallel fringes contained in these large aggregates are planar defects, mostly the stacking faults. There is no amorphous phase observable in the large aggregates. These results imply that the large aggregates are resulted from the coalescence of the nano-sized grains, not the soft agglomerates.

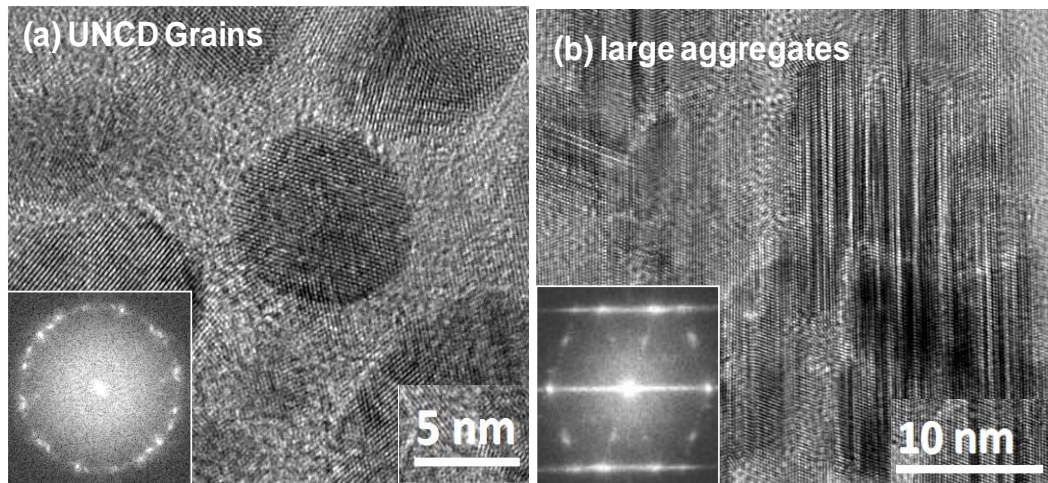


Fig. 3.5 HRTEM image of the (a) small grain region and (b) large grain region of N^+ ion implanted UNCD films. The inset shows the corresponding fourier transformed images.

That is, rigorous grain growth phenomenon has been induced. Restated, N^+ ion implantation alters the granular structure of UNCD films mainly via the dissociation of grain boundary phase, widened the grain boundaries in non-agglomerated region and induced the coalescence of grains to form large aggregates in the agglomerated region.

Post-implantation annealing induces dramatic modification on the granular structure of the UNCD films. Figure 3.4(c) reveals that there appear abundant large aggregates of dendrite geometry (about 20 nm x 200 nm in size) evenly distributed all over the samples. Figure 3.6(a) shows a typical aggregate. The HRTEM image shown in figure 3.6(b) reveals that the aggregate is actually a single grain. FT_1 & FT_2 images, which correspond to upper and lower portion of the aggregates, respectively, indicate that the different regions of the aggregates are lying along the same orientation, near $[01\bar{1}]$ zone axis. The microstructure of these two regions is very similar with each other, *i.e.*, they both contain stacking faults lying along the (111) lattice planes. These results indicate that the aggregates are large diamond grains resulted from the Oswald-ripening process. There also exist some smaller grains in the nearby regions. Figure 3.6(c) and FT_3 show one of the typical examples. However, even the small grains in the post-implantation annealed films are larger than as those in as-deposited UNCD films. The meta-stable carbon phase, the *i-carbon*, formed in the N ion implanted process is completely transformed into diamond due to the grain growth process during the annealing stage. TEM investigations, in conjunction with the Raman and XPS observations, reveal that the granular structure of UNCD films was modified markedly due to the N^+ ion implantation and post-implantation annealing process. First, the grain boundary amorphous carbon was

disintegrated, resulting in the formation of meta-stable *i-carbon*, which was then transformed into nano-graphites during the recrystallization of nano-sized diamond. Large aggregates were induced due to N⁺ ion implantation and transformed into more stable diamond in post-implantation annealing process.

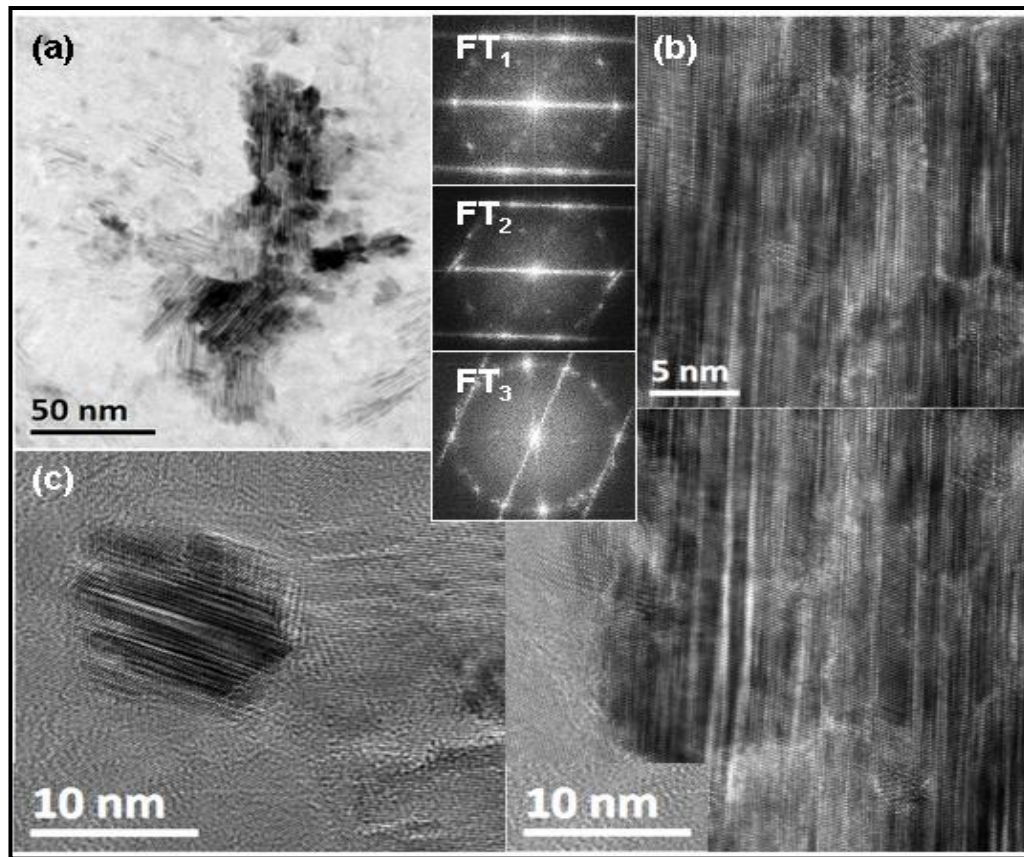


Fig. 3.6 The (a) bright field image of the post-implantation annealed UNCD films, which were N ion implanted with a fluence of 5×10^{15} ions/cm² and annealed at 600 °C for 30 min; (b, c) the HRTEM images of the large grain region (b) and small grain regions (c). The insets FT₁ and FT₂ are the FT-images of the upper and lower part of large grains region in (b), whereas inset FT₃ is the FT-image of the smaller grain region in (c).

3.3.3 Scanning Tunneling Spectroscopy (STS)

While the change in granular structure due to N⁺ ion implantation and post-implantation annealing processes is clearly illustrated, how the phase transformation processes enhance the EFE properties of UNCD films is still not clear. For the purpose of understanding the factors that alter the EFE properties of the films due to these processes, the local electrical properties of the film were investigated by STM and STS. As prepared UNCD film is highly resistive and STM measurements could not be done in this sample. The surface of as-prepared UNCD became conducting when sputter ion-etched with Ar⁺ ions for one minute by removing nearly 1 nm thickness at the surface. STM measurements are made after that. Figure 3.7(a) shows the high resolution STM image of as-prepared UNCD after 1 minute Ar⁺ ion sputtering. SEM image (not shown here) before and after Ar⁺ ion sputtering showed that the surface morphology is not changed due to sputtering. The root mean square (rms) roughness is found to be 0.7 nm in case of as-prepared UNCD films. The grain size is between 3 to 5 nm and a grain of ~5nm size, marked as “1”, is not very smooth due to sputtering. A typical grain boundary is marked as “2”. Figure 3.7(b) shows the current map of CITS image corresponding to Fig. 3.7(a) taken at a sample bias of -3.75V. Bright and dark regions in CITS image are visible with their shapes having similarity with the shapes of grain boundaries (2) and grains (1) of the STM image in Fig. 3.7(a) respectively. The CITS image (Fig. 3.7(b)) shows clearly that the emission sites are mainly located along the grain boundaries. The normalized conductance, $\frac{dI/dV}{I/V}$ against V provides the information on the distribution of the surface density of states (DOS) of the materials [28, 29]. From the variation of normalized

conductance $\frac{dI/dV}{I/V}$ versus V , shown in Fig. 3.7(c), the band gap is measured to be 4.8 eV at the UNCD grain (marked as dotted line) that is close to the theoretical value of 4.2 eV in nanodiamond and 3.8 eV at the grain boundary for as prepared UNCD. The singularity in the band gap region is removed by using an average value for I/V which is nonzero. Densities of states are not seen in the bandgap.

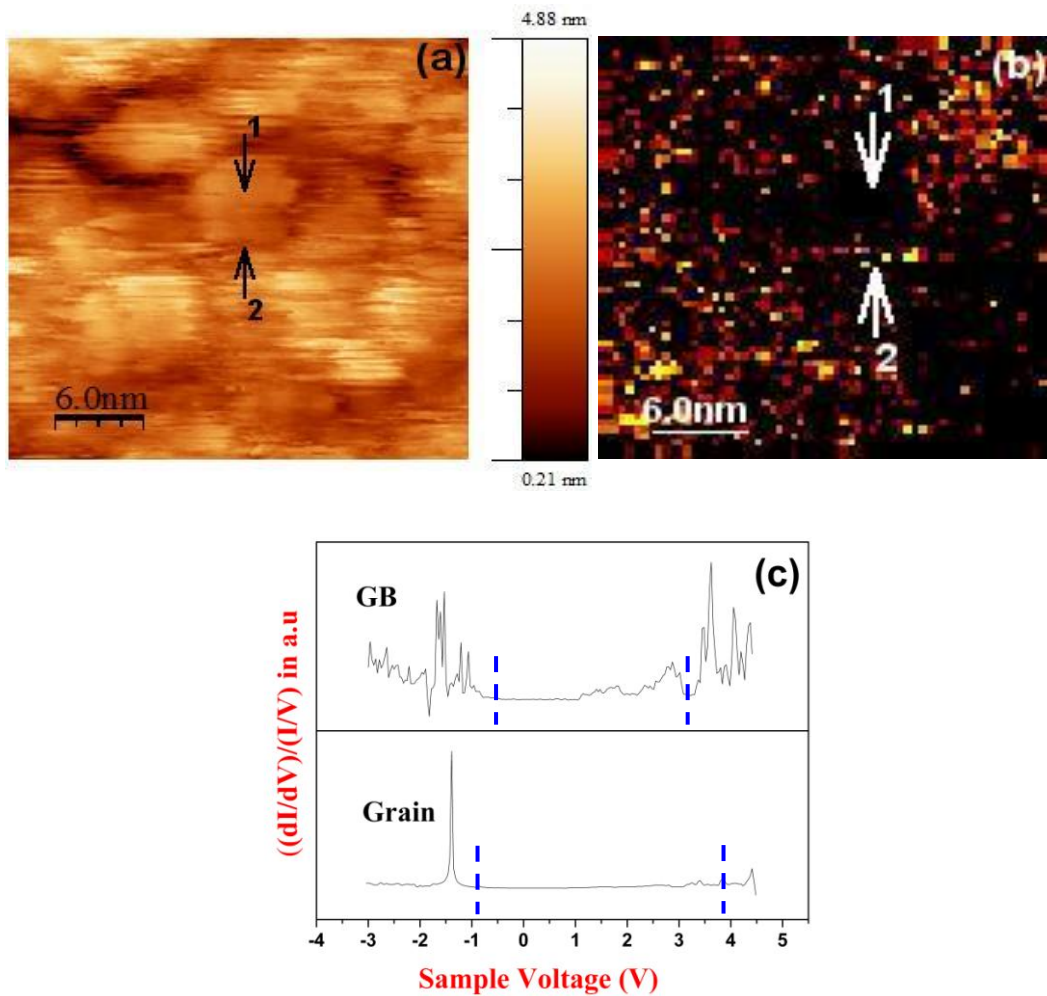


Fig. 3.7 (a) UHV STM picture of as-prepared UNCD sputter cleaned with Ar ions showing 1-grain, 2-grain boundary, (b) STS taken in CITS mode showing the current map and (c) normalized differential conductance, $\frac{dI/dV}{I/V}$, at the grain and grain boundary.

N^+ ion implantation introduces defects and sp^2 phase and expels hydrogen atoms trapped at the grain boundaries and makes the film more conductive [10]. Figure 3.8(a) is a typical STM topograph of the N ion implanted UNCD surface. Large globular structures are clearly observed in the STM image, representing the typical cauliflower structure of UNCD [30]. The surface morphology of the N implanted UNCD film is smooth, showing a root mean square (rms) roughness of 3.29 nm over a $0.5 \times 0.5 \mu m^2$ area as observed from STM measurement. We interpret the highly dense globular clusters as agglomerates of many nanocrystallites. The surface morphology resolved within the agglomerates is attributed to the small grains and grain boundaries as expected in the UNCD, which are marked as “3” and “4” in Figure 3.8(b). Magnified image of the cauliflower like agglomerates and the boundary between them could be seen. The current map and $\frac{\partial I}{\partial V}$ map, corresponding to Fig. 3.8(b), which is taken in CITS mode at a negative bias of 3.255 V are shown in Figs. 3.8(c) and Fig. 3.8(d) respectively. Again, these CITS images show clearly that the emission sites are mainly located along the grain boundaries. Bright contrast indicating better electron emission is also seen around the edges of the cauliflower like agglomerate structure.

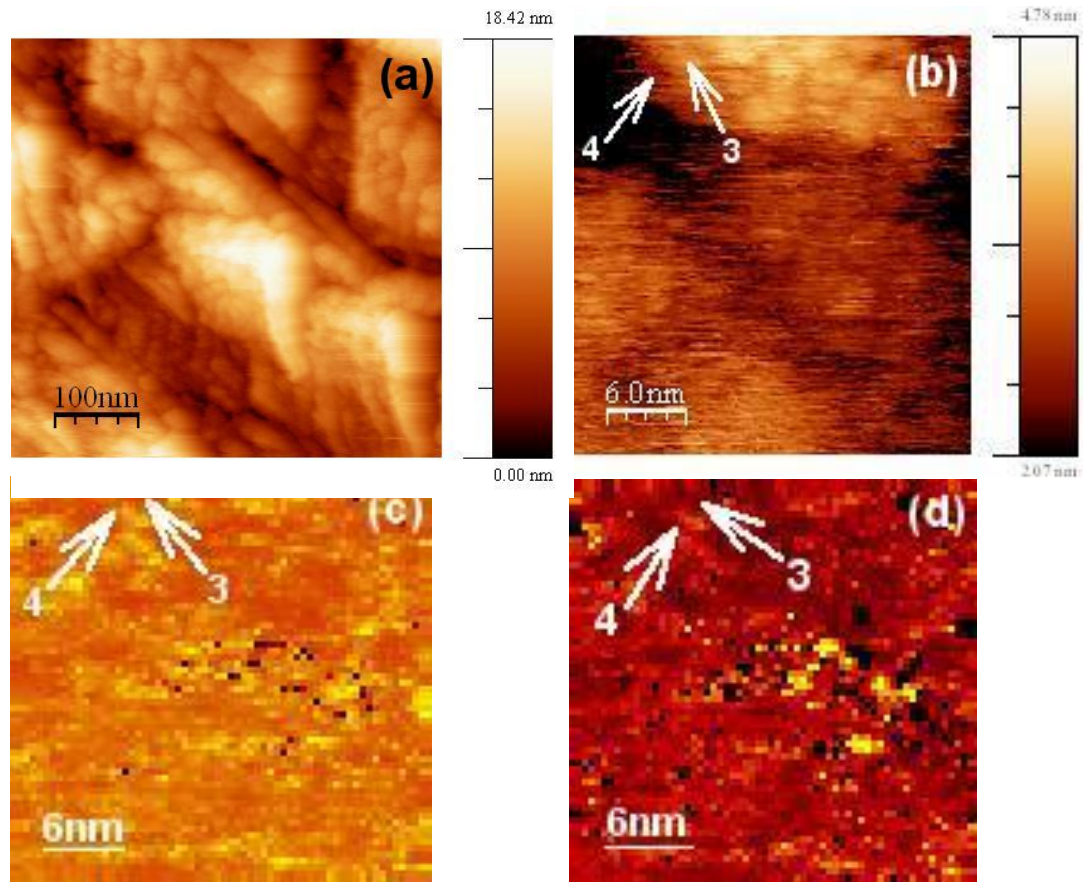


Fig. 3.8 (a) UHV STM image of UNCD after N^+ ion implantation with a fluence of 5×10^{15} ions/cm² showing globular clusters; (b) high resolution UHV STM image of the same film showing UNCD grains of 2-5 nm size and grain boundaries; (c, d) STS taken in CITS mode showing (c) the current map and (d) $\frac{\partial I}{\partial V}$ map at a negative bias of 3.255 V in N^+ ion implanted UNCD.

After post-implantation annealing of the sample at 600 °C in nitrogen gas atmosphere for 30 min, the film surface gets smoothed further and the rms roughness is 2.52 nm over a $0.5 \times 0.5 \mu\text{m}^2$ area (not shown) and the rms roughness over a $30 \times 30 \text{ nm}^2$ area is 0.5 nm (figure 3.9(a)). The surface smoothing upon annealing can be due to the graphitisation of the surface. Figure 3.9(a) shows grain sizes of nearly 3 to 20 nm

implying that some of the nanograins have coalesced, consistent with the TEM observation. The corresponding CITS image is shown in Fig. 3.9(b) which is taken at a sample bias of -3.25V. Typical grain and grain boundary in the image are marked as “5” and “6” and, again, it is obvious that grain boundary is the prominent electron emitter. Figure 3.9(c) is high magnification image taken within region “5” of figure 3.9(a). We could observe uniform grain sizes of nearly 3 nm.

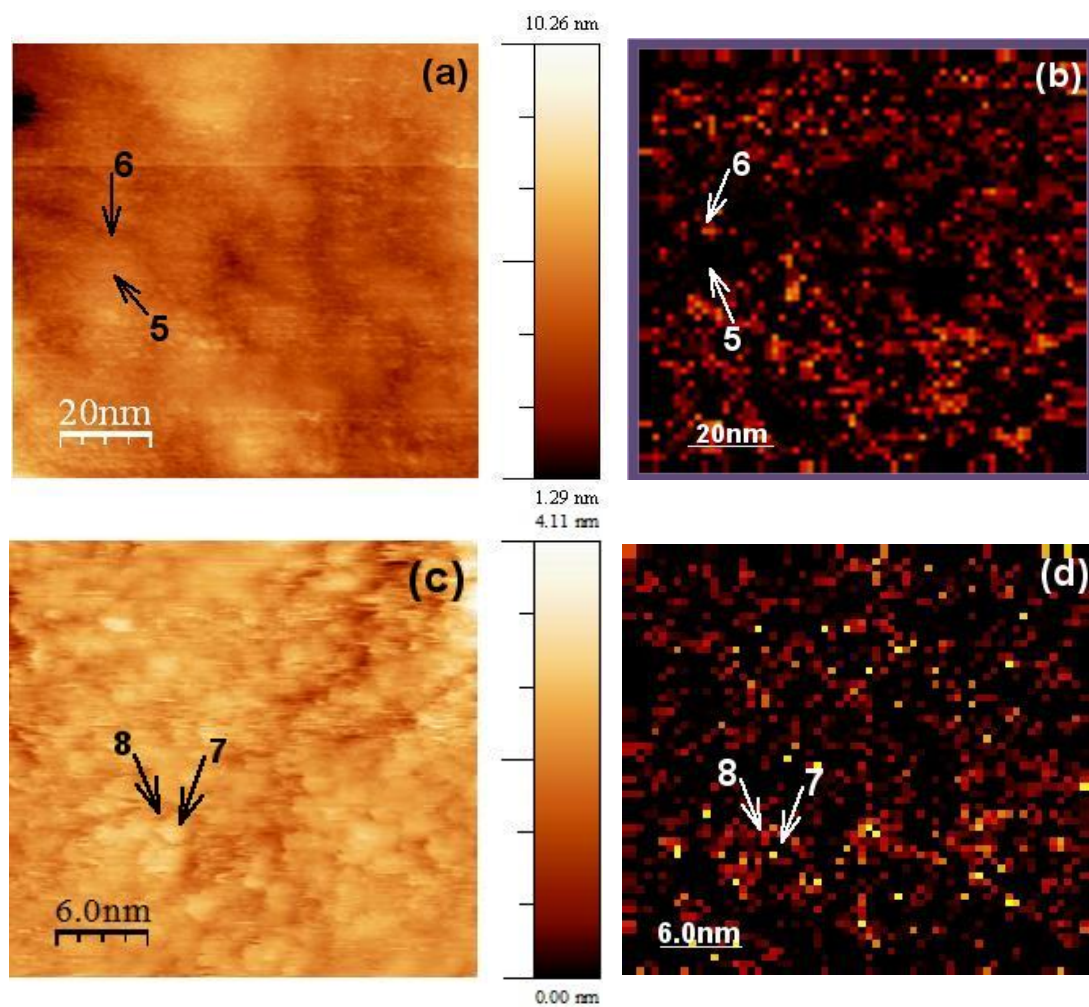


Fig. 3.9 (a) UHV STM picture of post-implantation annealed UNCD and (b) STS taken in CITS mode showing the current map (c) high resolution UHV STM image from region “5” in Figure 3.9(a) and its corresponding CITS image (d) showing the current map.

Typical grain and grain boundary in the image are marked as “7” and “8”. This indicates that larger grains observed in figure 3.9(a) are also composed of smaller grains. It is likely that these smaller grains which compose the larger grain have a preferred orientation, giving rise to the observed diffraction spots in TEM measurements. Figure 3.9(d) shows the current map of CITS image corresponding to figure 3.9(c) taken at the sample bias of -3.25 V. This image also shows bright contrast for the grain boundaries, indicating that grain boundaries are the prominent electron emission sites.

For the characterization of the local electronic properties of the N ion implanted and post-implantation annealed UNCD samples, I-V curves are taken from STS at various sample positions on grains and grain boundaries in the STM images shown in figure 3.8(b) and figure 3.9(c). The tunneling current under positive bias is lesser than that under negative bias implying that films have n-type conductivity. The I-V curves are shown in figure 3.10. Moreover, we observe a significant change in I-V characteristic curve at the grain and grain boundary for both N⁺ ion implanted as well as post-implantation annealed UNCD samples. We observe that grain boundaries (curves *ii* & *iv*) emit at a lower turn-on field compared to the grains (curves *i* & *iii*). Also the conductivity of the grain boundaries is better than that of grains in both the samples, consistent with the CITS image shown in figure 3.8(d) and figure 3.9(d). In addition, the conductivity gets significantly enhanced both at the grain and grain boundaries upon post-implantation annealing (curves *iii* & *iv*), as compared with those for as-implanted sample (curves *i* & *ii*).

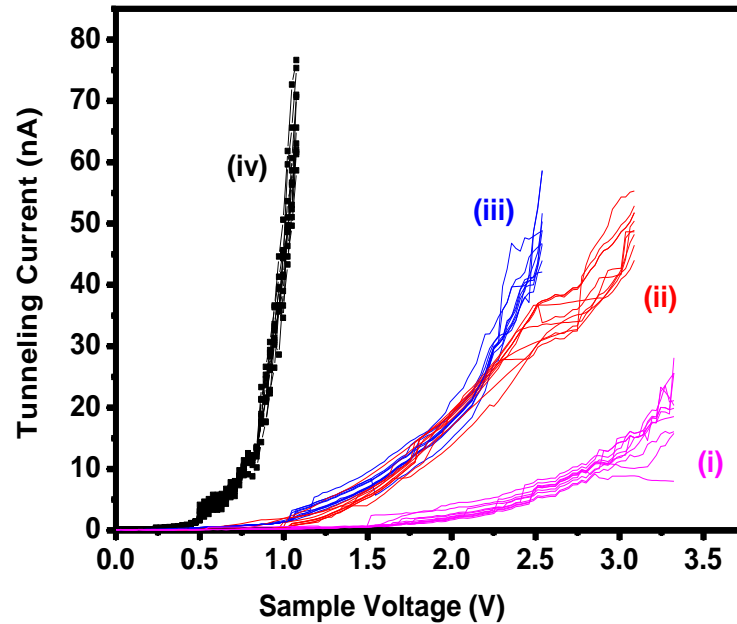


Fig. 3.10 I-V curves at the grain (i) and grain boundary (ii) of N^+ ion implanted UNCD films [marked as “3” & “4” in the high resolution UHV STM image, Fig. 3.8(b)] and at the grain (iii) and grain boundary (iv) of UNCD films after post-implantation annealing [marked as “5” & “6” in the high resolution UHV STM image, Fig. 3.9(b)]. In each region 10 numbers of I-V curves have been shown.

The I-V characteristic curves of STS measurements shown in figure 3.10 are used to calculate the normalized derivative of multiple averaged spectra, the normalized conductance $\frac{dI/dV}{I/V}$ at the grain and grain boundary of the N^+ ion implanted and post-implantation annealed UNCD samples. The normalized conductance corresponding to these locations are plotted in figure 3.11(a) and figure 3.11(b) for N^+ ion implanted and post-implantation annealed UNCD films, respectively. Again, the normalized conductance provides information on the surface local density of states (LDOS) [28, 29]. We get a band gap of about 3.88 eV on the UNCD grain from the spectra “i”

(figure 3.11(a)) for the N^+ ion implanted UNCD, which is smaller than 4.8 eV for as-deposited UNCD (Fig. 3.7(c)). Moreover, these small band gap value is smaller than the band gap of $E_{\text{gap}}=4.2$ eV for nanodiamond crystals that has been reported in literature [16, 30] and also proposed by theoretical calculations [32].

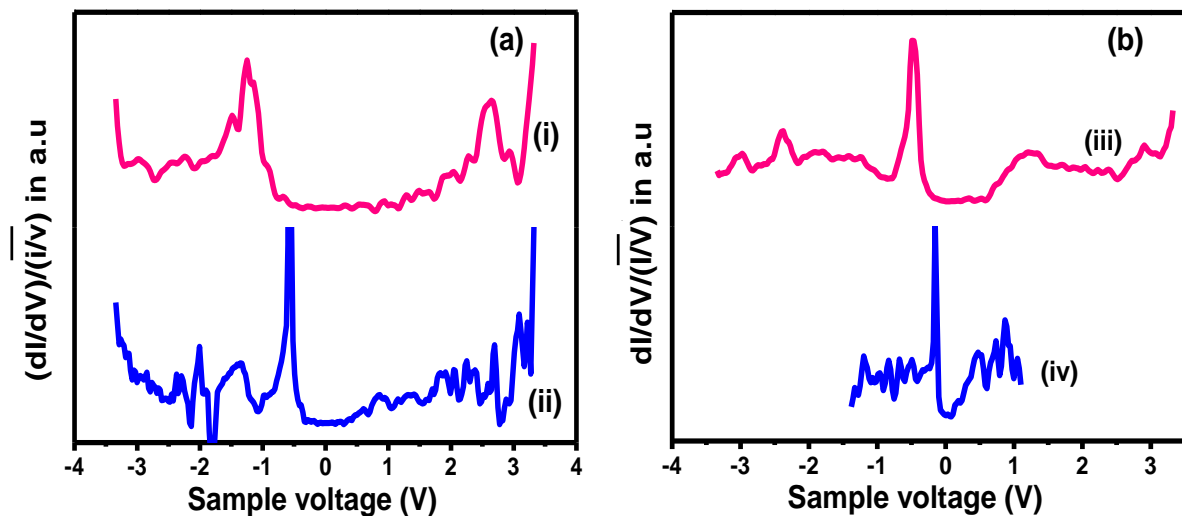


Fig. 3.11 (a) Normalized differential conductance ($\frac{dI/dV}{I/V}$) at the (i) grain and (ii) grain boundaries of N^+ ion implanted UNCD, (b) at (iii) grain and (iv) grain boundaries after post-implantation annealing. Each spectrum is averaged over 10 scanned spectra shown in the figure 3.10.

Lower bandgap of 3.88 eV could be due to N-doping upon implantation. Band structure calculation shows that band gap of the diamond is reduced by 25% after N doping [33]. The DOS within the bandgap are visible. Upon post-implantation annealing, the band gap of diamond grains reduces to 3.2eV and there is increase in density of states as observed in curve *iii* (Fig. 3.11(b)). Furthermore, band gap of grain boundary further reduces,

showing nearly metallic behavior (curve iv, Fig. 3.11(b)), indicating that it is mostly of sp^2 content. The significance of such an observation is discussed in the following section.

3.4 Discussion

The defects and sp^2 phase produced by N^+ ion implantation can introduce various defect levels at the diamond grain. Nitrogen substitution, which is confirmed by XPS measurements, can also introduce new electronic states in the band gap of diamond grain, associated with carbon and nitrogen in the grain boundaries, as suggested by the density functional tight binding calculations of Zapol [15]. Using charge-based deep level transient spectroscopy, it has been shown experimentally that the incorporated nitrogen atoms in UNCD induce donor levels with activation energy of 0.05 eV and the density of these shallow donors increases with increasing concentration of nitrogen [34]. The carbon dangling bond states hybridized with nitrogen lone pairs are above the Fermi level and donate electrons to the carbon defect states near the Fermi level causing it to shift upward, towards the delocalized π^* carbon band [15]. The upward shift of Fermi level can lower the effective potential barrier height, giving raise to the enhanced electron field emission. Moreover, in figure 3.11(a) (curve *ii*), we can see that the band gap for the grain boundary is much lesser, compared to that of the grains (curve *i*, Fig. 3.11(a)). It is due to the presence of a mixture of sp^2 , sp^3 and amorphous carbon phases at the grain boundary which will have higher conductivity [3]. Such an observation is in accord with the CITS images. The electrical conductivity cannot be expected to be metallic as in graphite because of the lack of spatial connectivity among these sp^2 bonded defects, which form localized states in the band gap. However, because of the possibility of transitions among

these states, the effective electronic gap in the grain boundary region is much smaller than that in a perfect crystal.

Upon post-implantation annealing, the bandgap of diamond grains reduces to 3.2 eV and there is increase in density of states as observed in curve *iii* (Fig. 3.11(b)). Post-implantation annealing heals the defects, forming complex stable defects and conversion of amorphous phase to sp^2 , enhance the doping of nitrogen and out diffusion of a certain fraction of nitrogen from diamond grains to the grain boundaries. The N doping can reduce bandgap further. Increase in DOS upon annealing can be due to the introduction of sp^2 phase in the diamond grain [35]. The high density of states within the band gap significantly reduces the potential barrier for field emitted electrons [16], which can be responsible for the lower turn-on field, enhanced field emission properties and also the I-V curves of STS measurements. Furthermore, band gap of grain boundary further reduces, showing nearly metallic behavior (curve *iv*, Fig. 3.11(b)), indicating that it is mostly of sp^2 content. The sp^2 content at the grain boundaries will also increase by annealing and also the nitrogen concentration will increase giving raise to metal like behavior.

Figure 3.11(a) and figure 3.11(b) show that the DOS are introduced in the band gap of grain only after nitrogen is implanted and there is increase in DOS upon post-implantation annealing. Upon N^+ ion implantation the material closer to the grain boundaries appears to be more susceptible to amorphization and graphitization giving raise to wider grain boundaries. Also diffusion of nitrogen atoms towards the grain boundaries also can increase the sp^2 content near the grain boundaries and cause the width

to increase. When UNCD is doped with nitrogen during growth by incorporating the nitrogen in plasma, both the grains and grain boundaries are large [2]. In case of 75 keV N^+ ion implantation, there is no grain coarsening but the grain boundaries become wider, which may create additional conduction path ways. Post implantation annealing shows coalescence of grains to form larger grains which are composed of smaller grains with preferred orientation.

Our results show that there is bonding of nitrogen with carbon, increase in sp^2 phase, which is nanocrystalline and introduction of DOS in the bandgap upon N-doping of UNCD. The grain boundaries have higher sp^2 content giving raise to metallic behavior and behave as the prominent electron emitters. These conducting grain boundaries which are narrow, form high conductive channels at the interface of ultra nanocrystalline diamond grains, and these channels provide strong field enhancement in the local electric field at the interface, giving raise to prominent electron emission from the grain boundaries. Our results support the possibility of a grain-boundary electron transport mechanism (conductivity-channel process) [15-17]. Even though CITS observations show that grain boundaries are the prominent electron emission sites at the nitrogen fluence of 5×10^{15} ions/cm², I-V curves show that emission is also coming from the grains but at a higher turn-on field. If the nitrogen ion fluence is increased further, sp^2 content and the density of states at the grains are expected to increase proportionally and band structure will show metallic behavior like that of grain boundaries and the grains may not remain purely as diamond.

3.5 Conclusion

The electron field emission property of the UNCD film gets enhanced upon N⁺ ion implantation and annealing. Raman spectroscopy, XPS and TEM measurements show the increase in sp^2 content in UNCD upon N⁺ ion implantation. Scanning tunneling microscopy and the I-V characteristics of STS clearly show distinct features for the diamond grains and grain boundaries for N⁺ implanted UNCD samples. Electronic band structure of UNCD film reveals a band gap of 4.8 eV at the grain and reduction in band gap, along with the increase in density of states within the band gap, upon N⁺ ion implantation and annealing process. The band gap at the grain boundary is lesser than that of the grain and shows nearly metallic behavior upon annealing. The observed decrease in bandgap and increase in density of states at the grains and metallic nature of the grain boundary could be responsible for the enhanced electron field emission properties of nitrogen implanted UNCD samples. STS in CITS mode shows grain boundaries are the prominent field emission sites and have higher conductivity. TEM and CITS measurements show the width of the grain boundaries increase upon N⁺ ion implantation. Our results at the nitrogen fluence of 5×10^{15} ions/cm² give evidence that the grain-boundary electron transport is the predominant mechanism for electron field emission in N doped UNCD.

3.6 References

- [1] T. D. Corrigan, D. M. Gruen, A. R. Krauss, P. Zapol, R. P. H. Chang, *Diamond and Relat. Mater.* **11**, 43 (2002).
- [2] J. Birrell, J. A. Carlisle, O. Auciello, D. M. Gruen, J. M. Gibson, *J. Appl. Phys.* **81**, 2235 (2002).
- [3] E. Rohrer, C. F. O. Graeff, R. Janssen, C. E. Nebel, H. Guettler, R. Zachai, *Phys. Rev. B* **54**, 7874 (1996).
- [4] D. Zhou, A. R. Krauss, L.C. Qin, T.G. McCauley, D.M. Gruen, T.D. Corrigan, R.P.H. Chang, H. Gnaser, *J. Appl. Phys.* **82**, 4546 (1997).
- [5] R. Kalish, *Carbon* **37**, 781 (1999).
- [6] S. Talapatra, J. Y. Cheng, N. Chakrapani, S. Trasobares, A. Cao, R. Vajtai, M. B. Huang, P. M. Ajayan, *Nanotechnology* **17**, 305 (2006).
- [7] S. Praver, R. Kalish, *Phys. Rev. B* **51**, 15711 (1995).
- [8] E. J. Correa, Y. Wu, J.G. Wen, R. Chandrasekharan, M. A. Shannon, *J. Appl. Phys.* **102**, 113706 (2007).
- [9] S. Praver, R. Kalish, M. Adel, V. Richter, *J. Appl. Phys.* **61**, 4492 (1987).
- [10] P. T. Joseph, N. H. Tai, C. Y. Lee, H. Niu, W. F. Pong, I. N. Lin, *J. Appl. Phys.* **103**, 043720 (2008).
- [11] P. Strobel, M. Riedel, J. Ristein, L. Ley, *Nature* **430**, 439 (2004).
- [12] Kalpataru Panda, B. Sundaravel, B. K. Panigrahi, P. Magudapathy, D. N. Krishna, K. G. M. Nair, H-C Chen, I-Nan Lin, *J. Appl. Phys.* **110**, 044304 (2011).

Chapter 3

- [13] J. F. Ziegler, J. P. Biersack, U. Littmark, *The Stopping and Ranges of Ions in Solids*, Pergamon, New York (1985).
- [14] R. H. Fowler and L. Nordheim, *Proc. R. Soc. London, Ser. A* **119**, 173 (1928).
- [15] P. Zapol, M. Sternberg, L.A. Curtiss, T. Frauenheim, D.M. Gruen *Phys. Rev. B* **65**, 45403 (2001).
- [16] O. A. Williams, S. Curat, J. E. Gerbi, D. M. Gruen, R. B. Jackman *Appl. Phys. Lett* **85**, 1680 (2004).
- [17] E. J. Correa, Y. Wu, J. G. Wen, R. Chandrasekharan, M. A. Shannon, *J. Appl. Phys* **102**, 113706 (2007).
- [18] V. Chakrapani, J. C. Angus, A. B. Anderson, S. D. Wolter, B. R. Stoner, G. U. Sumanaseker, *Science* **318**, 1424 (2007).
- [19] C. E. Nebel, *Science* **318**, 1391 (2007)
- [20] P. T. Joseph, N. H. Tai, C. H. Chen, H. Niu, H. F. Cheng, W. F. Pong, I. N. Lin, *J. Phys. D: Appl. Phys.* **42**, 105403 (2009).
- [21] P. T. Joseph, N. H. Tai, C. Y. Lee, H. Niu, H. F. Cheng, W. F. Pong, I. N. Lin, *PlasmaProcess.Polym.* **6**, S834 (2009).
- [22] A. C. Ferrari, J. Robertson, *Phys. Rev. B* **63**, 121405 (2001).
- [23] A. C. Ferrari, J. Robertson, *Phys. Rev. B* **61**, 14095 (2000).
- [24] A. Ilie, A. C. Ferrari, T. Yagi, S. E. Rodil, J. Robertson, E. Barborini, P. Milani, *J. Appl. Phys.* **90**, 2024 (2001).
- [25] Y. F. Chen, *Surf. Sci.* **380**, 199 (1997).

- [26] J. J. Li, W. T. Zheng, H. H. Wu, L. Sun, G. G. Gu, H. J. Bian, X. Y. Lu, Z. S. Jin, J. Phys. D: Appl. Phys. **36**, 2001 (2003).
- [27] P. F. Lai, S. Praver, L. A. Bursill, Diamond and Relat. Mater. **10**, 82 (2001).
- [28] R. M. Feenstra, Surf. Sci. **299**, 965 (1994).
- [29] R. M. Feenstra, P. Martensson, Phys. Rev. Lett. **61**, 4 (1988).
- [30] A. R. Krauss, O. Auciello, M. Q. Ding, D. M. Gruen, Y. Huang, V. V. Zhirnov, E. I. Givargizov, A. Breskin, R. Chechen, and E. Shefer, V. Konov, S. Pimenov, A. Karabutov, A. Rakhimov, N. Suetin, J. Appl. Phys. **89**, 2958 (2001).
- [31] S. Q. Lud, M. Niedermeier, P. S. Koch, P. Bruno, D. M. Gruen, M. Stutzmann, J. A. Garrido, Appl. Phys. Lett. **96**, 092109 (2010).
- [32] T. Sasagawa, Z. X. Shen, J. Appl. Phys. **104**, 073704 (2008).
- [33] J. W. Park, C. W. Sohn, B. H. Choi, Current Applied Physics **6**, 188 (2006).
- [34] V. I. Polyakov, A. I. Rukovishnikov, N. M. Rossukanyi, V. G. Pereverzev, S. M. Pimenov, J. A. Carlisle, D. M. Gruen, E. N. Loubnin, Diamond and Relat. Mater. **12**, 1776 (2003).
- [35] O. A. Williams, Nesladek, M. Daenen, S. Michaelson, A. Hoffman, E. Osawa, K. Haenen, R. B. Jackman, Diamond and Relat. Mater. **17**, 1080 (2008).

Direct Observation of Enhanced Electron Emission Sites in Nitrogen Ion Implanted Hybrid Structured nanocrystalline Diamond Films

4.1 Introduction

Ultra-nanocrystalline diamond (UNCD) films, has attracted great attention because of its better electron field emission (EFE) properties [1]. The UNCD film has ultra-small diamond grains (2 to 5 nm) and very smooth surface characteristics [1]. The grains are diamond, having a sp^3 character and the grain boundaries have a mixture of sp^2 , sp^3 , and amorphous carbon with the sp^2 character being predominant [2]. The decrease in diamond grain size increases the grain boundary (GB) volume fraction that contains non-diamond carbon, resulting in significant improvement in electrical properties for these films [2]. The non-diamond phase content and the size of diamond grains play a crucial role for the EFE properties of diamond films [1]. In an effort to increase the non-diamond phase content in the film so as to improve the EFE properties of diamond films, a modified nucleation and growth process was carried out where a UNCD film was used as the nucleation layer for the growth of microcrystalline diamond (MCD) film [3-5]. Such a two-step microwave plasma enhanced chemical vapour deposition (MPECVD) process resulted in MCD/UNCD diamond film with very unique granular structure, *viz.*, a hybrid granular structure, which neither contains micron sized diamond nor ultranano sized diamond structures. Such kind of hybrid granular structured MCD/UNCD films exhibit better EFE

properties than the conventional micro-, nano- or ultranano-crystalline diamond films [3-5]. However, the resulted EFE properties are still not satisfactory, as compared with the nano-carbon materials [6-8] indicating that there is still room for improvement. Ion implantation to different materials has been a long practice to modify the properties of carbon materials through controlled doping of variety of dopants [9-11]. Much work has been carried out with microcrystalline and nanocrystalline diamond films to modify their properties [12], which include the effort to improve the field emission properties by N^+ ion implantation [13]. In the last chapter, the effect of N^+ ion implantation on the EFE properties of UNCD films was discussed where substantial improvement in EFE properties upon N^+ ion implantation was reported. It seems that the effect of N^+ ion implantation on the EFE properties of MCD/UNCD hybrid films will be interesting due to its special microstructures and is the subject of mater of this chapter.

In this context, this chapter describes the EFE properties of a two-step MPECVD deposited MCD/UNCD hybrid films. How the EFE properties of these films are better than the single step MPECVD grown UNCD or MCD films are further discussed. Moreover, the effect of N^+ ion implantation/post-annealing processes in modifying the microstructure and EFE properties of the as-prepared MCD/UNCD films are discussed. Current imaging tunnelling spectroscopy (CITS) in scanning tunnelling spectroscopy (STS) mode is employed to detect the enhanced emission sites in these films after the N^+ ion implantation/post-annealing processes. High resolution transmission electron microscopy (HRTEM) is used to investigate the microstructural evolution of the MCD/UNCD films after the N^+ implantation and post-annealing processes. Further, the possible mechanisms for the enhancement in EFE properties are discussed on the basis of the experimental observations.

4.2 Experimental Details

The diamond films were grown on *n*-type mirror polished Si (100) substrates. The UNCD films were used as a nucleation layer to promote the growth of MCD films on it. The UNCD nucleation layer was grown on Si-substrates using the MPE-CVD process, in Ar-rich plasma ($\text{CH}_4/\text{Ar}/\text{H}_2=4/196/0$ sccm) conditions (1200 W, 100 torr, 60 min) to a thickness of 1 μm . The growth process was carried out at low temperature of 480 °C without any intentional heating of the substrates. Growth of the secondary MCD films on UNCD nucleation layer was carried out in the same MPECVD processor using H_2 -rich plasma ($\text{CH}_4/\text{Ar}/\text{H}_2=1/49/50$ sccm, 55 torr) with 1600 W microwave power for 60 min. Thus obtained composite films were designated as MCD/UNCD. The total thickness of the film after the secondary diamond film deposition is 1.7 μm . A 150 kV ion implanter was used to implant 75 keV nitrogen ions (N^+) on the MCD/UNCD films at room temperature upto a fluence of 5×10^{15} ions/ cm^2 . The base pressure was below 2×10^{-7} mbar during ion implantation. This ion fluence was so chosen to exceed the critical dose of over 1×10^{15} ions/ cm^2 which is required to improve the EFE properties of UNCD films [13]. After ion implantation, the films were annealed at 800 °C in N_2 atmosphere for 30 minutes. A schematic diagram of the N ion implanted MCD/UNCD films is shown in figure 4.1 below.

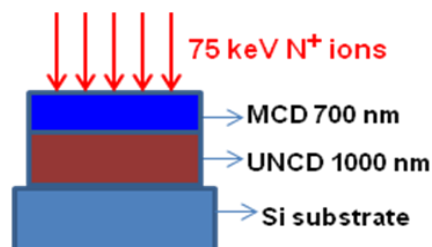


Fig. 4.1 Schematic diagram of MCD/UNCD hybrid films.

A homemade tuneable parallel plate capacitor setup, discussed in section 2.5 was used for the field emission measurements. The EFE properties were analyzed by Fowler–Nordheim (F-N) model [14]. The turn-on field is designated as the interception of the high and low-field segments of the F-N plots. The surface morphology of as-prepared, N⁺ ion implanted and post-annealed MCD/UNCD films were investigated by field emission scanning electron microscope (FESEM, CARL ZEISS, SUPRA 55) operated at 5 kV. The Raman spectra were recorded by using 514.5 nm line of an Ar-ion laser in Renishaw micro-Raman spectrometer (Model-INVIA). The chemical bonding structures were investigated by XPS (SPECS, Germany) which uses monochromatic Al K α radiation at 1486.74 eV as a probe. The detailed microstructures of MCD/UNCD films were examined by transmission electron microscope (TEM, JEOL 2100) operated at 200 kV.

Scanning tunnelling microscopy (STM) measurements were carried out in a UHV-STM apparatus (150 Aarhus, SPECS GmbH, Germany) at 10⁻¹⁰ mbar pressure. The scanning tunnelling spectroscopy (STS) spectra were obtained during scanning and the data presented here are reproducible over subsequent scans. STS in CITS mode was carried out which allows us to correlate the STM images with its surface local density of states (DOS) distributions [15].

4.3 Results and Discussions

4.3.1 Material Characteristics

The effect of N⁺ ion implantation and post-annealing processes in modifying the EFE properties of MCD/UNCD films are shown in figure 4.2 with the inset indicating the corresponding F-N plot, the variation of $\ln(J/E^2)$ versus $1/E$, of the corresponding field emission (J-E) curves. The turn-on field (E_0) designated here is the lowest value of the F-N plot, corresponding to the intersection of the low and high electric field

segments. Figure 4.2 shows that the turn-on field (E_0) for as-prepared UNCD is 13.3 V/ μm . It may be noted that the value of turn-on field of as-prepared UNCD film discussed in chapter 3 is 14.7 V/ μm , which is slightly higher than 13.3 V/ μm observed here. This could be due to the different film growth condition employed here. However, after the MCD film deposition on UNCD layer, E_0 value decreases to 10.3 V/ μm for the as-prepared MCD/UNCD films (curve II). Interestingly, E_0 value significantly decreases to 7.9 V/ μm for N^+ ion implanted films (curve III) and 7.4 V/ μm for the post-annealed films (curve IV). The current density (J_e) value for the as-prepared UNCD films is less than 0.001 mA/ cm^2 at 25 V/ μm . However, the J_e value is 0.07 mA/ cm^2 at an applied field of 17 V/ μm which further increases to 0.14 mA/ cm^2 for N^+ ion implanted and 0.57 mA/ cm^2 for the post-annealed films. The details of the EFE properties of as-prepared UNCD, as-prepared MCD/UNCD, N^+ ion implanted and post-annealed MCD/UNCD films are tabulated in Table 4.1.

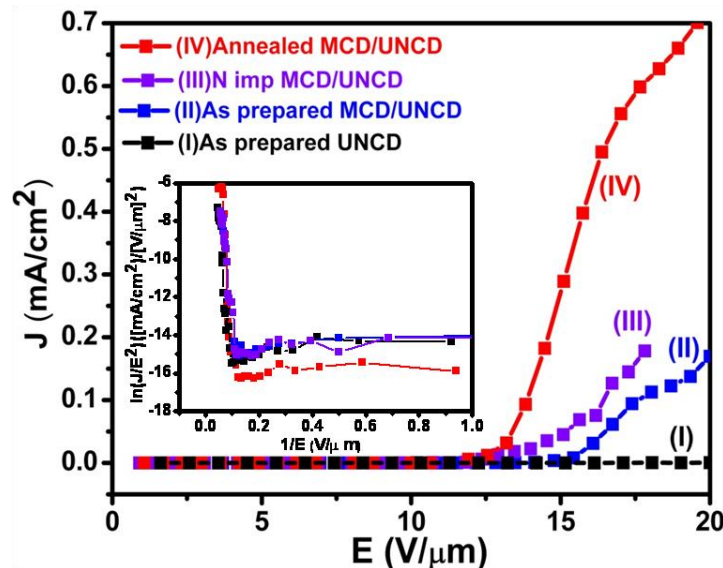


Fig. 4.2 Electron field emission properties of (I) as-prepared UNCD, (II) as-prepared MCD/UNCD (III) N^+ ion implanted MCD/UNCD and (IV) post-annealed MCD/UNCD films. The inset shows the F-N plot of the corresponding J-E graph.

Table 4.1 The EFE performances of as-prepared, N⁺ ion implanted and post-annealed MCD/UNCD films. EFE properties of as-prepared UNCD are given for comparison. E₀: the turn-on field estimated from the Fowler-Nordheim plots as the interception of the line segment extrapolated from high field and low field regime.

J_e: EFE current density at an applied field of 17 V/μm.

Samples	E ₀ (V/μm)	J _e (mA/cm ²)
As-prepared UNCD	13.3	< 0.01 (at 25 V/μm)
As-prepared MCD/UNCD	10.3	0.07
N ⁺ ion implanted MCD/UNCD	7.9	0.14
Post-annealed MCD/UNCD	7.4	0.57

To understand the mechanism behind the enhancement in EFE properties for N⁺ ion implanted and post-annealed films further, Raman, XPS, TEM, STM and STS measurements are carried out in more detail. Figure 4.3(a) to figure 4.3(d) show the FESEM images of as-prepared UNCD, as-prepared MCD/UNCD, N⁺ ion implanted MCD/UNCD and post-annealed MCD/UNCD films, respectively. As-prepared UNCD films (Fig. 4.3(a)) have small needle like structures. Interestingly, the as-prepared MCD/UNCD (Fig. 4.3(b)) films don't show the surface morphology of either MCD or UNCD films, even though MCD films are deposited on a layer of UNCD films. The surface of as-prepared MCD/UNCD films have few nanometres of diamond grains merged with each other, forming aggregates of about 100 to 200 nm in size. Interestingly, after N⁺ ion implantation, significant change in surface morphology is seen (Fig. 4.3(c)). Deep groovings along the boundaries of the aggregates are observed. The diamond grains become roundish shaped and sharp grain boundaries are clearly

seen in N^+ ion implanted films. Post-annealing process seems to fuse together the groovings, making the surface to look like cauliflower structures (Fig. 4.3(d)).

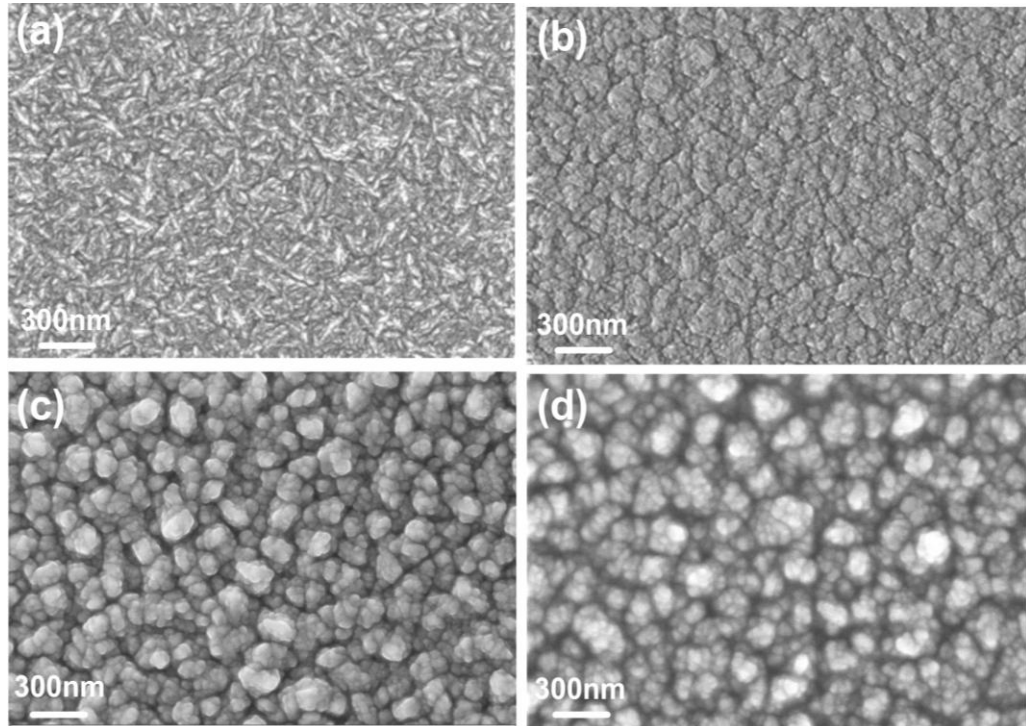


Fig. 4.3 SEM micrograph of the (a) as-prepared UNCD, (b) as-prepared MCD/UNCD (c) N^+ ion implanted and (d) post-annealed MCD/UNCD films.

Figure 4.4 (a,b,c) shows the Raman spectra of (a) as-prepared, (b) N^+ ion implanted and (c) post-annealed MCD/UNCD films. The Raman spectra of as-prepared UNCD (not shown here) is similar to that of the as-prepared MCD/UNCD. Raman spectra were de-convoluted by using multi-peak Lorentzian fitting method. Seven peaks were observed in as-prepared MCD/UNCD films as ν_1 (1133 cm^{-1}), ν_2 (1192 cm^{-1}), ν_3 (1450 cm^{-1}), D (1321 cm^{-1}), D^* (1362 cm^{-1}), G (1552 cm^{-1}) and nanographitic G' (1594 cm^{-1}) as illustrated in figure 4.4(a). D-band resonance peak at 1321 cm^{-1} is the characteristic of diamond phase. The ν_1 and ν_3 refer to the

transpolyacetylene ($trans(CH)_x$) phase present at the grain boundaries. ν_2 peak refer to the signature of nanodiamond phase [16].

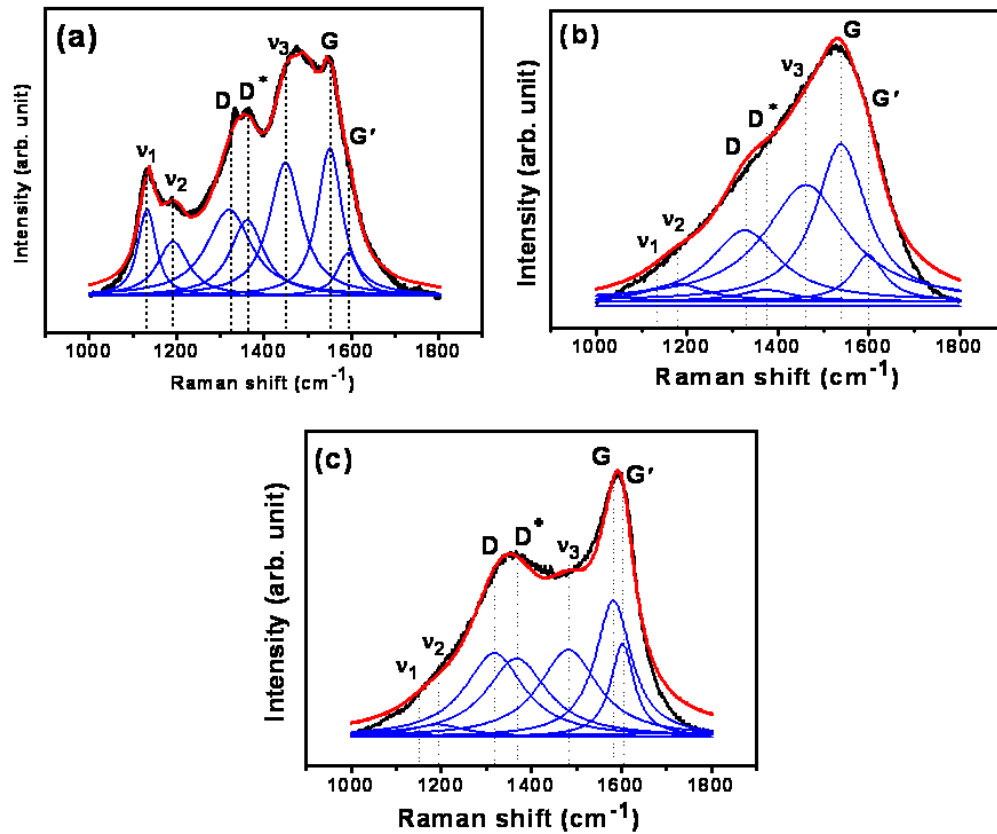


Fig. 4.4 Raman spectra from (a) as-prepared, (b) N^+ ion implanted and (c) post-annealed MCD/UNCD films recorded with 514.5 nm laser line.

Moreover, the Raman spectra D*-band (1362 cm^{-1}) and G-band (1552 cm^{-1}) resonance peaks, represents the disordered carbon and graphitic phase respectively [17, 18]. A shoulder peak around 1594 cm^{-1} (designated as G' band) is seen that possibly arises from the nanocrystalline graphitic content in the films [18].

The effect of N^+ ion implantation on altering the bonding characteristics of MCD/UNCD films is shown in figure 4.4(b). Smaller amount of ν_1 and ν_2 phases are seen in N^+ ion implanted films. However, the position of ν_3 peak is shifted to higher wave number sides (1463 cm^{-1}). The shifting is probably a sign of the breaking up of

transpolyacetylene chains due to the high ion fluence of N^+ ion implantation [16]. The ion implanted films show higher intensities of G peak indicating graphitization type of transitions [9]. Post-annealing of the N^+ ion implanted MCD/UNCD films increases the D^* peak markedly, inferring the increase in disordered carbon and nano-graphitic phase. The Raman spectra show I_{D^*}/I_G values (ratio of intensities of D^* -peak to G-peak) are 0.54, 0.32 and 1.02 for as-prepared, N-implanted and post-annealed MCD/UNCD films, respectively. The increase of I_{D^*}/I_G value from 0.54 in case of as-prepared film to 1.02 in post-annealed film implies the formation of nanographite and decrease in sp^3 content according to a three-stage model of increasing disorder in carbon materials [18, 19], *i.e.* there is conversion of sp^3 to sp^2 content. It is to be noted that visible Raman spectroscopy can only give information about the sp^2 -bonded carbon and only indirect information on the relative sp^3 content. The higher intensity of G'-band is observed after the annealing process (Fig. 4.4(c)).

The disorder/amorphous type Raman resonance peaks were converted into graphitic one due to annealing process of the ion implanted films. The position of G' peak is 1594, 1599 and 1603 cm^{-1} in as-prepared, N^+ ion implanted and post-annealed films respectively. The shifting of the G' peak to higher wave number side in N^+ ion implanted and post-annealed films is possibly due to the formation of nanocrystalline graphite from amorphous phase by the N^+ ion implantation/post-annealing processes [18]. The formation of nanographitic phase by the N^+ ion implantation and post-annealing process is also confirmed by the TEM study, which will be discussed shortly. The presence of defects, increase in sp^2 content upon N^+ ion implantation and presence of nanographitic phase can enhance the field emission properties of MCD/UNCD films [15].

4.3.2 XPS Results

To reveal the effect of N^+ ion implantation/post-annealing processes on the chemical bonding characteristics of MCD/UNCD films more precisely, XPS measurements were carried out. Figure 4.5 shows the C-1s photoemission spectra of as-prepared, N^+ ion implanted and post-annealed MCD/UNCD films. The data are fitted with Lorentzian peaks with binding energies at 284.5, 285.6, 285.2 and 286.1 eV corresponding to the sp^2 (C=C), sp^3 (C-C), C=N, C-N phases respectively with their relative intensities tabulated in Table 4.2.

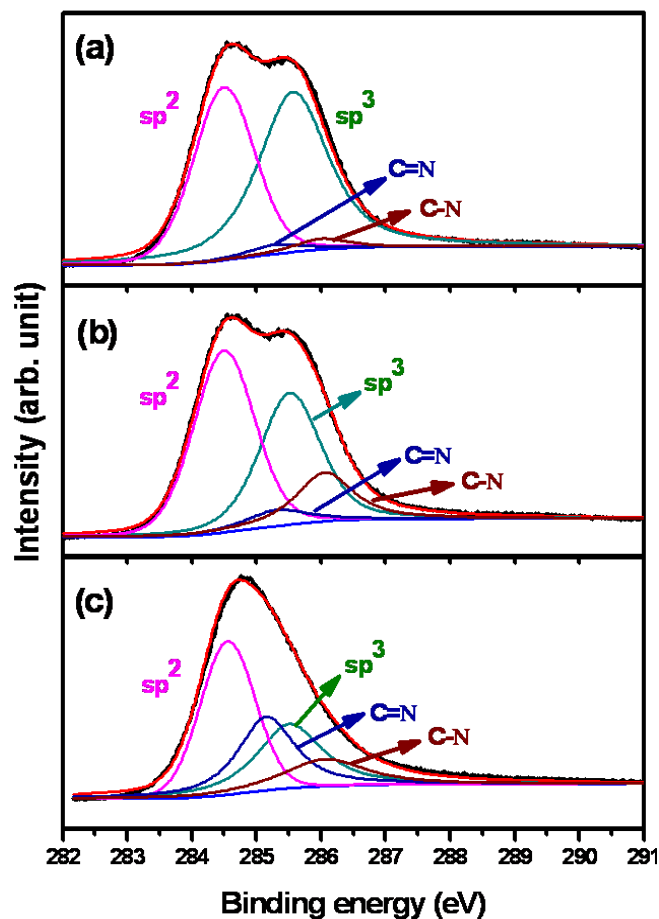


Fig. 4.5 C-1s XPS spectra from (a) as-prepared, (b) N^+ ion implanted and (c) post-annealed MCD/UNCD films.

The background was subtracted using Shirley's method [20]. The measurements were conducted without ion sputtering to avoid reconfiguration of the surface bonding structures. In as-prepared MCD/UNCD, sp^3 C–C bonding is predominant with a peak intensity of 53.9% while sp^2 C=C intensity is 42.9%. There is a little amount of nitrogen present in as-prepared film as C–N (1.9%) and C=N (1.3%) phases.

Table 4.2 Relative intensities of various components of C-1s XPS spectra from as-prepared, N^+ ion implanted and post-annealed MCD/UNCD films.

Peak position (eV)	Chemical bonding	Peak intensity (%) of MCD/UNCD film		
		As prepared	N^+ ion implanted	post-annealed
284.5	sp^2	42.9	44.11	46.8
285.6	sp^3	53.9	29.83	24.37
285.2	C=N	1.3	9.88	21.04
286.1	C–N	1.9	16.18	7.79

After N^+ ion implantation, sp^3 C–C peak intensity drastically decreases to 29.83% and sp^2 C=C peak intensity increases to 44.11%. Moreover, the N^+ ion implanted films clearly show the presence of C–N and C=N spectra as marked in figure 4.5(b). The appearance of these phases indicates that the chemical bonding between C and N is formed after the N^+ ion implantation process. Upon annealing (figure 4.5(c)), sp^2 (C=C) peak intensity increases further to 46.8%. The increase in sp^2 content upon N^+ ion implantation is consistent with Raman (Fig. 4.4(b)) and the earlier reported results [11]. Increase in C=N phase and decrease in C–N phase of post-annealed films indicate the loss of N atom from tetrahedral sp^3 site and increase in N atoms in

aromatic sp^2 (C=C) sites. There will be some loss of nitrogen and rearrangement of carbon atoms to form sp^2 C=C bonds [21].

4.3.3 Scanning Tunneling Spectroscopy (STS)

To reveal how the changes in microstructure and concentrations of sp^2 , sp^3 , C-N and C=N phases affect the EFE properties for these films, the local electronic properties of the films were investigated by STS in CITS mode, to directly reveal the emission sites in these films. STS measurement of as-prepared, N^+ ion implanted and post-annealed MCD/UNCD films are systematically performed to study the effect of each processing step on the number density of emission sites. As prepared MCD/UNCD films are resistive for STM measurements. The surface of as-prepared MCD/UNCD became conducting when sputter ion-etched with Ar^+ ions for one minute by removing nearly 1 nm thickness inside the XPS chamber. STM measurements are made after that. Figure 4.6(a) shows the STM image of as-prepared MCD/UNCD film surface. The root mean square (rms) roughness is found to be 17 nm over $1 \times 1 \mu m^2$ scanning area as measured by STM. In as-prepared MCD/UNCD films, the grains coalesce, forms bigger diamond aggregates, as also seen by SEM (Fig 4.3(b)). Such a typical bigger diamond aggregate is marked as “*i*” with the facet as “*ii*” in figure 4.6(a). Figure 4.6(b) is the CITS image corresponding to figure 4.6(a) taken at a sample bias of -2.5 V. Bright and dark regions in the CITS image are visible with their shapes having similarity with the shapes of grain “*i*” and facet “*ii*” of STM image in figure 4.6(a), respectively. Bright contrast in the CITS image represents better electron emission [22]. The CITS image reveals that the emission sites are mainly seen along the facets of the MCD/UNCD films, indicating that the emission sites are very less and are seen discontinuously throughout the sample surface. N^+ ion

implantation introduces defects, sp^2 phase and expels hydrogen from the grain boundaries and makes the film more conducting.

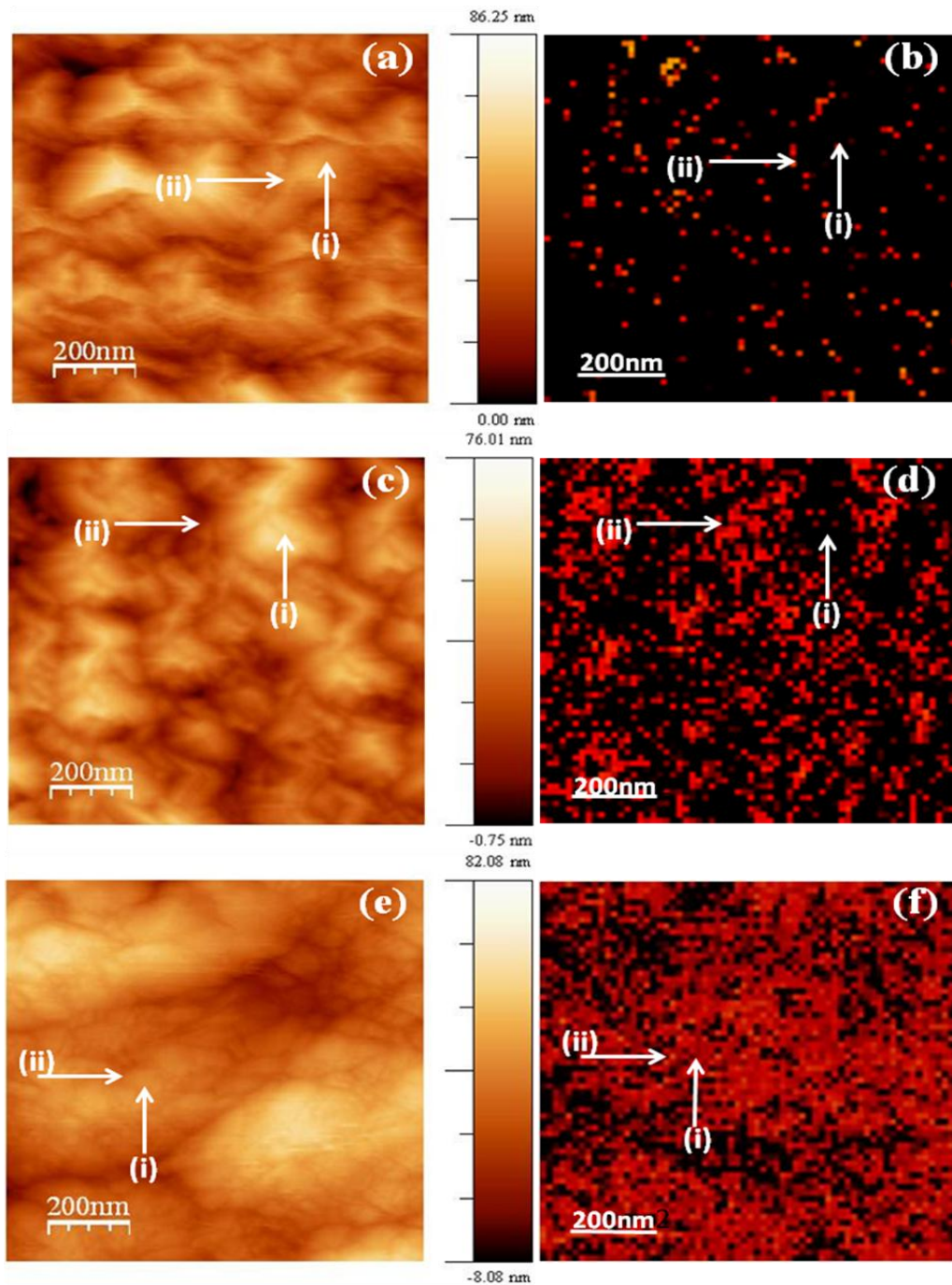


Fig. 4.6 The STM image of (a) as-prepared MCD/UNCD films with (b) the corresponding CITS image; the STM image of (c) N^+ ion implanted MCD/UNCD films with (d) the corresponding CITS; the STM image of (e) post-annealed MCD/UNCD films with (f) the corresponding CITS. Position (i) is within the grain and position (ii) is at grain boundary.

Figure 4.6(c) shows a typical STM topograph of the N^+ ion implanted MCD/UNCD surface with the corresponding CITS image shown in figure 4.6(d). Both acicular and roundish type structures are seen in the STM image. The highly dense acicular clusters are agglomerates of many small diamond grains. One typical large grain and facet is marked as “i” and “ii” in figure 4.6(c) with the same position marked as “i” and “ii” in the corresponding CITS image (Fig. 4.6(d)). Number density of bright emission sites is more in N^+ ion implanted films (Fig. 4.6(d)), comparing to as-prepared MCD/UNCD films (Fig. 4.6(b)).

For better understanding whether the large diamond grain as a whole emits or still it consists of smaller grains separated by grain boundaries (GBs), the High resolution STM (HRSTM) is taken in the region marked as “i” in figure 4.6(c) and figure 4.6(e). Interestingly, grain and GBs are seen in the HRSTM image, as shown in figure 4.7(a). Typical grain and GB are marked as “i” and “ii” in figure 4.7(a) with the corresponding CITS image in figure 4.7(b), which is taken at the same sample bias of -2.5 V. High resolution CITS image clearly shows emission sites are mainly located along the GBs of these smaller diamond grains (marked as “ii” in figure 4.7(b)). Emission sites are seen around most of the GB sites comparing to CITS image of as-prepared MCD/UNCD in figure 4.6(b). This indicates, few of the GB sites of as-prepared films are converted from resistive trans-polyacetylene phase to conductive amorphous one due to N^+ ion implantation. This fact is also supported by TEM observation which is discussed shortly.

Thus N^+ ion implantation/post-annealing processes have increased the number density of emission sites due to the introduction of defects, nanographitic phases, sp^2 , C-N and C=N phases. The film surface gets smoothed further after the post-annealing

and the rms roughness decreases to 8.1 nm over $1 \times 1 \mu\text{m}^2$ scanning area. The surface smoothing upon annealing could be due to the graphitisation of the surface as revealed by XPS. Figure 4.6(e) shows coalescence of the smaller grains occurs due to the annealing process and it forms typical cauliflower like structure as seen in SEM (Fig. 4.3(d)). The corresponding CITS image is shown in figure 4.6(f), taken at the sample bias of -2.5 V. Typical large grain and facet in this image are marked as “i” and “ii”.

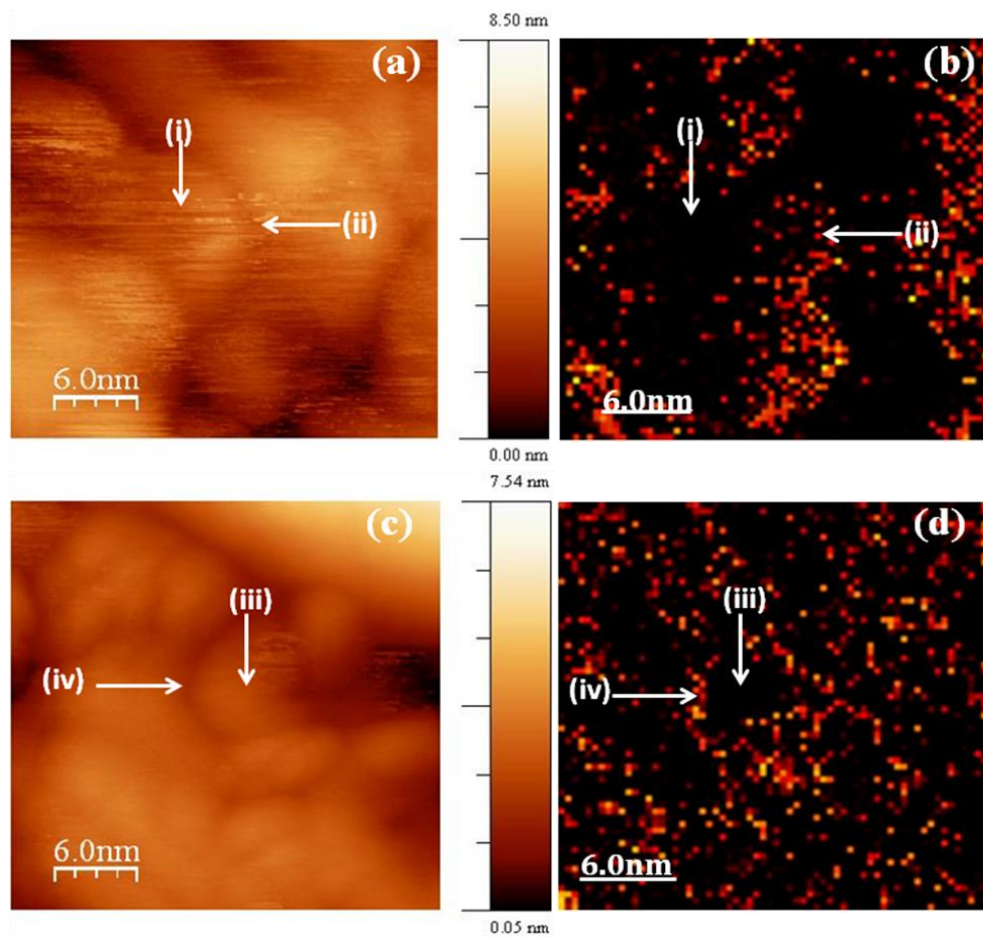


Fig. 4.7 The high resolution STM (HRSTM) image of (a) N^+ ion implanted MCD/UNCD films with (b) the corresponding CITS image; (c) that of the post-annealed MCD/UNCD films with (d) the corresponding CITS.

Interestingly, the emission site density increases significantly in post-annealed films than as-prepared and N^+ ion implanted films. It looks as if the whole film surface emits. The post-annealed MCD/UNCD film surface (Fig. 4.6(e)) is still made up smaller diamond particles. Figure 4.7(c) shows the HRSTM image taken within the diamond grain region marked as “i” in figure 4.6(e), revealing that larger diamond grains marked as “i” observed in figure 4.6(e) are actually composed of smaller grains separated by grain boundaries. The uniform diamond grain of sizes of nearly 5 nm is observed. Typical grain and grain boundary are marked as “iii” and “iv” in figure 4.7(c). Figure 4.7(d) shows the CITS image corresponding to figure 4.7(c) taken at the sample bias of -2.5 V. It is seen that the emission sites are more along the grain boundaries of the smaller grains marked as “iv” in figure 4.7(c), indicating that grain boundaries are the prominent electron emission sites. Thus the larger grains observed in figure 4.6(e) are actually composed of smaller grains of nearly 5 nm in size, with well separated grain and grain boundaries. The number densities of these smaller grains with emitting grain boundaries are large enough such that it appears as if the bigger diamond grain as a whole emits when one see in a coarse scale.

The local electronic properties are characterized by measuring the local current vs. voltage (I-V) curves of N^+ ion implanted and post-annealed MCD/UNCD films from STS measurements at various sample positions as on the grain and grain boundaries in HRSTM image shown in figure. 4.7(a) and figure 4.7(c), respectively. The tunnelling current under positive bias to the MCD/UNCD films is lesser than that under negative bias, implying that the films have *n*-type conductivity. Only the negative portion of the I-V curves are shown in figure 4.8, as the negatively biased current corresponds to the tunnelling of electrons from the diamond surface to the

tungsten tip and is proportional to the density of occupied states in the diamond. Ten reproducible I-V spectra corresponding to each emission sites were recorded during the I-V scanning. It should be noted that the curves 1 and 2 correspond to grain and GB of N^+ ion implanted films, respectively (locations “i” and “ii” in figure 4.7(a)), whereas curves 3 and 4 correspond to grain and grain boundary of post-annealed films, respectively (locations “iii” and “iv” in figure 4.7(c)). A significant change in I-V characteristic curves both at the grain and grain boundary for N^+ ion implanted and post-annealed MCD/UNCD films were observed.

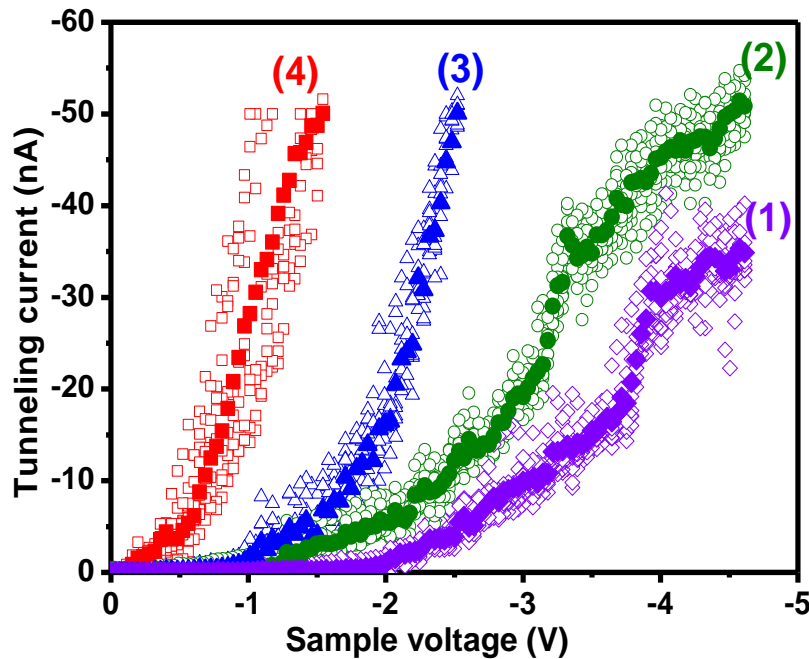


Fig. 4.8 The local I-V curves obtained in STS measurements at (1) the grain and (2) the grain boundary of N^+ ion implanted MCD/UNCD films [marked as “i” and “ii” in high resolution STM image in figure 4.7(a)]; those at (3) the grain and (4) the grain boundary of post-implantation annealed MCD/UNCD films [marked as “iii” and “iv” in high resolution STM image in figure 4.7(c)]. The thick line drawn corresponds to the average of 10, I-V curves at the designated points.

Post-annealed MCD/UNCD films (curves 3 and 4) emit better than N^+ ion implanted MCD/UNCD films (curves 1 and 2). Moreover, the grain boundaries (curves 2 and 4) emit at a lower sample bias compared to the grains (curves 1 and 3) for both films. Also the conductivity of the grain boundaries is better than that of grains in both films, which is consistent with the CITS image showing bright emissions around the grain boundaries in figure 4.7(b) and figure 4.7(d).

4.3.4 Transmission Electron Microscopy Results

The STS measurements illustrate clearly the benefit of N^+ ion implantation and post-annealing process on increasing the number density of the electron field emission sites. However, the authentic factor for such an effect is still not clear. It is suspected that the modification on the granular structure for these films due to N^+ ion implantation and post-annealing process is the key. To investigate the possible cause for such phenomena, the detail microstructure for these films was examined using TEM. Figure 4.9 shows the bright field TEM micrographs of the as-prepared, N^+ ion implanted and post-annealed MCD/UNCD films. Figure 4.9 reveals the true microstructure of the MCD/UNCD films, viz. all the films contain large diamond aggregates dispersed evenly among the ultra-small grain matrix, forming a duplex-granular structure. The selected area electron diffraction (SAED) pattern shown as insets in each figure contains ring shaped diffraction patterns, corresponding (111), (220) and (311) lattices of diamond, which indicates that the most of the materials are of diamond structure, even though Raman spectroscopy shows small or invisible resonance peaks corresponding to sp^3 -bonds for the films. The diffraction spots are spotty and are arranged in a ring geometry, which infers that the diamond grains are relatively large than as-prepared UNCD and are randomly oriented. N^+ ion

implantation and post- annealing processes seem to impose very limited modification on the granular structure for these films, except that the grains changed from equi-axed geometry to elongated rod geometry for the post-annealed samples (Fig. 4.9(c)). The duplex-granular structure is still preserved.

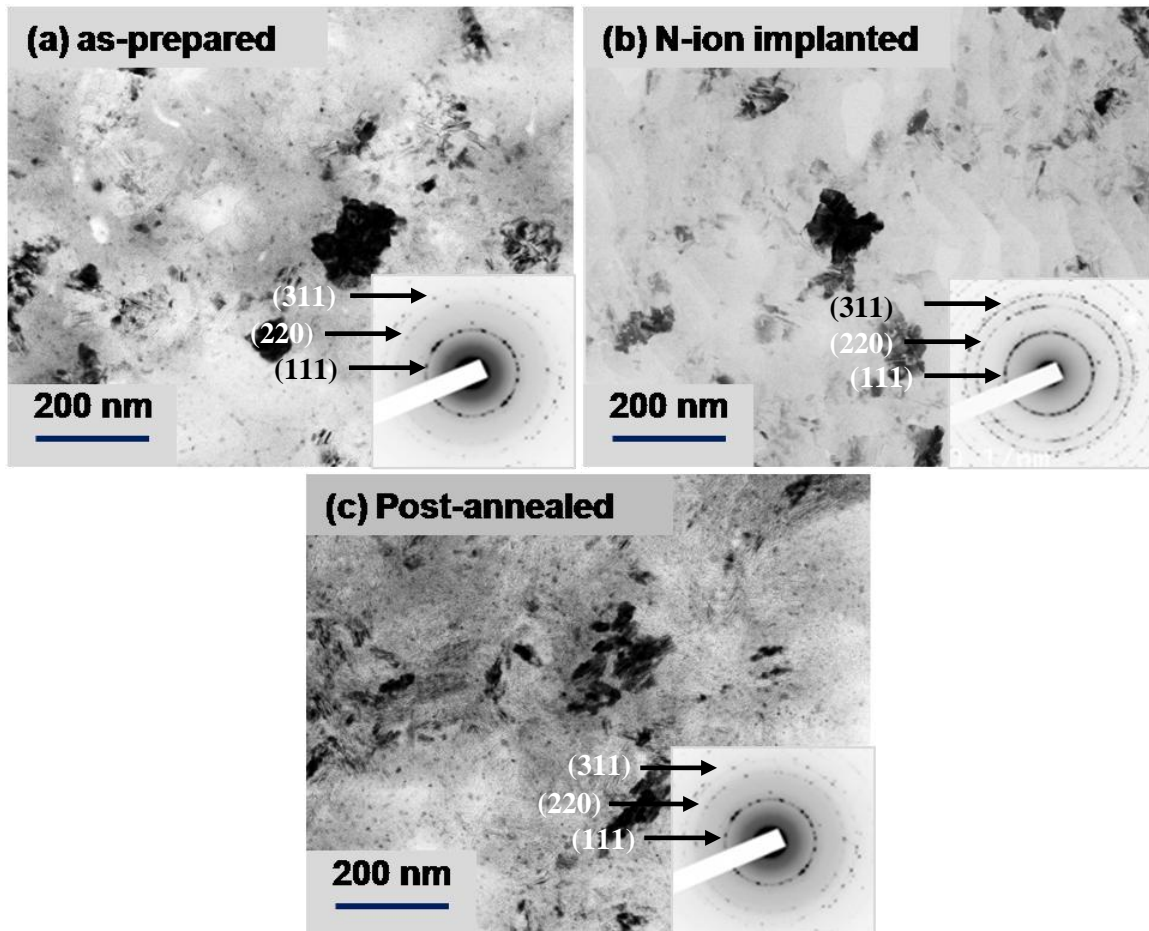


Fig. 4.9 The bright field TEM micrographs for (a) as-prepared, (b) N^+ ion implanted and (c) post-implantation annealed MCD/UNCD films.

However, more detailed investigation using high resolution TEM (HRTEM) revealed marked change in microstructure of the films induced by the N^+ ion implantation and post- annealing processes. Figure 4.10 shows the HRTEM images corresponding to the large diamond aggregates of the as-prepared, N^+ ion implanted

and post-annealed MCD/UNCD films along with the associated Fourier-transformed (FT) diffractograms, which corresponds to the whole structure image shown as insets (labelled as FT_{0a} , FT_{0b} and FT_{0c}). Figure 4.10(a) shows that, in the as-prepared MCD/UNCD films, the diamond aggregates contain large proportion of planar defects. There are regions containing parallel fringes with irregular spacing as marked by region 1.

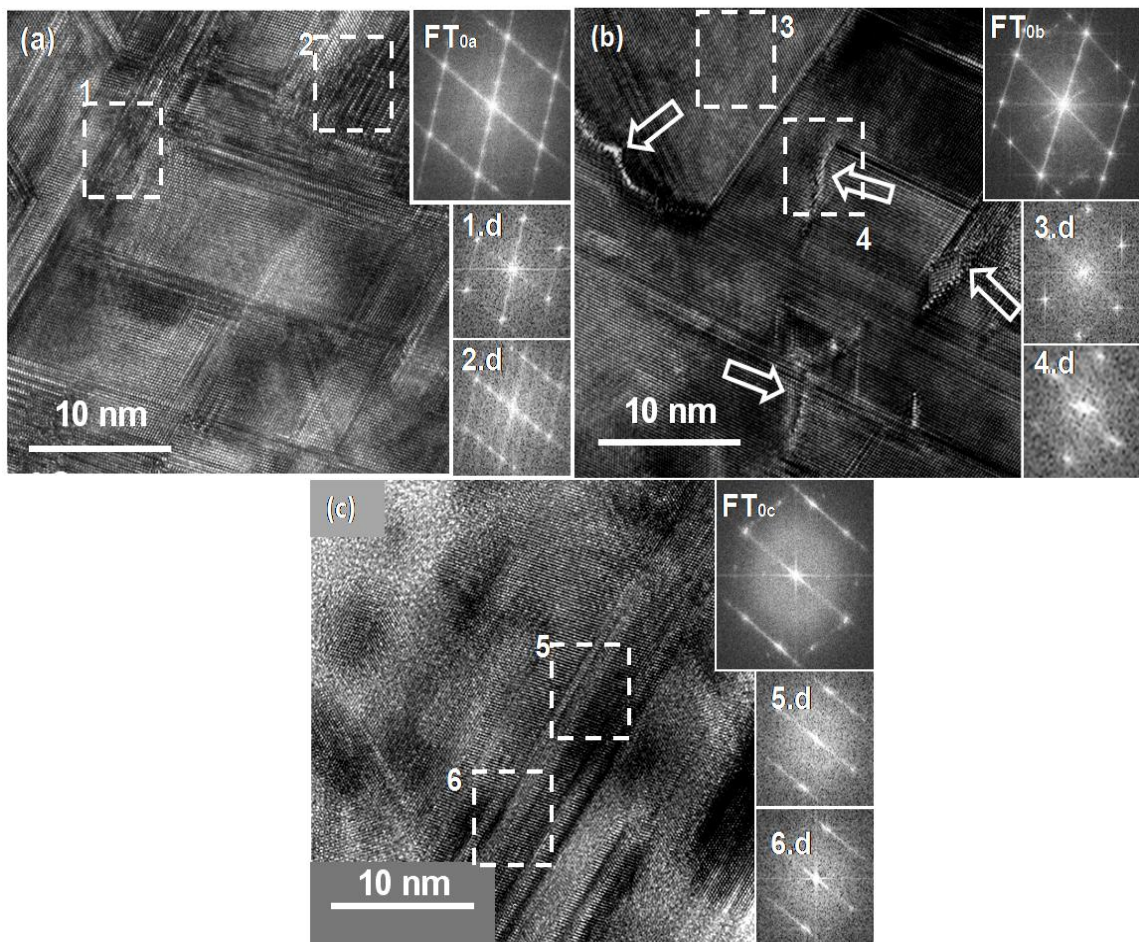


Fig. 4.10 The HRTEM image corresponding to the large diamond aggregates for (a) as-prepared, (b) N^+ ion implanted and (c) post-annealed MCD/UNCD films. The insets FT_{0a} , FT_{0b} and FT_{0c} show the FT images corresponding to the whole structure images “a”, “b” and “c”, respectively, and the FT_1 to FT_6 show the FT images corresponding to the areas “1” to “6”, respectively. ‘1.d’ d represents diamond at the marked positions 1.

The systematic diffraction spots in FT₂ image (insets, Fig. 4.10(a)) implied that the rel-rods associated with the major diffraction spots in the associated FT₁ image (inset, Fig. 4.10(a)) indicate that these fringes correspond to stacking faults [23]. There are regions containing parallel fringes with regular spacing as seen in regions 2. These fringes correspond to hexagonal diamond lattice [23], an allotropy of cubic diamond. Figure 4.10(b) shows that the planar defects, including the stacking faults and hexagonal diamond lattices, are still observable but are less in proportion for the N-ion implanted MCD/UNCD films. Moreover, there are regions where some irregularities were induced (indicated by arrows).

These irregularities could be point defects (voids) or line defects (dislocations), as implied by the shifting in diffraction spots in the FT image (FT₄) corresponding to region 4, with respect to the regular diamond lattices (region 3 and FT₃) in figure 4.10(b). Substitutional incorporation of N⁺ ions may occur that is expected to alter the electronic band structure of the diamond and can account for the change in band gap observed, which will be further discussed. Post-annealing the N⁺ ions implanted MCD/UNCD films lead to recrystallization process, which converted the amorphous carbon into nanographites and induced the coalescence of the diamond grains. The HRTEM image shown in figure 4.10(c) indicates that the elongated grains observed in figure 4.9(c) is actually a coalesced of small diamond grains. Notably, the nano-sized diamond grains were rotated to align in the same orientation due to the coalescence process that was highlighted by regions 5 and 6 (FT₅ and FT₆).

The phenomenon that the nano-graphite clusters were induced in accompanying the coalescence process is similar to one observed in the formation of duplex structure for the MCD/UNCD films [3-5]. However, the more marked effect, which enhanced

the EFE properties of the MCD/UNCD films, is the modification on the microstructure of the ultra-small grain regions. The induction of nano-graphite clusters can markedly improve the conductivity for the films. Figure 4.11(a) shows the typical TEM micrograph for an ultra-small grain region in as-prepared MCD/UNCD films, indicating that this region contains abundant nano-sized diamond grains (~ 5 nm) with very uniform size distribution. The microstructure of the ultra-small grain region of the N^+ ion implanted and post-annealed MCD/UNCD films is similar to the one shown in figure 4.11(a). HRTEM image for the ultra-small grain region of the as-prepared MCD/UNCD films is shown in figure 4.11(b), indicating that there is large proportion of amorphous phase existing at the boundaries of diamond grains, as implied by the FT image corresponding to the whole structure image (FT_{0b}). The N^+ ion implantation process disintegrated the grain boundary transpoly-acetylene phase, inducing the formation of nanographitic in the grain boundary regions. Such a phenomenon is illustrated by the FT image, FT_{0c}, and highlighted by FT₃ and FT₄-images corresponding to regions 3 and 4, respectively, in figure 4.11(c). Post-implantation annealing process recrystallize most of the amorphous phase into graphitic phase that is illustrated by the FT image, FT_{0d}, and highlighted by FT₅ and FT₆-images corresponding to regions 5 and 6 in figure 4.11(d).

Restated, the N^+ ion implantation and post-annealing processes markedly modified the microstructure of both the large diamond aggregates and the ultra-small diamond grains of the MCD/UNCD films. The electronic structure of the large diamond aggregates could be largely altered that facilitate the field emission behaviour for these films. However, more prominent effect due to these processes is the induction of nano-graphite phase between the ultra-small diamond grain regions that form an interconnected path for electron transport.

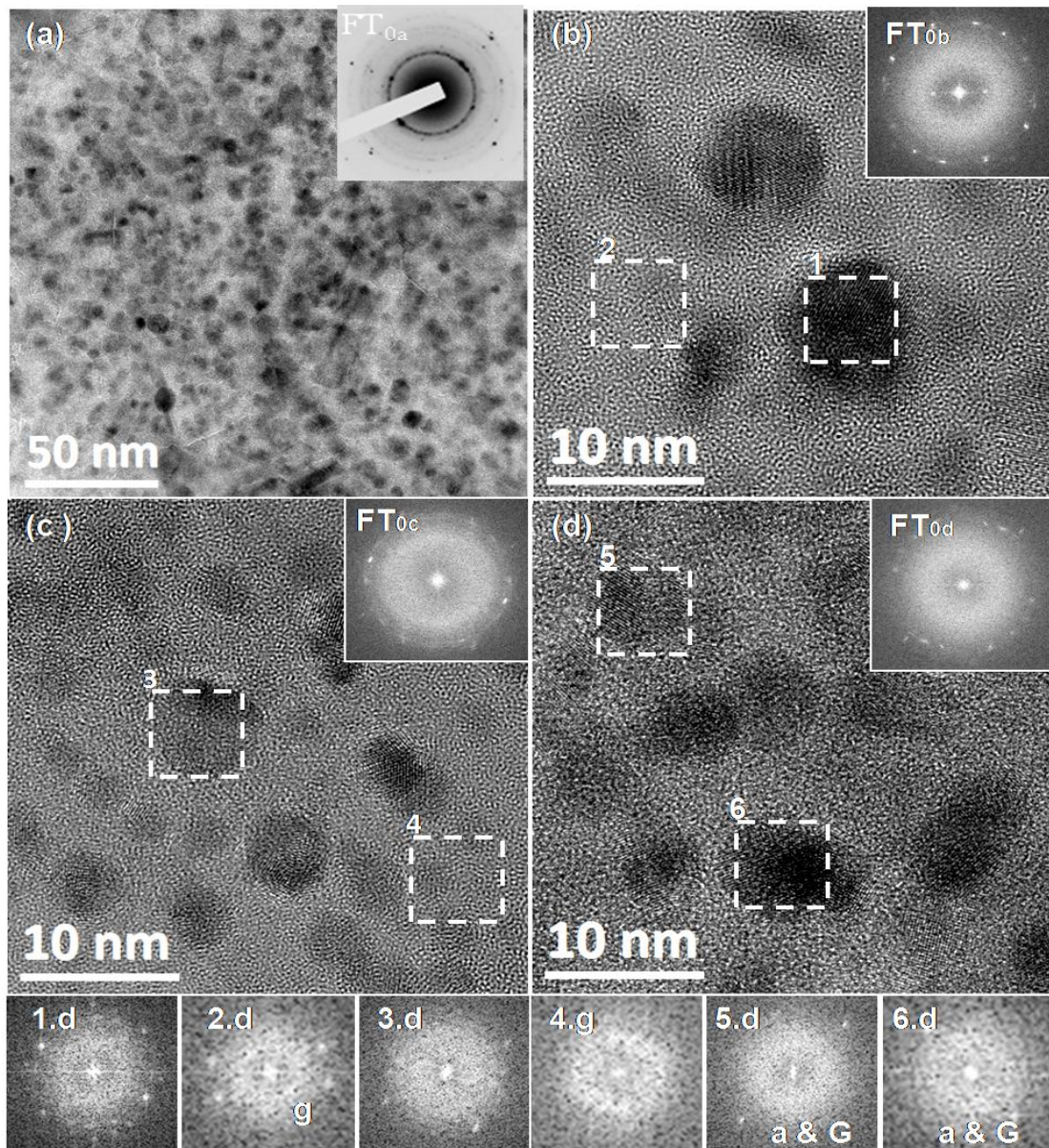


Fig. 4.11 (a) The bright field TEM micrograph and (b) the HRTEM image of a typical ultra-small grain region for as-prepared MCD/UNCD films; (b, c) the HRTEM image corresponding to a typical ultra-small grain region of (c) the N^+ ion implanted and (d) the post-annealed MCD/UNCD films. The insets FT_{0a} , FT_{0b} , FT_{0c} and FT_{0d} show the FT images corresponding to the whole structure images “a”, “b” and “c”, respectively, and the FT_1 to FT_6 show the FT images corresponding to the areas “1” to “6”, respectively. In ‘1.d’ d represents diamond at the marked positions 1.

4.4 Discussion

To investigate in detail the authentic factor that N^+ ion implantation and post-annealing process enhanced the EFE properties of MCD/UNCD films, the I-V characteristic curves recorded during the STS measurements (figure 4.8) were used to calculate the normalized conductance $\frac{dI/dV}{I/V}$ at the grain and grain boundary of the MCD/UNCD films. The normalized conductance vs. applied voltage provides information about the surface local density of states (LDOS) [24, 25]. The normalized conductance curves corresponding to these I-V curves are plotted in figure 4.12(a) and figure 4.12(b) for N^+ ion implanted and post-annealed MCD/UNCD films, respectively.

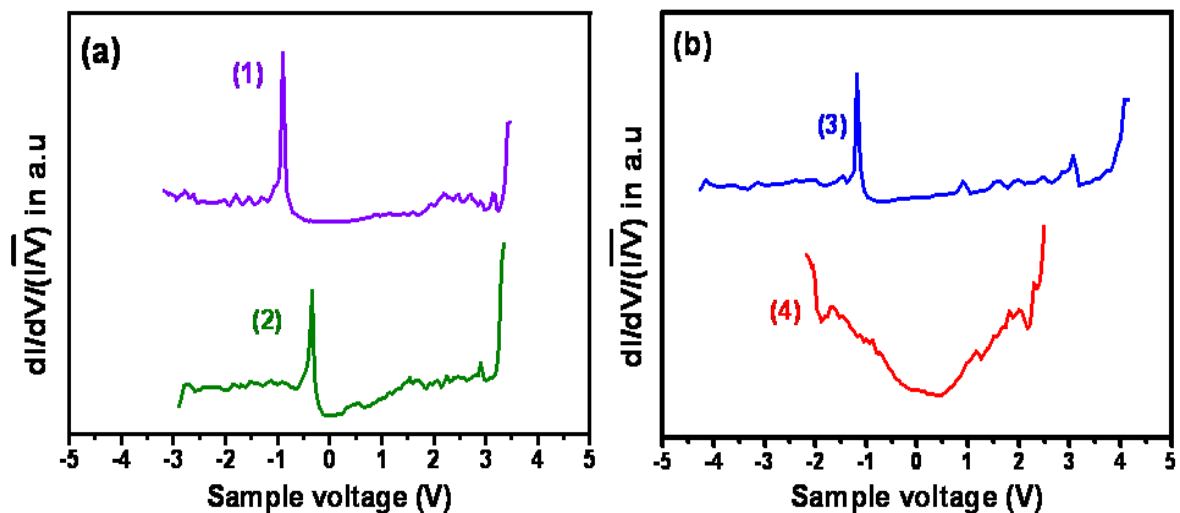


Fig. 4.12 Normalized differential conductance ($dI/dV)/(I/V)$ at (1) the grain and (2) the grain boundary of N^+ ion implanted MCD/UNCD films [marked as “i” and “ii” in high resolution STM image in figure 4.7(a)]; those at (3) the grain and (4) the grain boundary of post-implantation annealed MCD/UNCD films [marked as “iii” and “iv” in high resolution STM image in figure 4.7(c)]. Each spectrum is averaged over 10 scanned spectra shown in figure 4.8

From the I-V spectra corresponding to the grain of as-prepared MCD/UNCD films that were not shown here, the calculated band gap was about 4.65 eV, which is in accordance with the reported value for the nanocrystalline diamond grain. Interestingly, the band gap decreases to 3.7 eV corresponding to curve “1” in figure 4.8 at the diamond grain in N-ion implanted MCD/UNCD film as observed in curve “1”, figure 4.12(a)). The decrease in band gap is in accordance with the band structure calculation [26] that showed the reduction in the band gap of the diamond by 25% after N doping. There is an increase in density of states at the grain boundary sites of the N⁺ ion implanted films, curve “2” (Fig. 4.12(a)).

From the above-described electronic band structure, in conjunction with the TEM microstructural observation, one can assume that nitrogen ion implantation induced structural defects which can introduce electronic defect states in the band gap for the diamond grain. Nitrogen substitution, which is confirmed by XPS measurements, can also introduce new electronic states in the band gap of diamond grain, as suggested by the density functional tight binding calculations of Zapol [27, 28]. Moreover, band gap for the grain boundary is much lesser, compared to that of the grain, due to the presence of a mixture of sp^2 , sp^3 and amorphous carbon phases at the grain boundary (TEM observations) [29]. The grain boundary will have higher conductivity that can account for the significant electron emission from the GB sites, as observed in the CITS images (Fig. 4.7(b) and Fig. 4.7(d)). For the post-annealed films, the band gap of diamond grains reduces to 2.9 eV and there is increase in density of states as shown in curve 3 (Fig. 4.12(b)). Post-annealing removes the defects, forms complex stable defects and conversion of amorphous phase to nanographite clusters; enhances the doping of nitrogen and out diffusion of a certain

fraction of nitrogen from diamond grains to the grain boundaries. Increase in DOS upon annealing can be due to the introduction of stable defect complexes in the diamond grain [30]. The high density of states within the band gap significantly reduces the potential barrier for field emitted electrons [31], lowers the turn-on field and enhances the field emission properties. Furthermore, band gap of grain boundary further reduces, showing nearly metallic behaviour (curve 4, Fig. 4.12(b)). The sp^2 , nanographitic phase and nitrogen content at the grain boundaries increases by annealing process that gives rise to the observed metallic behaviour.

Restated, density of states are introduced in the band gap of diamond in N ion implanted and post-annealed films that enhances the EFE process. However, the grain boundaries mostly contain the nanographitic phase giving rise to metallic conductivity. These conductive grain boundaries form conducting channels at the interface of diamond grains, resulting in prominent electron emission from the grain boundaries. The grain boundaries are more susceptible to amorphization and graphitization upon the N^+ ion implantation and post-annealing [15], which is the authentic factor altering the EFE behaviour for the films. Our results show the possibility of a grain-boundary electron transport mechanism (conductivity-channel process) in MCD/UNCD films [12, 27, 31].

4.5 Conclusion

The electron field emission properties of the two-step MPECVD grown diamond (MCD/UNCD) films were markedly improved by N^+ ion implantation and post-annealing processes. N^+ ion implanted/post-annealed MCD/UNCD hybrid films show a low turn-on field of $((E_0)_{\text{MCD/UNCD}} = 7.4 \text{ V}/\mu\text{m})$ with large current density of $((J_e)_{\text{MCD/UNCD}} = 0.57 \text{ mA}/\text{cm}^2, \text{ at } 17 \text{ V}/\mu\text{m})$, which is markedly better than the as-

prepared MCD or UNCD. XPS measurements show increased sp^2 content and C-N bonding fraction in N^+ ion implanted and post-annealed films. Microstructural analysis reveals the mechanism behind the enhanced EFE properties in N^+ implanted/post-annealed films is due to the induction of point defects in the diamond lattices and the formation of nanographitic phase surrounding the small diamond grains. Current imaging tunnelling spectroscopy in scanning tunnelling spectroscopy mode directly shows the increased emission site densities in N^+ ion implanted/post-annealed MCD/UNCD films than as-prepared one. The formation of nanographitic phase confirmed from TEM studies is responsible in improving the emission sites in N^+ ion implanted/post-annealed films which is directly revealed by high resolution CITS images. The nanographites surrounding the small grain region formed an interconnected path throughout the film surface that facilitates the easy transport of electrons and thereby markedly enhances the EFE properties of the N^+ ion implanted/post-annealed MCD/UNCD films.

4.6 References

- [1] T. D. Corrigan, D. M. Gruen, A. R. Krauss, P. Zapol, R. P. H. Chang, *Diamond Relat. Mater.* **11**, 43 (2002).
- [2] W. Zhu, G. P. Kochanski, S. Jin, *Science* **282**, 1471 (1998)
- [3] C. S. Wang, H. C. Chen, H. F. Cheng, I. N. Lin, *J. Appl. Phys.* **105**, 124311 (2009).
- [4] H. F. Cheng, C. C. Horng, H. Y. Chiang, H. C. Chen, I. N. Lin, *J. Phys. Chem. C* **115**, 13894 (2011).

- [5] H. F. Cheng, H.Y. Chiang, C. C. Horng, H. C. Chen, C. S. Wang, I. N. Lin, J. Appl. Phys. **109**, 033711 (2011).
- [6] S. Fan, M. G. Chapline, N. R. Franklin, T. W. Tomblor, A. M. Cassell, H. Dai, Science **283**, 512 (1999).
- [7] S. Pandey, P. Rai, S. Patole, F. Gunes, G. D. Kwon, J. B. Yoo, P. Nikolaev, S. Arepalli, Appl. Phys. Lett. **100**, 043104 (2012).
- [8] M. Qian, T. Feng, H. Ding, L. Lin, H. Li, Y. Chen and Z. Sun, Nanotechnology **20**, 425702 (2009).
- [9] R. Kalish, Carbon **37**, 781 (1999).
- [10] S. Talapatra, J. Y. Cheng, N. Chakrapani, S. Trasobares, A. Cao, R. Vajtai, M. B. Huang, P. M. Ajayan, Nanotechnology **17**, 305 (2006).
- [11] S. Praver, Kalish, Phys. Rev. B **51**, 15711 (1995).
- [12] E. J. Correa, Y. Wu, J. G. Wen, R. Chandrasekharan, M. A. Shannon, J. Appl. Phys. **102**, 113706 (2007).
- [13] P. T. Joseph, N. H. Tai, Chi-Young Lee, H. Niu, W. F. Pong, I. N. Lin, J. Appl. Phys. **103**, 043720 (2008).
- [14] R. H. Fowler, L. Nordheim, Proc. R. Soc. London, Ser.A **119**,173 (1928).
- [15] K. Panda, B. Sundaravel, B. K. Panigrahi, P. Magudapathy, D. N. Krishna, K. G. M. Nair, H-C Chen, I-Nan Lin, J. Appl. Phys. **110**, 044304 (2011).
- [16] A. C. Ferrari, J. Robertson, Phys. Rev. B **63**, 121405 (2001).
- [17] J. Michler, Y. Von Kaenel, J. Stiegler, E. Blank, J. Appl. Phys., **81**, 187 (1998).
- [18] A. C. Ferrari, J. Robertson, Phys. Rev. B **61**, 14095 (2000).
- [19] A. Ilie, A. C. Ferrari, T. Yagi, S. E. Rodil, J. Robertson, E. Barborini, P. Milani, J. Appl. Phys. **90**, 2024 (2001).
- [20] Y. F. Chen, Surf. Sci. **380**, 199 (1997).

- [21] J. J. Li, W. T. Zheng, H. H. Wu, L. Sun, G. G. Gu, H. J. Bian, X.Y. Lu, Z. S. Jin, *J. Phys. D: Appl. Phys.* **36**, 2001 (2003).
- [22] K. Panda, B. Sundaravel, B. K. Panigrahi, P-C Huang, W-C Shih, H-C Chen, I-Nan Lin, *J. Appl. Phys.* **111**, 124309 (2012).
- [23] I. N. Lin, H. C. Chen, C. S. Wang, Y. R. Lee, C. Y. Lee, *CrystEngComm.* **13**, 6082 (2011).
- [24] R. M. Feenstra, *Surf. Sci.* **965**, 299 (1994).
- [25] R. M. Feenstra, P. Martensson, *Phys. Rev. Lett.* **61**, 4 (1988).
- [26] J. W. Park, C. W. Sohn, B. H. Choi, *Current Applied Physics* **6**, 188 (2006).
- [27] P. Zapol, M. Sternberg, L. A. Curtiss, T. Frauenheim, D. M. Gruen *Phys. Rev.B* **65**, 45403 (2001).
- [28] V. I. Polyakov, A. I. Rukovichnikov, N. M. Rossukanyi, V. G. Pereverzev, S. M. Pimenov, J. A. Carlisle, D. M. Gruen, E. N. Loubnin, *Diamond and Relat. Mater.* **12**, 1776 (2003).
- [29] E. Rohrer, C. F. O. Graeff, R. Janssen, C. E. Nebel, H. Guettler, R. Zachai, *Phys. Rev.B* **54**, 7874 (1996).
- [30] O. A. Williams, Nesladek, M. Daenen, S. Michaelson, A. Hoffman, E. Osawa, K. Haenen, R. B. Jackman, *Diamond and Relat. Mater* **17**, 1080 (2008).
- [31] O. A. Williams, S. Curat, J. E. Gerbi, D. M. Gruen, R. B. Jackman, *Appl. Phys. Lett.* **85**, 1680 (2004).

Direct Observation and Mechanism of Enhanced Electron Field Emission in Iron Coated Microcrystalline and Ultrananocrystalline Diamond Films

5.1 Introduction

Diamond has many desirable physical and chemical properties [1–3], and has been the focus of intensive research since the successful synthesis of diamond in the low pressure and low temperature chemical vapour deposition (CVD) process [4]. Diamond, a wide-band-gap semiconductor ($E_g = 5.5$ eV) with high resistivity, does not appear to be a suitable material for electron field emission (EFE) applications. The concentration of electrons in the conduction band is almost too negligible to be emitted in an undoped diamond. Despite the above mentioned disadvantages, diamond films have been extensively investigated for their applications in cold cathode emission displays and high-definition flat panel displays which need electron field emitting materials [2, 3]. The better field emitting properties of diamond films is due to their excellent Negative Electron Affinity (NEA) properties [5]. Diamond also possesses a very small barrier potential at its surface for the electrons to leave and emit into vacuum because of a low work function (3.5 eV). When the diamond surface is terminated with H atoms, it shows NEA characteristics [6, 7] and is the only known material that is stable in air with NEA. Moreover, field emission (FE) devices from diamond could operate with maximum stability and reliability since diamond has the most strongly bonded crystal structure.

Furthermore, diamond can operate at high temperature or high power because of its very high electrical breakdown field and high thermal conductivity properties that are highly beneficial to FE. With these attractive features of the diamond surface, deposited by a simple chemical vapour deposition process has created enormous interest in the applications of diamond as an electron field emitter. Generally, a good electron field emitter requires sufficient supply of electrons from the back contact materials, effective transport of electrons through the material and presence of efficient emission sites on the surface. Interestingly, the large band gap of diamond can be modified by doping with boron or nitrogen ions which introduces new inter-band states within the band gap, which facilitates the easy transport of electrons from valence band to conduction band and thereby improves the EFE properties [8]. However, the EFE properties are still not satisfactory implying the fact that most of the sample surfaces do not have NEA characteristics because they are not re-constructed (100) surfaces [5]. There are many efforts on modifying the surface of diamond films to enhance the NEA characteristics. Among the approaches, a thin layer of metallic iron (Fe) coating on diamond films, followed by post-annealing in H₂ atmosphere (Fe-coating/post-annealing) significantly improves the EFE properties [9-11]. However, the related mechanism for improved EFE properties from these modified surfaces is still not clear.

In this context, the present chapter describes the possible reasons for the enhancement in EFE properties of microcrystalline (MCD) and ultrananocrystalline diamond (UNCD) films after the Fe-coating/post-annealing processes. The Fe-coating/post-annealing processes enhanced the EFE properties of UNCD films more than that on MCD films. The possible reasons for enhanced EFE properties of Fe-coated/post-

annealed UNCD films than those of MCD films are explained by various analytical tools. Scanning tunneling spectroscopy (STS) in current imaging tunneling spectroscopy (CITS) mode was used to directly observe the enhanced emission sites and to determine the change in local electronic density of states (DOS) of diamond films after the Fe-coating/post-annealing processes. High resolution transmission electron microscopy (HRTEM) was used to investigate the microstructural evolution of these films due to the Fe-coating/post-annealing processes. Further, the possible reasons for the enhancement in EFE properties are discussed on the basis of above experimental observations. For simplicity, this chapter is divided into two parts as part 1, EFE properties of Fe-coated/post-annealed microcrystalline diamond films and part 2 describes the results relating to the EFE properties of Fe-coated/post-annealed ultrananocrystalline diamond films.

5.2 Experimental Details

The microcrystalline diamond (MCD) films were grown on *p*-type silicon (100) substrates in a microwave plasma enhanced chemical vapour deposition (MPE-CVD, IPLAS-Cyrannus) system. The substrates were first thoroughly cleaned by the standard Radio Corporation of America (RCA) cleaning procedure [12] which involves rinsing the silicon wafer sequentially in water-diluted hydrogen peroxide/ammonium hydroxide and hydrogen peroxide/hydrochloric acid solution. Further, the substrates were preseeded by ultrasonication method in a solution containing nanodiamond and titanium powder for 45 mins to facilitate the nucleation of diamond. The substrates were again ultrasonicated in methanol solution to remove the diamond and Ti nano-particles, which could have

possibly adhered to the surface. The MCD diamond films were grown in CH₄/H₂=1/99 sccm plasma excited by a 1400 W (2.45 GHz) microwave with 73 mbar total pressure for 1 h. The UNCD films were grown on the cleaned Si substrates in CH₄/H₂/Ar= 2/6/92 sccm plasma excited by 1200 W (2.45 GHz) microwave power with 200 mbar pressure for 1 h in the same MPE-CVD system. A thin layer of Fe (10 nm) was coated on the MCD and UNCD films by DC sputtering process for 1 min. The Fe coated MCD and UNCD films were then post-annealed in H₂ atmosphere, with a flow rate of 100 sccm for 5 min with heating and cooling rates of 15° C/min. EFE properties of Fe-coated and post-annealed MCD and UNCD films at lower temperatures (< 800 °C) had already been studied [11], where not much improvement in EFE properties were observed. Therefore, in the present study three Fe-coated MCD and UNCD films annealed at higher temperatures of 900°, 925° and 950 °C are selected to study the enhancement in EFE properties systematically. For simplicity the Fe-coated/post-annealed MCD and UNCD films at 900, 925 and 950 °C are designated as (Fe/MCD)₉₀₀, (Fe/MCD)₉₂₅, (Fe/MCD)₉₅₀, (Fe/UNCD)₉₀₀, (Fe/UNCD)₉₂₅, (Fe/UNCD)₉₅₀ respectively.

A home built tunable parallel plate capacitor setup (described in chapter 2) was used to measure the EFE properties of these samples. The separation of the anode Molybdenum (Mo) tip from the sample was measured using a digital micrometer and an optical microscope. The EFE properties were analyzed by the Fowler–Nordheim (F-N) model [13].

$$J(E) = AE^2 \exp\left[-\frac{B\phi^{3/2}}{E}\right], \text{ with } A = e^3 / 16\pi^2 h \phi t^2(y_0) \text{ and } B = 4/3e (2m/h^2)^{1/2} v(y_0)$$

where ϕ is the work function of the emitting material. J_e (in $\mu\text{A}/\text{cm}^2$) and E (in $\text{V}/\mu\text{m}$) are the EFE current density and applied field, respectively. The turn-on field was designated as the interception of the lines extrapolated from the high-field and low-field segments of F-N plots. The morphology and structure of the films were investigated by field emission scanning electron microscope (FESEM, Carl Zeiss, SUPRA 55). A High resolution diffractometer (GIXRD - STOE) using $\text{Cu-K}\alpha$ (0.154 nm) in 2θ range of 20° – 90° at an angle of incidence of 0.2° was used to detect the new phase formed due to the Fe-coating/post-annealing process. The Raman spectra were recorded in back scattering geometry using 514.5 nm line of an Ar-ion laser using Renishaw micro-Raman spectrometer (Model-INVIA). The chemical bonding structures were investigated by XPS using SPECS make photoelectron spectrometer which uses monochromatic Al $\text{K}\alpha$ radiation at 1486.74 eV as a probe. The detailed microstructure of the Fe-coated/post-annealed UNCD films was examined using high resolution transmission electron microscopy (HRTEM, JEOL 2100). Notably, in the transmission electron microscopy, when the elastically scattered electrons were diffracted coherently, diffraction contrast image (bright field image) will be resulted that provides the structure information of the sample. In the meantime, there were electrons, which were elastically but incoherently scattered. The scattering angle is closely related to the atomic number of the species involved. The heavier the species are, the larger the scattering angle. The incoherently scattered electrons were collected by a high angle annular detector and thus a high angle annular dark field (HAADF) image will be observed. The HAADF-image provides elemental distribution on the sample surface. Moreover, the HAADF images are taken

with the samples tilted step wisely (2°) and was replayed sequentially using software Tomography (JEOL), to obtain a 3D-tomography image.

Scanning tunneling microscopy (STM) measurements were carried out in a commercial UHV-STM (150 Aarhus, SPECS GmbH) at a base pressure of 10^{-10} mbar. The tunneling tips were prepared by electrochemical etching of tungsten tips of diameter 0.3 mm. The scanning tunneling spectroscopy (STS) spectra were obtained during scanning and the data presented here are the average of many reproducible spectra acquired during subsequent scans. STS was also used in the current imaging tunneling spectroscopy (CITS) mode which allows us to correlate the STM image with its surface local density of states (DOS) distribution.

5.3 PART-1 Electron Field Emission Properties of Fe-coated/post-annealed microcrystalline diamond films

5.3.1 Results

5.3.1.1 General Characteristics

Figure 5.1 shows the EFE properties of as-prepared and Fe-coated/post-annealed MCD films. Inset of the figure 5.1 shows the corresponding F-N plots. As seen from the current density (J) versus electric field (E) curves, the EFE properties are significantly enhanced due to the Fe coating and annealing processes (Fig. 5.1(ii) to Fig. 5.1(iv)), as compared to as-prepared MCD films (Fig. 5.1(i)). Better EFE properties are observed for (Fe/MCD)₉₀₀ (Fig. 5.1(iv)) films as compared to (Fe/MCD)₉₂₅ (Fig. 5.1(iii)) and

(Fe/MCD)₉₅₀ (Fig. 5.1(ii)) films. The turn-on field (E_0) decreased from 5.12 V/ μm in case of as-prepared MCD films to 3.42 V/ μm for (Fe/MCD)₉₀₀ films. The E_0 values are 4.1 and 4.52 V/ μm for (Fe/MCD)₉₂₅ and (Fe/MCD)₉₅₀ films, respectively.

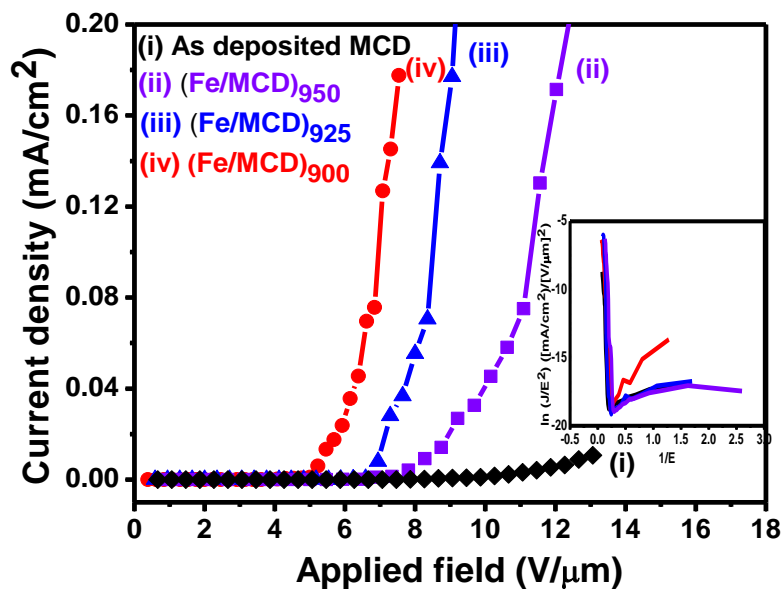


Fig. 5.1 The EFE properties of as-deposited MCD (i), Fe-coated and post-annealed MCD films at (ii) 950 °C (iii) 925 °C (iv) 900 °C. Inset shows the F-N plot for the corresponding J-E curves.

Better current density (J_e) of 170 $\mu\text{A}/\text{cm}^2$ is measured for (Fe/MCD)₉₀₀ films at an electric field of 7.5 V/ μm , while these values are 30 and 3 $\mu\text{A}/\text{cm}^2$ when annealing temperature increased to 925 °C and 950 °C, respectively at the same electric field. The J_e value for as prepared MCD films is only 1.15 $\mu\text{A}/\text{cm}^2$ at 7.5 V/ μm . The EFE properties of the samples are summarized in Table 5.1.

Table 5.1 The EFE properties of as-prepared and Fe-coated/post-annealed MCD films at different temperatures.

Samples	Turn-on field (E_0 in V/mm)	Current density at 7.5 V/ μm (J_e in $\mu\text{A}/\text{cm}^2$)
As prepared MCD film	5.12	1.15
(Fe/MCD) ₉₀₀	3.42	170
(Fe/MCD) ₉₂₅	4.10	30
(Fe/MCD) ₉₅₀	4.52	3

The enhancement in EFE properties of Fe coated and post-annealed diamond films are due to the modification of the surface structures. The FESEM image of the Fe-coated/post-annealed film at 900 °C film, which shows best emission, is shown in figure. 5.2. The inset in the figure shows the image of as-prepared MCD film.

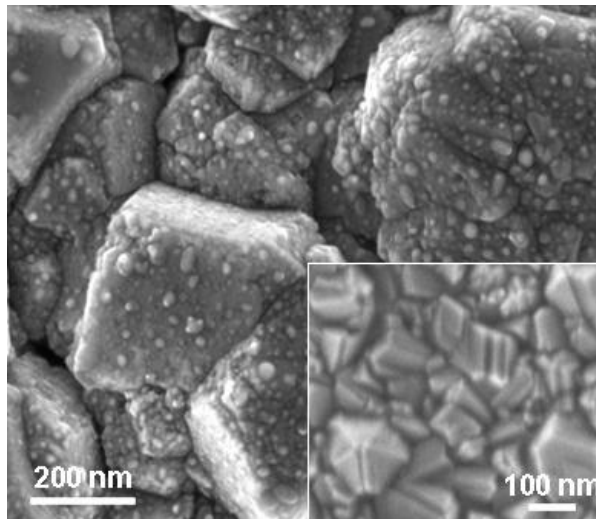


Fig. 5.2. SEM image of Fe-coated/post-annealed (900 °C) MCD film with the inset showing the SEM picture of as-prepared MCD film.

While as-prepared MCD films contain large diamond grains about hundreds of nanometers with faceted geometry (inset of Fig. 5.2), annealing the Fe coated MCD films at 900 °C forms nano-particles of size 5-10 nm on the MCD film surface.

The GIXRD pattern of Fe/MCD films annealed at 900 °C (Fig. 5.3) shows three strong peaks at 43.99°, 55.99° and 75.48°, which correspond to the diamond (111), Fe₃C (212) and Fe₃C (322) phases, respectively [14-15].

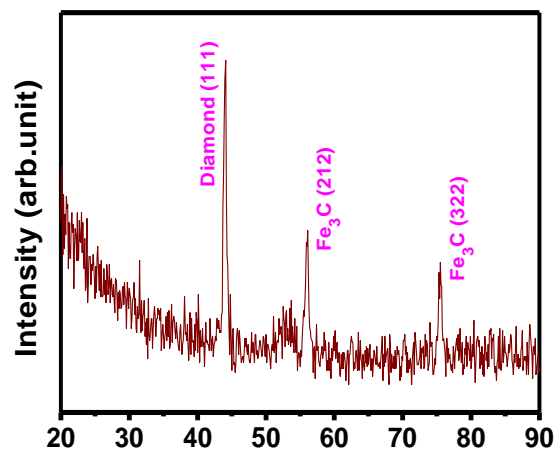


Fig. 5.3 GIXRD pattern of Fe coated MCD film post-annealed at 900 °C showing the presence of Fe₃C phase on the surface.

The faceted granular structure degrades slowly when post-annealing temperature is increased from 900 °C to 925 and 950°C (SEM micrographs not shown) respectively.

In order to understand as how the annealing process modifies the chemical bonding state of the Fe-coated/post-annealed MCD films, Raman and XPS measurements were carried out. Figure 5.4 shows the Raman spectra of as-grown and Fe-coated/post-annealed films. The Raman spectra are fitted with Lorentzian peaks with peak positions at 1191, 1339, 1357, 1470, 1559 and 1608 cm⁻¹ which are marked as ν₁, D, D*, ν₃, G and G*

respectively. D is sharp and the dominant peak in all films and it corresponds to F_{2g} zone center optical phonon of diamond indicating that MCD films are basically sp^3 bonded. The shift in wave number from 1332 to 1339 cm^{-1} is due to the stress in the films. ν_1 and ν_3 correspond to vibrations from trans-polyacetylene groups present at the grain boundaries. G peak is the characteristic of graphite (sp^2 bonded carbon) and G^* corresponds to nanographite phase in the film surface.

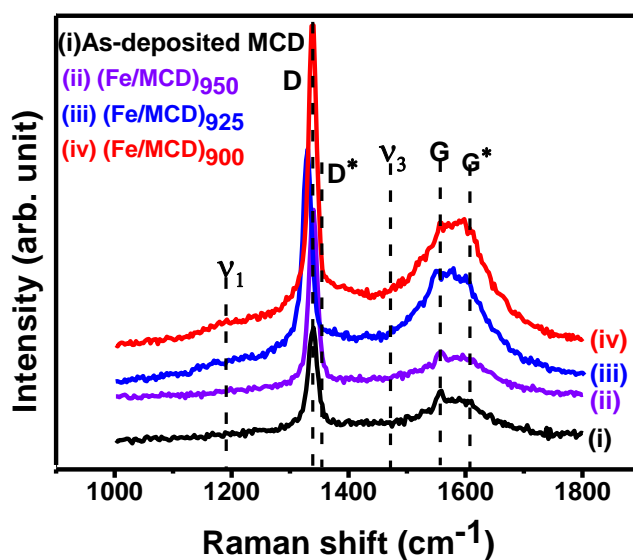


Fig. 5.4 Raman spectra of as-deposited (i), Fe-coated/post-annealed MCD films at (ii) 950 °C (iii) 925 °C and (iv) 900 °C.

Since the Raman signal is several times sensitive to the sp^2 -bonded carbon in comparison to the sp^3 -bonded carbons, the presence of sp^2 -related Raman resonance peaks does not imply the existence of a large proportion of sp^2 -bonded materials in these MCD films. D^* peak corresponds to disordered carbon. It is due to the presence of amorphous carbon at the grain boundaries in as-deposited MCD films. The D^* -peak intensity is higher in case of Fe coated/post-annealed MCD films, indicating that there is some amorphous carbon at

the Fe/diamond interface. Also the intensities of G and G* peaks are higher. The Raman spectra of 950 °C annealed sample is similar to as-prepared MCD film indicating that there is only a little amount of Fe left on the surface. Although the peak intensities of D, G and G* are higher in low temperature annealed Fe-coated/post-annealed films [reported in reference 11] but the related EFE properties are still not good. It seems that the D, G and G* phase fractions have little role in the EFE properties for the Fe-coated/post-annealed films. The formation of Fe₃C and nanographitic phases on the film surface for higher temperature annealed films (here at 900 °C) which have significant impact on the EFE properties, will be discussed by TEM and XPS shortly. These results imply that the surface layer of diamond films are transformed to more *sp*²-bonded graphite or amorphous carbon by Fe-coating/post-annealing processes, while the diamond material underneath has remained as such.

5.3.1.2 XPS Results

The XPS C-1s photoemission spectra of as-prepared MCD, (Fe/MCD)₉₀₀, (Fe/MCD)₉₂₅ and (Fe/MCD)₉₅₀ films are presented in figure 5.5(a), 5.5(b), 5.5(c) and 5.5(d) respectively. The background was subtracted using Shirley's method [16]. XPS measurements were carried out without Ar-ion sputtering to avoid reconfiguration of the surface bonding structures. The data were fitted with Lorentzian peaks with binding energies at 284.4, 285.0 and 286.1 eV corresponding to *sp*², *sp*³ and C-O (C-O-C) bonding of the C-1s spectra respectively [8]. The relative intensities of each peak obtained from the C 1s spectra are summarized in Table 5.2(a). In C-1s spectra of as-prepared MCD films, the *sp*² bonding is only 34.1%, while its concentration significantly increased to

52.4% after the Fe-coating/post-annealing process in $(\text{Fe}/\text{MCD})_{900}$ films. Further increase in annealing temperature degrades the sp^2 nature of the Fe-coated MCD films.

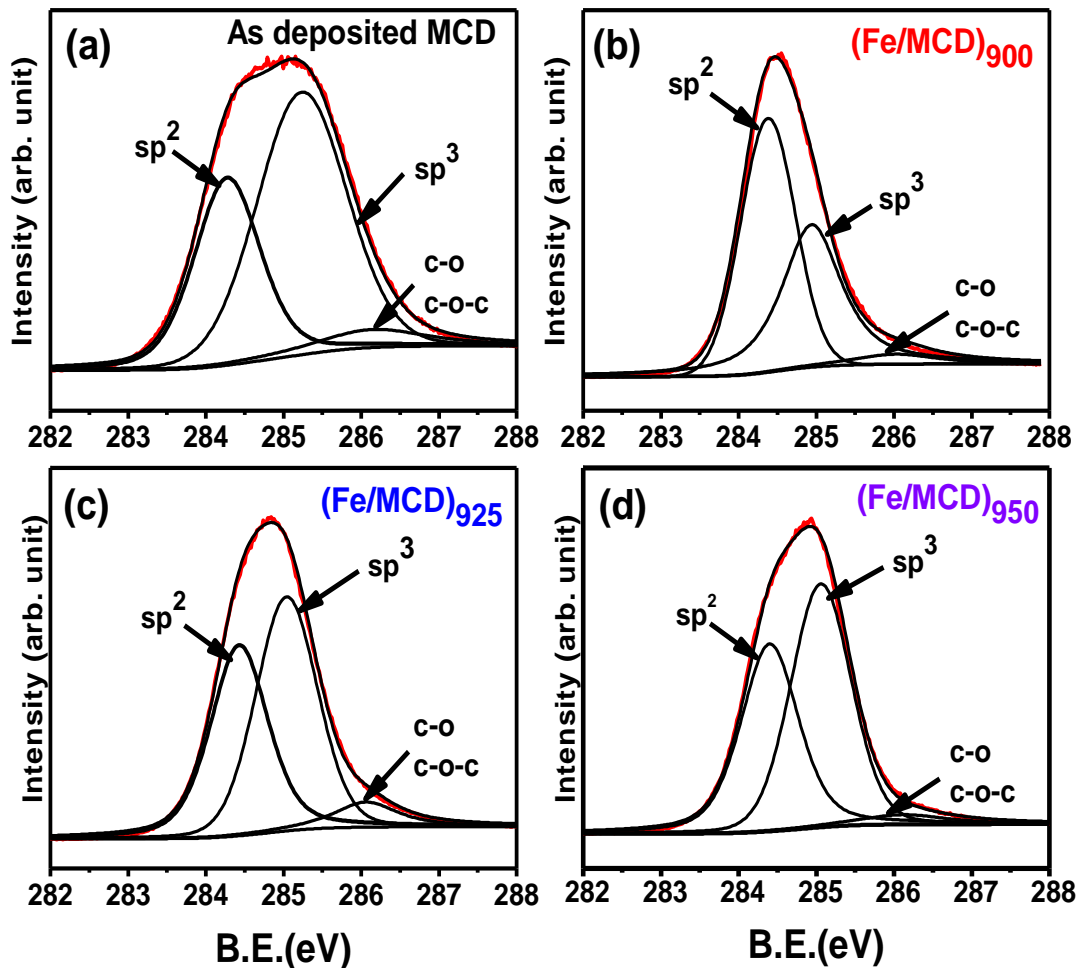


Fig. 5.5 XPS C-1s spectra of (a) as-deposited MCD films. (b), (c), and (d) are for Fe-coated/post-annealed MCD films, annealed at temperatures of 900 °C, 925 °C and 950 °C respectively.

In contrast, the sp^3 phase was 60% in as-prepared films, compared to only 43.3% in $(\text{Fe}/\text{MCD})_{900}$ films. Small amount of C-O (C–O–C) peaks are seen in as-prepared and Fe-coated/post-annealed films at a binding energy of 286.1 eV, which disappears as soon as the surface is Ar^+ ion sputtered for one minute in the XPS chamber.

Table 5.2 Relative intensities of various components of (a) C-1s XPS spectra and (b) Fe $2p_{3/2}$ spectra from as-prepared, (Fe/MCD)₉₀₀, (Fe/MCD)₉₂₅ and (Fe/MCD)₉₅₀ films.

Peak position (eV)	Chemical Bonding	Peak intensity (%)			
		as-prepared MCD	(Fe/MCD) ₉₀₀	(Fe/MCD) ₉₂₅	(Fe/MCD) ₉₅₀
(a) 284.4	sp^2	34.1	52.4	42.5	40.7
285.0	sp^3	60	43.3	50.2	54.1
286.1	C-O (or C-O-C)	5.9	4.3	7.3	5.2
(b) 707.0	Fe ⁰	-	33.4	31.1	27.6
708.1	Fe ₃ C	-	36.2	32.2	18.6
710.9	Fe ₂ O ₃	-	30.4	36.7	53.8

Figure 5.6 shows Fe $2p$ XPS spectra of post-annealed Fe/MCD films. Strip marked areas represent the Fe- $2p_{3/2}$ and $2p_{1/2}$ spectra. The data were fitted with Lorentzian peaks with binding energies at 707.0, 708 and 710.9 eV, corresponding to the Fe⁰, Fe₃C and Fe₂O₃ phases respectively, of the Fe- $2p_{3/2}$ peak [17, 18]. The relative intensities of each peak obtained from the Fe- $2p_{3/2}$ spectra are summarized in Table 5.2(b). As shown in Fig. 5.6 and Table 5.2(b), the peak intensities of Fe⁰ & Fe₃C phases are 33.4% and 36.2% for (Fe/MCD)₉₀₀ films (Fig. 5.6(a)), 31.1% and 32.2% for (Fe/MCD)₉₂₅ (Fig. 5.6(b)) and 27.6% and 18.6% for (Fe/MCD)₉₅₀ (Fig. 5.6(c)) films respectively. The concentrations of Fe and Fe₃C phases are more in (Fe/MCD)₉₀₀ films as compared to (Fe/MCD)₉₂₅ and (Fe/MCD)₉₅₀ films, which are annealed at higher temperatures. Further increase in annealing temperature, decreases the amount of Fe (or Fe₃C) phases and increases the

Fe_2O_3 phase on the surface of diamond films and this is found to degrade the EFE properties [11].

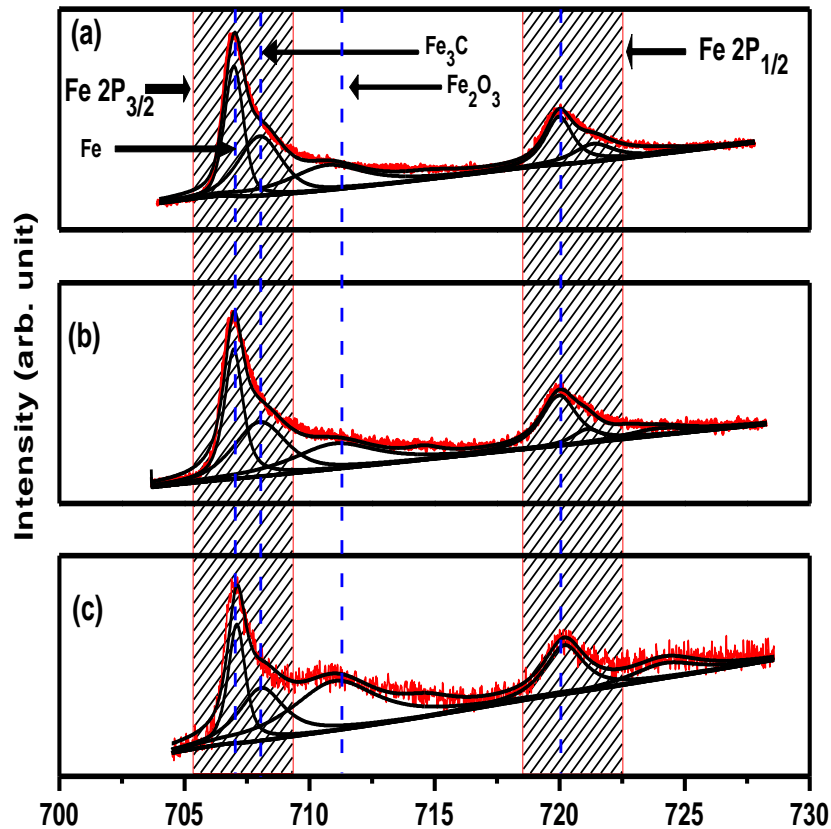


Fig. 5.6 XPS spectra for Fe-2p spectra of Fe coated/post annealed MCD films at different temperatures of (a) 900 °C (b) 925 °C (c) 950 °C respectively.

One possible reason for the presence of Fe_2O_3 phase is the oxidation of Fe-particles, which had occurred instantaneously when the Fe-coated MCD films were taken from the sputtering chamber to the annealing furnace. The increase in concentration of sp^2 and Fe (Fe_3C) phases are the factors responsible for the enhancement in EFE properties for these $(\text{Fe}/\text{MCD})_{900}$ films [8].

5.3.1.3 Transmission Electron Microscopy Results

To understand the nature of nano-sized particles present on the surface of (Fe/MCD)₉₀₀ film, the detailed microstructure of the film was examined by TEM. It should be noted that, in the preparation of thin foil for TEM examination, the (Fe/MCD)₉₀₀ samples were ion-milled from the Si-side such that thin foil contains mainly the layer near the surface of the sample. Figure 5.7(a) shows a typical TEM micrograph of the (Fe/MCD)₉₀₀ film.

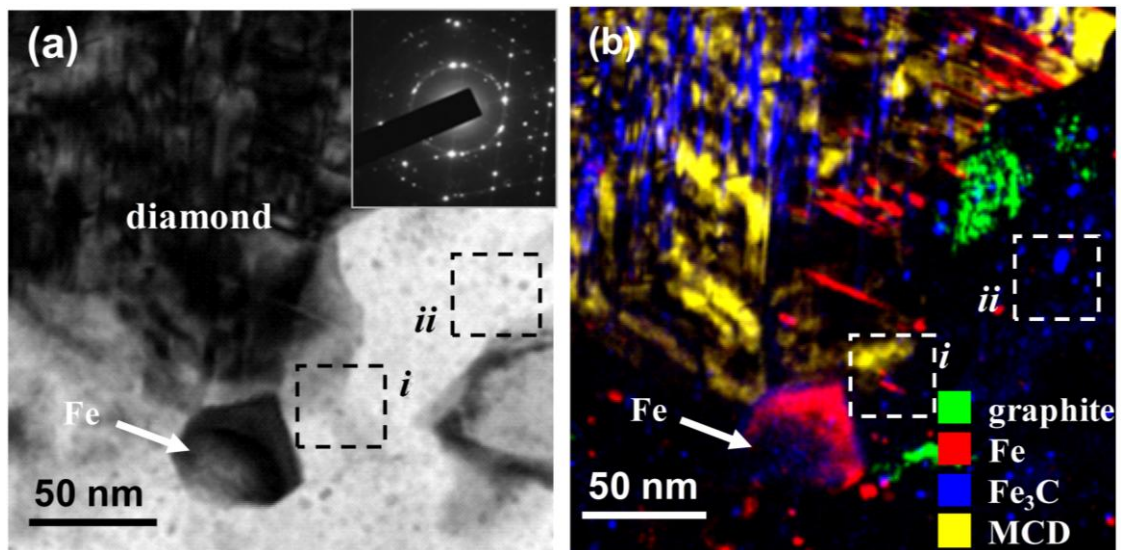


Fig. 5.7 The (a) bright field (BF) and (b) dark field (DF) images of a typical region in (Fe/MCD)₉₀₀ film. Inset shows the SAED pattern for the whole area.

Besides the large diamond grains, there are numerous ultra-small clusters (~5 to 10 nm), that are evenly distributed over the (Fe/MCD)₉₀₀ film surface, which are also seen in SEM image shown in figure 5.2. Selected area electron diffraction (SAED) shown in inset of this figure indicates that the ultra-small clusters are randomly oriented Fe₃C clusters. There are rare, residual large Fe-particles distributed on the film surfaces. One of the Fe-

particles is indicated by arrow in figure 5.7(a). Dark-field images were taken from a different part of SAED, *i.e.*, from the diffraction spots corresponding to graphite, Fe, Fe₃C and diamond separately and the images were then superimposed to clearly illustrate the distribution of the phase constituents. Figure 5.7(b) shows the distribution of the nano-graphite (green color), Fe-particles (red color) and Fe₃C-clusters (blue color) contained in these films. The enlarged micrographs shown in Figures 5.8(a) and 5.8(b) reveal, respectively, the detailed microstructures of the region near the large diamond particle (area “*i*”, Fig. 5.7(a)) and the small cluster region (area “*ii*”, Fig. 5.7(a)) for the (Fe/MCD)₉₀₀ film. Figure 5.8(a) shows that the area 1 is diamond, as indicated by Fourier-transformed diffractogram (FT₁).

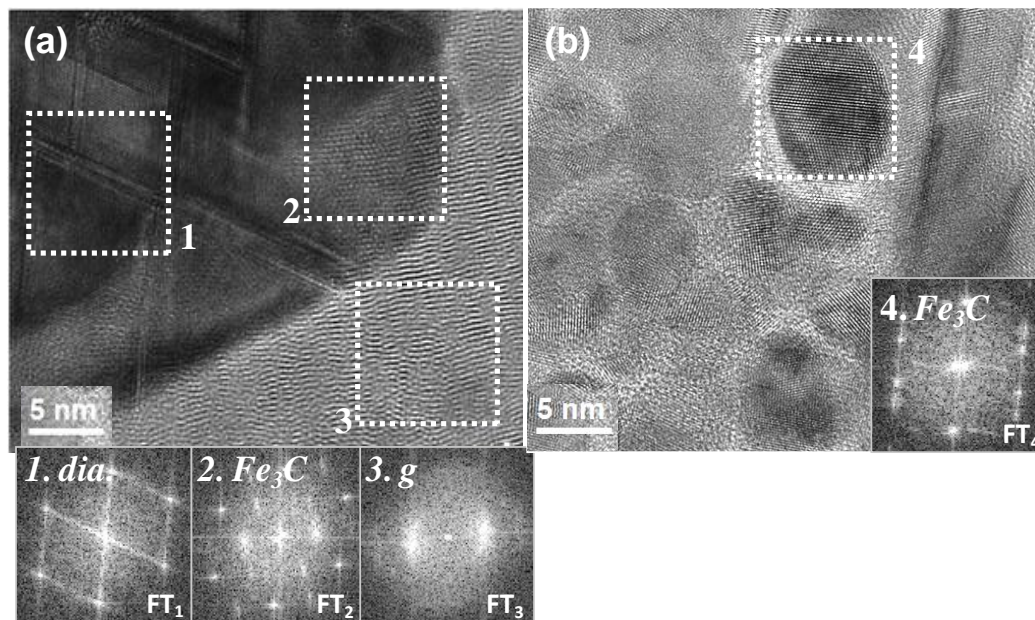


Fig. 5.8 The HRTEM micrographs corresponding to the (a) region “*i*” and (b) region “*ii*” in Fig. 5.7(a), showing the presence of Fe₃C particles and the associated graphitic layer. The insets show the Fourier-transformed diffractogram of the designated areas.

In the region nearby the diamond grains, there exists an interaction zone about 5 to 10 nm in thickness. The FT image (FT₂) shown in figure 5.8(a) indicates that the interaction zone is of Fe₃C phase. Interestingly, there appears a graphitic phase about tens of nanometer in thickness outside the Fe₃C layer, which is indicated by the FT image FT₃. In contrast, figure 5.8(b) indicates that the small clusters contained in the region “*ii*” of figure 5.7(a) are mainly the smaller Fe₃C particles, which is highlighted by the area 4 and the FT image FT₄. There seems to be a thin layer of graphitic phase surrounding the small Fe₃C particles.

The presence of the nanographitic phase enhances the transport of electrons that facilitates the field emission process, which is similar to the EFE properties of graphene composite [19, 20]. The remaining unsolved question is how the nanographite is formed by the Fe-coating/post-annealing process. It has to be noted that the formation mechanism of carbon nanotubes (CNTs) has been proposed as follows: the carbon species is first dissolved into a catalyst and re-precipitated out, resulting in either a top-growth or bottom-growth process for CNTs [21-24]. The same dissolution and re-precipitation processes also occur for the nano-sized Fe-clusters formed on the diamond surface. Presumably, the Fe-clusters catalytically dissociated the diamond, transported the carbon species through the Fe-clusters, and reprecipitated them out at the other side of the clusters, resulting in nano-graphite on the surface of these Fe-clusters. The Fe₃C nano-clusters resulted, when the Fe clusters containing some dissolved carbons are quickly cooled below the re-precipitation temperature.

5.3.1.4 Scanning tunneling spectroscopy

For the purpose of understanding how the change in concentrations of sp^2 , sp^3 , Fe (or Fe_3C) phases affect the EFE properties of these films, the local electronic properties of the films were investigated by STS. Only the STS measurements of the as-prepared and $(Fe/MCD)_{900}$ films are illustrated here. Figure 5.9(a) shows the image of as-prepared MCD film and its corresponding CITS image is shown in figure 5.9(b). Bright contrast in the CITS image shows better electron emission [8]. The CITS image of as prepared MCD film (Fig. 5.9(b)) shows that the emission is mostly from the facets of the micron-sized diamond grains. One such typical MCD grain and grain boundary is marked as "1" and "2" respectively in figure 5.9(a) and the corresponding CITS image, taken at a bias of -3.5 V to the sample, is shown in figure 5.9(b), revealing the dark and bright contrast corresponding to the grain (point "1") and the grain boundary (point "2"), respectively. Thus, in as-prepared MCD films, only the facets of the diamond grains emit electrons. In contrast, figure 5.9(c) shows the STM surface morphology of $(Fe/MCD)_{900}$ film and its corresponding CITS image, taken at the same bias of -3.5 V, is shown in figure 5.9(d). The CITS image in figure 5.9(d) clearly illustrates that, in comparison to the as-prepared MCD films, the emission sites are significantly more in $(Fe/MCD)_{900}$ film surface. Typical diamond grain and grain boundary are marked as "3" and "4" respectively in figure 5.9(c) and its corresponding CITS image (Fig. 5.9(d)). The emission is seen from throughout the diamond grains in $(Fe/MCD)_{900}$ films rather than only from the facets of the diamond grains in the case of as-prepared MCD films.

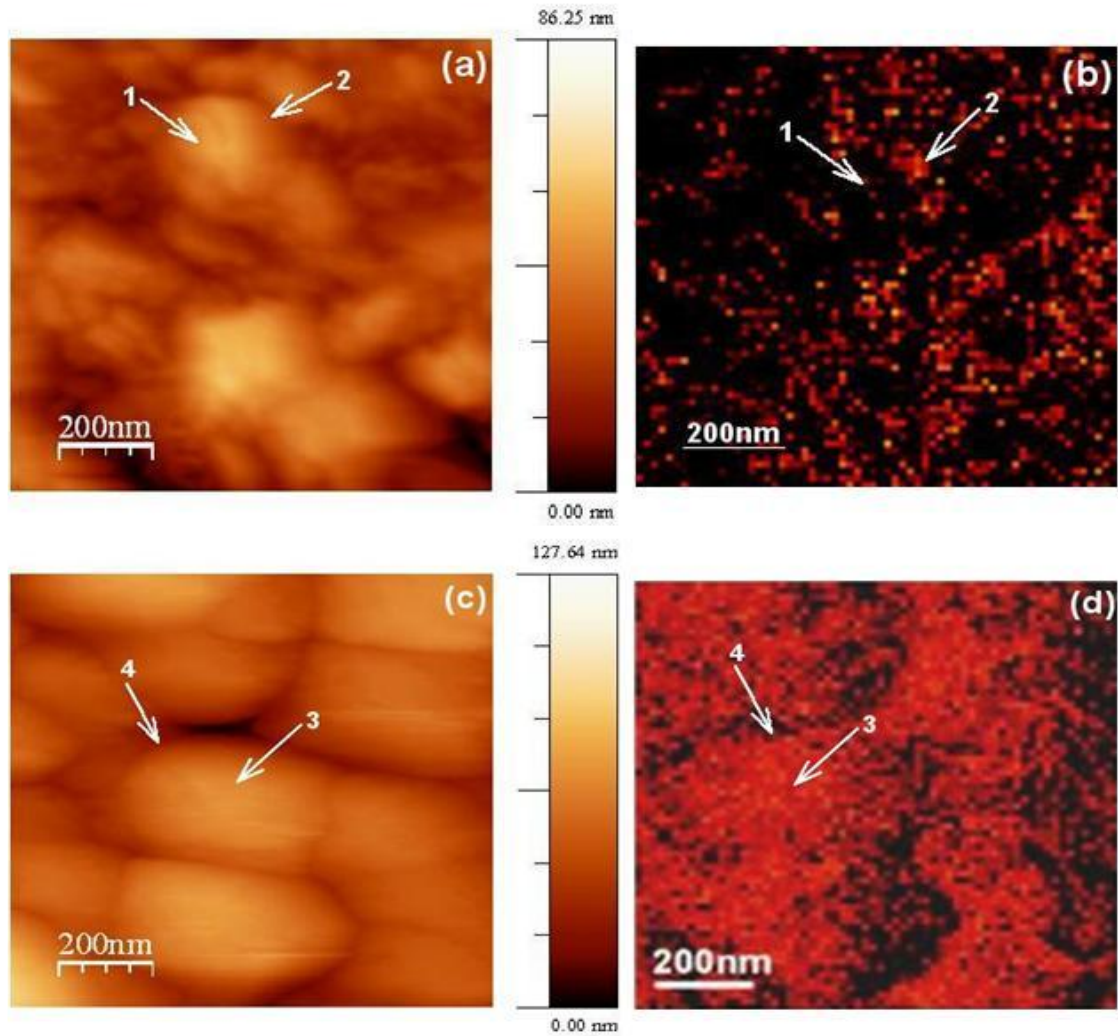


Fig. 5.9 (a) UHV STM image of as-deposited MCD films with the corresponding CITS image in (b). (c) Fe coated/post-annealed (900 °C) MCD film with corresponding CITS image in (d). The CITS images are taken in STS mode at a sample bias of -3.5 V. Increased emission sites after the Fe coating and annealing process is clearly seen in CITS image (d) compared to (b).

To know more precisely how the Fe-coating/post-annealing process enhances the number density of emission sites, the high resolution STM (HRSTM) image and the corresponding CITS image are taken which are shown in figure 5.10(a) and figure 5.10(b) respectively.

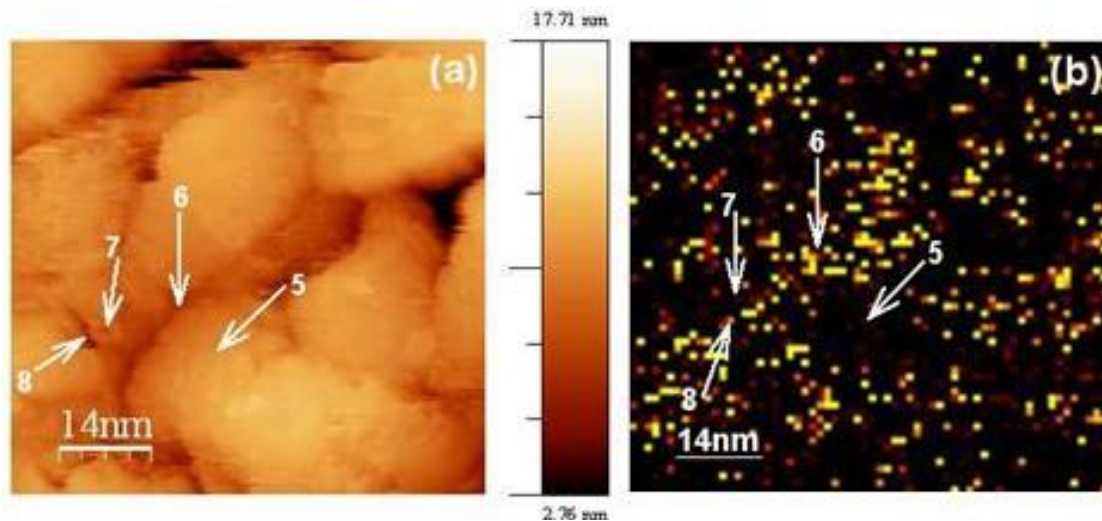


Fig. 5.10 (a) HRSTM image of Fe-coated/post-annealed (900 °C) MCD film (b) corresponding CITS image taken in STS mode at a sample bias of -3.5 V.

CITS image is taken at the same sample bias of -3.5 V. Again, bright contrast in CITS image indicates better electron emission. HRSTM image shown in figure 5.10(a) reveals that the large diamond grains (shown in Fig. 5.9(c)) are actually composed of many nanometer sized particles of varying diameter from 5 to 20 nm. One typical bigger-sized particle (~ 20 nm, marked as "5"), with its boundary marked as "6", is shown in figure 5.10(a). However, still smaller-sized particles of average size ~5 nm could also be seen. Such a grain is marked as "7" and its boundary is marked as "8". Interestingly, the emission sites are seen from the boundaries of these bigger-sized (~ 20 nm) and smaller-sized (~ 5 nm) particles, as the corresponding CITS image (Fig. 5.10(b)) shows bright emission in the boundaries of these different sized nanoparticles (points "6" and "8"). Hence it can be concluded that in case of $(\text{Fe}/\text{MCD})_{900}$ films, the micron-sized diamond grain consists of many nanoparticles of average grain size 5 to 20 nm. The boundaries of these nanoparticles emit and make interconnected path throughout the film surface due to

their high densities. The concentration of these nanoparticles are so much high in (Fe/MCD)₉₀₀ films that it seems as if the whole micron-sized diamond grains emit in lower magnification scale (Fig. 5.9(d)).

For the characterization of the local electronic properties of (Fe/MCD)₉₀₀ films, local current-voltage (I-V) curves are taken in STS mode from various sample positions. The tunneling current under positive bias is less than that under negative bias, implying that the films have *n*-type conductivity. Only the negative portion of the I-V curves are shown in figure 5.11(a) as the negatively biased current corresponds to the tunneling of electrons from the diamond surface to the tungsten tip and is proportional to the density of occupied states of the diamond. Three reproducible I-V spectra were recorded during the scanning of the STM image. Conductivity at the boundaries surrounding the smaller-sized nano-particles (marked as '8' in Fig. 5.10(a)) and the bigger-sized nano-particles (marked as "6" in Fig. 5.10(a)) show ohmic behavior (shown as curves "i" in Fig. 5.11(a)). Significant enhancement in conductivity has been observed (15 nA at -0.5 V) at these marked points. The smaller-sized nanoparticles (marked as '7' in Fig. 5.10(a)) also show high conductivity as shown in curves "ii" in Fig. 5.11(a) but it requires nearly about 1.0 V to attain the same 15 nA tunneling current. These smaller particles could be the graphitic encapsulated Fe₃C particles, as shown in TEM observation. Some bigger-sized nanoparticles marked as '5' in the HRSTM image, figure 5.10(a) also show tunneling current (curves "iii", Fig. 5.11(a)) but requires slightly more sample bias (-1.8 V) to attain the same (15 nA) tunneling current. The local I-V characteristic curves at the facets of the as-prepared MCD grains (*e.g.* from area '2' in Fig. 5.9(a)) also show high conductivity as in the curves "i" shown in figure 5.11(a). It is to be noted here that for diamond grains in as

prepared MCD films (*e.g.* ‘1’ in Fig. 5.9(a)), it requires still higher bias voltage of -4.0 V to get the same value of (15 nA) tunneling current. The behavior of enhanced tunneling current from the boundaries of Fe, Fe₃C nanoparticles in Fe coated and post-annealed films also explains the superior EFE properties in (Fe/MCD)₉₀₀ films compared to as prepared MCD in a microscopic scale. The I-V characteristic curves of STS measurements shown in figure 5.11(a) are used to deduce the normalized derivative of multiple averaged spectra, the normalized conductance $dI/dV/(I/V)$. The normalized conductance spectra corresponding to the curves ‘i’, ‘ii’ and ‘iii’ in figure 5.11(a) which are plotted in figure 5.11(b), provides information about the distribution of the surface density of states (DOS) of the films [25, 26].

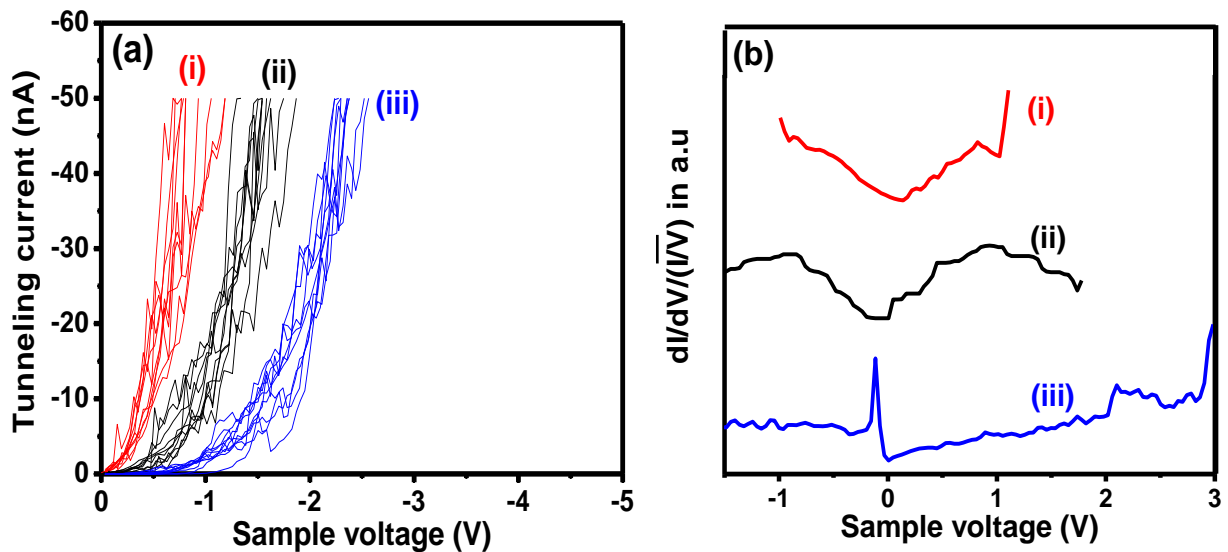


Fig. 5.11 (a) Tunnelling current vs. voltage (I-V) curves and (b) normalized differential conductance $(dI/dV)/(I/V)$ curves at various locations: (i) at boundaries of nano-particles, marked as ‘6’ and ‘8’ in Fig. (5.10a), (ii) on the smaller-sized (~5 nm) Fe₃C nanoparticles, marked as ‘7’ in Fig. 5.10(a), and (iii) on the bigger-sized (20-25 nm) oxidized Fe nanoparticle, marked as ‘5’ in Fig. 5.10(a).

From the normalized conductance curve “*i*” in figure 5.11(b), nearly zero band gap (metallic type) is measured for the boundaries, which are marked as point ‘6’ and ‘8’ in the HRSTM image (Fig. 5.8(a)). The nanographitic phase surrounding the Fe (bigger particles) or Fe₃C (smaller particles) nanoparticles (Fig. 5.8(a,b)), shows this metallic behavior. Band gap calculation on the smaller-sized (2 to 5 nm) particle also shows nearly metallic behavior (band gap 0.2 eV, curve “*ii*”, Fig. 5.11(b)). It may be the graphitic layer encasing the smaller-sized Fe₃C nanoparticles. The smaller sized Fe₃C particles were formed by the reaction of Fe with diamond at high temperature of 900 °C, as evident from TEM observations. However, band gap calculation on the bigger-sized nanoparticle shows a gap value of 1.98 eV, as shown in the curve “*iii*” of figure 5.11(b). The large band gap in Fe particle may be due to the presence of thin oxide layer enveloping the Fe particle as a Fe₂O₃ phase, as evident from the XPS results shown in figure 5.6. Restated, the nanographitic phase present at the boundary of these Fe (or Fe₃C) nanoparticles seems to be the main conducting channel for electrons in addition to the facets. The formation of nanographitic phase can improve the EFE properties of diamond films which has already been discussed in previous studies [27, 28], where the heavy-ion irradiation significantly enhances the EFE behavior of diamond films via the induction of the nanographitic phase.

5.4 PART-2 Electron Field Emission Properties of Fe-coated/post-annealed ultrananocrystalline diamond (UNCD) films

5.4.1 Results

5.4.1.1 General characteristics

The FESEM images of the Fe-coated/post-annealed UNCD films are shown in figure 5.12. Figure 5.12(a) shows the image of as-deposited UNCD films. The surface morphology of as-deposited UNCD films was modified significantly due to the Fe coating/post-annealing processes. While the as-deposited UNCD films contain small diamond grains, the Fe coated/post-annealed films have 5~10 nm particles (showing bright contrast) lying on the surface of UNCD (Figs. 5.12(b) to 5.12 (d)).

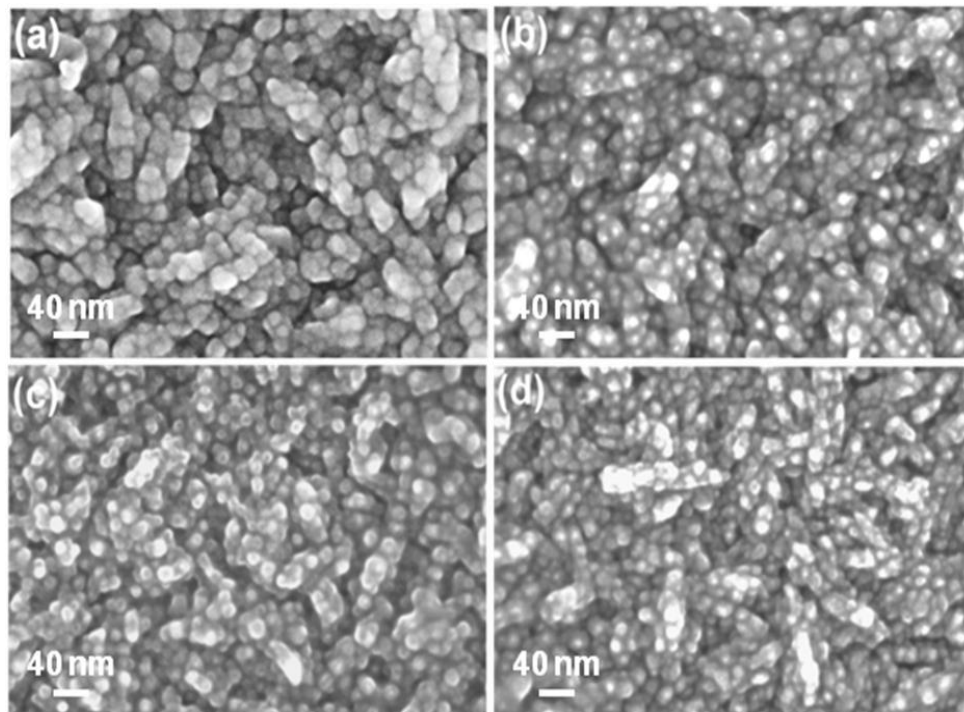


Fig. 5.12 FESEM image of (a) as-deposited (b) 900 °C (c) 925 °C (d) 950 °C Fe-coated/post-annealed UNCD films. Presence of Fe nanoparticles is clearly seen as white contrast on the surface of UNCD films.

These small nanoparticles could be the Fe or Fe₃C nanoparticles formed by the reaction of Fe with diamond when annealed at high temperature [29]. From the FESEM micrograph and XPS analysis (discussed shortly) it is seen that the concentration of these roundish type nanoparticles are more in (Fe/UNCD)₉₀₀ films than (Fe/UNCD)₉₂₅ and (Fe/UNCD)₉₅₀ films. However, films annealed beyond 900 °C, shows less concentration in Fe (Fe₃C) nanoparticles and seen to merge with each other forming dendritic like structures (Fig. 5.12(c) and Fig. 5.12(d)).

The occurrence of the new phase like Fe₃C is also evident from the GIXRD pattern of the (Fe/UNCD)₉₀₀ film, shown in figure 5.13.

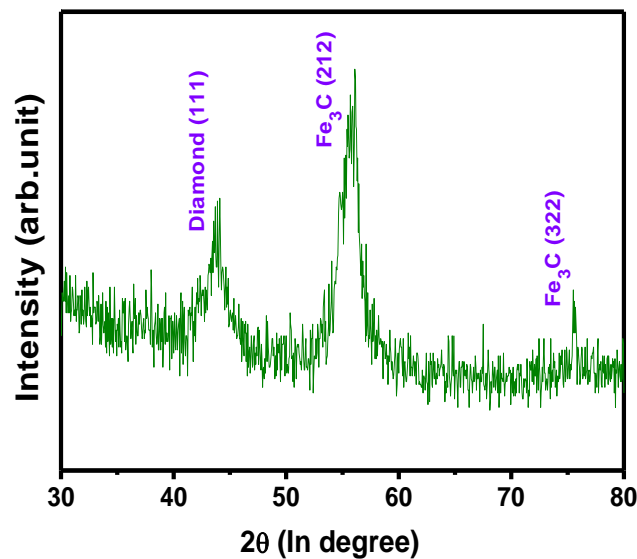


Fig. 5.13 GIXRD pattern of Fe-coated/post-annealed (900 °C) UNCD film showing the presence of Fe₃C phase on the surface.

It shows three strongest peaks at 43.99°, 55.99° and 75.48°, corresponding to the diamond (111), Fe₃C (212) and Fe₃C (322) phases, respectively [14-15]. EFE properties of as-deposited and Fe-coated/post-annealed UNCD films are shown in Figure 5.14 with the

inset indicating the corresponding F-N plots. From the current density vs electric field (J- E) curves, it is clearly evident that the EFE properties of as-deposited films are significantly enhanced due to the Fe-coating/post-annealing processes (Figs. 5.14 (ii) to (iv)), as compared to as-deposited UNCD films (Fig. 5.14 (i)). The EFE properties are better in case of (Fe/UNCD)₉₀₀ (Fig. 5.14 (iv)) films as compared to (Fe/MCD)₉₂₅ (Fig. 5.14 (iii)) and (Fe/MCD)₉₅₀ (Fig. 5.14 (ii)) films. The turn-on field (E_0) decreased from 4.95 V/ μm (in case of as-deposited UNCD films) to 1.98 V/ μm for (Fe/UNCD)₉₀₀ films.

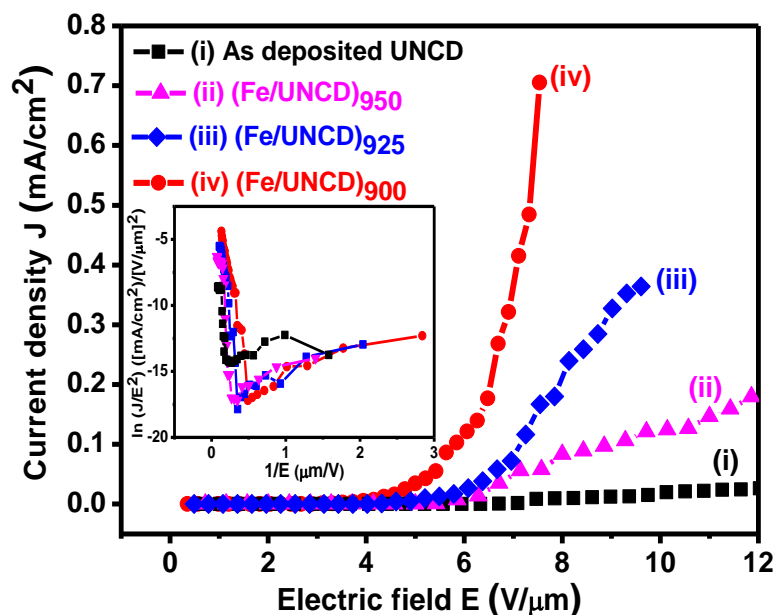


Fig. 5.14 EFE properties of (i) as- deposited UNCD films and (ii) 950 °C (iii) 925 °C (iv) 900 °C Fe-coated/post-annealed UNCD films. Inset shows the F-N plots derived from the corresponding J-E curves.

The E_0 -values are 2.77 and 3.47 V/ μm for (Fe/UNCD)₉₂₅ and (Fe/UNCD)₉₅₀ films, respectively. A current density (J_e) of 705 $\mu\text{A}/\text{cm}^2$ at an electric field of 7.5 V/ μm is measured for (Fe/UNCD)₉₀₀ films, while these values decreased to 167 and 57 $\mu\text{A}/\text{cm}^2$ when annealing temperature increased from 900 °C to 925 °C and 950 °C, respectively, at

the same electric field. The J_e value for as-deposited UNCD films is only $9 \mu\text{A}/\text{cm}^2$ at $7.5 \text{ V}/\mu\text{m}$. The turn-on field for $(\text{Fe}/\text{UNCD})_{900}$ films is even better and the current density is comparable to those of as-prepared CNTs [30, 31]. Notably, the EFE properties of the Fe-coated/post-annealed UNCD films are better than our Fe-coated/post-annealed MCD films, discussed in section 5.3 of this chapter. The better EFE properties of Fe-coated/post-annealed UNCD films than that of the MCD films may be due to the special microstructure of UNCD films which provides sufficient number of grain boundary volume fraction than Fe-coated/post-annealed MCD films. The EFE properties of the Fe-coated/post-annealed UNCD films are summarized in Table 5.3.

Table 5.3 The EFE properties of the as-deposited and Fe-coated/post-annealed UNCD films.

Samples	Turn-on field (E_0 in $\text{V}/\mu\text{m}$)	Current density (J_e in $\mu\text{A}/\text{cm}^2$) at $7.5 \text{ V}/\mu\text{m}$
As prepared UNCD film	4.95	9
$(\text{Fe}/\text{UNCD})_{900}$	1.98	705
$(\text{Fe}/\text{UNCD})_{925}$	2.77	167
$(\text{Fe}/\text{UNCD})_{950}$	3.47	57

The bonding structures of the UNCD films after the Fe-coating/post-annealing processes were revealed by Raman and XPS measurements. The Raman spectra of as-grown and Fe-coated/post-annealed UNCD films are shown in Figure 5.15.

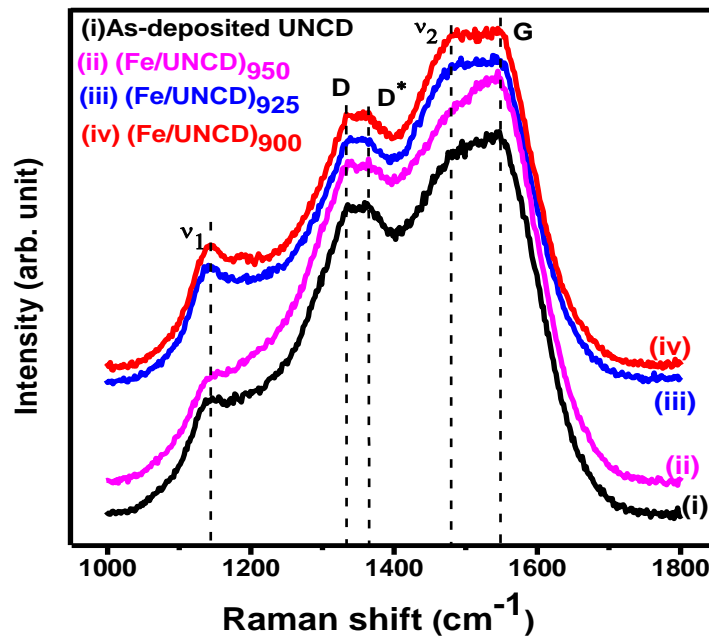


Fig. 5.15 Raman spectra of as-deposited (i) and Fe-coated/post-annealed UNCD films at (ii) 950 °C (iii) 925 °C and (iv) 900 °C respectively.

The Fe-coating/post-annealing processes insignificantly change the Raman spectra of UNCD films. The Raman spectra shows peak positions at 1143, 1333, 1364, 1481 and 1549 cm^{-1} which are marked as ν_1 , D, D^* , ν_2 and G, respectively. All the films contain broad ν_1 , ν_2 , D^* and G Raman resonance peaks, which is due to the small grain size of the films [32]. The D band is the characteristic resonance peak of diamond, whereas the D^* is the defect peak and G peaks are the characteristics of graphitic phases [33].

5.4.1.2 XPS Results

Figures 5.16(a), 5.16(b), 5.16(c) and 5.16(d) shows the XPS C-1s spectra of as-deposited, (Fe/UNCD)₉₀₀, (Fe/UNCD)₉₂₅ and (Fe/UNCD)₉₅₀ films, respectively. XPS measurements were done without Ar^+ ion sputtering to avoid reconfiguration of the surface bonding structures.

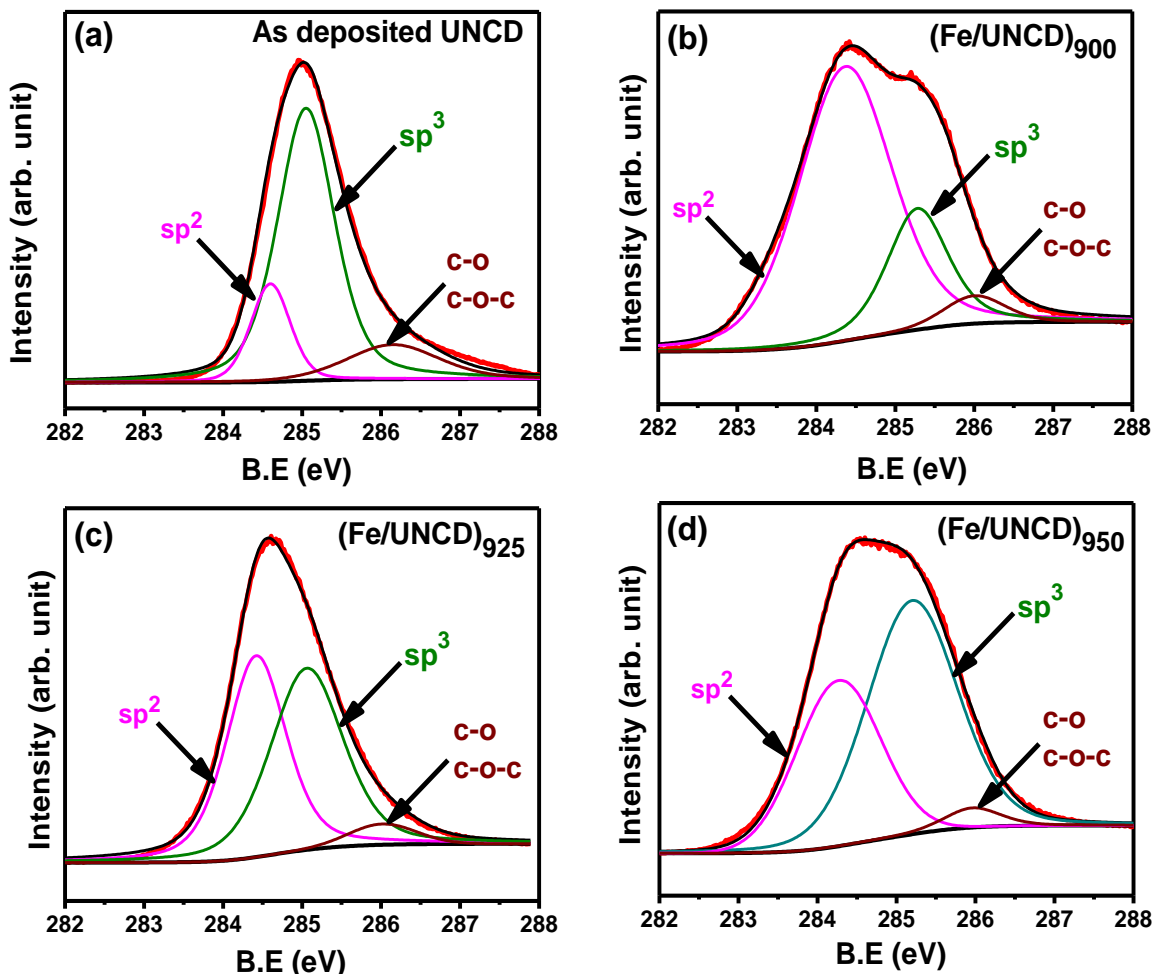


Fig. 5.16 The XPS C-1s spectra of (a) as-deposited UNCD films and (b) 900 °C (c) 925 °C and (d) 950 °C Fe-coated/post-annealed UNCD films. The enhanced sp^2 phase is clearly seen in Fe-coated UNCD film annealed at 900 °C.

The background was subtracted using Shirley's method [16]. The data were fitted with Lorentzian peaks with binding energies at 284.4, 285 and 286.1 eV corresponding to sp^2 , sp^3 and C-O(C-O-C) bonding of the C-1s spectra, respectively [8]. Table 5.4 (a) depicts the relative intensities of each element from the C-1s spectra. The XPS C-1s spectra shows the sp^2 phase fraction was only 18.5% in as-deposited UNCD films, which

significantly increased to 71.6% after the Fe-coating/post-annealing process in (Fe/MCD)₉₀₀ films. Further increase in post-annealing temperature degrades the sp^2 phase fraction to 46.5% and 34.4% in (Fe/UNCD)₉₂₅ and (Fe/UNCD)₉₅₀ films as shown in figure 5.16(c) and figure 5.16 (d), respectively. Similarly, the sp^3 phase fraction is 68.6% in as-deposited UNCD films, while it decreased to 23.6% in (Fe/UNCD)₉₀₀ films. A little amount of C–O/C–O–C peaks were seen in as-deposited and Fe-coated/post-annealed UNCD films at binding energy of 286.1 eV, which disappeared as soon as the surface was sputtered with Ar⁺ ion for one minute in XPS chamber. The C–O/C–O–C peaks may be due to the presence of oxide layers on the Fe-coated UNCD films while taking to annealing setup. Fe-2*p* XPS spectra of (Fe/UNCD)₉₀₀ films are shown in Figure 5.17. Fe-2*p*_{3/2} and 2*p*_{1/2} spectra are shown by strip marked area. The data were fitted with Lorentzian peaks with binding energies at 707.1, 708.2 and 711.1 eV, corresponding to the Fe⁰, Fe₃C and Fe₂O₃ phases, of the Fe-2*p*_{3/2} peak respectively [34, 18].

Table 5.4 The C-1*s* and Fe 2*p* XPS peaks of the as-deposited and Fe-coated/post-annealed UNCD films.

	Peak position (eV)	Chemical Bonding	Peak intensity (%)			
			as-deposited UNCD	(Fe/UNCD) ₉₀₀	(Fe/UNCD) ₉₂₅	(Fe/UNCD) ₉₅₀
(a)	284.4	sp^2	18.5	71.6	46.5	34.4
	285.0	sp^3	68.6	23.6	49.4	59.8
	286.1	C-O (or C-O-C)	12.9	4.8	4.1	5.8
(b)	707.1	Fe ⁰	-	49.6	37.3	31.1
	708.2	Fe ₃ C	-	39.2	38.2	25.2
	711.1	Fe ₂ O ₃	-	11.2	24.5	43.7

The relative peak intensities obtained from the Fe-2*p*_{3/2} spectra are summarized in Table 5.4 (b). As shown in figure 5.17(a) and Table 5.4, the peak intensities of Fe⁰ and Fe₃C phases are 49.6% and 39.2% for (Fe/UNCD)₉₀₀ films, 37.3% & 38.2% for (Fe/UNCD)₉₂₅ (Fig. 5.17 (b))m, 31.1% and 25.2% for (Fe/UNCD)₉₅₀ (Fig. 5.17(c)) films respectively.

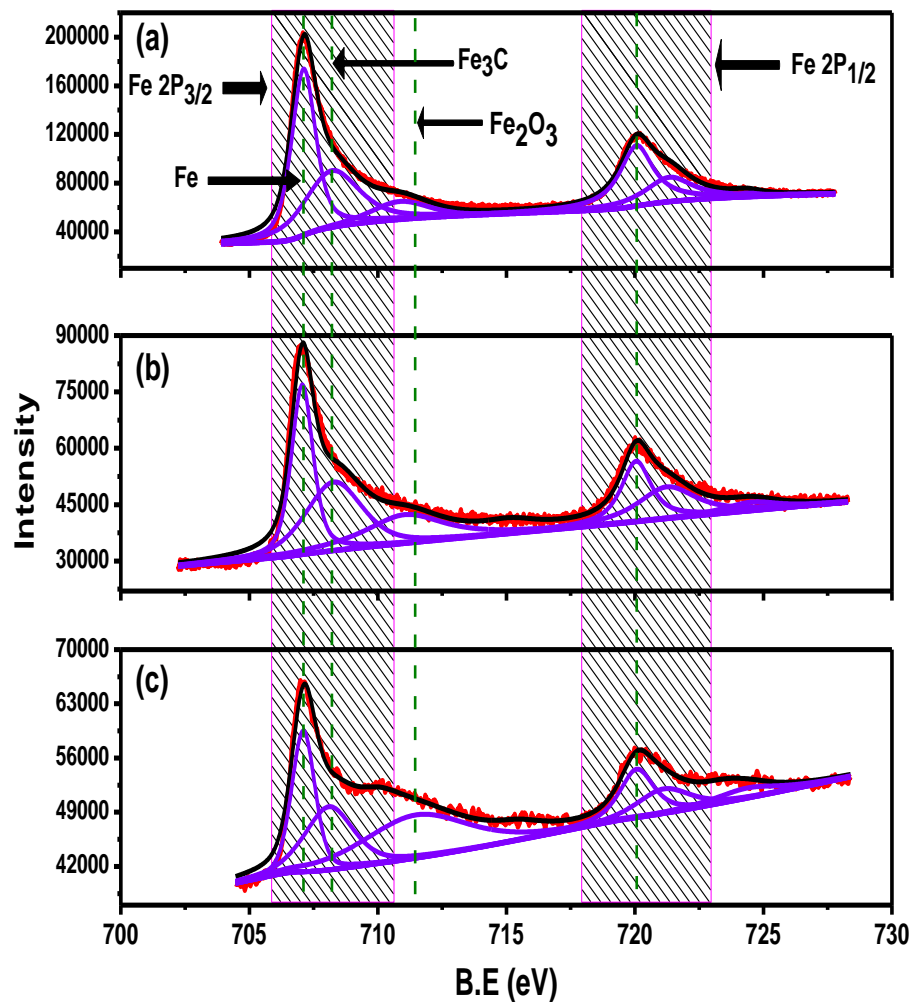


Fig. 5.17 Fe 2*p* XPS spectra of Fe-coated/post-annealed UNCD films, at (a) 900 °C (b) 925 °C (c) 950 °C.

The concentration of Fe and Fe₃C phases are more in (Fe/UNCD)₉₀₀ films compared to films annealed at higher temperatures in, (Fe/UNCD)₉₂₅ and (Fe/UNCD)₉₅₀ films. Increase in post-annealing temperature, further to 925 °C and 950 °C, lowers the Fe (or Fe₃C) phase and increases the Fe₂O₃ phase on the surface of UNCD films, which degrades the EFE properties. One possible reason for the presence of Fe₂O₃ phase on the Fe coated UNCD films is the oxidation of Fe-particles, which occurred instantaneously when the Fe-coated films were taken from the sputtering chamber to the annealing setup. The factors responsible for better EFE properties for these (Fe/UNCD)₉₀₀ films are the enhanced sp^2 and Fe (Fe₃C) phase contents. It should be noted that the XPS spectra represent mostly the surface characteristics of the films, which may not be necessarily the same as the phases contained in the films.

5.4.1.3 Transmission Electron Microscopy Results

To understand the microstructural evolution induced by the Fe-coating/post-annealing processes due to the Fe-to-diamond interaction, the microstructure of the (Fe/UNCD)₉₀₀ films, which exhibits the best EFE performance were examined using TEM. It should be noted that in the preparation of the samples for TEM investigation, the samples were ion-milled from the Si side such that the thin foil contains mainly the materials near the surface region of the UNCD films. Figure 5.18(a) shows the typical bright field image acquired under STEM mode in TEM for the (Fe/UNCD)₉₀₀ films. Inset in figure 5.18 (a) shows the SAED of the same region acquired in TEM mode. The diffraction spots are arranged in a smooth ring, implying that this region mainly contains randomly oriented ultra-small diamond grains.

By changing the camera length (CL) in the STEM, the electrons incoherently (but elastically) scattered by different species can be resolved, provided that the correlation between the scattering angle and the atomic number of the species inducing the incoherently scattering process was known. For the (Fe/UNCD)₉₀₀ films shown in figure 5.18 (a), only iron and carbon (diamond, graphite or amorphous carbon) species were involved. The contribution of the two species can be clearly resolved systematically by changing the CL in acquiring the HAADF signals. Figure 5.18 (b) illustrates a typical composed-HAADF image, which is superposition of three HAADF images acquired using different CL-values, CL₁=400 mm (yellow color), CL₂=127.3 mm (cyan color) and CL₃=93 mm (red color), that corresponds to diamond, Fe₃C and Fe phase, respectively. The Energy dispersive X-ray spectrum (EDS) in STEM mode corresponding to the yellow, pink and red regions designated as 1 to 6 in figure 5.18 (b) are plotted as profiles 1, to 6 in figure 5.19.

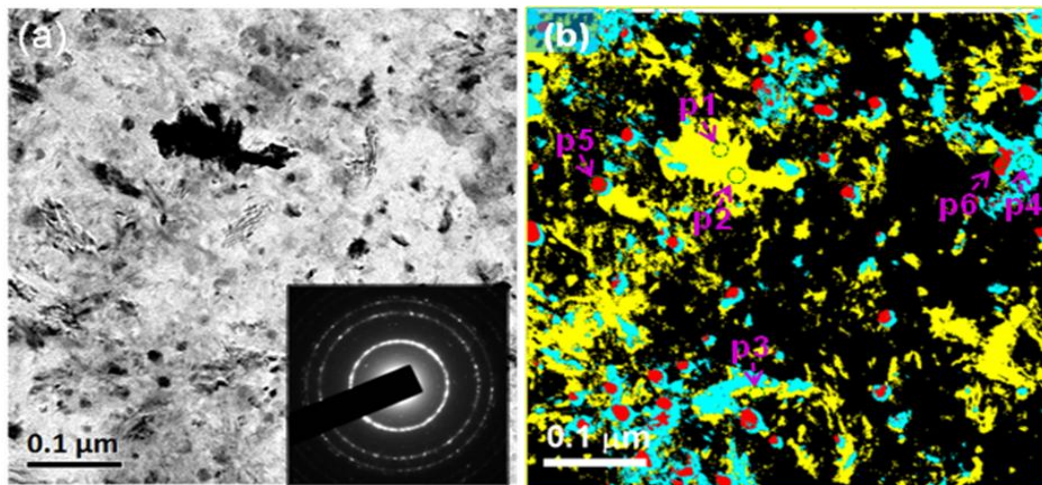


Fig. 5.18 The (a) STEM bright field, BF, and (b) high angle annular dark field, HAADF, images corresponding to BF image for the UNCD films, which were Fe-coated/post-annealed at 900 °C.

The EDS spectra clearly indicate that the profiles 1 and 2 corresponding to locations 1 and 2 contain mostly the carbon (diamond or graphite).

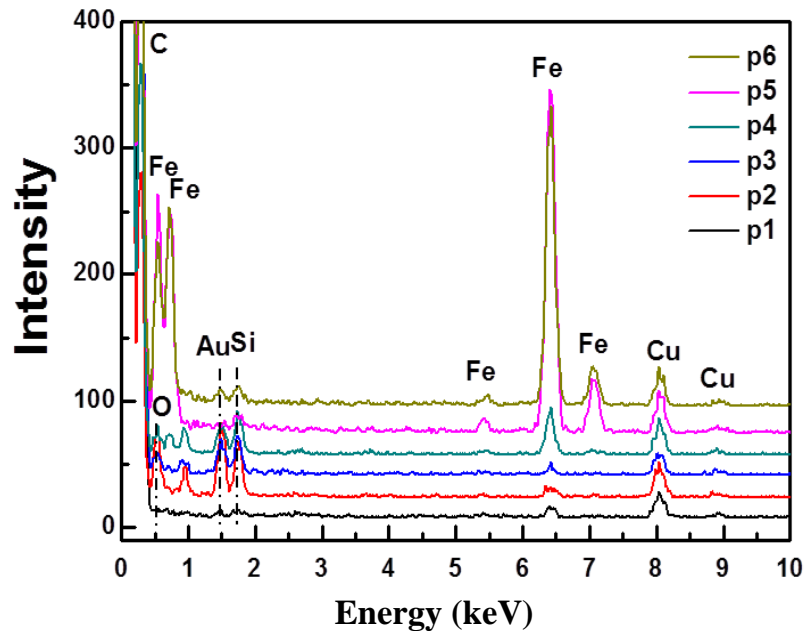


Fig. 5.19 The EDS (STEM) spectra for the UNCD films, which were Fe-coated/post-annealed at 900 °C. The spectra 1 to 6 correspond to the locations 1 to 6 designated in Fig. 5.18(b).

The EDS spectra 5 and 6 corresponding to location 5 and 6 contains large Fe-signals, indicating that the red-colored region, which corresponds to smallest CL-value ($CL_3=93$ mm), is mainly Fe-clusters. The small Cu, Au and Si signals are presumably the contaminations from the underlying substrates and the Cu-mesh induced in the ion-milling process. The EDS spectra 3 and 4 corresponding to locations 3 and 4 contains both Fe and C signals, implying this cyan-colored region might be the compound of Fe and C, most probably, the Fe_3C -clusters.

The high resolution TEM (HRTEM) images corresponding to the yellow and cyan designated in HAADF image are shown in figure 5.20(a) and 5.20 (b), respectively. Fourier-transformed diffractogram (FT_{0a}) corresponding to figure 5.20 (a) shows that the yellow region is diamond. The streaks along 111 direction shown in FT_{0a} indicate that the films contain large proportion of stacking faults. The stacking faults are highlighted by the parallel fringes with irregular spacing [35] (area 1 and FT_1 , Fig. 5.20 (a)). In contrast, figure 5.20 (b) and FT images (FT_{0b}) indicate that the cyan color region (Fig. 5.18(b)) contains Fe and Fe_3C clusters, besides the diamond grains. The existence of Fe clusters is highlighted by the FT image (FT_3) corresponding to area 3, whereas that for Fe_3C clusters is illustrated by FT_4 corresponding to area 4. These results confirm that the locations with yellow, cyan and red color in figure 5.18(b) are diamond, Fe_3C and Fe clusters, respectively. Moreover, structure image corresponding to regions 3 and 4 and the associated FT-image (FT_3 and FT_4) reveal that there are the graphitic phase located in adjacent to the diamond or Fe_3C clusters (indicated by arrow). These results indicate that the formation of graphite phase is closely related to the presence of Fe clusters. Presumably, the Fe clusters, which were formed by the coalescence of Fe-coating, catalytically dissociated the diamond at post-annealing temperature, dissolved the carbons and transported them to the other side of Fe clusters against the diamond, re-precipitated them out to form nano-graphite clusters. Such a process is similar with the formation mechanism of carbon nanotubes. In this case, the Fe clusters help for the growth of carbon nanotubes [21-24]. Presumably, the Fe_3C clusters were formed when the carbon species were frozen inside the Fe clusters during cooling stage of post-annealing process.

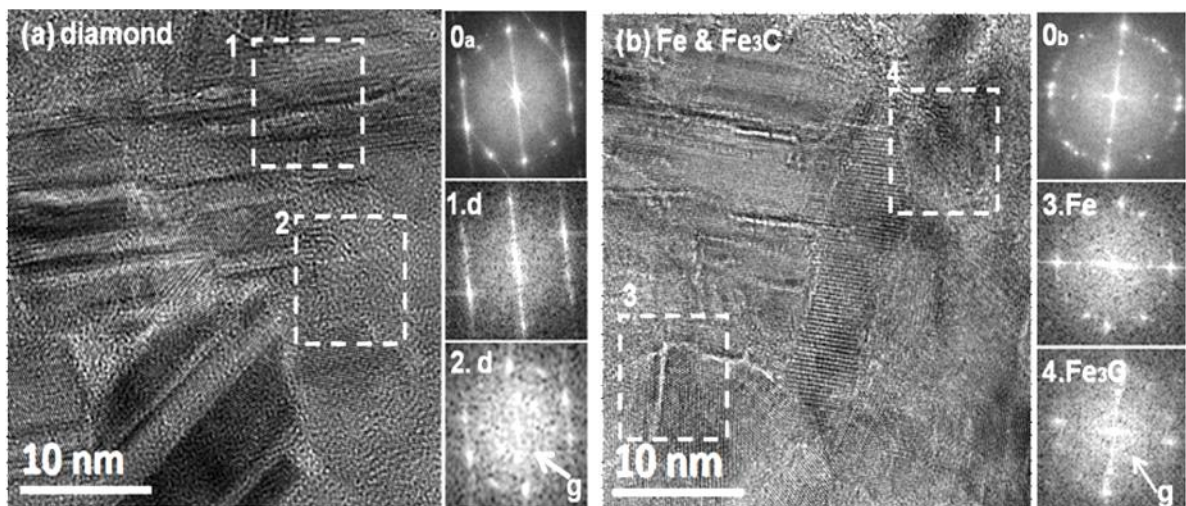


Fig. 5.20 The HRTEM images corresponding to (a) the yellow region and (b) the cyan region in the HAADF image (Fig. 5.18(b)) for the UNCD films, which are Fe-coated/post-annealed at 900 °C. Fourier transformed diffractogram [FT_{0a}] is marked as 0a, FT_{0b} as 0b and 1.d, 2.d represents diamond at marked location 1 and 2 respectively.

While the HRTEM microscopic investigation provides direct evidence that the nanographitic phase was induced by the Fe and diamond interaction, the more important microstructural information, such as the geometry and distribution of these phases, is still missing. The understanding of microstructural information necessary for understanding the authentic mechanism that enhances the EFE properties of the materials due to the Fe-coating/annealing processes, the HAADF imaging technique for identifying the distribution of species in (Fe/UNCD)₉₀₀ films is further investigated by utilizing the 3D-tomography in TEM. Figure 5.21(a) shows the stereographic projection of the 3D tomography for the Fe-coated/annealed UNCD films, whereas the figure 5.21(b) shows the X-Y projection of these images, revealing the distribution of the Fe (red color), Fe₃C (white color) and nanocarbon clusters (nanodiamond or nanographite, yellow color). These micrographs illustrate more clearly that the Fe and Fe₃C clusters are of spherical

geometry and are located on the surface of the UNCD films. The Fe and Fe₃C clusters, about tens of nanometers in size, are mixed together, implying that, while some of the Fe clusters interacted with diamond, forming Fe₃C, and some of them remained intact. These figures show that the nano-graphitic phase actually formed in adjacent to the Fe₃C (or Fe) clusters. These observations support the arguments that the graphitic phase was induced by the Fe and diamond interaction, forming a continuous network that facilitated the electron transport and enhanced the EFE properties.

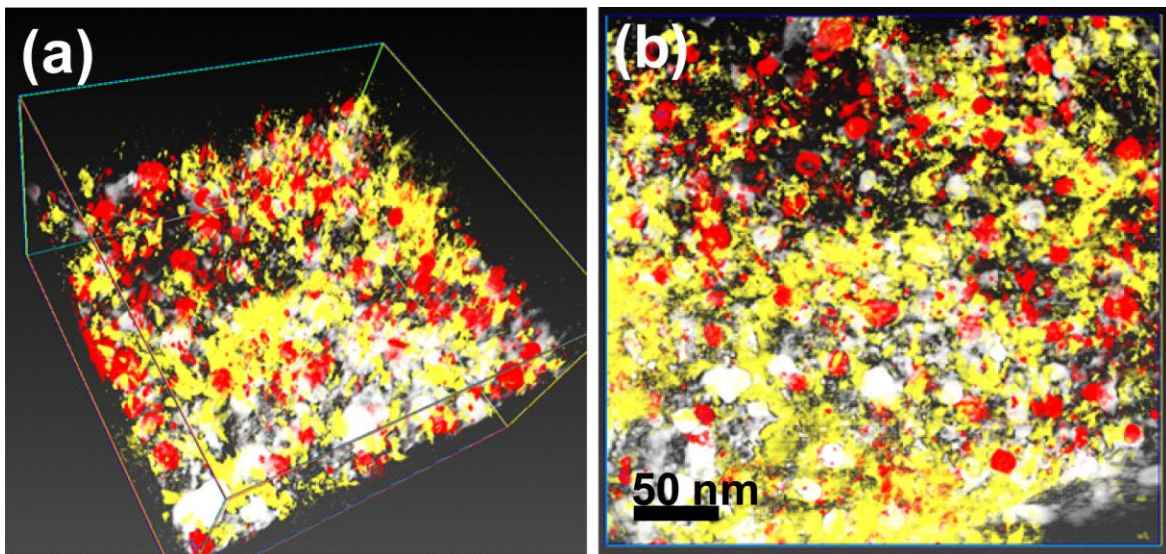


Fig. 5.21 The TEM 3D-tomography of the UNCD films, which were Fe-coated/post-annealed at 900 °C showing the presence of Fe (red color), Fe₃C (white) and nanodiamond or nanographite (yellow) phases on the surface : (a) the stereographic projection and (b) the X-Y projection.

5.4.1.4 Scanning Tunneling Spectroscopy

To reveal as to how the changes in microstructure and concentration of sp^2 , sp^3 , Fe (or Fe₃C) phases, significantly affect the EFE properties in a microscopic scale, the local electronic properties of these films were investigated by STS. STS measurements of as-

deposited and $(\text{Fe}/\text{UNCD})_{900}$ films are illustrated to reveal the change in surface electronic properties due to the Fe-coating/post-annealing processes. Figure 5.22(a) shows the image of an as-deposited UNCD film with its corresponding CITS image in figure 5.22 (b). It seems that the small diamond grains in UNCD films merged with each other and forms a bunch, marked as point "1" in figure 5.22 (a). Bright and dark contrasts are seen in CITS image shown in figure 5.22 (b). Bright contrast in the CITS image shows better electron emission [8]. The emission sites are seen around the grain boundaries of the bunch of diamond grains as seen from the CITS image shown in figure 5.22 (b). Such a typical bunch of diamond grain and grain boundary is marked as "1" and "2", respectively, in figure 5.22 (a) and the corresponding CITS image, taken at a bias of -1.8 V to the sample, is presented in figure 5.22 (b). The as-deposited UNCD film shows a few bright spots indicating less emission sites on the surface. In CITS image, the dark and bright contrast marked as point "1" and point "2" corresponds to the same grain (point "1") and the grain boundary (point "2") of the bunch of diamond grains in STM image shown in figure 5.22 (a). Thus, in as- deposited UNCD films, few emission comes only from the GBs of diamond bunch grains. Moreover, the STM surface morphology of $(\text{Fe}/\text{UNCD})_{900}$ film with its corresponding CITS image, are shown in figure 5.22 (c) and 5.22 (d), respectively. Small nano particles, which are presumed to be Fe-clusters, cover the whole UNCD surface and marked as arrows are seen from the STM image in figure 5.22 (c). The CITS image is taken at the same sample bias of -1.8 V. CITS image taken from the Fe-coated/post-annealed UNCD film (Fig. 5.22 (c)) clearly shows significant bright spots *i.e.*, significant increase in number density of emission sites than as-deposited UNCD films shown in figure 5.22 (b). A typical bunch of diamond grain with grain boundary is

marked as "3" and "4", respectively, in figure 5.22 (c). Interestingly, the emission sites are seen throughout the bunch of diamond grain in $(\text{Fe}/\text{UNCD})_{900}$ film rather than only from the GBs, in case of as-deposited UNCD films, shown in figure 5.22 (b).

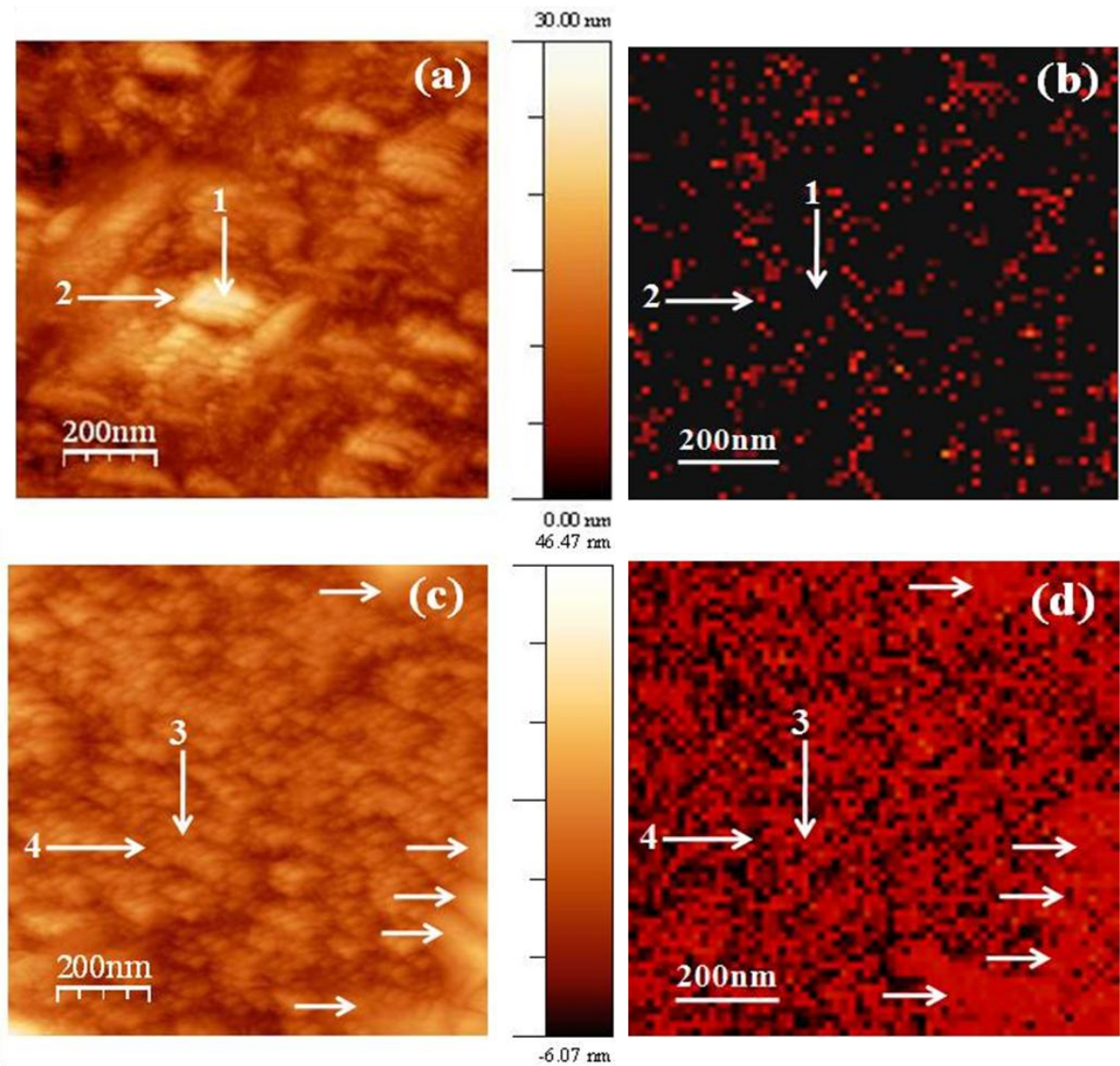


Fig. 5.22 (a) UHV STM image of as-deposited UNCD films with the corresponding CITS image in (b). (c) Fe coated/post-annealed UNCD film at 900 °C with corresponding CITS image in (d). Enhanced emission sites of the Fe-coated/post-annealed film are clearly seen in the CITS image (d) than as-deposited one in (b).

To reveal the actual emission sites in as-deposited and (Fe/UNCD)₉₀₀ films, the HRSTM images are taken along with their corresponding CITS images. The HRSTM image of as-deposited UNCD film with the corresponding CITS image is shown in figure 5.23(a) and figure 5.23 (b), respectively. CITS images are taken at the same sample bias of -1.8 V. HRSTM image shown in figure 5.23 (a) is taken from the position “1” (shown in Fig. 5.22 (a)) shows that the bunch of diamond grain actually composed of many nanometer sized particles of varying diameter from 5 to 10 nm. A typical grain and grain boundary is marked as point “5” and “6”, respectively, in HRSTM image in figure 5.23 (a). It is seen that only the GB sites of the UNCD grains emit by comparing the HRSTM image (Fig. 5.23(a)) with its corresponding CITS (Fig. 5.23(b)) image. However, careful observations reveal that not all the GB sites emit as fewer bright spots are seen around the diamond grains as shown in figure 5.23(b) marked as green arrows. The corresponding positions in STM image (Fig. 5.23(a)) is also marked with green arrow marks. In CITS image in figure 5.23(b), it can be seen that only one side of the green arrow mark show bright spots whereas the other side black region is seen. This means that all the GB sites don't emit electrons. This can be explained as some GB sites consist of the transpolyacetylene phases which blocks the easy transport of electrons and hence lowers the emission process [36, 37]. Hence, in as-deposited UNCD films, only few of the GB sites are made of amorphous carbon phase, which helps in better emission processes [8].

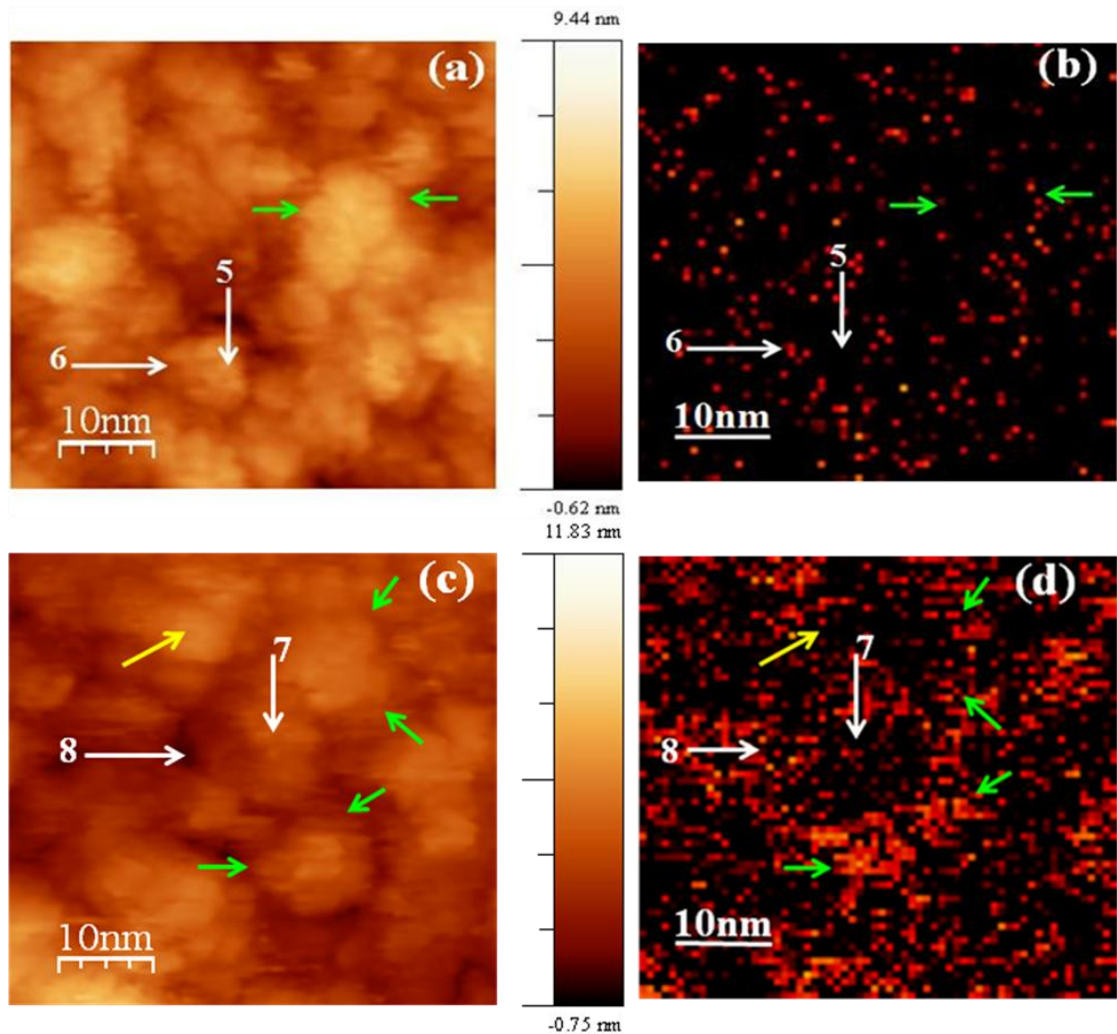


Fig. 5.23 HRSTM image of (a) as-deposited UNCD film with the corresponding CITS image in (b) Fe-coated/post-annealed UNCD film at 900 °C (c) with the corresponding CITS image in (d).

The HRSTM image of the $(\text{Fe}/\text{UNCD})_{900}$ film was taken from the region 3 indicated in figure 5.22(c). The HRSTM image and its corresponding CITS image is shown in figure 5.23(c) and 5.23(d), respectively. Nanoparticles of various sizes (~ 5 to 10 nm) are seen in Fe-coated/post-annealed films in figure 5.23(c). They could be the Fe (or Fe_3C)

nanoparticles as observed during TEM studies. Interestingly, significant increase in emission sites are observed in (Fe/UNCD)₉₀₀ films as more bright spots are seen around the Fe (or Fe₃C) nanoparticles shown in figure 5.23(d). Moreover, not only the emission site density increases but also the width of the bright spots increases. The increase in width of the emission site densities surrounding the Fe (or Fe₃C) nanoparticles are shown by green arrow marks in figure 5.23(d). The increase in width and density of emission sites is clearly revealed by comparing the HRSTM CITS image of as-deposited (Fig. 5.23(b)) with (Fe/UNCD)₉₀₀ film surfaces (Fig. 5.23(d)). It seems that the transpolyacetylene and amorphous carbon phase present at the GB sites of the as-deposited films disappears after the Fe coating/annealing process. The GB sites of the (Fe/UNCD)₉₀₀ films showing enhanced emission sites could be due to the presence of nanographitic phase. This fact is also consistent with our TEM results which show the formation of a few layer nanographitic phases surrounding the Fe (Fe₃C) nanoparticles. Hence it can be concluded that in case of (Fe/UNCD)₉₀₀ films, the surface contains abundant amounts of Fe (Fe₃C) nanoparticles whose boundaries are made up of nanographitic phases. These nanographitic phase content boundaries help in easy transport of electrons around the Fe (or Fe₃C) nanoparticles and thus make an interconnected path throughout the sample surfaces due to their high densities as seen in CITS image shown in figure 5.22(d). Interestingly, the concentration of these nanographitic containing Fe (or Fe₃C) nanoparticles is higher in (Fe/UNCD)₉₀₀ films which shows best EFE properties, confirmed from XPS. The whole (Fe/UNCD)₉₀₀ film surface shows bright emission as shown in figure 5.22(d), due to the presence of high densities of Fe (or Fe₃C) nanoparticles. Moreover, high resolution CITS image reveals that the emission site

density increases around the Fe (Fe_3C) nanoparticles as shown in figure 5.23(d). Even for a lower input bias, the electrons start to emit from the surface of $(\text{Fe}/\text{UNCD})_{900}$ films and hence less turn-on field, as the nanographitic phases help for easy transport of electrons on the film surface which is difficult in as-deposited films due to the lack of these nanographitic phases.

To obtain more insight into the local electronic properties of as-deposited and Fe coated/annealed UNCD films, the local current-voltage (I-V) curves are taken in STS mode from various sample positions. The tunneling current under positive bias is less than that under negative bias, indicating that the films have *n*-type conductivity. Only the negative portions of the I-V curves are shown in figure 5.24(a). Three reproducible I-V spectra were recorded during the scanning of the $(\text{Fe}/\text{UNCD})_{900}$ film. The reproducible I-V spectra (10 each) are shown by dots and the average of these curves are plotted as thick line. Conductivity at the boundaries surrounding the Fe (Fe_3C) nano-particles marked as '8' in figure 5.23(c) and at the green color arrow marked positions show ohmic behavior (shown as curves "iii" in Fig. 5.24(a)). These boundaries could be the nanographitic phase surrounding the Fe (Fe_3C) nanoparticles, also evidenced from TEM study. Significant conductivity has been measured (30 nA at -0.6 V) from these positions. The nanoparticles (marked as '7' in Fig. 5.23(c)) also show high conductivity as shown in curves "ii" in figure 5.24(a) but it requires nearly -1.7 V to attain the same 30 nA tunneling current. These nanosized particles could be the graphitic encapsulated Fe_3C particles, as seen during TEM observation. Few nanoparticles marked as yellow color arrow marked in HRSTM image in figure 5.23(c) also show high tunneling current (curves "i", Fig. 5.24(a)) but needs more input bias of -2.4 V to attain the same 30 nA tunneling

current. The local I-V characteristic curves at the GBs of as-deposited UNCD grains (*e.g.* from area ‘6’ in figure 5.23(a)) also show high conductivity as the curves “iii” shown in figure 5.24(a).

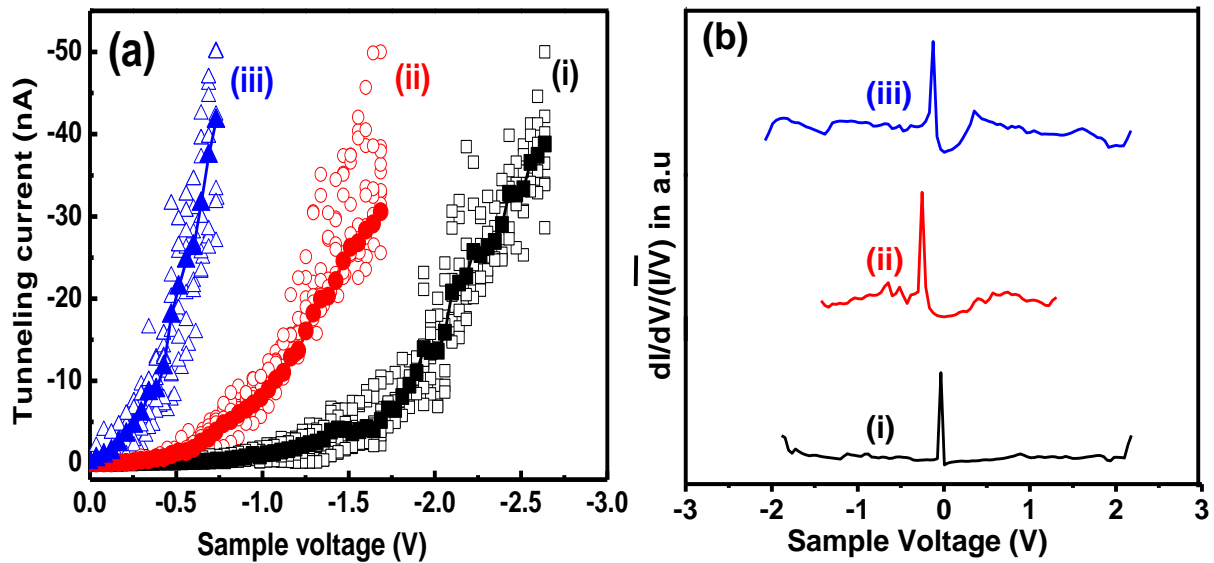


Fig. 5.24 The (a) I-V characteristic curves (thick curve represents the average over the 10 I-V curves at each mentioned point) and (b) normalized differential conductance ($dI/dV/(I/V)$) curves at various locations: (i) boundaries of nano-particles, marked as ‘6’ and ‘8’ in Fig. 5.23 with the green colored arrow positions, (ii) on the yellow arrow marked nanoparticles, marked in Fig. 5.23(c), and (iii) on the oxidized Fe nanoparticle, marked as ‘7’ in Fig. 5.23(c).

It is to be noted here that, diamond grains in as- deposited UNCD (*e.g.* ‘5’ in Fig. 5.23(a)), requires higher bias of -2.9 V to get the same value of 30 nA tunneling current. The enhanced tunneling current from the boundaries of Fe, Fe₃C nanoparticles in Fe-coated/post-annealed UNCD films also explains the superior EFE properties of (Fe/UNCD)₉₀₀ than the as-deposited UNCD films in a microscopic scale.

Figure 5.24(b) shows the normalized conductance $dI/dV/(I/V)$ versus sample bias voltage (V) curves, which are calculated from the I-V characteristic curves measured during the experiments. The normalized conductance spectra [$dI/dV/(I/V)$ versus sample voltage (V) curves] corresponding to the curves “i”, “ii” and “iii” in figure 5.24(a) are shown in figure 5.24(b), which provides information about the distribution of the surface density of states (DOS) of the film [25,26]. The normalized conductance curve “iii” in figure 5.24(b), shows nearly zero band gap (metallic type) for the boundaries, which are marked as point ‘8’ and the green color arrow marks in the HRSTM image (Fig. 5.23(c)). These are the nanographitic phases surrounding the Fe or Fe₃C nanoparticles which are also evidenced from TEM study. Band gap calculations on the yellow arrow marked nanoparticle show nearly metallic behavior (band gap 0.16 eV, curve “ii”, Fig. 5.24(b)). It could be the Fe₃C nanoparticles whose boundaries show bright emission as shown in figure 5.23(d). The formation of the Fe₃C phase was formed by the reaction of Fe with diamond at high temperature of 900 °C, as evident from XPS study. However, band gap calculations from curves shown as “i” in figure 5.24(a) show a gap value of 1.98 eV, as shown in the curve “i” of figure 5.24(b). The large band gap in Fe particle may be due to the presence of thin oxide layer enveloping the Fe particle as a Fe₂O₃ phase, as evident from the XPS study shown in figure 5.17. Restated, the nanographitic phase present at the boundary of these Fe (or Fe₃C) nanoparticles seems to be the main conducting channel for the electrons in addition to the GBs of UNCD.

5.4.2 Why EFE properties of Fe-coated/post-annealed UNCD films are better than that of Fe-coated/post-annealed MCD films?

Generally, in diamond films having micron-sized grains, electrons are transported along the grain boundaries and are emitted from these sites [38, 39]. The density of emission sites is smaller for diamond films with larger grain size (MCD films), as the emission comes from the facets of these micron sized diamond grains. STS in CITS mode in case of as-prepared MCD shown in figure 5.9(b) reveals that the emission sites form a network of hundreds of nanometer in size. However, in case of (Fe/MCD)₉₀₀ films, the emission site density is large (Fig. 5.9(d)). HRSTM image and its corresponding CITS image (Figs. 5.10(a) and 5.10(b)) reveal that the boundaries of the Fe (or Fe₃C) nanoparticles make interconnected paths for electron transport so that the emission site densities are significantly enhanced. The enhancement in EFE properties is thus accounted by the increased number density of emission sites in Fe-coated/post-annealed MCD films in a microscopic scale. Similarly, Fe-coating/post-annealing processes also enhance the EFE properties of the UNCD films. However, the (Fe/UNCD)₉₀₀ films show markedly superior EFE properties, *i.e.*, smaller turn-on field (E_0) and larger EFE current density (J_e), comparing to those for (Fe/MCD)₉₀₀ films. The authentic factor, resulting in such a phenomenon is attributed to the unique granular structure of the UNCD films. The nano-sized and uniformly distributed grains of UNCD films resulted in markedly smaller and densely populated Fe-clusters, which, in turn induced more finer and higher populated nano-graphite clusters. The enhanced EFE properties of (Fe/UNCD)₉₀₀ than (Fe/MCD)₉₀₀ can also be attributed to the availability of significant amount of grain boundary volume fraction in UNCD films than MCD film, which consists of the

nanographitic phase. In addition to the large amount of grain boundary volume fraction, the concentration of nanographitic phase is more in (Fe/UNCD)₉₀₀ films. This fact is clearly seen by comparing XPS and TEM results of (Fe/UNCD)₉₀₀, table 5.2 and fig 5.7(b) respectively, with (Fe/MCD)₉₀₀, table 5.4 and fig. 5.21(b). More importantly, the concentration of the Fe (or Fe₃C) nanoparticles is more when the Fe coated UNCD films are annealed at 900 °C in H₂ atmosphere, as compared with those in Fe-coated MCD films. The presence of nanographitic phase around the Fe (or Fe₃C) nanoparticles in (Fe/UNCD)₉₀₀ samples is presumed to serve as an electron transport medium as well as electron emission sites. The TEM and STM studies indicate markedly larger emission site density for the (Fe/UNCD)₉₀₀ films that has resulted from the higher number density of nano-graphite (Fe and Fe₃C) clusters formed on the (Fe/UNCD)₉₀₀ films. The increase in emission site densities revealed by CITS images (fig. 5.9(d), for (Fe/MCD)₉₀₀ and 5.22(d), for (Fe/UNCD)₉₀₀) also explain the markedly larger EFE current density for (Fe/MCD)₉₀₀ and (Fe/UNCD)₉₀₀ films than their respective as-prepared films in a microscopic scale [(J_e)_{Fe/MCD} = 170 μA/cm² at 7.5 V/μm with (J_e)_{MCD} = 1.15 μA/cm² for as-grown MCD films, (J_e)_{Fe/UNCD} = 705 μA/cm² at 7.5 V/μm with (J_e)_{UNCD} = 9 μA/cm² for as-grown UNCD films]. It seems that the nanographitic phase surrounding the Fe (Fe₃C) nanoparticles in both (Fe/MCD)₉₀₀ or (Fe/UNCD)₉₀₀ films, formed by the reaction of Fe with diamond at 900 °C annealing, play a significant role in EFE properties for these films.

5.5 Conclusion

A thin layer of Fe-coating and subsequent post-annealing at high temperature of 900 °C is seen to modify the surface characteristics and significantly enhance the EFE properties of MCD and UNCD films. However, the Fe-coating/post-annealing processes enhanced the EFE properties of UNCD films more than that of MCD films. The increased number densities of emission sites in (Fe/UNCD)₉₀₀ and (Fe/MCD)₉₀₀ films than their respective as-deposited one are clearly observed from the high resolution CITS images. Microstructural analysis indicates that the mechanism behind the enhanced EFE properties is the formation of nanographitic phase at the boundaries of the Fe (or Fe₃C) nanoparticles, which are formed by the reaction of Fe clusters with diamond films during the annealing process. Furthermore, XPS and TEM results revealed high concentration of nanographitic phases in (Fe/UNCD)₉₀₀ films than (Fe/MCD)₉₀₀. These nanographitic phases are presumed to serve as an electron transport medium as well as electron emission sites. The improved emission properties arising due to the nanographitic phase in (Fe/UNCD)₉₀₀ films are also directly confirmed from the high resolution CITS images. The unique granular structure of the UNCD films also facilitates the better EFE properties for (Fe/UNCD)₉₀₀ films. The Fe-coated/post-annealed UNCD films with better EFE properties open up a new path way for the development of next generation high-definition flat panel displays.

5.6 References

- [1] J. E. Field, 'The Properties of Diamonds', Academic, London, (1979).
- [2] H. Liu, D. S. Dandy, *Diamond Relat. Mater.* **4**, 1173 (1995).
- [3] J. C. Angus, H. A. Will, W. S. Stanko, *J. Appl. Phys.* **39**, 2915 (1968).
- [4] B.V. Spitsyn, L. L. Bouilov, B. V. Derjaguin, *J. Cryst. Growth* **52**, 219 (1981).
- [5] F. J. Himpsel, J. A. Knapp, J. A. Van Vechten, D. E. Eastman, *Phys. Rev. B* **20**, 624 (1979).
- [6] B. B. Pate, *Surf. Sci.* **83**, 165 (1986).
- [7] J. V. D. Weide, Z. Zhang, P. K. Baumann, M. G. Wensell, J. Bernholc, R. J. Nemanich, *Phys. Rev. B* **50**, 5803 (1994).
- [8] K. Panda, B. Sundaravel, B. K. Panigrahi, P. Magudapathy, D. N. Krishna, K. G. M. Nair, H-C Chen, I-Nan Lin, *J. Appl. Phys.* **110**, 044304 (2011).
- [9] A. Lamouri, Y. Wang, G. T. Mearini, I. L. Krainsky, J. A. Dayton, Jr., W. Mueller, *J. Vac. Sci. Technol. B* **14**, 2046 (1996).
- [10] I. N. Lin, Y. H. Chen, H. F. Cheng, *Diamond Relat. Mater.* **9**, 1574 (2000).
- [11] P. C. Huang, W. C. Shih, H. C. Chen, I. N. Lin, *JJAP* **50**, 08KE04 (2011).
- [12] W. Kern, *J. Electrochem. Soc.* **137**, 1887 (1990).
- [13] R. H. Fowler, L. Nordheim, *Proc. R. Soc. London, Ser. A* **119**, 173 (1928).
- [14] J. Thewlis, A. R. Davey, *Phys. Rev. B*, **49**, 9341 (1994).
- [15] E. J. Fasika, G. A. Jeffrey, *Acta Crystallogr.* **19**, 463 (1965).
- [16] Y. F. Chen, *Surf. Sci.* **380**, 199 (1997).
- [17] *Chem. Res. Chinese Universities* **3**, 26, (2010).
- [18] T. Fujii, F. M. F. de Groot, G. A. Sawatzky, *Phys. Rev. B*, **59**, 4 (1999).

- [19] G. Eda, H. E. Unalan, N. Rupesinghe, G. A. J. Amaratunga, M. Chhowalla, *Appl. Phys. Lett.* **93**, 233502 (2008).
- [20] Z. S. Wu, S. Pei, W. Ren, D. Tang, L. Gao, B. Liu, F. Li, C. Liu, H. M. Cheng, *Adv. Mater.* **21**, 1756 (2009).
- [21] D. C. Li, L. Dai, S. Huang, A. W. H. Mau, Z. L. Wang, *Chem. Phys. Lett.* **316**, 349 (2000).
- [22] E. F. Kukovitsky, S. G. L'vov, N. A. Sainov, *Chem. Phys. Lett.* **317**, 65 (2000).
- [23] S. B. Sinnott, R. Andrews, D. Qian, A. M. Rao, Z. Mao, E. C. Dickey, F. Derbyshire, *Chem. Phys. Lett.* **315**, 25 (1999).
- [24] A. Gorbunov, O. Jost, W. Pompe, A. Graff, *Carbon* **40**, 113 (2002).
- [25] R. M. Feenstra, *Surf. Sci.*, **965**, 299 (1994).
- [26] R. M. Feenstra, P. Martensson, *Phys. Rev. Lett.* **61**, 4 (1988).
- [27] H. C. Chen, U. Palnitkar, W. F. Pong, I. N. Lin, A. P. Singh, R. Kumar, *J. Appl. Phys.* **105**, 083707 (2009).
- [28] H. C. Chen, K. Y. Teng, C. Y. Tang, B. Sundaravel, S. Amirthapandian, I. N. Lin, *J. Appl. Phys.* **108**, 123712 (2010).
- [29] Y. Kai-yu, X. Wei, Z. Yu, Z. Wei-tao, W. Xin *Chem. Res. Chinese Universities* **26**, 348 (2010).
- [30] H-F Cheng, Y-M Tsau, T-Y Chang, T-S Lai, T-F Kuo, I-N Lin, *Diamond Relat. Mater.* **12**, 486 (2003).
- [31] B. B. Wang, Q. J. Cheng, X. Chen, K. Ostrikov, *J. Alloy. Compd.* **509**, 9329 (2011).

- [32] D. Zhou, D. M. Gruen, L. C. Qin, T. G. McCauley, A. R. Krauss, *J. Appl. Phys.* **84**, 1981 (1998).
- [33] A. C. Ferrari, J. Robertson, *Phys. Rev. B* **61**, 14095 (2000).
- [34] Y Kai-yu, X, Wei, Z Yu, Z, Wei-tao, Wang, Xin, *Chem. Res. Chinese Universities*, **26**, 348 (2010).
- [35] I. N. Lin, H. C. Chen, C. S. Wang, Y. R. Lee, C. Y. Lee, *CrystEngComm*, **13**, 6082 (2011).
- [36] F. Piazza, A. Golanski, S. Schulze, G. Relihan, *Appl. Phys. Lett.* **82**, 358 (2003).
- [37] D. Pradhan, I. N. Lin, *ACS Appl. Mater. Interfaces* **1**, 1444 (2009).
- [38] M. W. Geis, N. N. Efremow, J. D. Woodhouse, M. D. Mcaleese, M. Marchywka, D. G. Socker, J. F. Hochedez, *IEEE Electron Device Lett.* **12**, 456 (1991).
- [39] R. Krauss, O. Auciello, M. Q. Ding, D. M. Gruen, Y. Huang, V. V. Zhirnov, E. I. Givargizov, A. Breskin, R. Chechen, E. Shefer, V. Konov, S. Pimenov, A. Karabutov, A. Rakhimov, N. SuetinL, *J. Appl. Phys.* **89**, 2598 (2001).

Brief Summary of the Thesis Work and Future Prospectives

6.1 Summary with future Prospectives

Diamond films have been extensively investigated for their application as electron field emitters due to their negative electron affinity and low effective work function properties. Microcrystalline diamond (MCD) films and ultra nanocrystalline diamond (UNCD) films were deposited on silicon substrate by a two-step microwave plasma enhanced chemical vapour deposition (MPECVD) method. In this thesis work, a systematic study has been made to improve and understand the mechanism of electron field emission (EFE) properties by (i) nitrogen ion (N^+) implantation to ultrananocrystalline diamond (UNCD) films, (ii) N ion implantation to hybrid structured micro/ultranano crystalline diamond (MCD/UNCD) films and by (iii) deposition of a thin layer of iron (Fe) on microcrystalline and ultrananocrystalline diamond films followed by post-annealing. This chapter summarises the important results of the thesis along with the scope for future work.

1. In chapter 3, the electron field emission properties of nitrogen ion implanted UNCD films are discussed [1]. The electron field emission properties of the UNCD films get enhanced upon N^+ ion implantation and annealing. Raman spectroscopy and XPS measurements show the increase in sp^2 content of UNCD films upon N^+ ion implantation. I-V characteristics of scanning tunneling spectroscopy (STS) clearly show distinct features for the diamond grains and grain boundaries present in the N^+ ion implanted UNCD films. Electronic band structure of UNCD film reveals a band

gap of 4.8 eV at the grain and reduction of band gap, along with the increase in density of states within the band gap, upon N^+ ion implantation and annealing. The band gap at the grain boundary is less than that of the grain and shows nearly metallic feature upon annealing. The observed decrease in band gap and increase in density of states at the grains and metallic nature of the grain boundary could be responsible for the enhanced field emission properties of N^+ ion implanted UNCD samples. STS in CITS mode shows that grain boundaries are the prominent field emission sites and they have higher conductivity. TEM and CITS measurements show that the width of the grain boundaries increase with N^+ ion implantation. Results at implanted nitrogen fluence of 5×10^{15} ions/cm² give evidence that the grain-boundary electron transport is the predominant mechanism for the electron field emission in N doped UNCD [1].

Moreover, the location, distribution and concentration of N dopants play a crucial role for the electronic application of N doped nanostructured carbon materials [2, 3]. Therefore, it is necessary to confirm the exact position, distribution and concentration of N dopants. Further experimental works are still needed to elucidate the diverse N-doping configurations within the film. In this context, the combined use of both AFM/STM measurements could reveal the location, distribution and chemical identification of dopants in atomic scale which have significant influence for device fabrication. Moreover, efficient doping of nanocrystalline diamond films has still to be developed for better application of diamond as a electron field emitter.

2. In chapter 4, the electron field emission properties of a hybrid diamond nanostructure was discussed [4, 5]. A layer of UNCD film is used as the nucleation layer for the growth of a MCD layer on it. The resulting hybrid diamond structure,

MCD/UNCD, is a unique material exhibiting better EFE properties than the conventional micro, nano or ultrananocrystalline diamond films. N^+ ion implantation has been made to further enhance the EFE properties of the hybrid MCD/UNCD diamond structure. XPS measurements show increased sp^2 content and C-N bonding fraction in N^+ ion implanted and post-annealed films. Scanning tunnelling spectroscopy in current imaging tunnelling spectroscopy mode clearly shows increased number density of emission sites in N^+ ion implanted/post-annealed MCD/UNCD hybrid structured films than as-prepared one. Transmission electron microscopic analysis reveals that the N^+ ion implantation/post-annealing processes induced the formation of defects in the diamond grains that increased the density of states within the band gap of diamond films [4, 5]. Moreover, the formation of nanographitic phase surrounding the small diamond grains enhanced the conductivity at the diamond grain boundaries [4].

Further, in the growth of hybrid structure diamond film, the growth parameters such as thickness of each MCD or UNCD layer, percentage of precursor gases *i.e.* CH_4/H_2 or $CH_4/Ar/H_2$, on the EFE properties of hybrid diamond structure has to be studied in detailed. Since nanographitic phase is the key for the enhanced EFE properties [6, 7] of N implanted hybrid structured diamond films, N could be doped during the growth of each MCD or UNCD layer and then the EFE properties of the hybrid structure can be studied. Moreover, the Fe coating/post-annealing processes, as discussed in chapter 5, on hybrid structured diamond films is expected to enhance the EFE properties further.

3. In chapter 5, the electron field emission properties of Fe coated/post-annealed microcrystalline and ultrananocrystalline diamond films were discussed

[8, 9]. The improvement in EFE properties were explained by Raman, XPS, TEM and STM. TEM analysis indicates the mechanism for improvement in EFE properties is due to the formation of nanographitic phase at the boundaries of the Fe (or Fe₃C) nanoparticles, formed due to the reaction of Fe clusters with diamond films during the annealing process. These nanographitic phases are presumed to serve as an electron transport medium as well as electron emission sites. The improved emission properties arising due to the nanographitic phase in Fe-coated/post-annealed UNCD films are also directly confirmed from the high resolution CITS images [9]. The role of the nanographitic phase in improving the emission sites of Fe coated/post-annealed UNCD films is clearly shown by the current imaging tunnelling spectroscopy (CITS) images [9]. Moreover, the Fe-coating/post-annealing processes enhanced the EFE properties of UNCD films more than that on MCD films. A detailed study is made to understand the enhanced EFE properties of Fe-coated/post-annealed UNCD films than that of MCD films. The enhanced EFE properties of Fe-coated/post-annealed UNCD films is attributed to the availability of significant amount of grain boundary volume fraction in UNCD films than that of MCD film, which consists of the nanographitic phase. In addition to the large amount of grain boundary volume fraction, the concentration of nanographitic phase is more in Fe-coated/post-annealed UNCD films.

Further, the effect of Fe film thickness on the EFE properties of these diamond structures can be examined. Since nanographitic phase formation is the key for the enhanced EFE properties of diamond films, other metallic coating such as Ag, Au, Cr and Ni can be attempted.

6.2 Reference

- [1] Kalpataru Panda, B. Sundaravel, B. K. Panigrahi, P. Magudapathy, D. N. Krishna, K. G. M. Nair, H-C Chen, I-Nan Lin, *J. Appl. Phys.* **110**, 044304 (2011)
- [2] A. S. Bernard, M. Sternberg, *J. Phys. Chem. B* **110**, 19307 (2006)
- [3] L. Zhao, *Science* **333**, 999 (2011)
- [4] Kalpataru Panda, Huang-Chin Chen, B. Sundaravel, B.K Panigrahi, I-Nan Lin *J. Appl. Phys.* **113**, 054311 (2013).
- [5] Kalpataru Panda, B. Sundaravel, H-F Cheng, C-C Horng, H-Y Chiang, H-C Chen, I-N Lin, *Surf. Coat. Tech.*, DOI:10.1016/j.surfcoat.2012.05.107.
- [6] D. Pradhan, I. Nan Lin, *ACS Appl. Mater. Interfaces* **7**, 1444 (2009).
- [7] P. T Joseph, N-H Tai, C-Y Lee, H. Niu, H-F Cheng, W-F Pong, I-Nan Lin, *Plasma Process. Polym.* **6**, S834 (2009).
- [8] K. Panda, B. Sundaravel, B. K. Panigrahi, P-C Huang, W-C Shih, H-C Chen, I-N Lin, *J. Appl. Phys.* **111**, 124309 (2012).
- [9] Kalpataru Panda, B.Sundaravel, B.K. Panigrahi, H-C Chen, P-C Huang, W-C Shih, S-C Lo, L-J Lin, C-Y Lee, I-Nan Lin, *J. Appl. Phys.* **113**, 094305 (2013).

Tribological properties of Nitrogen ion implanted ultrananocrystalline diamond films

A.1 Introduction

Surface engineering provides an excellent means of combining the low friction properties and high wear resistance of different materials and components by incorporating the technology of surface treatment and coating techniques [1]. After an impressive progress in the understanding of tribological performance of solid bulk materials, spectacular developments in last twenty years have emerged from the recognition of distinctive role of thin films, both solid and fluid, in tribology. The operating surfaces might exhibit quite different properties from those of the underlying bulk material [2]. Recently, fundamentals of coatings tribology were reviewed in a generalized approach on the basis of friction and wear mechanisms of coated surfaces in sliding conditions by Holmberg et al. [3]. Moreover, diamond and diamond like carbon coatings have attracted much attention because of their superhardness, high thermal conductivity and low friction behavior [4]. Further, diamond film coatings have attracted tremendous interest in recent years from both the industrial and scientific communities, and their friction and wear properties have, in particular, been the subject of numerous scientific studies [5, 6].

Successful tribological applications of diamond films include coatings for tools, optical components, biological implants, structural materials for microelectromechanical

Appendix

systems (MEMS) and other related devices [7-9]. Applications of DLC films are significantly more established, with uses in hard disk coatings, aerospace bearings, automotive parts, orthopedic implants, and cutting blades [7-9]. In this context, ultrananocrystalline diamond (UNCD) films exhibit unique tribological properties due to their nanocrystalline grain size. The increase in surface to volume ratio of atoms in UNCD films result in distinct physical and chemical properties as compared to bulk diamond [10].

Nanostructured specimen such as nanocrystalline and ultra nanocrystalline diamond (NCD/UNCD) films synthesized by Microwave Plasma Enhanced Chemical Vapour Deposition (MPECVD) technique has unique multifunctional properties compared to bulk diamond [11]. These films exhibit special properties due to the small dimension of the diamond nanocrystallites [12]. The application oriented interest in nanocrystalline diamond films are increasing due to its unique and specific properties such as high hardness, high elastic modulus, high stiffness, high fracture toughness, high thermal conductivity, low thermal expansion, chemical resistivity, chemical inertness, low friction coefficient and high wear resistance [13]. All these above properties make it an attractive material for many engineering applications including cutting tools and mechanical assembly devices which always requires high wear resistance with low friction [13]. Moreover, the friction and wear properties of nanostructured diamond films is anisotropic and depends on the chemical reactivity of the surface, crystallite size, crystallographic orientation, dangling covalent bonds, sliding direction of oriented planes, surface roughness, transfer layer, test environment, and test parameters such as loading and sliding velocity [14-16]. In addition to all known important properties and parameters of

these nanocrystalline diamond surfaces, which influence the tribological behavior, the amount of hydrogen and the sp^3/sp^2 bonding ratio play a significant role on the friction and wear properties [17]. In this context, N^+ ion implantation can be used to tailor the sp^3/sp^2 ratio and formation of more sp^2 bonded network by properly selecting the dose and energy of N^+ ions [18]. This behavior was mainly studied on MCD and NCD films, which includes efforts to improve the field emission behavior. Presently, there is little report which deals with the tribological properties of nitrogen ion implanted UNCD films. Ion implantation to UNCD films causes desorption of hydrogen from the hydrocarbon network present at the grain boundaries resulting in depassivation of dangling bonds. Nitrogen incorporation into the carbon network is found to promote the sp^2 phase fraction of carbon bonding, most likely due to the inherent sp^2 hybridization of the N-electrons. This in turn promotes low friction coefficient, better wear resistance, durability, and reduced internal stresses [19].

This study aims to explore the possible reasons for the improvement in tribological properties of nitrogen ion implanted/post-annealed UNCD films. Detailed structural characteristics have been analyzed by various analytical techniques which explain the nanomechanical and tribological behavior of N^+ ion implanted/post-annealed UNCD films.

A.2 Experimental methods

UNCD films were grown on *n*-type silicon substrates in a MPECVD system (IPLAS-Cyrannus) [20]. A 150 kV ion implanter was used to implant 75 keV nitrogen ions with a fluence of 5×10^{15} ions/cm² on the UNCD films, at room temperature and a pressure below 2×10^{-7} mbar. After implantation, the films were annealed at 600 °C in N_2

Appendix

atmosphere for 30 minutes. The chemical bonding structures were investigated by X-ray photoelectron spectroscopy (XPS) using SPECS make photoelectron spectrometer which uses monochromatic Al K α radiation at 1486.74 eV as a probe. Nanoindentation measurements (CSM Instruments, Switzerland) were performed with a diamond Berkovich indenter with a loading-unloading rate of 4 mN/min. This was performed up to a maximum load of 1.4 mN. Oliver and Pharr method [21] was used to calculate the elastic modulus and hardness of the films. Scratch tests were performed using a Revetest scratch tester (CSM Instruments, Switzerland). A spheroconical diamond indenter with a radius of curvature of 200 μ m was used as the scratching element. Normal load was applied progressively from 1 to 10 N and scratch length was kept constant at 3 mm. Rotational mode of a ball on disk nanotribometer, NTR² (CSM Instruments, Switzerland) was used to carry out tribological tests. Contacting 100Cr6 steel ball sliding against the static film is 1.5 mm in diameter. Sliding speed of the film against the ball and normal load were kept constant at 2 cm/s and 5 mN, respectively. Total sliding distance for each measurement was 10 m. Tribological experiments were conducted in ambient atmospheric condition with relative humidity of 55 %. The surface morphology and wear tracks on the UNCD films were analyzed using a Field Emission Scanning Electron Microscope (FESEM, CARL ZEISS SUPRA 55) and an OXFORD Energy Dispersive X-ray Spectrometer (EDX). The Raman spectra on the surface and wear track were recorded in back scattering geometry using 514.5 nm line of an Ar-ion laser using Renishaw micro-Raman spectrometer (Model INVIA). For simplicity, as-prepared, N⁺ ion implanted and post implanted annealed films are designated as UNCD(I), UNCD(II) and UNCD(III), respectively.

A.3 Results and discussion

A.3.1 Surface morphology of UNCD film examined by FESEM

FESEM micrographs [Figure A.1(a,b,c)] show significant change in surface morphology of UNCD films after the N^+ ion implantation/post annealing processes. Microstructure of the as-prepared films resemble large agglomerates of diamond grains in UNCD(I).

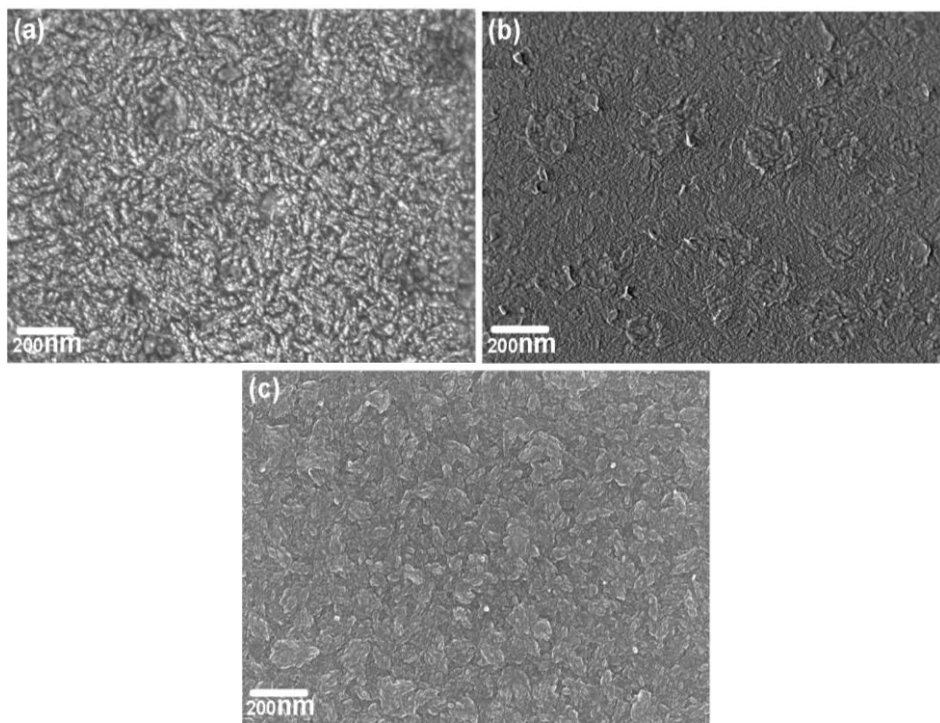


Fig. A.1 FESEM surface morphology of (a) UNCD(I) (b) UNCD(II) and (c) UNCD(III) films.

Agglomerates are composed by fine diamond grains. Further, it can be noticed that such structure disappeared and a smoother surface appeared after the N^+ ion implantation [UNCD(II)]. Cauliflower-like morphology appears after the post-annealing process in [UNCD(III)].

A.3.2 XPS analysis of UNCD films

XPS measurements are carried out to understand how N^+ ion implantation/post-annealing processes attribute to the chemical bonding state of UNCD films. The C-1s photoemission spectrum of UNCD(I), UNCD(II) and UNCD(III) films are shown in figure A.2. N^+ ion implantation influences the sp^2/sp^3 ratio and affects the degree of ordering of sp^2 bonding, inducing formation of amorphous carbon network [22].

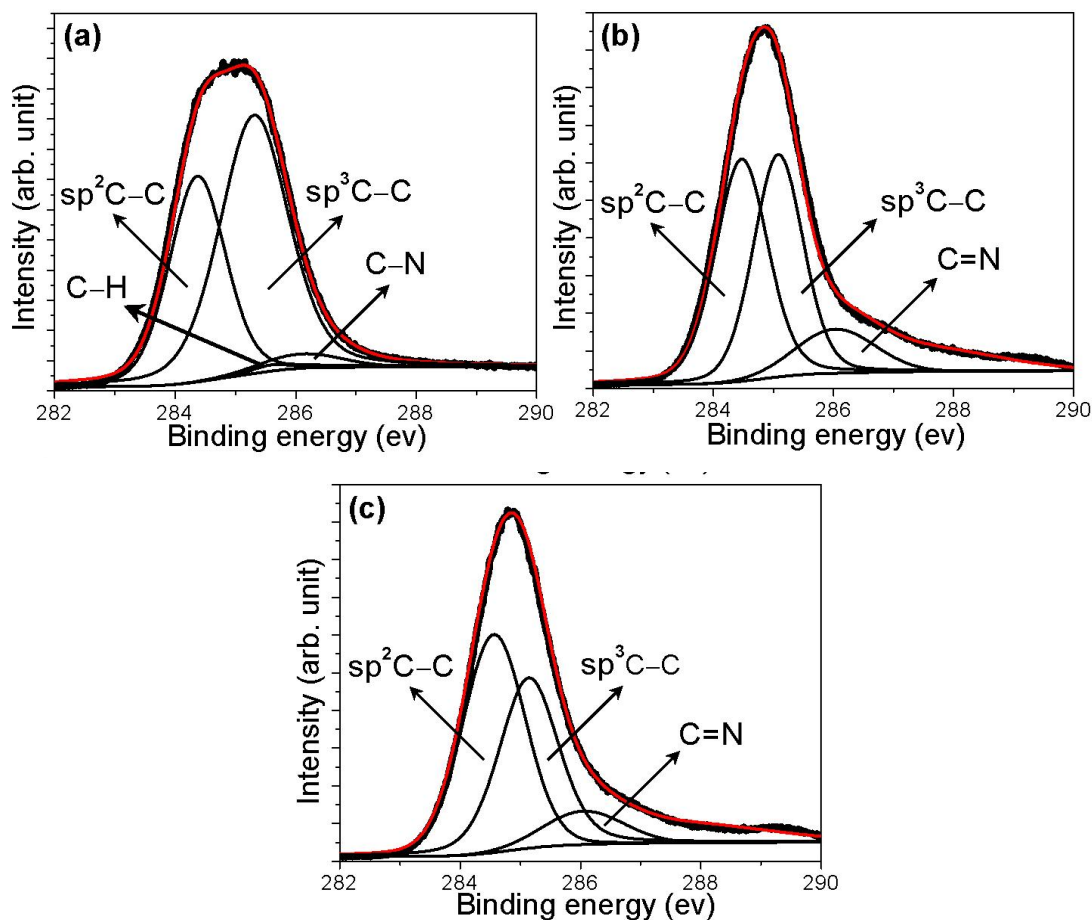


Fig. A.2 XPS C-1s spectra of (a) UNCD(I) (b) UNCD(II) and (c) UNCD(III) films.

Appendix

Relative intensities of these peaks are tabulated in Table A.1. In UNCD(I), sp^3 C–C bonding is predominant at 285.1 eV with a peak intensity of 60.1% while sp^2 C=C present at 284.4 eV with a peak intensity of 37.8%. UNCD(I) film has negligible amount of nitrogen content, which may come during the synthesis process while it increases considerably in N^+ ion implanted, UNCD(II) [figure A.2(b)] and post-annealed, UNCD(III) [figure A.2(c)] films. In UNCD(II), sp^3 C–C peak intensity decreases to 44.5% and sp^2 C=C peak intensity increases to 42.4 %. It is due to the implantation induced conversion of sp^3 to sp^2 bonding [18]. In particular, the ratio of C- sp^3 /C- sp^2 decreases from 1.58 in UNCD(I) to 0.94 and 0.81 in UNCD(II) and UNCD(III) films respectively.

Table A.1 XPS results of UNCD(I), UNCD(II) and UNCD(III) films.

Peak position (eV)	Chemical bonding	Peak intensity (%)		
		UNCD(I)	UNCD(II)	UNCD(III)
284.4	sp^2 C=C	37.8	42.4	53.2
285.1	sp^3 C–C	60.1	44.5	38.2
286.0	C=N	----	13.1	8.6
286.2	C–N	2.1	----	----

It confirms the implantation induced graphitization/amorphization in case of N^+ ion implanted and post-annealed films. The N^+ ion implanted films clearly shows the presence of C=N bonding. This indicates that the chemical bonding between C and N atoms occur during the implantation process. Moreover, the boundary phase as C–H bonding is absent in N^+ ion implanted and post-annealed films. In UNCD(III), sp^2 C=C

peak intensity increases further to 53.2% with the decrease in sp^3 C–C peak intensity to 38.2%. This is attributed to thermally driven transformation of sp^3 to sp^2 phase. It is also known that the thermal stability of sp^2 is higher than sp^3 bonding phase. In UNCD(III) films, the C=N peak intensity decreases compared to UNCD(II). Decrease in intensity of C=N peak upon annealing is due to the lower thermal stability of C=N bonds [23]. In post-annealed films, there will be loss of nitrogen and rearrangement of carbon atoms to form sp^2 C–C bonds.

A.3.3 Raman spectroscopy of UNCD films

The Raman spectra of UNCD (I), UNCD (II) and UNCD (III) films are shown in figure A.3 (a,b,c) respectively. The peaks are de-convoluted using multi-peak Lorentzian fitting method. The spectra shows characteristic feature of UNCD films. A peak at 1369 cm^{-1} , designated as D band that represents zone-edge A_{1g} mode due to the disorder and a comparatively broad G peak centered around 1543 cm^{-1} corresponding to sp^2 network is seen in all these films. These features are thoroughly studied by Ferrari et al. [24] Details of Raman spectra are presented in Table A.2. Diamond D^* peak around 1331 cm^{-1} is observed in visible Raman spectra. UNCD(I) shows a G peak centered at 1543 cm^{-1} indicating prevalence of ordered sp^2 phase. The broadening of the G peak in UNCD(II) film, is related to the disordering of sp^2 clusters due to N^+ ion implantation which ultimately causes amorphization of the graphitic phase. Peak broadening is also related with internal stress, sp^2 admixtures and defects produced due to the N^+ ion implantation. N^+ ion implantation also changes the bonding characteristics of the carbon atoms in

UNCD films. In UNCD(III), the FWHM(G) is found to narrow compared to UNCD(I) and UNCD(II), which indicates the formation of ordered sp^2 clusters.

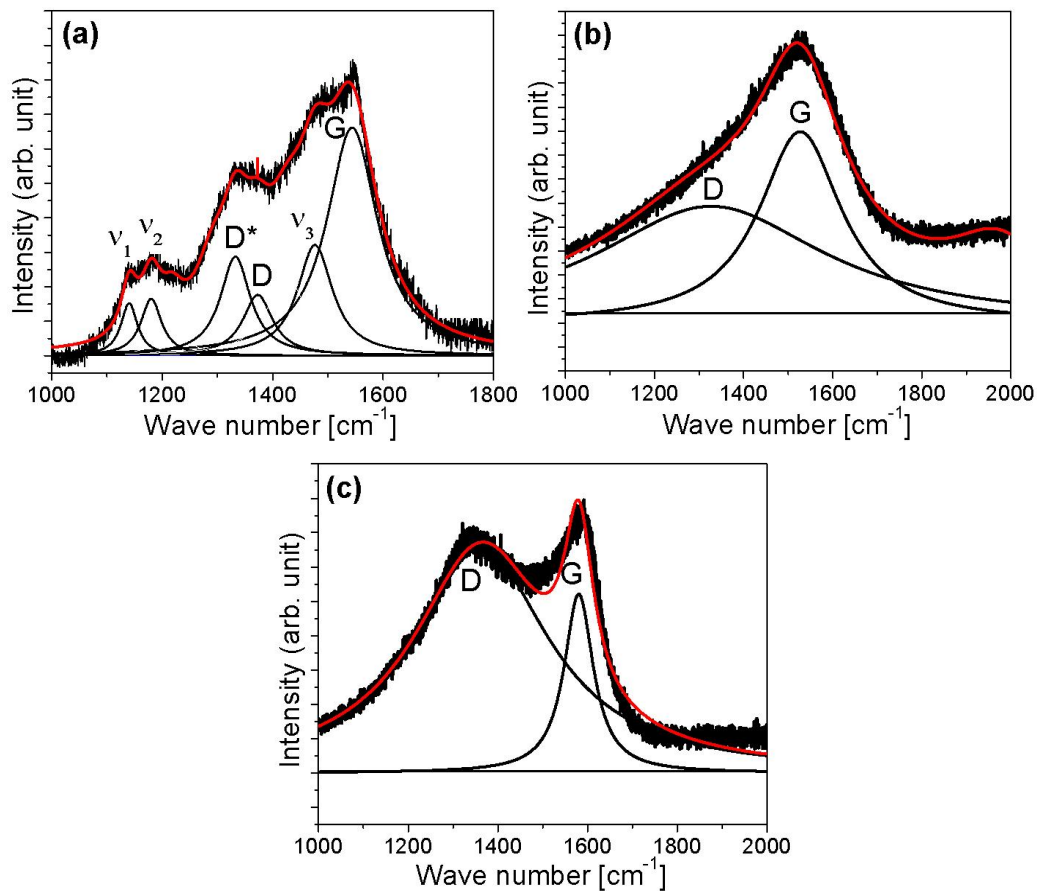


Fig. A.3 Raman spectra of (a) UNCD(I) (b) UNCD(II) and (c) UNCD(III) films.

Table A.2 Raman spectroscopic results of (a) UNCD(I) (b) UNCD(II), (c) UNCD(III).

No	[D*(cm ⁻¹)]	[D(cm ⁻¹)]	[G(cm ⁻¹)]	[I(D)/I(G)]	[FWHM(G) (cm ⁻¹)]
(a)	1331	1374	1543	0.3	110
(b)	-----	1327	1527	0.6	118
(c)	-----	1353	1576	1.14	29

Broad FWHM(G) arises due to bond length and bond angle disorder in sp^2 based aromatic rings. Such local structural alterations like sp^2 clustering and ordering always shift the G peak position [24]. UNCD(III) exhibits highest G band shift (1576 cm^{-1}), and this may be related with ordering of sp^2 clusters and formation of crystalline graphite. In contrast to the G peak dispersion, the I(D)/I(G) ratio and the D peak show maximum dispersion for microcrystalline and nanocrystalline graphites. This dispersion decreases with increasing disorder. The integrated intensity ratio [I(D)/I(G)] of the D and G peaks conventionally indicates the degree of long range ordering in clustered aromatic sp^2 bonding [25]. The D peak indicates disordering in graphitic phase but ordering of an amorphous carbon structure [24]. Increase in I(D)/I(G) values and shifting of G band towards higher frequency side implies the formation of nanographitic matrix and decrease in sp^3 content in amorphous carbon. Three other Raman spectra peaks such as ν_1 , ν_2 (C–H in plane bending) and ν_3 (C=C stretch) bands in UNCD(I), centered at 1140 cm^{-1} , 1180 and 1479 cm^{-1} , respectively, are observed due to the vibration of trans-polyacetylene (TPA) segment present at the grain boundaries [26]. Broader features of these bands signifies disorder TPA chain while higher frequency of ν_1 is a typical fingerprint of transformation of TPA to transpolymeric a-C:H at the grain boundaries [26]. These bands are absent in UNCD(II) and UNCD(III) films, possibly an indication of the breaking of TPA chains to transpolymeric a-C:H due to the N^+ ion implantation and post annealing processes. As TPA states are unstable at high temperatures, these features disappear when UNCD films are annealed at high temperatures [27]. Further, it may be concluded that the structure of

the sp^2 phases and sp^2/sp^3 ratio are significantly modified by the N^+ ion implantation and post-annealing processes.

A.4 Mechanical properties of UNCD films

A.4.1 Nanoindentation

The load-displacement curves obtained for UNCD(I), (II) and (III) films are shown in figure A.4. Shift of load-displacement curves towards lower penetration depths in UNCD(I) is observed. A increase in maximum penetration depth, at the same indentation load, points towards a decrease in penetration resistance of UNCD(II) and UNCD(III) films. The ratio of the elastic work to total work, characterizes the elastic fraction of the total work done during an indentation cycle [28]. A larger value of this ratio indicates that the material is stiffer which in turn indicates the higher hardness of the material. In this context, UNCD(I) shows highest hardness (H) and elastic modulus (E) as 28 GPa and 610 GPa, respectively. These values decreases to 21 GPa and 482 GPa in UNCD(II) films. In UNCD(III), these values are minimum as 16 GPa and 378 GPa respectively. The key parameters in bonding of UNCD films are the sp^3/sp^2 content, clustering and orientation of the sp^3/sp^2 phase. These characteristics lead to influence the H and E values of the films [29]. The decrease in H and E values is related to the increase in sp^2/sp^3 bonding ratio. However, the sp^3 content is directly related with the hardness and elastic constants of UNCD films [29, 30]. As it is evidenced from XPS and Raman spectroscopy that sp^3/sp^2 fraction is higher in UNCD(I) where the H and E values are higher.

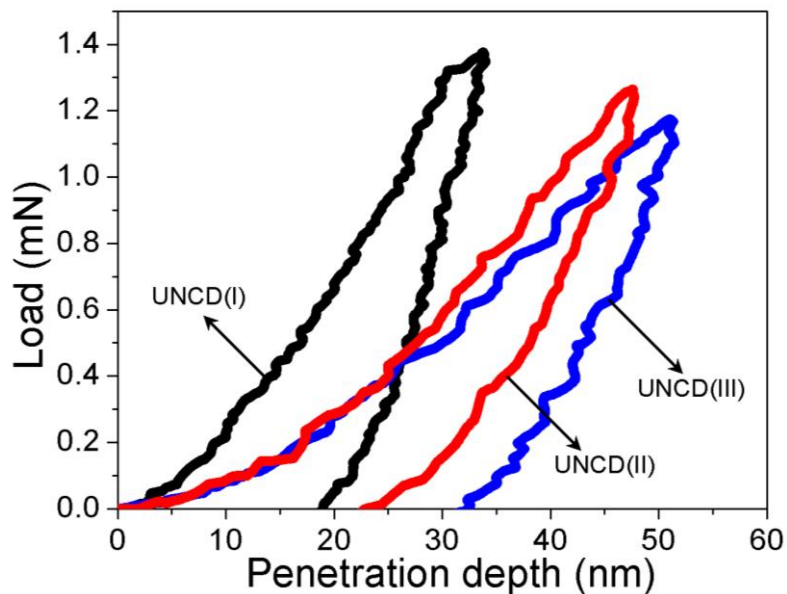


Fig. A.4. Nanoindentation load-displacement curves of (a) UNCD(I) (b) UNCD(II) and (c) UNCD(III) films.

A.4.2 Micro scratch test of UNCD films

The scratch test was performed under progressive loading to determine the scratch resistance of the films. In figure A.5, the applied normal load [$F_n(N)$] versus resulting friction coefficient and acoustic emission (AE) peaks are displayed as a function of the scratch track length. It is seen that the critical load for failure of the film UNCD(II) and UNCD(III) occurs after 5 N of normal force. However, UNCD(I) shows adhesive failure after 2.5 N which may be due to residual stress at the interface which causes to break the interlocking of the bonds. This implies that the film is damaged by interfacial spallation and ploughing at critical load. The trend in friction coefficient during scratch test matches with the evolution of AE curves. This value is low up to ~ 0.08 in UNCD(III) films up to a normal load of ~ 3 N, after that this increases upto ~ 0.6 . In UNCD(I) and UNCD(II), friction coefficients are found to be higher compared to UNCD(III). Low value of friction

coefficient is caused by elastic deformation, while high values points to the formation of cracks, fracture and spallation of the films. The onset of film spallation is observed by the rapid change in acoustic response as well as by visual inspection of the scratch. Similar behavior was studied by Shane et al. and Buijnsters et al [31, 32].

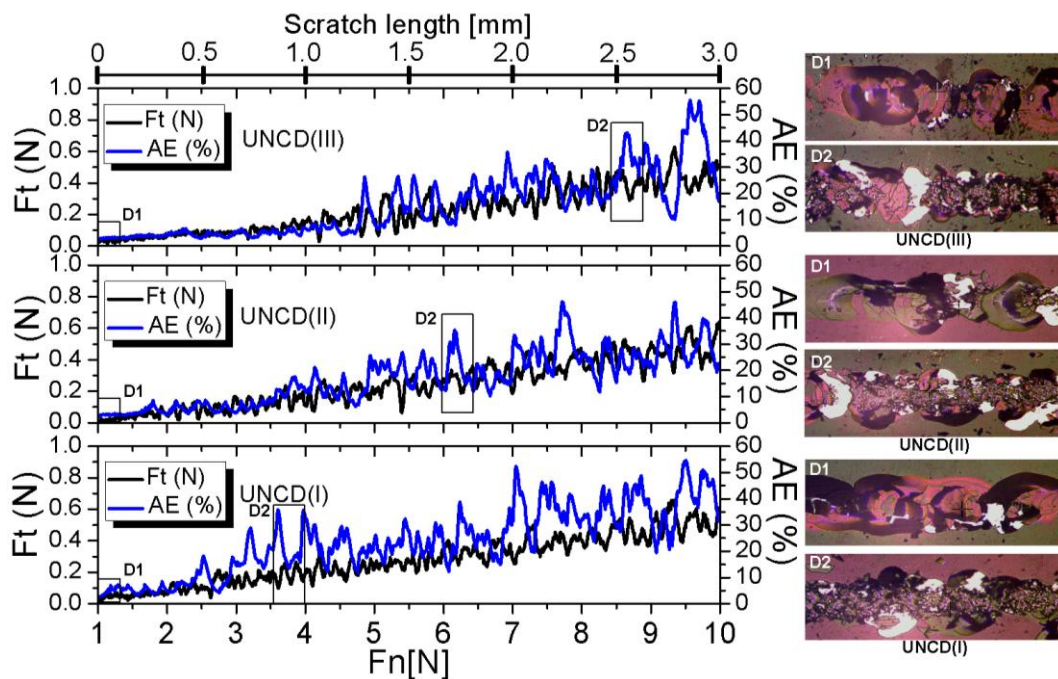


Fig. A.5 Scratch resistance test of (a) UNCD(I) (b) UNCD(II) and (c) UNCD(III) films, optical images are shown with the corresponding film.

The fluctuation of the friction coefficient and acoustic emission can be attributed to the trapping of the broken sharp asperities from the films. At low region of normal load small scale cracks and partially distributed shell shaped spallation are observed in all the films. This region in graph is indicated as D1, which corresponds to D1 in the optical image. However, large scale fracture and interfacial spallation are observed in different regions of the films during the loading as shown by D2.

A.4.3 Tribological properties of UNCD films

Coefficient of friction is found to be 0.15 in UNCD(I) while this values reduce to 0.09 and 0.05 in UNCD(II) and UNCD(III), respectively, as shown in figure A.6. The corresponding micrograph of worn ball contact surfaces are shown as inset of figure A.6. Penetration depth and wear rate of ball counterface is shown in figure A.7. This clearly demonstrate that the total penetration depth is 196 nm [Fig. A.7(a)] which corresponds to a high wear rate of $1.2 \times 10^{-9} \text{ mm}^3/\text{Nm}$ in UNCD(I). In UNCD(II), the film has less deformed. In this case, adhesive and abrasive wear mechanism is dominated by ball counterface. Ball has lower hardness and elasticity while the film is hard with high elastic modulus which resist the plastic deformation and wear of the film during sliding. In UNCD(II), penetration depth of ball and wear rate is found to 178 nm and $4.8 \times 10^{-11} \text{ mm}^3/\text{Nm}$. In UNCD(III), the penetration depth is negligible and a high wear resistance $2.8 \times 10^{-11} \text{ mm}^3/\text{Nm}$ is obtained. It is known that the deformation and wear rate not only depends on the hardness and elasticity of the UNCD film but also on the contribution of sp^2/sp^3 ratio, hydrogen concentration and surface energy [29]. High sp^2 concentration in UNCD can reduce the internal stress which leads to deform the specimen less. This in turn lowers the surface energy and hence enhances the slip behavior. Contact area of ball is observed to be less in UNCD(III) which increases in UNCD(I) and UNCD(II). The wear rate of the sliding ball is calculated by the method proposed by Liang et al [33]. Calculated wear rate of ball is found to be high $3.8 \times 10^{-6} \text{ mm}^3/\text{Nm}$ in ball sliding against UNCD(I). However, this values are $5.6 \times 10^{-7} \text{ mm}^3/\text{Nm}$ and $1.2 \times 10^{-7} \text{ mm}^3/\text{Nm}$ in UNCD(II) and (UNCD(III), respectively.

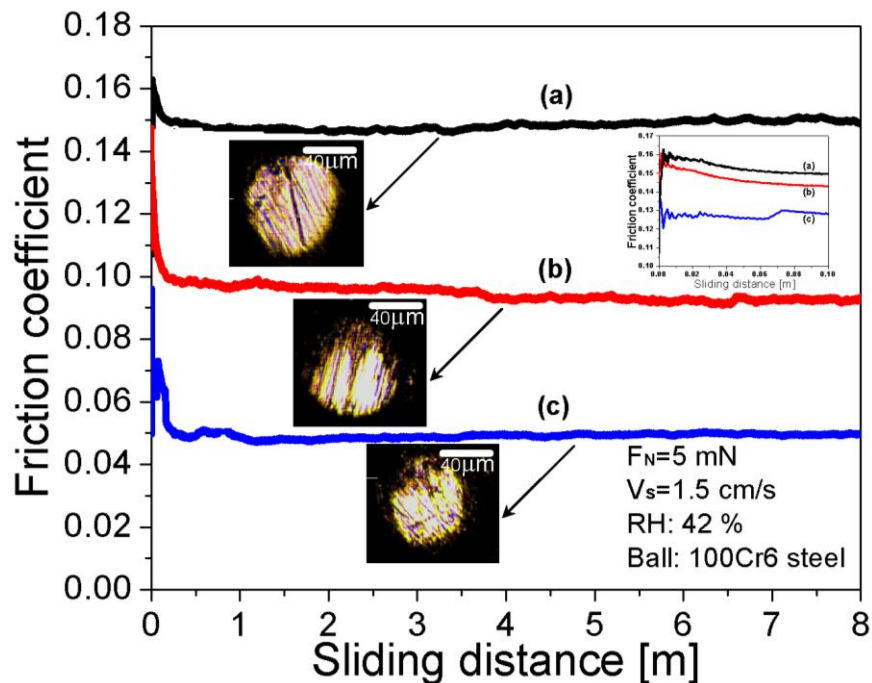


Fig. A.6 Coefficient of friction recorded on (a) UNCD(I) (b) UNCD(II) and (c) UNCD(III). In inset of this figure, the evolution of the coefficient of friction during the initial passes is shown. Optical images of ball sliding face are shown. In inset friction coefficient of initial passes are drawn.

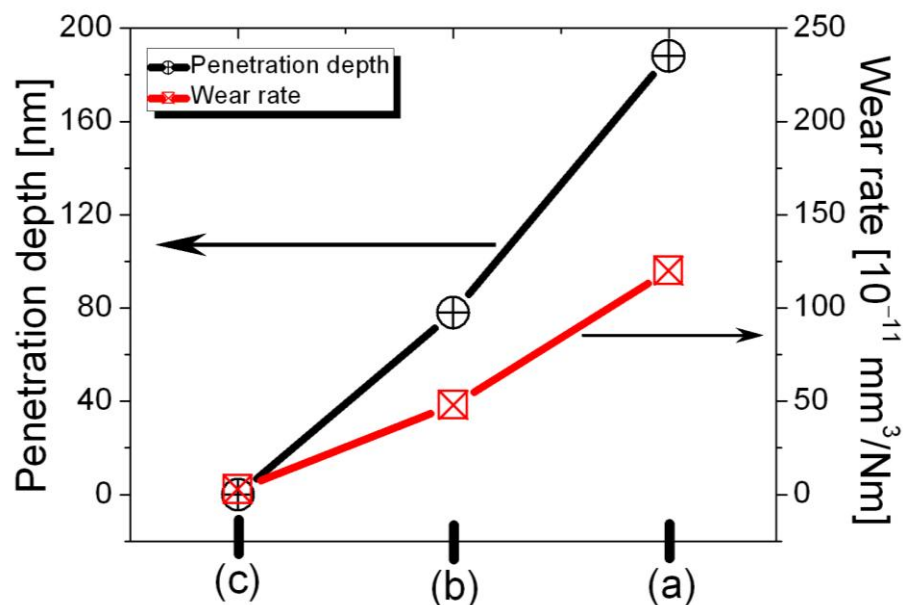


Fig. A.7 Penetration depth and wear rate of (a) UNCD(I) (b) UNCD(II) and (c) UNCD(III).

Appendix

From these results it is found that the wear loss from the ball surface is higher than compared to UNCD film surface. High wear rate of ball due to plugging and micro abrasion is possible if the film has high hardness and elastic modulus compared to the ball. Several physical, chemical, contact mechanical and topographical phenomena are involved for analyzing the coefficient of friction of UNCD films.

As it is explained by XPS (Fig. A.2) that sp^3/sp^2 bonding ratio is dominated in UNCD(I) film, which is found to decrease in UNCD(II) and UNCD(III) due to transformation of sp^3 to sp^2 bonding. Increase in sp^2/sp^3 bonding ratio and improved crystalline phase in UNCD(II) and UNCD(III) compared to UNCD(I) is examined by Raman spectroscopic results (Fig. A.3). It has been shown that, higher volume fraction of grain boundaries with sufficient amount of a-C:H easily passivates the dangling σ bonds present in the nanocrystalline diamond film, causing ultra low friction and extremely low wear in ambient atmospheric conditions [34]. Concentration of hydrogen is high in UNCD(I) due to formation of TPA chain observed by XPS and Raman spectroscopy. In this specific film, mechanism of chemical passivation works, but due to high stress in the film the deformation is easy during tribo test by which free active sites of dangling bonds get enhanced which cause to increase the adhesion. High conductive specimen can provide an additional channel for energy dissipation besides the excitation of phonons, giving rise to an electronic contribution to friction [35]. Intrinsically, high conductivity of the grain and grain boundaries are responsible for reduction in the electrostatic adhesion [36]. This is phenomenological valid for UNCD(II) and UNCD(III). If the conductivity of the diamond surface is low, this can generate tribo induced charging and hence locally increase the electrostatic interaction of the charged particles leading to increase the

electrostatic component of adhesion [36]. Interaction of electrostatic adhesion is known to be stronger compared to adhesive force, generated by the electronic excitation of phonon. In this context, electrostatic component of friction coefficient is high in UNCD(I). Besides the reduced electronic vibration of phonons in low conductive medium, the accumulation of charge may produce the tribo- plasma which leads to increase the adhesive force at sliding surfaces. This has been extensively studied by Nakayama [37]. It has also been observed from STS study that conductivity increases in UNCD(III) and UNCD(II) compare to UNCD(I) [38].

Microstructure is found to be one of the important factors that influence the friction and wear of carbon based materials. In UNCD(II) and (III), hardness and elastic modulus are less compared to UNCD(I) film. We have discussed that hardness and elastic modulus decreases due to N^+ ion implantation and subsequent post annealing. This causes internal stress relaxation in the film. However, high hardness and high elastic modulus have normally high wear resistance. In this case, UNCD(I) should show less friction and high wear resistance. But it has high friction and high wear rate due to the presence of internal and interfacial stress in the film. Despite the low hardness and low elasticity, wear tracks of UNCD(II) and UNCD(III) are not found to be severely deformed under the tribological sliding conditions. This is explained by low internal stress present in the film which resists to pill off from the substrate. In UNCD(I), high friction coefficient is also dominated by severe adhesive and abrasive wear mechanism and formation of larger sliding contact area. However, slippery behavior of surface due to high sp^2 bonding lowers the adhesion between sliding surfaces. Slipperiness behavior of surface reduces sliding resistance and lowers the adhesive/abrasive wear [39].

A.5 wear track analysis

A.5.1 EDAX analysis of wear track

EDAX elemental analysis of the wear tracks is shown in figure A.8. Basically, five elements such as C, O, Si, Fe and N are observed in all these three tracks. Percentage of C is highest (85.12 wt%) in UNCD(III), [Fig. A.8(c)].

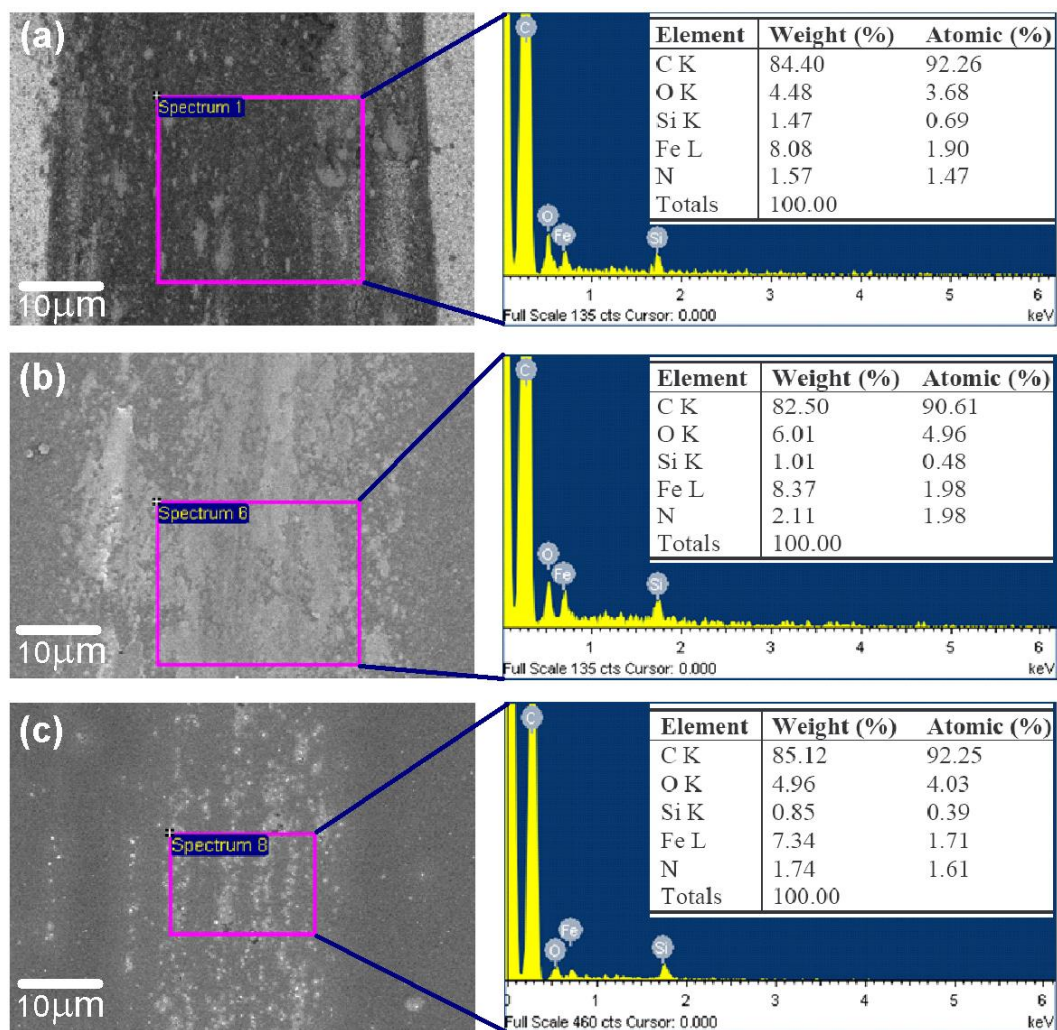


Fig. A.8 EDAX analysis of the wear track formed in (a) UNCD(I) (b) UNCD(II) and (c) UNCD(III) films.

However, carbon content is more or less similar in UNCD(I) and UNCD(II) films [Fig. A.8(a) and Fig. A.8(b)]. Tribological tests performed in the ambient atmospheric condition which may account for the presence of oxygen constituent in the wear tracks. The wt% of O and Fe are 6.01 and 8.37 wt%, respectively. The wt% of Fe is 7.34 in UNCD(III) track. Little amount of silicon is also detected from the substrate exposing during the tribo test. Silicon may come from the matting ball, as it is known that 100Cr6 steel ball contains 0.35 wt% of silicon. However, nitrogen is high 2.11 wt% in N⁺ ion implanted [UNCD(II)] films. After annealing nitrogen reduces to 1.74 wt% in UNCD(III) films.

A.5.2 Raman spectral analysis of wear track

It is seen from figure A.9 that the trend in Raman spectra of the wear tracks are similar with the spectra recorded from the surface of the films. However, the intensity of spectra such as D, G, ν_1 , ν_2 and ν_3 peaks in wear track formed on UNCD(I) films [Fig A.9(a)] decreases significantly compared to the spectral intensity obtained from the virgin film surface [Fig A.3(a)]. It is observed that the D (1365 cm^{-1}) and G (1557 cm^{-1}) band positions in wear track of UNCD(I) films are shifted towards lower and higher frequencies, respectively, comparing to the virgin film surface. This behavior indicates formation of strain in sp^2 and sp^3 sites [25]. This may also reduce the crystalline properties of sp^2 clusters. TPA related peaks such as ν_1 (1135 cm^{-1}), and ν_3 (1470 cm^{-1}) are also shifted towards lower frequency side which is an indication of disordered and formation of short range chains of TPA constituents in grain boundaries of UNCD(I) films. Increase in I(D)/I(G) values in wear track compared to film surface of UNCD(I),

shows disorder while broader FWHM(G) reveals amorphization in the wear tracks. In case of wear tracks, formed on UNCD(II), the D and G bands shifted towards lower wave number sides due to tribochemical reaction [Fig A.9(b)].

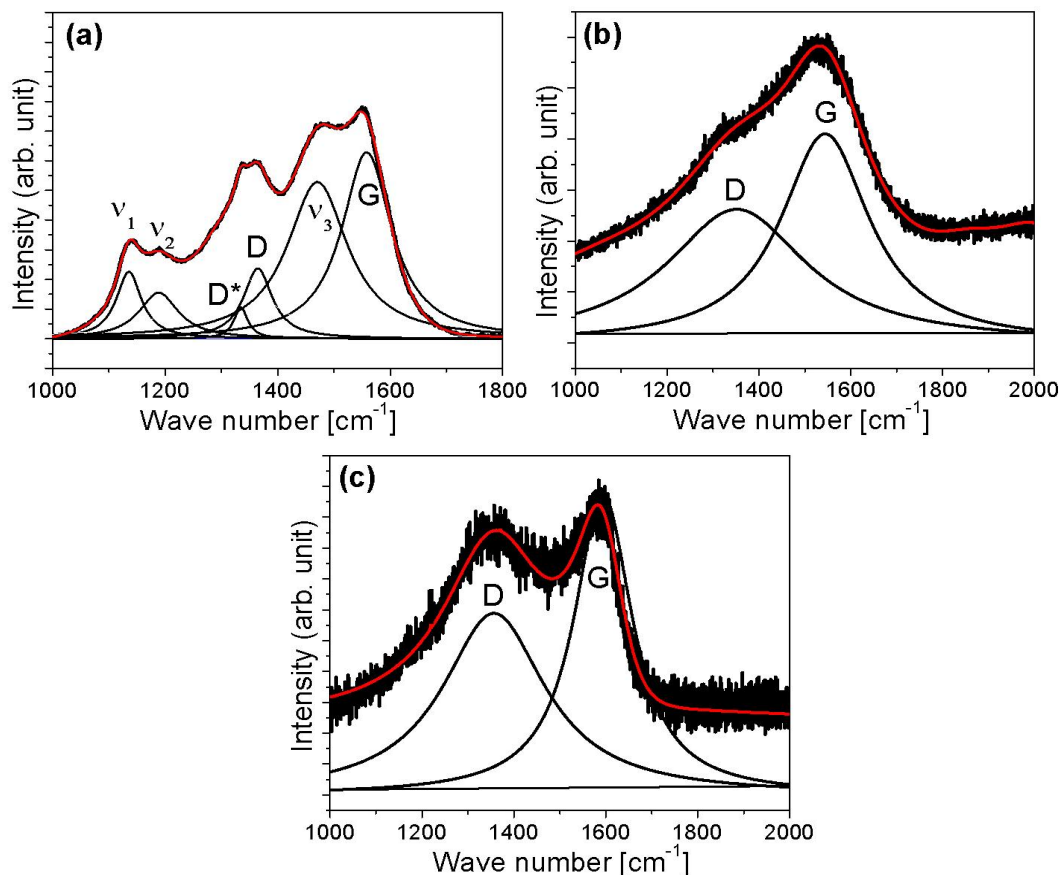


Fig. A.9 Raman spectroscopy of wear track on films (a) UNCD(I) (b) UNCD(II) and (c) UNCD(III).

The detail of the spectra is given in Table A.3. The shift of G band towards higher frequency side is an indication of improved crystallinity of sp^2 clusters in UNCD(III). This also occurs due to the strain localization in sp^2 and sp^3 sites during sliding [24].

Table A.3 Raman spectroscopic results obtained from the wear tracks of UNCD films (a) UNCD(I) (b) UNCD(II), (c) UNCD(III).

No	[D*(cm ⁻¹)]	[D(cm ⁻¹)]	[G(cm ⁻¹)]	[I(D)/I(G)]	[FWHM(G) (cm ⁻¹)]
(a)	1332	1365	1557	0.82	123
(b)	-----	1351	1531	0.56	92
(c)	-----	1351	1596	0.62	78

Decrease of width and peak shift of G band towards higher frequency is attributed to a progressive reduction of defects such as bond-angle and bond-bending disorder in the sp^2 amorphous carbon cluster [24]. Low value of FWHM(G) and higher value of I(D)/I(G) is an indication of graphitization. I(D)/I(G) value is found to be low in wear track of UNCD(II) and UNCD(III) films, due to disorder accompanied by strain. In case of UNCD(III), the D band position is more or less similar to the film surface but G peak position gets shifted towards high frequency side (1596 cm⁻¹). This indicates clustering and ordering of sp^2 carbon lattice and subsequent transformation to nanocrystalline graphite [Fig A.9(c)] [24]. On the other hand, polymerization of a-C:H, may reduce the FWHM(G), consistent with the disorder. In UNCD(III) films, graphitization is a prominent feature which causes to decrease the I(D)/I(G) values to 0.62 from 1.14. This leads to the formation of larger clusters due to the tribochemical reaction. These results are characteristic of carbon with crystalline features [40].

A.6 Conclusion

The chemical and bonding characteristic of as- deposited UNCD films are modified due to N⁺ ion implantation and subsequent post annealing. C_{sp^2}/C_{sp^3} is found to be 0.81

for as- deposited film and this ratio increases to 0.94 and 1.58 while modifying the film with implantation and annealing process, respectively. This modification process decreases the hardness and elastic modulus, related to the increase in sp^2/sp^3 ratio in the films. Chemical structure of UNCD films changed and I(D)/I(G) value are found to low in wear tracks of modified UNCD surfaces. The chemical state, structure and microstructure of these films are well correlated with tribological properties. Synergetic combination of all the above factors and properties found to influence the friction coefficient.

A.7 References

- [1] R. J. Wakelin, Annual Review of Materials Science **4**, 221 (1974).
- [2] D. Dowson, C. M. Taylor, T. H. C. Childs, M. Godet, G. Dalmaz, Proceedings of the 19th Leeds-Lyon Symposium on Tribology, Elsevier Science Publishers, The Netherlands (1992).
- [3] K. Holmberg, H. Ronkainen, A. Matthews, Ceram. Intl. **26**, 787 (2000).
- [4] Kenneth Holmberg, Allan Matthews, Helena Ronkainen, Tribol. Inter. **31**, 107 (1998).
- [5] A. Erdemir, C. Donnet, 'Modern Tribology Handbook', CRC Press, 871 (2000).
- [6] A. Erdemir, J. Eng. Tribol. **216**, 387 (2002).
- [7] A.V. Sumant, A. R. Krauss, D. M. Gruen, O. Auciello, A. Erdemir, M. Williams, A. F. Artiles, W. Adams, Tribol. Trans. **48**, 24 (2005).

Appendix

- [8] O. Auciello, S. Pacheco, A. V. Sumant, C. Gudeman, S. Sampath, A. Datta, R. W. Carpick, O. Auciello, S. Pacheco, A. V. Sumant, C. Gudeman, S. Sampath, A. Datta, R. W. Carpick, V.P. Adiga, P. Zurcher, Z. Ma, H. C. Yuan, J. A. Carlisle, B. Kabius, J. Hiller, *IEEE Microw. Mag.* **8**, 61 (2008).
- [9] X. Xiao, J. Wang, J. A. Carlisle, B. Mech, R. Greenberg, R. Freda, M. S. Humayun, J. Weiland, O. Auciello, *J. Biomed. Mater.*, **77B**, 273 (2006).
- [10] X. Liu, F. Klauser, N. Memmel, E. Bertel, T. Pichler, M. Knupfer, A. Kromka, D. Steinmuller-Nethl, *Diamond Relat. Mater.* **16**, 1463 (2007)
- [11] A. Orlando, S. V Anirudha. *Diamond Relat. Mater.* **19**, 699 (2010).
- [12] F. R Kloss, M. Najam-Ul-Haq, M. Rainer, R. Gassner, G. Lepperdinger, C. W Huck, G. Bonn, F. Klauser, X. Liu, N. Memmel, E. Bertel, J. A Garrido, D. Steinmuller-Nethl., *J. Nanosci. Nanotechnol.* **7**, 4581 (2007).
- [13] A. Olszyna, J. Smolik, *Thin Solid Films* **459**, 224 (2004).
- [14] L. Pastewka, S. Moser, P. Gumbsch, M. Moseler, *Nature Mater.* **10**, 34 (2011).
- [15] G. Zilibotti, M. C Righi, M. Ferrario, *Phys. Rev.B* **79**, 75420 (2009).
- [16] A. R Konicek, D. S Grierson, P. Gilbert, W. G Sawyer, A. V Sumant, R. W Carpick, *Phys. Rev. Lett.* **100**, 235502 (2008).
- [17] D. S Grierson, R. W Carpick, *Nanotoday* **2**, 12 (2007).
- [18] Praver S, Kalish R. Ion-beam-induced transformation of diamond. *Phys. Rev.B* 1995;51:15711–22
- [19] A. Khurshudov, K. Kato, D. Sawada, *Tribology Letts.* **2**, 13 (1996).
- [20] P. T Joseph, N. H Tai, C. Y Lee, H. Niu, W. F Pong, I. N Lin., *J. Appl. Phys.* **103**, 43720 (2008).

Appendix

- [21] W. C Oliver, G. M Pharr, *J Mater Res* **7**, 1564 (1992).
- [22] K. L Ma, W. J Zhang, Y. S Zou, Y. M Chong, K. M Leung, I. Bello, S. T Lee, *Diamond Relat. Mater.* **15**, 626 (2006).
- [23] J. J Li, W. T Zheng, H. H Wu, L. Sun, G. G Gu, H. J Bian, X. Y Lu, Z. S Jin, *Journal of Physics D: Applied Physics*, **36**, 2001 (2011).
- [24] A. C Ferrari, J. Robertson, *Phys. Rev.B* **61**, 14095 (2000).
- [25] M. J Matthews, M. A Pimenta, G. Dresselhaus, M. S Dresselhaus, M. Endo, *Phys. Rev.B*, **59**, 6585 (1999).
- [26] H. Kuzmany, R. Pfeiffer, N. Salk, B. Gunther, *Carbon* **42**, 911 (2004).
- [27] R. Pfeiffer, H. Kuzmany, P. Knoll, S. Bokova, N. Salk, B. Günther, *Diamond and Relat. Mater.* **12**, 268 (2003).
- [28] J. H Ayesha, P. R Munroea, M. Hoffmana, P. J Martina, B. A. Berkovich, *J Mater Res* **23**, 1862 (2008).
- [29] A. C Ferrari, J. Robertson, R. Pastorelli, M. G Beghi, C. E Bottani, *Appl. Phys. Lett* **75**, 1893 (1999).
- [30] Y. Lifshitz, *Diamond Relat. Mater.* **5**, 388 (1996).
- [31] A. C Shane, B. James, Y. K Vohra, W. R Lacefield, J. E Lemons, *J. Appl. Phys.* **91**, 5347 (2002).
- [32] J. G Buijnsters, P. Shankar, W. J. P Enckevort van, J. J Schermer, J. J Meulen, *Thin Solid Films* **474**, 186 (2005).
- [33] L. Qi, A. Stanishevsky, Y. K Vohra, *Thin Solid Films* **517**, 800 (2008).
- [34] N. Sharma, N. Kumar, B. Sundaravel, K. Panda, W. M. D. Kamarrudin, S. Dash, B. K Panigrahi, A. K Tyagi, I. N Lin, B. Raj, *Tribol. Inter.* **44**, 980 (2011).

Appendix

- [35] K. Marcin, G. Enrico, G. Urs, M. Laurent, R. Simon, M. Ernst, *Nature Materials* **10**, 119 (2011).
- [36] A. Erdemir, C. Donnet, *Journal of Physics D: Applied Physics* **39**, 311 (2006).
- [37] K. Nakayama, *Surf. Coat. Technol.* **188**, 599 (2004).
- [38] K. Panda, B. Sundaravel, B. K. Panigrahi, P. Magudapathy, D. N. Krishna, K. G. M. Nair, H-C Chen, I-Nan Lin, *J. Appl. Phys.* **110**, 044304 (2011).
- [39] Y. Song, R. N Premachandran, M. Zou, Y. A Wang, *Thin Solid Films*, **518**, 3801 (2010).
- [40] Z. Qun-feng, D. Guang-neng, X. You-bai, *Applied Surface Science*, **254**, 3859 (2008).

Publications

Included in Thesis

- 1. Direct observation of enhanced emission sites in nitrogen implanted hybrid structured ultrananocrystalline diamond films.**

Kalpataru Panda, Huang-Chin Chen, B. Sundaravel, B.K Panigrahi, I-Nan Lin, J. Appl. Phys. **113**, 054311 (2013).

- 2. The induction of nanographitic phase on Fe coated diamond films for the enhancement in electron field emission properties.**

Kalpataru Panda, B.Sundaravel, B.K. Panigrahi, H-C Chen, P-C Huang, W-C Shih, S-C Lo, L-J Lin, C-Y Lee, I-Nan Lin, J. Appl. Phys. **113**, 094305 (2013).

- 3. Tribological properties of N⁺ ion implanted ultrananocrystalline diamond films.**

Kalpataru Panda, N. Kumar, B. K. Panigrahi, S. R. Polaki, S. Dhara, B. Sundaravel, S. Dash, A. K. Tyagi, I-Nan Lin, Tribol. Inter. **57**, 124 (2013).

- 4. Direct observation and mechanism of increased emission sites in Fe-coated microcrystalline diamond films.**

Kalpataru Panda, B. Sundaravel, B. K. Panigrahi, P-C Huang, W-C Shih, H-C Chen, I-N. Lin, J. Appl. Phys. **111**, 124309 (2012).

- 5. N-ion implantation of micro/nanocrystalline duplex structured diamond films for enhancing their electron field emission properties.**

Kalpataru Panda, B. Sundaravel, H-F Cheng, C-C Horng, H-Y Chiang, H-C Chen, I-N Lin, Surf. Coat. Tech, DOI:10.1016/j.surfcoat.2012.05.107.

- 6. Structural and electronic properties of nitrogen ion implanted ultra nanocrystalline diamond surfaces.**

Kalpataru Panda, B. Sundaravel, B. K. Panigrahi, P. Magudapathy, D.N. Krishna, K.G.M. Nair, H-C Chen, I-Nan Lin, J. Appl. Phys. **110**, 044304 (2011).

- 7. Enhanced electron field emission by tuning the microstructure of diamond films for plasma illumination application.**

Kalpataru panda et. al. (Manuscript under preparation)

- 8. Improved Electron field emission properties of N⁺ ion implanted hybrid structured diamond films for plasma illumination application.**

Kalpataru panda et. al. (Manuscript under preparation)

Not included in Thesis

1. STM observation of surface transfer doping mechanism in 3 keV nitrogen ion implanted UNCD films.

B. Sundaravel, **Kalpataru Panda**, R. Dhandapani, B.K. Panigrahi, K.G.M. Nair, I-Nan Lin, AIP Conf. Proc. **1512**, 384 (2013).

2. Structural and electrical properties of conducting diamond Nanowires.

K J Sankaran, Y-F Lin, W-B Jian, H-C Chen, **Kalpataru Panda**, B. Sundaravel, C-L Dong, N-H Tai, I-N Lin, ACS Appl. Mater. Interfaces, **5**, 1294 (2013).

3. Tribological and electrical properties of nanocrystalline Cu films deposited by DC magnetron sputtering.

M. Geetha, N. Kumar, **Kalpataru Panda**, S. Dhara, S. Dash, B.K. Panigrahi, A.K. Tyagi, R. Jayavel, V. Kamaraj, Tribol. Inter. **58**, 79 (2013).

4. An easy route to make superhydrophobic surface.

Kalpataru Panda, N. Kumar, S. R. Polaki, B. K. Panigrahi, AIP Conf. Proc. **1447**, 767 (2012).

5. Engineering the Interface Characteristics of Ultrananocrystalline Diamond Films Grown On Au-Coated Si Substrates.

K. J. Sankaran, **Kalpataru Panda**, B. Sundaravel, H-C Chen, I-N Lin, C-Y Lee, N-H Tai, ACS Appl. Mater. Interfaces, **4**, 8 (2012).

6. Electrophoresis of nanodiamond on the growth and electron field emission properties of UNCD films on silicon nanowires.

T-H Chang, **Kalpataru Panda**, B. K. Panigrahi, S-C Lou, C Chen, H-C Chan, I-N Lin, N-H Tai, J. Phys. Chem. C, **116**, 16740 (2012).

7. Enhancement of electron field emission properties of TiO_{2-x} nanoplatelets by N-Doping.

N. C. Raut, Tom Mathews, **Kalpataru panda**, B. Sundaravel, S. Dash, A. K. Tyagi RSC Advances, **2**, 812 (2012).

8. Enhanced Field Emission Properties of Electrochemically Synthesized Self-Aligned Nitrogen-Doped TiO₂Nanotube Array Thin Films.

R. P Antony, T. Mathews, **Kalpataru Panda**, B Sundaravel, S. Dash, A. K. Tyagi, J. Phys. Chem. C, **116**, 16740, (2012).

9. Tribological properties of nanocrystalline diamond films deposited by hot filament chemical vapor deposition

N. Kumar, **Kalpataru Panda**, S. Dash, C. Popov, J.P. Reithmaier, B.K. Panigrahi, A.K. Tyagi, Baldev Raj, AIP Advances, **2**, 032164 (2012).

10. Effect of N⁺ ion implantation on micro/nano tribological properties of nanocrystalline diamond films.

Kalpataru Panda, N. Kumar, B.K. Panigrahi, S. R. Polaki, S. Dash, A. K. Tyagi, I-Nan Lin, Tribol. Inter. **57**, 184 (2012).

11. Tribological properties of ultrananocrystalline diamond and diamond nanorod films.

Kalpataru Panda, N. Kumar, K.J. Sankaran, B.K. Panigrahi, S. Dash, H-C Chen, I-N Lin, N-H Tai, A.K. Tyagi, Surf. Coat. Tech, **207**, 535 (2012).

12. Effect of CH₄/H₂ plasma ratio on ultra-low friction of nano-crystalline diamond coating deposited by MPECVD technique.

N. Sharma, N. Kumar, B. Sundaravel, **Kalpataru Panda**, W. David, M. Kamarrudin, S.Dash, B.K. Panigrahi, A.K. Tyagi, I-N Lin, B. Raj, Tribol. Inter, **44**, 980 (2011).

13. Microstructure and chemical characteristic dependent friction coefficient mechanism in nanocrystalline diamond films.

Kalpatru Panda, N. Kumar, S.R. Polaki, B.K. Panigrahi, S. Dash, A.K. Tyagi, I-Nan Lin, (Submitted).

14. The influence of nitrogen concentration on microstructure and tribological properties of Fe-N thin films.

S. Chakravarthy, N. Kumar, R. Gupta, **Kalpataru Panda**, T. R Ravindran, B. K Panigrahi, S. Dash, A. K Tyagi, G. Amarendra (Submitted).

Conferences Presentation

1. Enhanced field emission and scanning tunneling microscopy studies of iron coated microcrystalline diamond films

Kalpataru panda, B. Sundaravel, B.K. Panigrahi, K.G.M Nair, I-Nan Lin, ICONSAT, Hyderabad, 2012, India.

2. Synthesis and characterization of silicon nanowire arrays

Kalpataru Panda, S. Amirthapandian, S. Santra, B.K Panigrahi, International conference on electron nanoscopy, 2011, Hyderabad, India.

3. Electronic and field emission properties of ultrananocrystalline diamond surfaces

Kalpataru Panda, B. Sundaravel, B. K. Panigrahi, K. G. M. Nair, I-Nan Lin, International Conference on Carbon Nanotechnology, IIT Kanpur, 2010, India.

4. Large area synthesis of Silicon nanowires to increase the thermoelectric

performance Kalpataru Panda, B. Sundaravel and B.K Panigrahi, **IBSA nanoschool**, Chennai, 2010, India.

**5. Synthesis of helical carbon nanotubes and their field emission characteristics,
International Conference on Carbon Nanotechnology:**

R. Kamalakannan, **Kalpataru Panda**, B. Sundaravel, T. paul, T. R. Ravindran, M. Kamruddin, and A. K. Tyagi, , International Conference on Carbon Nanotechnology, IIT Kanpur, 2010, India.